



Briggs, Joseph Henry (2021) *The analysis, experimental characterisation and prototyping of technologies for making quantum noise limited detections of gravitational waves*. PhD thesis, University of Glasgow.

<http://theses.gla.ac.uk/82330/>

Copyright and moral rights for this work are retained by the author

A copy can be downloaded for personal non-commercial research or study, without prior permission or charge

This work cannot be reproduced or quoted extensively from without first obtaining permission in writing from the author

The content must not be changed in any way or sold commercially in any format or medium without the formal permission of the author

When referring to this work, full bibliographic details including the author, title, awarding institution and date of the thesis must be given

Enlighten: Theses

<https://theses.gla.ac.uk/>  
[research-enlighten@glasgow.ac.uk](mailto:research-enlighten@glasgow.ac.uk)

**The Analysis, Experimental Characterisation and  
Prototyping of Technologies for Making Quantum  
Noise Limited Detections of Gravitational Waves**

Joseph Henry Briggs

Wednesday 14<sup>th</sup> July, 2021

Submitted in fulfillment of the requirements for the Degree of Doctor  
of Philosophy

School of Physics and Astronomy  
College of Science and Engineering  
University of Glasgow



University  
of Glasgow

# Abstract

The detection of gravitational waves is essential for developing our understanding of the Universe. Systems such as inspiralling binaries of black holes and neutron stars produce gravitational waves, and much of the information carried by a gravitational wave cannot be obtained via any other means. Gravitational waves interact weakly with matter, so kilometre-scale interferometers, such as the LIGO detectors, are the only instruments which have directly measured the strain induced in space-time by gravitational waves. To more accurately determine the parameters of individual sources and to refine statistical models of these systems, it is vital that the sensitivity of these interferometers is increased.

To reduce the quantum shot noise of the LIGO detectors, they require a low noise, high power laser. This thesis contains experimental characterisation of the prototype for the laser that will be used during LIGO's fourth observation run. This laser generated over 100 W of amplitude stabilised light in the  $HG_{00}$  mode making it an important step towards reaching the design sensitivity of the LIGO detectors.

---

A current shunt was compared to an *acousto-optic modulator* (AOM) for use as the actuator in the control loop for stabilising the laser’s amplitude. It was found that the AOM was more reliable and more versatile than the current shunt, and so it was recommended that the AOM was used during LIGO’s fourth observation run. However, the current shunt may allow for  $\sim 10$  W more power to be delivered to the interferometer, so this should be considered when the maximum laser power that is used by LIGO is limited by the power wasted by the AOM.

Balanced homodyne detection is a key part of the upgrade from advanced LIGO to LIGO A+. To lower the quantum noise of the detectors by harnessing the quantum nature of light, it is crucial that the balanced homodyne detector has minimal loss. Mode mismatches between the interferometer and the output mode cleaners are a source of loss; therefore, active optics for mode matching between the interferometer and the output mode cleaner will be used.

In this thesis, the uncertainty in the radii of curvature of the optics in the *signal recycling cavity* (SRC) was used to calculate the distribution of modes which may be present at the *signal recycling mirror* (SRM). For the *LIGO Livingston Observatory, LA., USA* (LLO), it was found that the uncertainty in the radii of curvature of an optic known as SR3 is the largest source of uncertainty in the beam parameter at the SRM. From a measurement of the SRC’s Gouy phase, the arm mode at the SRM was inferred to have a width of 1.8 mm and a defocus of  $-0.28 \text{ m}^{-1}$ . Visualisations for the amount of these modes which the active optics should be able to correct for were created, and it was found that for LIGO A+, a mode mismatch up to 5% can be entirely corrected with the active optics.

---

Third-generation ground-based gravitational wave detectors, such as the Einstein Telescope and LIGO Cosmic Explorer, will be far more sensitive and be able to probe deeper into the Universe than the current generation of detectors. The increase in sensitivity may be achieved with cryogenically cooled crystalline silicon test masses, but the wavelength of light used in current gravitational wave detectors,  $1\mu\text{m}$ , will not be compatible with these test masses due to them being opaque to this wavelength. Instead, these test masses may work with  $2\mu\text{m}$  light.

High quantum efficiency photodiodes are required if the detector's quantum noise is to be minimal, so off-the-shelf extended InGaAs photodiodes that are sensitive to  $2\mu\text{m}$  light were characterised in the context of the unique requirements of a gravitational wave detector. Both quantum efficiency and  $1/f$  dark noise rise as the reverse bias of an extended InGaAs photodiode increases. A maximum reverse bias was found for the eight photodiodes that were tested such that their dark noises were below the shot noise of a typical current ( $\sim 10\text{mA}$ ) generated by the photodiode used to sense the gravitational wave signals in an interferometer. The effect of temperature on the dark noise was also investigated.

It was found that current off-the-shelf extended InGaAs photodiodes will not be suitable for third-generation detectors as they do not have sufficient quantum efficiency while they are biased such that their dark noise is below shot noise in the frequency band of interest in ground-based gravitational wave detection. Cooling may help reduce this noise, but this poses a significant engineering challenge and the quantum efficiency requirement is still unlikely to be met. Significant amounts of research into the optimal conditions for manufacturing extended InGaAs photodiodes

---

would be needed before using them in a third-generation detector is viable.

# Acknowledgements

I would like to thank Ken Strain for his supervision and advice during the course of my PhD. He set a great example of how to be a scientific thinker, and he was an invaluable source of experience and knowledge. Ken always made time to answer my questions, explain things to me and give me feedback on the work that I was doing.

I am grateful to Bryan Barr for his assistance and insights. Many times throughout my PhD, Bryan offered his time and energy to help me understand how I could solve a problem I was having, and his practical advice was indispensable. I also want to thank Stefan Hild for his guidance, enthusiasm, and encouragement during the first two years of my PhD.

Regarding the production of this thesis, I would like to thank Ken Strain, Bryan Barr, Harry Ward, Giles Hammond and Peter Veitch. They highlighted numerous places where I could improve its clarity, spotted typos and suggested structural changes. Of course, any remaining typos are solely my responsibility.

---

Thanks to my friends for all the walks up mountains, pub trips, the coffee breaks and all the fun conversations. I couldn't know a better bunch of people to spend my free time with.

I would like to thank Dwayne Spiteri for being a great friend and housemate. The writing of this thesis happened during an unusual year, and it was certainly made easier by having him around. I would also like to thank him for his (not always solicited) opinions about what I was thinking about and working on.

I would like to thank my family for their never-ending love. Mum, Dad, James and Isabelle have encouraged and supported me at every stage of my life so far. They are always there for me and have helped me at many times to get the best out of life. I cannot be more grateful for my family and I would not be the person I am today without them.

To Catriona, thank you for your love, care and support. You bring so much vibrancy, warmth and joy to the lives of all the people you know, and I feel so incredibly lucky to be with you. Your companionship has given me a great sense of happiness and fulfilment, and my life has been made so much more wonderful by sharing it with you.

# Declaration

I declare that the work described in this thesis was carried out by me and has not been presented in any previous application for a degree at the University of Glasgow or any other institution. The chapters in this thesis and the contributions of others to them are described below.

**Chapter 1** This chapter contains introductory information pertaining to ground-based gravitational wave interferometry and the LIGO detectors.

**Chapter 2** In this chapter, experiments to do with the prototype of the laser that will be used for LIGO's fourth observation run are described. My contribution to this work was in the setup of the optical table and the taking of measurements. These tasks were completed with help from Nina Bode, Matthew Heintze and Michael Fyffe. Rick Savage and Maik Frede contributed to discussions of how this should be done. The diagnostic breadboard was supplied by the AEI. The design of the prototype was undertaken by others. The outcome of this project was published in [1]. The photographs of the laser were taken by Michael Fyffe. This work was carried out at the LIGO Livingston Observatory as part of the LSC fellows programme and was funded by the STFC long-term attachment scheme.

---

**Chapter 3** In this chapter, simulations of the LIGO Livingston interferometer were performed to investigate the effect of mismatch between the arm cavities and the output mode cleaners. This work was aided by discussions with Ken Strain, Stephen Webster, Bryan Barr and Carl Blair.

**Chapter 4** In this chapter, a review is given for the motivations and phase noise requirement of the balanced homodyne detection scheme that will be installed as part of the LIGO A+ detectors.

**Chapter 5** In this chapter, a method for showing the effectiveness of the active optics for adjusting the mode matching between the interferometer and the output mode cleaners for the LIGO A+ detectors is described. With this method, I showed the range of mode mismatches that the active optics in HAM6 will be able to correct. The design of the optical layout was undertaken by me, Ken Strain, Mark Barton, Russell Jones and Stephen Webster. As part of this, I wrote an algorithm for finding mode matching solutions; Stephen Webster provided useful input into this.

**Chapter 6** The experiments reported on in this chapter were done under the supervision of Ken Strain and Bryan Barr. Sebastian Steinlechner supplied the IG24x500S4i and IG26x500S4i photodiodes. I would like to thank Sean Leavey and Andrew Long for their helpful discussions about photodiodes.

**Chapter 7** The in-air apparatus was constructed with help from Russell Jones and Stephen Craig. The laser, send/receive circuits and CDS infrastructure were repurposed from the MOSES experiment at the Glasgow 10 m prototype interferometer worked on by Bryan Barr, Neil Gordon, Jennifer Wright, Borja Sorazu and Ken Strain. The high voltage power supply used to drive the PZT in this experiment was designed by Andrew Spencer and Steven O'Shea. The in-vacuum experiment

---

was performed with repurposed apparatus left over from a previous experiment run by Stefan Hild. The auxiliary suspensions were designed by Jan-Simon Hennig and Russell Jones. The balanced homodyne suspension and coil drivers were designed by Sebastian Steinlechner.

**Other Credits** Many of the figures in this thesis were created with Matplotlib [2]. Diagrams of optical layouts were often created with an open source collection of graphics produced by Alexander Franzen [3]. The work in this thesis was facilitated by the University of Glasgow and was funded by the STFC (award number: 1947199).



# Contents

<b>Abstract</b>	<b>i</b>
<b>Acknowledgements</b>	<b>v</b>
<b>Declaration</b>	<b>vii</b>
<b>1 The Fundamentals of Gravitational Wave Interferometers</b>	<b>1</b>
1.1 Introduction . . . . .	1
1.2 The Astrophysical Origins of Gravitational Waves . . . . .	2
1.3 Measuring Gravitational Waves with an Interferometer . . . . .	4
1.3.1 Using Fabry-Perot Cavities in the Arms of a Michelson Interferometer to Enhance its Sensitivity . . . . .	8
1.4 Sources of Noise in Gravitational Wave Interferometers. . . . .	10
1.4.1 Laser Power and Shot Noise . . . . .	10
1.4.2 Using Power Recycling to Reduce Shot Noise . . . . .	15
1.4.3 Using Signal Recycling to Shape Quantum Noise . . . . .	15
1.4.4 Reducing Shot Noise by Removing Light in Higher Order Modes with a Mode Cleaner Cavity. . . . .	17
1.4.5 Radiation Pressure Noise and the Standard Quantum Limit . . . . .	18

1.4.6	Coating Thermal Noise and Other Noise Sources . . . . .	19
1.5	Reducing Shot Noise with Non-Classical States of Light . . . . .	20
1.6	Interferometry Techniques to Beat Quantum Limits . . . . .	22
1.7	The Effect of Loss Mechanisms Within the Interferometer on Mea- suring Quantum States of Light . . . . .	24
1.8	Photodiodes . . . . .	25
1.9	Overview of the LIGO Detectors . . . . .	27
1.10	The Future of Ground-based Gravitational Wave Detectors . . . . .	28
1.11	Conclusion . . . . .	30
<b>2</b>	<b>A Prototype High Power Laser for LIGO’s Fourth Observation Run</b>	<b>33</b>
2.1	Introduction . . . . .	33
2.2	Concept for LIGO’s New Laser . . . . .	36
2.2.1	Non-Planar Ring Oscillators . . . . .	36
2.2.2	The neoVAN-4S-HP Solid-State Amplifier . . . . .	37
2.2.3	The Pre Mode Cleaner Cavity . . . . .	37
2.3	Layout of the Prototype Laser System . . . . .	38
2.4	The Power Transmitted by the Pre Mode Cleaner . . . . .	46
2.4.1	The Effect of Cooling on the Amplifier’s Power and Beam Quality . . . . .	49
2.4.2	Alignment Procedure for the Amplifiers . . . . .	53
2.5	Intensity Stabilisation of a 100 W Beam . . . . .	55
2.5.1	The Concept and Requirements for Intensity Stabilisation Servo	56
2.5.2	Free-Running Noise of the Prototype Laser . . . . .	57

2.5.3	Power Control Actuators . . . . .	61
2.5.4	Open-Loop Transfer Function of the Intensity Stabilisation Servo . . . . .	69
2.5.5	Measurement of the Intensity Stabilisation of a 100 W Beam to the Inner-Loop Requirement . . . . .	74
2.6	Pointing Noise of the Beam Entering the Pre Mode Cleaner . . . . .	77
2.7	Frequency Noise of the Prototype Laser . . . . .	78
2.7.1	Calibrating the Mixer Signal and the PZT, and Modelling the Open Loop Transfer Function for Locking the Pre Mode Cleaner	82
2.7.2	Frequency Noise Measurement . . . . .	88
2.8	Conclusion . . . . .	89
<b>3 Analysis of the Uncertainty of the Beam Parameter of the Arm Mode at the Signal Recycling Mirror . . . . . 93</b>		
3.1	Introduction . . . . .	93
3.1.1	The Mode Matching Between the Arm Cavities, the Signal Recycling Cavity, and the Output Mode Cleaner . . . . .	95
3.1.2	Loss due to Mode Mismatch . . . . .	96
3.1.3	Measurements of the Mode Matching Between the Arm Cav- ities and the Output Mode Cleaner at the LIGO Livingston Observatory Made Between 2018–2019. . . . .	98
3.2	Modelling Interferometers with Mode Mismatches Using FINESSE . . . . .	99
3.2.1	Thin and Thick Beam Splitters . . . . .	101
3.3	Modelling of a Michelson Interferometer with Fabry-Perot Arm Cav- ities and a Signal Recycling Cavity . . . . .	105

3.3.1	Determining Tunings for DC readout . . . . .	109
3.4	The Beam Parameter of the Arm Mode at the Signal Recycling Mirror	113
3.5	Power Transmitted Through the Signal Recycling Mirror for a Mode Mismatch Between the Arm Cavity and the Signal Recycling Cavity .	124
3.5.1	Change of Finesse of the Signal Recycling Cavity . . . . .	128
3.6	Conclusion . . . . .	129
<b>4</b>	<b>Balanced Homodyne Detection for LIGO A+</b>	<b>133</b>
4.1	The Principles of and Motivations for Balanced Homodyne Detection	134
4.1.1	Alternatives to Balanced Homodyne Detection . . . . .	136
4.1.2	Quantum Mechanical Description of Balanced Homodyne De- tection . . . . .	137
4.1.3	Other Motivations for Implementing Balanced Homodyne De- tection in LIGO A+ . . . . .	139
4.2	The Local Oscillator Path . . . . .	140
4.2.1	The Local Oscillator Path Length Stability Requirement . . .	141
4.3	Conclusion . . . . .	147
<b>5</b>	<b>Analysis of the Active Wavefront Control for the Balanced Homo- dyne Detector for LIGO A+</b>	<b>151</b>
5.1	The Optics for Mode Matching the Interferometer and the Output Mode Cleaners . . . . .	152
5.2	Method for Visualising the Effectiveness of Systems with Active Op- tics for Mode Mismatching . . . . .	160
5.2.1	A Description of Mode Matching in Terms of Hermite-Gaussian Modes . . . . .	161

---

5.2.2	Calculating Mode Matching Using The Gaussian Beam Parameter . . . . .	161
5.2.3	Waist-Defocus Phase Space Visualisations . . . . .	162
5.2.4	Visualising how the Active Optics for Mode Matching Expand the Area of Waist-Defocus Space Representing Acceptable Input Modes . . . . .	164
5.2.5	Optimising Waist-Defocus Space Coverage in Favour of Expected Mode Errors . . . . .	169
5.3	Conclusion . . . . .	170
<b>6</b>	<b>Characterisation of Photodiodes for Detecting 2<math>\mu</math>m Light</b>	<b>171</b>
6.1	Quantum Efficiency, Power Handling and Dark Noise Requirements for Photodiodes in a Gravitational Wave Detector . . . . .	172
6.2	What is an Extended InGaAs Photodiode? . . . . .	174
6.3	Selection of Off-the-shelf Extended InGaAs Photodiodes . . . . .	179
6.4	The Effect of Reverse Bias on the Quantum Efficiency of an Extended InGaAs Photodiode . . . . .	180
6.4.1	Method . . . . .	182
6.4.2	Results . . . . .	186
6.5	Dark Current and Dark Noise in Extended InGaAs Photodiodes . . . . .	188
6.5.1	The Dependence of Dark Noise and Dark Current on Reverse Bias in Extended InGaAs Photodiodes . . . . .	191
6.5.2	The Dependence of Dark Noise and Dark Current on Temperature in Extended InGaAs Photodiodes . . . . .	196

6.6	The Saturation Limit of the IG22x1000S4i, IG24x500S4i and IG26x500S4i . . . . .	197
6.7	Excess Noise in the IG24x500S4i . . . . .	199
6.8	Noise Properties of an InSb Detector . . . . .	206
6.9	Discussion . . . . .	209
6.10	Conclusion . . . . .	212
<b>7</b>	<b>Shot Noise Calibration Measurements Based on a Mach-Zehnder Interferometer</b>	<b>215</b>
7.1	Shot Noise in a Mach-Zehnder Interferometer . . . . .	216
7.1.1	Apparatus for the In-Air Mach-Zehnder. . . . .	217
7.1.2	Calibration . . . . .	223
7.1.3	Measurement of Shot Noise . . . . .	224
7.2	Noise in an In-Vacuum Mach-Zehnder Interferometer and the Effect of Misalignment Between the Local Oscillator and Signal Beam . . .	227
7.2.1	Apparatus for the In-Vacuum Mach-Zehnder . . . . .	230
7.2.2	Calibration and Locking of the In-Vacuum Mach-Zehnder . . .	233
7.2.3	Measurement of the Differential Arm Signal . . . . .	234
7.2.4	The Effect of Misalignment on the Size of a Signal in an In- terferometer . . . . .	238
7.3	Conclusion . . . . .	240
<b>8</b>	<b>Conclusion</b>	<b>243</b>
<b>A</b>	<b>Dark Noise Spectra of Photodiodes</b>	<b>247</b>
A.1	Dark Noise as a Function of Reverse Bias . . . . .	247

A.2	Dark Noise as a Function of Temperature . . . . .	252
A.3	Noise of a Photocurrent Generated by an InSb Detector as a Function of Bias . . . . .	256
<b>B</b>	<b>Photodiode Circuits</b>	<b>257</b>
B.1	A Transimpedance Amplifier for Measuring the Dark Noise of Pho- todiodes . . . . .	258
B.1.1	Transfer Function . . . . .	263
B.1.2	Noise Measurement . . . . .	263
B.2	A Transimpedance Amplifier for Making Shot Noise limited Measure- ments of 10 mA Photocurrents . . . . .	266
B.3	Simulations with LISO . . . . .	270
B.4	Transfer Function Calculation With MATLAB . . . . .	270
<b>C</b>	<b>The Control and Data System</b>	<b>273</b>
<b>D</b>	<b>FINESSE Simulations</b>	<b>277</b>
D.1	Mode Matching the Laser to the Arm Cavity . . . . .	277
D.2	Interferometer Parameters . . . . .	281
D.2.1	Radii of Curvature of optical components . . . . .	281
D.2.2	Spacings . . . . .	281
D.2.3	Parameters used in the Main Simulation . . . . .	284
D.3	Finding the Correct Way to Model a Beam Splitter . . . . .	285
D.4	Main Simulation . . . . .	286
<b>E</b>	<b>Algorithm for Finding a Three-Optic Mode Matching Solution with 45° Gouy Phase Separation between two of the Optics</b>	<b>291</b>

Contents

---

E.1	Method . . . . .	293
<b>F</b>	<b>Light and Gaussian Modes</b>	<b>297</b>
F.1	The Fundamental Gaussian Mode . . . . .	297
F.1.1	The Complex Beam Parameter . . . . .	299
F.1.2	Astigmatism . . . . .	301
F.2	Gaussian Beams Traversing Optical Layouts . . . . .	302
F.3	Higher Order Modes and Optical Imperfections . . . . .	303
<b>G</b>	<b>Mode Matching Between Two Astigmatic Beams</b>	<b>307</b>
	<b>Acronyms</b>	<b>311</b>
	<b>Bibliography</b>	<b>315</b>

# List of Figures

1.1	Sketch of the effect of a gravitational wave interacting with a Michelson interferometer. . . . .	9
1.2	Comparison between the phase of the light reflected from a mirror versus the phase of light reflected from a cavity as the position of the mirror/end mirror is changed. . . . .	11
1.3	Sensitivity Curves for the aLIGO and LIGO A+ detectors. . . . .	14
1.4	Sketch of a LIGO detector. . . . .	29
2.1	Concept for the laser LIGO will use during its fourth observation run.	36
2.2	Sketch of the optical layout for the prototype laser. . . . .	39
2.3	Photograph showing the seed and amplifiers in the prototype laser. . . . .	42
2.4	Photograph showing the optics between the second amplifier and the pre mode cleaner. . . . .	43
2.5	Photograph of the pre mode cleaner. . . . .	44
2.6	Photograph of the diagnostic breadboard. . . . .	45
2.7	Power incident and transmitted by the pre mode cleaner over a 55 hour trial run. . . . .	48
2.8	Cartoons of the water cooling layout for the prototype laser. . . . .	50

2.9	The effect of the second amplifier's temperature on the power of the beam that is in the fundamental Gaussian mode. . . . .	51
2.10	Mode scans of the beam produced by the second amplifier for different amplifier temperatures. . . . .	52
2.11	The intensity noise requirement for the pre stabilised laser. . . . .	58
2.12	The concept for the intensity stabilisation of the laser. . . . .	59
2.13	The free running noise of the beam after the NPRO, the first amplifier, the second amplifier and the pre mode cleaner. . . . .	60
2.14	A sketch of how the transfer function of the acousto-optic modulator was measured. . . . .	63
2.15	Measurement of the transfer function of the acousto-optic modulator.	64
2.16	A sketch of how the transfer function of the current shunt was measured.	66
2.17	Measurement of the transfer function of the current shunt. . . . .	67
2.18	Sketch showing the amplitude stabilisation servo and how its open-loop transfer function was measured. . . . .	71
2.19	Measurement of the open-loop transfer function of the pre stabilised laser's intensity stabilisation servo. . . . .	72
2.20	A block diagram of the components in the intensity stabilisation servo.	73
2.21	The noise of the prototype laser while its intensity was being stabilised.	76
2.22	The pointing noise of the prototype laser. . . . .	79
2.23	Sketch of the servo used to lock the pre mode cleaner. This sketch also shows how the open-loop transfer function of the pre mode cleaner locking servo was measured. . . . .	81
2.24	Block diagram of the servo for locking the pre mode cleaner. . . . .	83

---

2.25	Measurement of the Pound-Drever-Hall signal used to calibrate the pre mode cleaner error signal. . . . .	85
2.26	Measurement of the light reflected by the pre mode cleaner as a ramp was applied. This was used to calibrate the servo's control signal. . .	86
2.27	Measurement of the open-loop transfer function of the servo for locking the pre mode cleaner. . . . .	87
2.28	Frequency noise of the beam exiting the pre mode cleaner. . . . .	90
3.1	Sketch showing the parts of the aLIGO detectors discussed Chapter 3.	94
3.2	FINESSE simulation of a Michelson interferometer showing how incorrectly implemented beam splitters can yield erroneous results. . . . .	103
3.3	Schematic of the main simulation in Chapter 3. . . . .	106
3.4	Tunings of the end test masses used to produce a DC offset for the simulations with arm cavities. . . . .	110
3.5	Tunings of the input test masses used produce a DC offset for the simulations without arm cavities. . . . .	111
3.6	The Gaussian width of the beam that is transmitted through the signal recycling mirror as a function of the error in the focal length of SR3 and SR2. . . . .	117
3.7	The radius of curvature of the beam that is transmitted through the signal recycling mirror as a function of the error in the focal length of SR3 and SR2. . . . .	118
3.8	The Gouy phase of the beam that is transmitted through the signal recycling mirror as a function of the error in the focal length of SR3 and SR2. . . . .	119

3.9 The Gouy phase between the input test masses and the signal recycling mirror as a function of the strength of the thermal lensing in the input test masses. . . . . 120

3.10 Test used to determine an appropriate number of higher order modes to use in the simulation. . . . . 121

3.11 The probability distribution of the focal lengths of SR2 and SR3, and the deduced combination of SR3 and SR2 focal length based on a measurement of the signal recycling cavity’s Gouy phase. . . . . 122

3.12 Distribution of beam parameters at the signal recycling mirrors. . . . 123

3.13 The percentage of light that is in higher order modes as a function of the focal length of SR3. . . . . 126

3.14 Simulated power of the beam’s fundamental mode and the power in its higher order mode as the mode mismatch is changed. . . . . 127

3.15 Ratio of power in the fundamental mode and the power in higher order modes as the signal recycling mirrors reflectivity changes. . . . 128

4.1 Sketch of a balanced homodyne detector. . . . . 135

4.2 Sketch of how the local oscillator will be delivered to the balanced homodyne detector for LIGO A+. . . . . 142

4.3 The linear response function between strain and signal, expressed in units of radians/gravitational wave strain, at the anti-symmetric port of the interferometer. . . . . 144

4.4 Sensitivity curve for the A+ detectors expressed in units of  $\text{rad}/\sqrt{\text{Hz}}$ . 146

4.5 The path length noise that is acceptable between the anti-symmetric and local oscillator beams in LIGO A+. . . . . 148

---

4.6	A sketch showing why the motion of BHDBS2 needs to be counted twice. . . . .	149
5.1	Sketch of the balanced homodyne detection scheme for LIGO A+. . .	153
5.2	Combinations of optical powers for the OFI lens, OMx1 and OMx2 that match the interferometer to the output mode cleaners. . . . .	156
5.3	Loss due to astigmatism as a function of angle of incidence upon the mirrors for mode matching in HAM6. . . . .	157
5.4	Beam size and Gouy phase within HAM6. . . . .	159
5.5	Sketch of the waist-defocus representation for a Gaussian beam interacting with a simple optical layout. . . . .	165
5.6	Sketch showing how the expansion of the area of waist-defocus space by active optics is computed. . . . .	167
5.7	Coverage of the waist-defocus space provided by the active optics for mode matching in HAM6. . . . .	168
6.1	Optical layout used for measuring the effect that increasing the reverse bias of a photodiode had on its quantum efficiency and saturation limit. . . . .	184
6.2	The dependency of the FD10D's quantum efficiency on its reverse bias.	187
6.3	Shot noise measurement of a photocurrent produced by the FD10D used to prove the increase in photocurrent was due to an increase in its quantum efficiency. . . . .	189
6.4	Investigation of the saturation limit of the FD10D. . . . .	190
6.5	Dark noise of the FD10D as a function of reverse bias. . . . .	193

## List of Figures

---

6.6	Dark noise and dark current for each photodiode as a function of reverse bias. . . . .	194
6.7	A difference of two orders of magnitude in dark noise between two nominally identical photodiodes. . . . .	195
6.8	Apparatus used to control the temperature of the photodiodes. . . . .	197
6.9	Dark noise and dark current for each photodiode as a function of temperature. . . . .	198
6.10	Saturation limits of the IG22x1000S4i, IG24x500S4i and IG26x500S4i. . . . .	200
6.11	Unexplained excess white noise produced by the IG24x500S4i. . . . .	202
6.12	A noise projection measurement was performed to determine if the excess noise in the photocurrent produced by the IG24x500S4i was due to bias noise. . . . .	203
6.13	Ideality factor of the IG24x500S4i. . . . .	204
6.14	Photocurrent flowing through the forward biased IG24x500S4i. . . . .	205
6.15	Noise of the photocurrent produced by an InSb detector exposed to room temperature aluminium. . . . .	207
6.16	Dark current and dark noise of an InSb detector as a function of reverse bias. . . . .	208
7.1	Sketches of a Mach-Zehnder interferometer and an interferometer with a balanced homodyne detector. . . . .	217
7.2	Photograph of the in-air Mach-Zehnder interferometer. . . . .	218
7.3	Sketch of the optical layout for the in-air Mach-Zehnder interferometer. . . . .	219
7.4	The transfer function of the electronics for whitening the photodiode signal. . . . .	222

---

7.5	Circuit diagram for the electronics used to keep the in-air Mach-Zehnder locked to the middle of a fringe. . . . .	223
7.6	Calibration of the in-air Mach-Zehnder interferometer. . . . .	225
7.7	The amplitude spectral density of the difference between the two photodiodes' signals in the in-air Mach-Zehnder experiment. . . . .	228
7.8	Analysis of the noise due to scattering and the frequency noise of the NPRO in the in-air experiment. . . . .	229
7.9	Sketch of the in-vacuum Mach-Zehnder. . . . .	231
7.10	Photographs of the components used for the in-vacuum Mach-Zehnder. . . . .	232
7.11	Flow diagram showing each block of the servo used to lock the in-vacuum Mach-Zehnder. . . . .	236
7.12	The closed-loop and open-loop transfer functions of the servo used to lock the in-vacuum Mach-Zehnder. . . . .	237
7.13	Differential arm signal contaminated by scattered light noise in the in-vacuum experiment. . . . .	239
7.14	Measurement of the effect of misalignment on a signal in an interferometer. . . . .	241
A.1	Dark noise of the IG24x500S4i at 21°C for a series of reverse biases. . . . .	248
A.2	Dark noise of the IG26x500S4i at 21°C for a series of reverse biases. . . . .	248
A.3	Dark noise of the IG22x1000S4i at 21°C for a series of reverse biases. . . . .	249
A.4	Dark noise of the G12183-010k at 21°C for a series of reverse biases. . . . .	249
A.5	Dark noise of the G12183-005k at 21°C for a series of reverse biases. . . . .	250
A.6	Dark noise of the G12182-010k at 21°C for a series of reverse biases. . . . .	250
A.7	Dark noise of the G12182-005k at 21°C for a series of reverse biases. . . . .	251

## List of Figures

---

A.8	The dependence of dark noise on temperature for the FD10D at 1.8V reverse bias. . . . .	252
A.9	The dependence of dark noise on temperature for the G12183-010k at 1.0V reverse bias. . . . .	253
A.10	The dependence of dark noise on temperature for the G12183-005k at 1.0V reverse bias. . . . .	253
A.11	The dependence of dark noise on temperature for the G12182-010k at 1.0V reverse bias. . . . .	254
A.12	The dependence of dark noise on temperature for the G12182-005k at 1.0V reverse bias. . . . .	254
A.13	The dependence of dark noise on temperature for the IG24x500S4i at 1.0V reverse bias. . . . .	255
A.14	The dependence of dark noise on temperature for the IG26x500S4i at 1.0V reverse bias. . . . .	255
A.15	The noise of the photocurrent produced by the P5968 as a function of bias. . . . .	256
B.1	A circuit used to measure the dark noise of photodiodes under different reverse biases. . . . .	259
B.2	A circuit used to measure the dark noise of photodiodes under different reverse biases. . . . .	260
B.3	Ultra-low bias voltage noise circuit used to validate measurements made with other circuits. . . . .	261
B.4	The FD10D shows the same dark noise in the ultra-low bias noise and regular test circuit. . . . .	262

---

B.5	Transfer function of the transimpedance amplifier for measuring the dark noise of photodiodes. . . . .	264
B.6	Noise of the transimpedance amplifier for measuring the dark noise of photodiodes. . . . .	265
B.7	Transimpedance amplifier designed for making shot noise limited measurements of photocurrents. . . . .	267
B.8	Transfer function of the transimpedance amplifier designed for making shot noise limited measurements of photocurrents. . . . .	268
B.9	Noise of the transimpedance amplifier designed for making shot noise limited measurements of photocurrents. . . . .	269
C.1	An example of a MEDM screen used to interface with CDS. . . . .	274
C.2	Noise floor of the digitised input signals recorded by the Glasgow CDS. . . . .	275
D.1	Optimisation of the parameters used in the <code>gauss</code> command to mode match the laser to the arms in the simulations described in Chapter 3. . . . .	280
E.1	Examples of optical layouts which the mode matching algorithm could be applied to. . . . .	295
E.2	Sketch used to explain an algorithm for mode matching. . . . .	296



# List of Tables

1.1	Summary of observation runs for LIGO, Virgo and KAGRA. . . . .	5
2.1	Transfer function for each part of the intensity stabilisation servo. . .	75
3.1	Summary of mode matching measurements made at LIGO Livingston by on-site scientist. . . . .	104
3.2	The tunings used for the arm-cavity simulation to get 30mW of light at the dark port. . . . .	112
3.3	The tunings used for the no-arm-cavity simulation to get 30mW of light at the dark port. . . . .	112
5.1	Mechanical and optical properties of the LIGO A+ HAM6 layout. . .	158
5.2	Target for losses in HAM6. . . . .	160
6.1	Information from the datasheets of the photodiodes that were tested.	181
7.1	Elements of the in-vacuum servo and their transfer functions. . . . .	235
D.1	The aLIGO design values of the radii of curvature of the optics inside the signal recycling cavity and the arms. . . . .	281

D.2	The measured values of the radii of curvature of the optics at LLO that make up the signal recycling cavity and the arms. . . . .	282
D.3	Measured spacings between the optics at LLO. . . . .	282
D.4	Design values for spacings between optics in aLIGO. . . . .	283
D.5	Parameters used in an earlier FINESSE model of LLO. . . . .	283
D.6	Thickness of the optics between and including the ITM and the SRM.	283
D.7	Parameters for the major components of the simulation. . . . .	284
F.1	ABCD matrices for simple optical components . . . . .	303

# Chapter 1

## The Fundamentals of Gravitational Wave Interferometers

### 1.1 Introduction

On the 14<sup>th</sup> of September 2015, the detection of a gravitational wave emanating from two coalescing black holes signalled the beginning of a new era for astronomy [4]. The information carried by a gravitational wave is undisturbed by the matter between the observer and the astrophysical body that is emitting them, thus it gives astronomers valuable information which cannot be obtained from the electromagnetic radiation emitted by that body. Gravitational wave astronomy also allows for direct observations of objects that do not emit electromagnetic radiation,

e.g. black holes without an accretion disk. Therefore, it is important that large numbers of gravitational wave signals are measured to develop our understanding of the Universe.

However, gravitational waves are incredibly weak and the detection of them is a science in and of itself. This chapter will outline how a gravitational wave interferometer, such as LIGO [5], can be used to detect these signals and the fundamental noise sources these detectors face. While there are other important sources of noise, the suppression of quantum noise is crucial to achieving the sensitivity required to detect gravitational waves; therefore, quantum noise is the focus of this chapter.

## 1.2 The Astrophysical Origins of Gravitational Waves

Gravitational waves produced by inspiralling pairs of massive objects, such as *binary black holes* (BBHs) (e.g. [4,6–8]), *binary neutron stars* (BNSs) [9,10], and a source which is either a BBH or a binary consisting of a black hole and a neutron star (NSBH) [11], have been detected. Every confirmed gravitational wave signal as of November 2020 is summarised in [12].

Important astrophysical and cosmological results have been obtained using the detections in [12]. The first direct detection<sup>1</sup> of a gravitational wave [4] validated Einstein’s general theory of relativity [13], and allowed for the masses, spins and

---

<sup>1</sup>Hulse and Taylor attributed the orbital decay of a BNS to the emission of gravitational waves. For this work, they shared the Nobel prize in 1993. However, this was not an observation of the gravitational wave itself.

distances of the black holes to be directly measured [14]. The first detection of gravitational waves from a BNS was accompanied by an electromagnetic counterpart. This detection allowed for a measurement of the Hubble constant [15] to be made, added constraints to the equation of state for neutron stars [16], and provided an explanation for the origin of heavy elements such as gold [17].

The waveform of the gravitational radiation emitted from these systems is known as a chirp because the frequency of the gravitational wave signal increases as the two objects get closer to merging [18]. The cut-off frequency is determined by the radius of the objects that will merge; for the signals which have been measured, the cut-off frequencies were between 100 Hz and 10 kHz. A typical gravitational wave strain amplitude,  $h$ , of these types of systems, all of which have a total mass of  $10M_{\odot} - 100M_{\odot}$  and are between 100 Mpc to 10 Gpc away from Earth, is  $h \sim 10^{-21} - 10^{-23}$ .

Einstein's general theory of relativity accurately describes the gravitational waves measured with the LIGO and Virgo interferometers [19]. Gravitational waves are emitted from systems such as two inspiralling black holes because the mass distribution of the system is not spherically or rotationally symmetric (see e.g. [20] or [21]). As the coupling between mass and the curvature of space-time is weak, gravitational waves are only observable from systems that have large masses moving at relativistic velocities.

In addition to binary systems, other astrophysical phenomena will emit gravitational waves. Asymmetries in pulsars [22, 23] and magnetars [24] will cause them to

emit a gravitational wave with a frequency that evolves so slowly that it is essentially monochromatic. When the core of a star collapses as it goes supernova, a burst of gravitational radiation may be emitted [25,26]. Burst signals may also be generated immediately after a BNS merges [27]. Weaker sources that future gravitational wave interferometers may detect include: a stochastic background level of gravitational waves due to the merging of compact binaries from all over the universe [28], dark matter [29,30], and sources that existed during the early universe [31,32].

To improve statistical models of the systems that emit gravitational waves, the number of detections needs to be increased. To detect continuous wave signals, the *signal to noise ratio* (SNR) of  $h$  improves with the square-root of the total observing time of the detector [33]. With longer observation times, it is more likely that an exotic event will be measured. For these reasons, gravitational wave detectors are operated for year long time-scales with minimal interruption. These are known as observation runs. Between observation runs, the detectors undergo hardware upgrades. The previous, current and future observation runs are summarised in Table 1.1; a more comprehensive overview can be found in [34].

### 1.3 Measuring Gravitational Waves with an Interferometer

Gravitational waves are propagating transverse perturbations in the curvature of space-time, and can be split into a basis set containing two polarisations, plus and cross (e.g. [20] or [21]). The effect these waves have, in the local Lorentz frame,

### 1.3. Measuring Gravitational Waves with an Interferometer

Obs. Run	Dates	Detections	Detectors
O1	12/09/2015 - 19/01/2016	3	aLIGO
O2	30/11/2016 - 25/08/2017	8	aLIGO, Virgo
O3a	01/04/2019 - 01/10/2019	39	aLIGO, Virgo
O3b	01/11/2019 - 30/04/2020	23	aLIGO, Virgo
O4	2021	-	aLIGO, Virgo, KAGRA
O5	2025	-	LIGO A+, Advanced Virgo, KAGRA, LIGO India

Table 1.1: Summary of observation runs for LIGO, Virgo and KAGRA [5, 35, 36]. This table includes detections that were made up to November 2020; analysis of the O3 data is ongoing.

on free test masses on Earth is to move them by a small amount <sup>2</sup>.

To detect plus-polarised gravitational waves, the end mirrors of a Michelson interferometer can be used as the test masses. These mirrors are referred to as *end test masses* (ETMs). A suspended mass will behave in the same way as a free mass when it is driven above its resonant frequency, so the ETMs need to be suspended [37]. A sketch of a gravitational wave interacting with a Michelson interferometer is shown in Figure 1.1. The amount the test masses move,  $\Delta L$ , when they are at a distance of  $L$  away from the origin of the local Lorentz frame due to

<sup>2</sup>In the local Lorentz frame of the beam splitter, for any feasible Earth based detector, the effect of a gravitational wave on the wavelength of the light is negligible compared to its effect on the positions of the test masses due to the strong equivalence principle: all non-gravitational laws of physics which can be expressed in a special relativistic form have the same form in a local Lorentz frame (e.g. [20]). For a gravitational wave with a frequency of 100 Hz and a wavelength  $\lambda_{\text{GW}} = 3,000$  m, in the local Lorentz frame, the metric has the form  $g_{\alpha\beta} = \eta_{\alpha\beta} + \mathcal{O}(h)$ , where  $\eta_{\alpha\beta}$  is the Minkowski space-time metric and  $\mathcal{O}(h)$  is a perturbation of the order  $(\frac{2\pi L}{\lambda_{\text{GW}}})^2 h$ . The Minkowski space-time metric is flat, so in the local Lorentz frame the metric is, essentially, flat and the gravitational waves cause the test masses to move by  $\Delta L = hL/2$ . Maxwell's equations are modified by a term that is of the order  $\frac{\delta\lambda_{\text{EM}}}{\lambda_{\text{EM}}} \sim (\frac{2\pi L}{\lambda_{\text{GW}}})^2 h$ , and so if  $(\frac{2\pi L}{\lambda_{\text{GW}}})$  is small, as it would be for an Earth based interferometer, then the effect of the gravitational wave on the light is much smaller than the effect of the gravitational wave on the test masses.

an incoming plus-polarised gravitational wave of strain  $h$  is

$$\Delta L = \frac{1}{2}Lh. \quad (1.1)$$

Interferometers are sensitive to arm length changes that are on the order of one wavelength,  $\lambda_{\text{EM}}$ , of the light they are operated with, as they measure the light's phase. As a plus-polarised gravitational wave will move the test masses in anti-phase, the difference between the phase of light when it recombines at the beam splitter after reflecting from the test masses,  $\Delta\phi$ , is

$$\Delta\phi = \frac{4\pi}{\lambda_{\text{EM}}}Lh. \quad (1.2)$$

$\Delta\phi$  is known as the *differential phase*, and differential effects, such as differential test mass motion or light being back scattered into just one arm, result in the light acquiring differential phase. The wavelength current interferometers operate with,  $\lambda_{\text{EM}} = 1064 \text{ nm}$ , was selected because test masses with low noise and low optical absorption and mirror coatings with low loss and low thermal noise can be fabricated for this wavelength [38].

The gravitational wave strain is converted into power fluctuations of light at the *anti-symmetric* (AS) port due to the two light fields from the arms interfering at the beam splitter (see Figure 1.1). When on the *dark fringe*, the interferometer is configured so that there is a small, static offset difference in the arm lengths corresponding to a phase  $\phi_0$ . This results in a small amount of light ( $\sim 10 \text{ mW}$ ) at the AS port for the signal light to beat with, and so the variation in the power

of the light at the AS port depends linearly on the gravitational wave strain. This technique is known as DC readout [39, 40]. At the beam splitter, the electric field,  $E_{AS}$ , emerging from the AS port due to the interference of the beams returning from the ETMs,  $E_y$  and  $E_x$ , due to a differential phase,  $\Delta\phi = \phi_0 + \frac{4\pi}{\lambda_{EM}}Lh$ , is

$$E_{AS} = \frac{E_y}{\sqrt{2}} - \frac{E_x}{\sqrt{2}}, \quad (1.3)$$

$$\propto \sqrt{\frac{P_0}{2}} \left( \frac{e^{i\Delta\phi/2}}{\sqrt{2}} - \frac{e^{-i\Delta\phi/2}}{\sqrt{2}} \right), \quad (1.4)$$

where  $P_0$  is the power of the beam injected into the beam splitter by the laser. The power of the beam at the AS port,  $P_{AS}$ , is

$$P_{AS} \propto E_{AS}^* E_{AS}, \quad (1.5)$$

$$= P_0 \sin^2 \left( \frac{\Delta\phi}{2} \right), \quad (1.6)$$

$$\sim \frac{P_0 \phi_0^2}{4} + \frac{P_0 \phi_0}{2} \frac{4\pi}{\lambda_{EM}} Lh. \quad (1.7)$$

In the absence of a gravitational wave signal, the DC light at the AS port is related to the static offset by  $\phi_0 = 2\sqrt{\frac{P_{AS}}{P_0}}$ , where  $\overline{P_{AS}}$  is the average of  $P_{AS}$ . As we are interested in a fluctuating signal, the DC offset from Equation (1.7) can be removed, allowing for the signal at the AS port to be written as

$$P_{AS} = \sqrt{P_0 \overline{P_{AS}}} \frac{4\pi}{\lambda_{EM}} Lh. \quad (1.8)$$

Therefore, it is in principle possible to measure the differential motion of the ETMs due to a gravitational wave's strain by placing a photodiode in the beam emerging

from the AS port of a Michelson interferometer.

### 1.3.1 Using Fabry-Perot Cavities in the Arms of a Michelson Interferometer to Enhance its Sensitivity

For a Michelson interferometer, the arm length which maximises the fluctuating part of  $\Delta\phi$  is 1/4 of the wavelength of a gravitational wave. Gravitational wave signals from BBHs and BNSs have frequencies of  $\sim 100$  Hz; therefore, the wavelength of the gravitational wave will be of the order  $\sim 1000$  km. It is not possible to construct a Michelson interferometer with  $\sim 1000$  km arms on Earth.

The sites that were available to construct the LIGO detectors allow for 4 km arms. To reach the optimal arm length on a 4 km site, the number of times,  $B$ , that the light bounces off of the ETMs needs to be increased. Numerically,  $B$  should be  $\sim 250$ . This means that Equation (1.2) becomes

$$\Delta\phi = \frac{4\pi}{\lambda_{\text{EM}}} BLh. \quad (1.9)$$

Fabry-Perot cavities are used to increase the effective number of times light bounces off the ETMs<sup>3</sup>. Cavities are formed by placing an *input test mass* (ITM) in each arm near the beam splitter. When a photon enters a cavity, it remains in

---

<sup>3</sup>Herriott delay lines were considered as a means of achieving more bounces off the ETMs, however due to difficulty in manufacturing mirrors which do not scatter light, delay line interferometers fell out of favour. In principle, both delay lines and Fabry-Perot cavities would perform equally well due to the Mizuno limit [41].

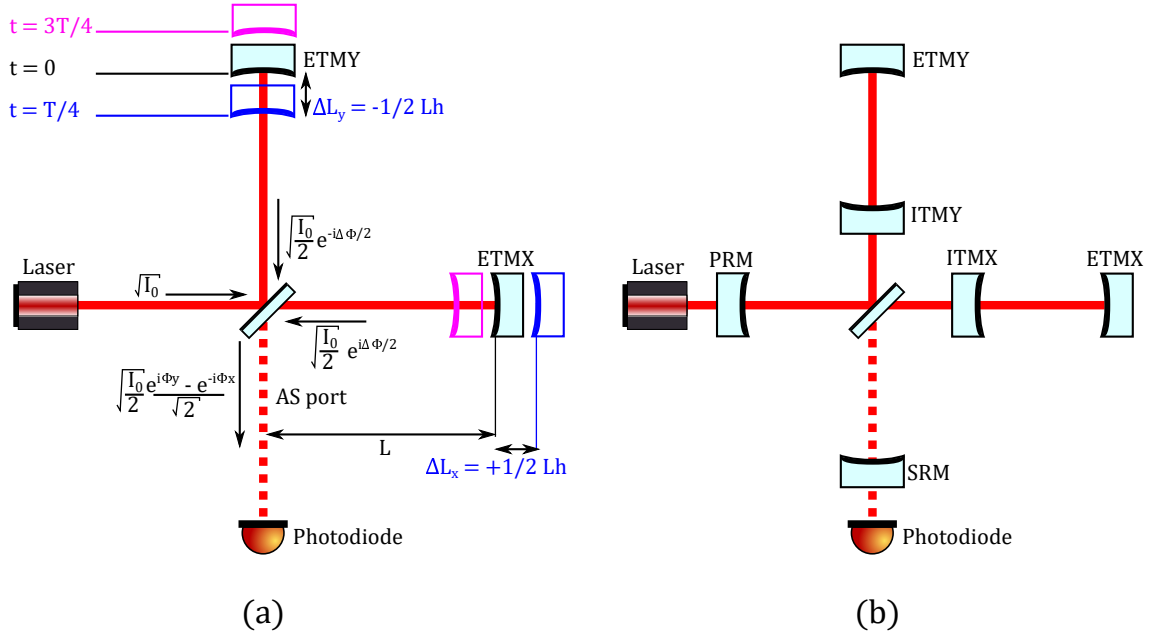


Figure 1.1: (a) A sketch of the effect a gravitational wave has on a Michelson interferometer. The positions of the test masses, ETMX and ETMY, at different times during the gravitational wave's period is shown by the blue and pink mirrors. The electric fields within the interferometer are indicated:  $\sqrt{P_0}$  is the laser's amplitude and  $\pm\Delta\phi/2$  is the phase acquired by the light as it travels up and down the arms. (b) To reach the sensitivity needed to detect gravitational waves, several mirrors need to be added to the basic Michelson interferometer: ITMX and ITMY boost the signal generated in the arms, the *power recycling mirror* (PRM) increases the power at the beam splitter, and the SRM can be used to shape the quantum noise of the interferometer.

the cavity for an average number of bounces that is determined by the reflectivity of the mirrors. Interferometers measure the difference in phase of the electromagnetic fields in the arms,  $\Delta\phi_{\text{EM}} = \frac{d\phi_{\text{EM}}}{d\phi_{\text{ETM}}}\Delta\phi_{\text{ETM}}$ , so when a Fabry-Perot cavity is near or on resonance, the Fabry-Perot cavity enhances the detectors sensitivity as the slope  $\frac{d\phi_{\text{EM}}}{d\phi_{\text{ETM}}}$  is much greater for a Fabry-Perot cavity than it is for a mirror. This is illustrated in Figure 1.2. The exact way this happens is dependent on the frequency of the gravitational wave and the reflectivity of the mirrors, with the arm cavity acting as a low pass filter (e.g. see [41, Chapter 3], [42, Appendix D], [43] or [44]).

## 1.4 Sources of Noise in Gravitational Wave Interferometers.

As the strain induced by a gravitational wave causes a minuscule change in the phase accumulated by light in the arm cavities, suppressing the noise below this signal is the main obstacle faced when trying to measure a gravitational wave. From Equation (1.9), for a gravitational wave strain of  $h_{\text{rms}} \sim 10^{-23}$  interacting with LIGO, the beams interfering at the beam splitter will have a difference in phase of  $\sim 10^{-11}$  rad.

### 1.4.1 Laser Power and Shot Noise

The shot noise associated with detecting a coherent state, such as that created by the laser, can limit the sensitivity of the interferometer. To reduce the shot noise of a

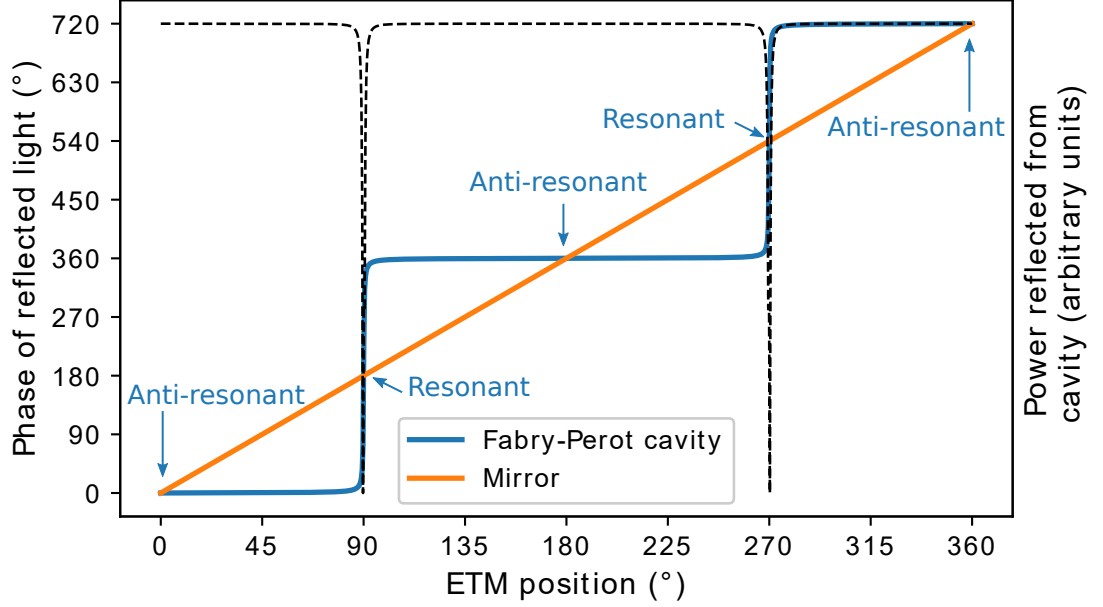


Figure 1.2: This figure shows the difference between the phase of the light reflected from a mirror versus the phase of light reflected from a cavity as the position of the mirror/end mirror is changed. The orange line shows the extra round trip phase acquired by light in the arm if the ETM is moved one wavelength ( $360^\circ$ ) and the blue line shows the same thing for a Fabry-Perot cavity. The phase of the light reflected from the cavity rapidly changes as it moves through the resonance. The interferometers sensitivity is proportional to the slope  $\frac{d\phi_{EM}}{d\phi_{ETM}}$ , and so a Fabry-Perot cavity can increase the sensitivity of the interferometer. The power of the light that is reflected from the cavity is indicated by the black dashed line.

measurement, the energy,  $\mathcal{E}$ , used in the measurement needs to be increased, and this corresponds to a increasing the laser power. The uncertainty in energy,  $\Delta\mathcal{E}$ , that is associated with a measurement of the time between two events,  $\Delta T$ , is determined by the time-energy uncertainty principle,  $\Delta\mathcal{E}\Delta T \geq \hbar/2$ . The uncertainty in the phase,  $\Delta\phi$ , of a light beam with angular frequency  $\omega_{EM}$  is related to the measurement time by  $\Delta\phi = \omega_{EM}\Delta T$  [45]. The phase is averaged over a time corresponding to half the gravitational wave's period, so  $\Delta T = \frac{1}{2f_{GW}}$ . The energy used in the measurement is  $\mathcal{E} = P_0\frac{1}{2f_{GW}} = \hbar\omega_{EM}N$ , where  $P_0$  is the power of the laser and  $N$  is the number of photons detected in the averaging time. As the laser is in a coherent state (e.g. [46,47]), the uncertainty in detecting  $N$  photons is  $\Delta N = \sqrt{N}$ ; therefore, the uncertainty in the energy used in the measurement is  $\Delta\mathcal{E} = \hbar\omega_{EM}\sqrt{N}$ . Using the expressions for  $\Delta\mathcal{E}$  and  $\Delta\phi$ , the uncertainty principle may be used to obtain

$$N \geq \frac{1}{4(\Delta\phi)^2}. \quad (1.10)$$

The amplitude spectrum of the power at the AS port,  $P_{ASrms}$ , measured by the photodiode over a time corresponding to a bandwidth of  $\Delta f$  will depend on the amount of light at the dark port,

$$P_{ASrms} = \sqrt{2P_{AS}\hbar\omega_{EM}\Delta f}. \quad (1.11)$$

The conversion from the power of the light at the AS port to gravitational wave

strain,  $h/P_{\text{AS}}$ , can be inferred from Equation (1.8),

$$\frac{h}{P_{\text{AS}}} = \frac{1}{\sqrt{P_0 P_{\text{AS}}}} \frac{\lambda_{\text{EM}}}{4\pi L B}, \quad (1.12)$$

and so the amplitude spectrum of the strain corresponding to the shot noise of the light at the AS port is

$$I_{\text{ASrms}} = \sqrt{\frac{\hbar c \lambda_{\text{EM}} \Delta f}{4\pi P_0 L^2 B^2}}. \quad (1.13)$$

Equation (1.13) assumed the frequency response of the interferometer to a gravitational wave is flat, however the arm cavities have a low pass filtering effect on the signal, and so the shot noise will rise as  $f$  above the characteristic frequency of the arm cavity. This can be seen in the spectral densities of the LIGO detectors' noise (Figure 1.3).

To make the photon shot noise be a factor of 10 below the expected gravitational wave signal, Equation (1.9) and Equation (1.10) show that, for a LIGO-like interferometer, the required number of photons to measure a gravitational wave with a strain amplitude of  $h_{\text{rms}} = 10^{-23}$  is  $\sim 10^{22}$ . For a gravitational wave signal with a frequency of 100 Hz, the laser power incident on the beam splitter would need to be  $\sim 1$  MW.

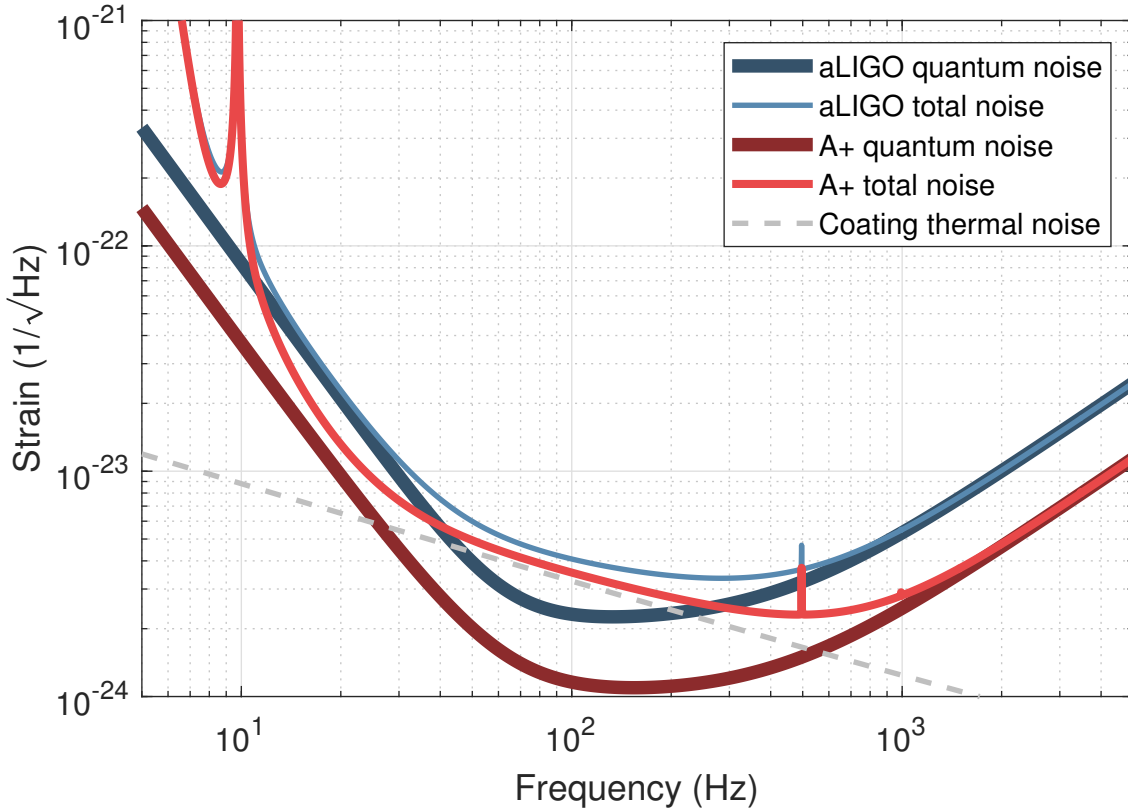


Figure 1.3: The light blue and light red lines show the design sensitivity of the aLIGO and LIGO A+ detectors. The noise due to radiation pressure and photon shot noise is shown in dark blue (aLIGO) and dark red (A+). These two noise sources make up the detectors' quantum noise. Above 10 Hz, quantum effects are one of the limiting sources of noise. Below 10 Hz, classical noise sources, e.g. seismic motion, limit the sensitivity of the detectors. Above 100 Hz, shot noise limits the sensitivity of detectors. Shot noise rises with  $f$  due to the arm cavities. Below 100 Hz, the quantum noise goes as  $1/f$  due to radiation pressure. Coating thermal noise will limit the A+ detectors' sensitivity in a band around 100 Hz.

### 1.4.2 Using Power Recycling to Reduce Shot Noise

Single frequency continuous wave lasers with a power of 1 MW do not exist, so to increase the laser power that is incident upon the beam splitter, a *power recycling cavity* (PRC) can be used [48–50]. When the interferometer is on the dark fringe, most of the light from the laser gets reflected by it. Thus, the interferometer is, effectively, a mirror. Drever [51] proposed that a mirror, known as the PRM, could be placed between the laser and the interferometer to form a cavity. A sketch of this is shown in Figure 1.1. The total power impinging on the beam splitter would be increased by making wavelength-scale position changes, i.e. *tuning*, of the position of the PRM such that the light reflected from the interferometer and the light from the laser add in phase, i.e. the reflected light power would be ‘recycled’. Current laser sources that can be operated for year-long timescales are capable of producing of the order 100W, see Chapter 2, and so the power recycling factor needs to be  $\sim 10^4$ . This technique has been implemented at LIGO [52] and other large-scale interferometers [35, 36].

### 1.4.3 Using Signal Recycling to Shape Quantum Noise

An interferometer’s bandwidth depends on the amount of time that the signal-carrying light spends in the arms. Meers suggested that the signal light could be recycled in a similar fashion to how power is recycled [48]. The detection bandwidth can be altered by introducing a mirror, known as the SRM, at the output of the interferometer between the photodiode and the beam splitter. A coupled cavity,

known as the SRC, will be formed by the SRM, ITM and ETM. A sketch of this is shown in Figure 1.1. The finesse of the arm cavities as seen by the light emerging at the AS port depends on the tuning of the SRM. There are two common modes of operation: *resonant sideband extraction* (RSE) [53, 54] and *signal recycling*. Alternatively, the SRM can be tuned so that the interferometer is optimised for a narrow band of frequencies, e.g. [55].

When in RSE mode, the SRM is tuned so that the SRC is anti-resonant, thus broadening the interferometer’s sensitivity ‘bucket’ at the expense of losing peak sensitivity. Originally, RSE was motivated by needing to reduce the thermal load on the beam splitter by increasing the finesse of the arm cavities [54]. However, by increasing the finesse of the arm cavity, the bandwidth of the interferometer is reduced. To retain the desired arm cavity finesse from a sensitivity point of view, the SRM can be made more highly reflective and tuned so that the finesse of the arm cavity experienced by the signal is lowered.

In signal recycling mode, the SRM is tuned so that the SRC is resonant. This deepens the sensitivity bucket at the expense of bandwidth. The trade-off between bandwidth and peak sensitivity comes from the conservation of energy. From an energy argument, the sensitivity of a detector to gravitational waves is determined by the detector’s bandwidth and the energy within this bandwidth; so for the same amount of power at the beam splitter, this can be thought of as a fundamental limit to the interferometer’s sensitivity. This is known as the Mizuno limit [41].

#### 1.4.4 Reducing Shot Noise by Removing Light in Higher Order Modes with a Mode Cleaner Cavity.

All light that is detected by the output photodiode contributes to the total shot noise of the measurement; therefore, only light which carries signal should be incident on the photodiode to enhance the SNR of the measurement. In an ideal interferometer, the light emerging at the AS port will be a beam that is defined by the mode that is resonant within the arm cavity. To minimise diffraction loss, and due to the reduction in purity of higher order modes due to mode degeneracy and imperfect mirrors [56], the light in the arm cavity will be in the *fundamental Gaussian mode*. However, due to optical imperfections, e.g. astigmatism, and the *radio-frequency* (RF) side-bands used to control the interferometer, the light emerging from the AS port contains light in higher order modes. This undesired light is referred to as *junk light*. A mathematical description of Gaussian beams can be found in Appendix F.

To remove junk light, mode cleaners are used (e.g. [57, 58]). A mode cleaner is a high finesse cavity that strips away light in higher order modes and the control sidebands. The LIGO *output mode cleaner* (OMC) [57] is a monolithic fused silica bow-tie cavity that has a round-trip of  $\sim 1$  m. As higher order modes acquire a different amount of phase as they propagate compared to the fundamental Gaussian mode, an optical cavity can be designed such that when the fundamental mode resonates, the higher order modes do not. These higher order modes will be suppressed by a factor proportional to the cavity's finesse. However, it is possible for some higher order modes to not be suppressed if their round trip Gouy phase is

nearly the same as that of the fundamental mode; thus, the cavity is designed so that only higher order modes which carry an insignificant amount of light will do this. The control sidebands are attenuated if they are outwith the cavity's linewidth. The beam transmitted by the mode cleaner will be predominantly in the fundamental mode, and so the SNR of the signal measured by the photodiode will be maximised.

### 1.4.5 Radiation Pressure Noise and the Standard Quantum Limit

Radiation pressure noise is a quantum effect that arises due to the uncertainty in the momentum that light imparts to the test masses when it is reflected from them [46]. These quantum fluctuations will give rise to a differential force on the ETMs, meaning that this noise couples as  $1/f^2$  to the measurement of the positions of the ETMs. A fluctuating force,  $F$ , arises due to the beam's shot noise. If the power of the beam is  $P$ , the amplitude spectral density of this force is  $F = 2\sqrt{2\hbar\omega_{EM}P}/c$ , where  $c$  is the speed of light. Thus, the amplitude spectral density of a mirror's position due to radiation pressure is

$$\Delta x_{\text{RPN mirror}} = \frac{\sqrt{\hbar\omega_{EM}P}}{\sqrt{2}mc\pi^2 f^2}. \quad (1.14)$$

To reduce the effect of radiation pressure noise, the LIGO test masses are 40 kg. The effect of radiation pressure noise on the LIGO detectors' sensitivity can be seen in Figure 1.3.

When the laser power is increased, the relative shot noise decreases while radi-

ation pressure noise increases, so a balance can be struck between the two types of noise. For a laser which produces a coherent state, i.e. a classical laser, the *standard quantum limit* (SQL) [46, 59, 60] sets an optimal laser power for a given ETM mass which minimises the total quantum noise. In a Michelson interferometer, the SQL sets a bound that follows a  $1/f$  slope. For a given power, the interferometer's quantum noise will reach this limit at only one frequency.

The quantum noise of an interferometer with an SRM that is tuned to either signal recycling mode or RSE mode will also reach the SQL at one frequency; however, for an arbitrary detuning of the SRM, the quantum noise of the interferometer will drop below the SQL at some frequencies due to non-linear optical effects [61].

#### 1.4.6 Coating Thermal Noise and Other Noise Sources

There are many classical sources of noise to overcome in a gravitational wave interferometer. The most notable of these is the noise associated with the Brownian motion of atoms in the amorphous mirror coating layers of the test masses [62]. Current detectors are designed around the expected noise level that can be achieved with these coatings. This will be one of the limiting sources of noise in the A+ detector, as shown in Figure 1.3. Other noise sources include seismic noise from the motion of the Earth, Newtonian noise from pressure waves in the Earth's crust, residual gas pressure noise that alters the refractive index of the arms, and the noise associated with the interferometer's electronics (e.g. [63, 64]).

## 1.5 Reducing Shot Noise with Non-Classical States of Light

The two-photon formalism developed by Caves and Schumaker [65, 66] can be used to describe how non-classical states of light can improve the sensitivity of an interferometer. In this framework, light is analogous to a quantum simple harmonic oscillator. A simple harmonic oscillator can be described by two orthogonal components, such as the momentum and position quadratures; for light, a convenient basis to use are the *amplitude* and *phase* quadratures. The amplitude and phase quadratures,  $\hat{\mathbf{X}}$  and  $\hat{\mathbf{Y}}$  respectively, defined in terms of annihilation and creation operators of the electromagnetic field,  $\hat{a}$  and  $\hat{a}^\dagger$ , are

$$\hat{\mathbf{X}}(t) = \frac{1}{2} (\hat{a}(t) + \hat{a}^\dagger(t)), \quad (1.15)$$

$$\hat{\mathbf{Y}}(t) = \frac{1}{2i} (\hat{a}(t) - \hat{a}^\dagger(t)). \quad (1.16)$$

From this formalism, an uncertainty relation between the phase and amplitude quadratures can be derived:

$$\Delta\hat{\mathbf{X}}\Delta\hat{\mathbf{Y}} \geq \frac{1}{2}. \quad (1.17)$$

If the uncertainty in one quadrature is reduced, the uncertainty in the other is increased. Such a light field is *squeezed*. The phase of the squeezed field which has the minimum uncertainty is defined as the squeezing angle.

As the gravitational wave signals will be in the phase quadrature of the light, it

would be advantageous to, by the uncertainty principle, move noise to the undetected amplitude quadrature from the detected phase quadrature; this can be achieved by using squeezed light. Squeezed light is created with an optical parametric amplifier; this is a device which generates correlated photons by converting single higher energy photons into two lower energy photons. This squeezed vacuum light is injected into the interferometer from the AS port so that the observed noise within the interferometer is squeezed. This technique has been implemented at LLO [67] and GEO600 [68].

However, fluctuations in the amplitude quadrature of the light perturb the position of the test masses; thus, they couple to the signal at the AS port. During LIGO's third observation run, the squeezing angle had to be tuned to prevent radiation pressure noise from limiting the BNS range of the detector [67].

To infer the quantum state of a light field, a technique known as *balanced homodyne detection* (BHD) can be used to observe one quadrature of the light field [69]. By combining the signal light field that is to be measured with a much stronger *local oscillator* (LO) light field on a beam splitter, the quantum state of the signal light field is encoded in the combined beams' power. The relative phase between the signal and local oscillator determines the quadrature of the quantum state that will be observed. Chapter 4.1 explores this in more detail.

## 1.6 Interferometry Techniques to Beat Quantum Limits

Squeezed light and an effect known as ponderomotive squeezing [59], can be used to surpass the SQL at some frequencies. Ponderomotive squeezing arises due to the natural correlations between the phase and amplitude quadratures of the light created by the interferometer. A demonstration of the SQL being surpassed at the LIGO Livingston detector can be found in [70]. Although [70] shows the SQL was beaten at some frequencies, the noise at other frequencies was increased relative to if no squeezing was used. The LIGO detectors are operated for broadband gravitational wave sensitivity, but sub-SQL interferometer configurations could be used if detecting certain astrophysical sources with merging frequencies around the frequency at which the SQL is beaten was of interest.

To avoid the increase in radiation pressure noise that is experienced when squeezed light is used, a frequency dependent squeezer can be utilised [59]. The light's squeezing angle can be rotated as a function of frequency. This is done by reflecting the light from a high finesse detuned *filter cavity*. At frequencies within the linewidth of the cavity, the light reflected from the filter cavity will experience a phase shift and so the squeezing angle will be rotated; in contrast, at frequencies outside the cavity's linewidth, the light incident upon the cavity is reflected without experiencing any phase shift and so the squeezing angle is not rotated. At low frequencies, the amplitude quadrature can be squeezed and thus the interferometer's radiation pressure noise can be decreased. At high frequency, the phase quadrature can be

---

squeezed and thus the interferometer's shot noise can be decreased. A frequency dependent squeezed light source that is suitable for LIGO has been demonstrated [71] and frequency dependent squeezing will be part of the A+ detector.

Variational readout is a technique where quantum noise due to radiation pressure is removed from the measurement by using a frequency dependent homodyne angle [59]. This is realised in a similar way to frequency dependent squeezing; the AS beam is coupled to a filter cavity and thus the detected quadrature of the beam emerging from this cavity is frequency dependent. This beam is then measured on photodiodes using a conventional BHD scheme. Variational readout schemes are sensitive to small amounts of loss within the filter cavity, and so this technology is not mature enough to be implemented into current gravitational wave detectors.

To beat the bandwidth limit, energy has to be injected into the system. Using white-light cavities as a means of increasing a detectors bandwidth have been studied [72–74]. However, these interferometer configurations have yet to be experimentally demonstrated.

There are several sub-SQL schemes which avoid the quantum noise problems related to making a position measurement of the test masses. If a momentum measurement of the test masses could be made, then a random imparting of 'position' would not affect future measurements of the momentum [75]. This is a type of quantum non-demolition measurement. As a speed measurement is being made, the displacement noise would rise as  $1/f$  instead of  $1/f^2$ ; this type of measurement can be made with a speed meter interferometer [76–78].

## 1.7 The Effect of Loss Mechanisms Within the Interferometer on Measuring Quantum States of Light

Loss in the optical path from the arm cavities to the readout photodiodes results in less signal as well as more noise. The decrease in signal is straight forward to understand: if there are fewer photons to measure, then the signal will be smaller. For coherent light, the signal is proportional to the power and the noise is proportional to  $\sqrt{\text{power}}$ , so the SNR is proportional to  $1/\sqrt{\text{power}}$ ; thus, loss results in a decrease in the SNR.

As gravitational wave detectors implement squeezing to decrease the quantum noise in the detection quadrature, it is important to preserve the quantum state of the signal field by having minimal loss. Real optical components have physical attributes that result in incident light power being wasted. These mechanisms are known as losses, and examples of these include absorption and scattering. A lossy optical component can be modelled as an ideal one downstream of a beam splitter whose splitting ratio represents the loss (e.g. [47, Section 2]). The incoming light enters a beam splitter; some light is directed to the ideal component and some gets lost. In the remaining input to the beam splitter, vacuum fluctuations can enter. Some of these fluctuations will make it to the ideal component, and so the state of the light that is detected is contaminated with extra vacuum fluctuations compared to if there was no loss. The factor by which the shot noise increases,  $\epsilon$ , due to a

simple loss mechanism, such as a non-ideal photodiode (see Section 1.8), is given by

$$\epsilon = \sqrt{\frac{1}{\eta} - 1}, \quad (1.18)$$

where  $0 < \eta < 1$  is the efficiency ( $1 - \text{loss}$ ) of the component.

Mode matching losses have a greater contribution to the total shot noise compared to losses of the same size generated by a simpler mechanism [79]. This source of loss can be reduced through careful design of the optical layout. Mirrors with a tuneable radius of curvature can be used to ensure that there is minimal loss due to mode mismatch. This is the focus of Chapter 5.

## 1.8 Photodiodes

Photodiodes are used to sense the signal-containing light from the interferometer via the OMC (see Section 1.4.4)<sup>4</sup>. A photodiode is a square-law detector that produces a current that is proportional to the power of the light incident on the detector. The photodiode's *quantum efficiency* is the fraction of photons that are absorbed by the photodiode producing a photocurrent; a quantum efficiency less than unity is a source of loss. Photodiodes are usually operated with a *reverse bias* – cathode held at a positive voltage relative to the anode – to widen their depletion region, thus improving their quantum efficiency and bandwidth (see Section 6.2 for more detail).

---

<sup>4</sup>In this thesis, unless specified, I will be talking about the ‘DC’ photodiodes used to sense the gravitational wave signal. There are other types of photodiodes used in gravitational wave detectors, e.g. RF photodiodes; these are not discussed.

Due to its bandgap, InGaAs is a widely used semiconductor for detecting 1-1.6 $\mu\text{m}$  light, and suitable InGaAs photodiodes were available for the current generation of gravitational wave detectors. The requirements for the photodiodes used in a gravitational wave detector are discussed in Section 6.1. Usually, off-the-shelf InGaAs photodiodes are of the order 1 mm in diameter to keep their junction capacitance low enough for high-speed operation<sup>5</sup> and to keep their dark current low. Photodiodes often follow a *p-doped, intrinsic, n-doped* (PIN) semiconductor structure (see Section 6.2) as this design can yield photodiodes with high quantum efficiency and fast response times. InGaAs PIN photodiodes can often detect up to 100 mW of light power, and they can be operated at room temperature.

Since future gravitational wave detectors may need to operate with 2  $\mu\text{m}$  light (see Section 1.10), the current photodiodes may be replaced with devices capable of sensing light with a wavelength of 2  $\mu\text{m}$ . ‘Extended’ InGaAs photodiodes may be used to do this. Extended InGaAs is an industry term for InGaAs photodiodes with cut-off wavelengths that are above 1.6  $\mu\text{m}$ . Based on conversations with four photodiode manufactures and distributors [80–83], it is unlikely that commercially available extended InGaAs photodiodes for detecting 2  $\mu\text{m}$  light that are suitable for a gravitational wave detector exist. As discussed in Chapter 6, it is difficult to produce defect-free extended InGaAs, and defects in extended InGaAs photodiodes can cause the noise and quantum efficiency of the photodiode to be degraded. It may be noted that previous experiments in squeezing at 2  $\mu\text{m}$  have been limited by the properties of the extended InGaAs photodiode that was used [84, 85]. In [84],

---

<sup>5</sup>High-speed operation ( $> 100$  kHz) is not needed for a photodiode that is used to sense the light which contains the gravitational wave signal.

the photodiode was not reverse biased to minimise noise from the photodiode which would have limited the experiment; this came at the expense of the photodiode's quantum efficiency being degraded, and the total observed squeezing was limited by the photodiode's quantum efficiency. The characterisation of some extended InGaAs photodiodes is described in Chapter 6.

## 1.9 Overview of the LIGO Detectors

The LIGO detectors are dual-recycled Fabry-Perot Michelson interferometers with 4 km arms [5]. One of these is at LLO and the other is at the *LIGO Hanford Observatory, WA., USA* (LHO). The layout of the detectors is shown in Figure 1.4 [86] and their sensitivity curves are shown in Figure 1.3 [87, 88]. The term dual-recycled refers to the fact that the interferometers use both power and signal recycling. The interferometers are housed within vacuum systems comprised of several *horizontal access modules* (HAM) and basic symmetric chambers (BSCs). Figure 1.4 includes all the optics from the *pre-stabilised-laser* (PSL) to the photodiodes that detect the main beam.

The first cavity after the PSL is the *input mode cleaner* (IMC); this provides a beam with high spatial purity for the interferometer and is used in the initial locking sequence as a stable frequency reference. The PRC features two extra mirrors, known as PR2 and PR3, in addition to the PRM. The role of these mirrors is to make the round trip Gouy phase sufficient so that it is stable; the signal recycling cavity also has three mirrors for the same reason [52]. The beam passes through the *output*

*Faraday isolator* (OFI), and is steered into the OMC. The gravitational wave signal is encoded in the beam transmitted by the OMC, so photodiodes monitor this light.

## 1.10 The Future of Ground-based Gravitational Wave Detectors

The next generation of ground-based gravitational wave detectors include the Einstein Telescope [89,90], LIGO Voyager [91] and LIGO Cosmic Explorer [92–94]. LIGO Voyager will be a cryogenic interferometer installed in the current LIGO infrastructure and will be a factor of  $\sim 2$  more sensitive than LIGO A+. The Einstein Telescope and Cosmic Explorer interferometers will be ten times larger than the current generation of interferometers and will be able to: test the no-hair theorem, test alternative theories of gravity, test models of string theory, measure objects with large redshifts to learn about the formation of cosmological structures, measure closer to the big bang than is possible with electromagnetic telescopes, detect cosmic strings, probe the physics of neutron stars and measure what happens during a supernova. As well as this, the third generation of gravitational wave detectors may measure signals from exotic sources which have not yet been theorised.

The current generation of gravitational wave detectors are limited by the thermal noise around 100 Hz, see Figure 1.3, due to the Brownian motion of the molecules that make up the mirror coatings [95]. Since these thermally driven fluctuations are a limiting source of noise, proposed future gravitational wave detectors may use

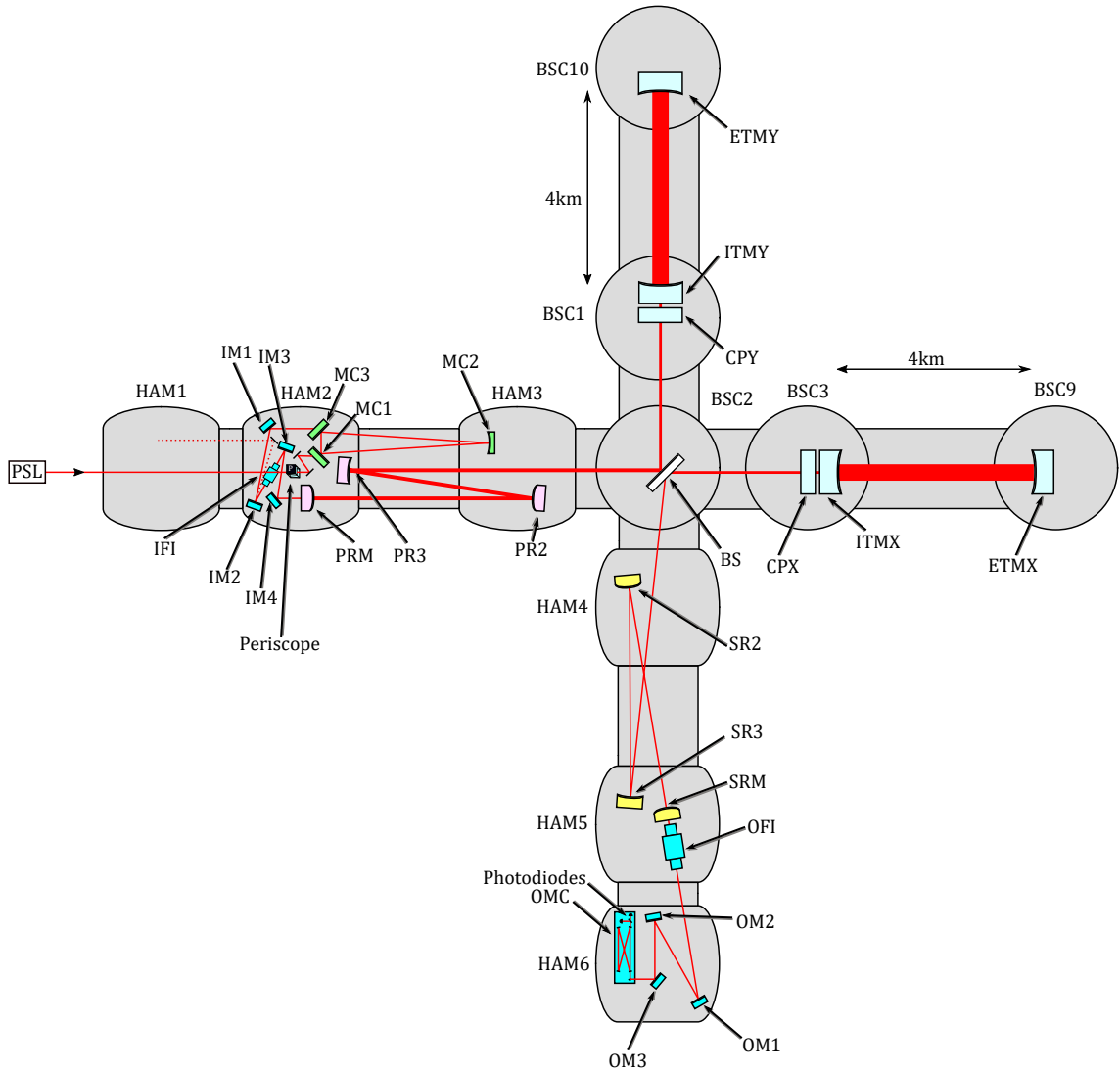


Figure 1.4: Sketch of a LIGO detector. The input and output optics — IM1-4, the input periscope, OM1-3, the OMC, the input Faraday isolator and the OFI — are shown in blue. The IMC mirrors are shown in green. The power recycling mirrors are shown in pink. The arm cavity mirrors are shown in pale blue. The signal recycling cavity mirrors are shown in yellow. The beam leaves BS at an angle due to the BS being wedged. Angles in the recycling cavities are exaggerated and the arms are shortened for clarity.

cryogenically cooled mirrors.

However, the material that the test masses are currently made from, fused silica, has undesirable noise properties when it is cooled [96] and so the future test masses may be made of crystalline silicon; crystalline silicon is opaque at  $1\ \mu\text{m}$  [97] and since light will be required to transmit through them, this forces a change from a  $1\ \mu\text{m}$  laser. Additionally, cryogenically cooled mirror coatings may not be compatible with the current laser wavelength [98–100]. Therefore, future gravitational wave detectors may use either a  $1.5\ \mu\text{m}$  or  $2\ \mu\text{m}$  wavelength laser [93,94].  $2\ \mu\text{m}$  is of interest as there have been promising designs for low noise mirror coatings that are optimised for this wavelength [101].

## 1.11 Conclusion

Further detections of gravitational waves will lead to a better understanding of the Universe. To reach the design sensitivity of the LIGO detectors, among other upgrades, the input laser power needs increasing. To further lower the LIGO detectors noise floor, the A+ upgrade will utilise frequency dependent squeezed light. For this to be successfully implemented, the quantum state of the light field must be accurately detected with a balanced homodyne readout and losses in the readout must be minimal.

As there is potential to reduce the noise floor that will limit the A+ detector by using cryogenic mirror coatings that are compatible with  $2\ \mu\text{m}$  light, future detectors

may use a 2  $\mu\text{m}$  laser; this leads to the question: is laser technology at this wavelength sufficiently mature to enable quantum limited gravitational wave detectors? BHD and photodiodes with high quantum efficiency and low dark noise will be required for any future interferometer.



## Chapter 2

# A Prototype High Power Laser for LIGO's Fourth Observation Run

### 2.1 Introduction

The LIGO detectors require high input power, nominally 125 W at 1064 nm [102], to decrease the shot noise which limits their sensitivities at frequencies above 100 Hz. The original laser for aLIGO cannot reach the required power without generating excess pointing noise. In this chapter, the new laser layout is discussed. The *pre mode cleaner* (PMC) throughput power, beam quality, intensity noise, pointing noise and frequency noise of the prototype laser were measured. The prototype of the new laser was able to produce 100 W of intensity stabilised light. The pointing noise was

measured to be above the requirement; however, this prototype was made in a lab which was noisier than the room in which the PSL is housed, and the pointing noise may be improved by reducing turbulence in the water-cooling system. While the 125 W nominal power level was not obtained, this layout can provide  $\sim 30$  W more power than the laser which was used for LIGO's third observation run. With additional work in optimising the setup, the maximum output power of this laser may be increased.

If coherent light from a laser is detected, the amplitude spectral density,  $\sigma$ , of the shot noise associated with the laser's power,  $P$ , is  $\sigma = \sqrt{\frac{hc}{\lambda}P}$ , so the SNR,  $P/\sigma$ , scales with  $\sqrt{P}$ . Alternatively, to decrease the shot noise limit, the wavelength could be decreased; however, the LIGO detectors operate at 1064 nm due to the availability of mirror coatings with low absorption and low thermal noise. As thermal noise limits current detectors, cryogenically cooled mirrors and test masses may be used in future interferometers, and these will likely work with 1.5  $\mu\text{m}$  or 2  $\mu\text{m}$  light [101].

In the field of ground-based gravitational wave detection, high power refers to lasers with powers of the order 100 W. High power is a loosely defined term as lasers ranging from 100 W to 100 kW are called high power in the literature [103–113]. Pulsed lasers are often used to reach high powers, however gravitational wave detectors must use a single frequency, narrow linewidth, continuous wave laser, so a pulsed laser would be unsuitable. As the power is increased, other properties of the laser tend to be degraded. It needs to operate uninterrupted on year-long timescales; this poses a major engineering challenge.

The laser for LIGO must be linearly polarised, have high spatial purity, low intensity noise and low frequency noise. These requirements are detailed in [102]. To overcome the technical challenges that come with the high power and low noise requirements for the LIGO laser, the *master-oscillator-power-amplifier* (MOPA) topology was selected. This type of laser is based on a high-performance seed laser which is then amplified. As amplifiers are linear and coherent, the low noise properties of the seed laser characterises the noise of the high-power beam.

LIGO's original laser was able to generate  $\sim 150$  W of power in the HG00 mode [114]. This laser used an injection-locked *high power oscillator* (HPO) as the means for obtaining the target power. The HPO was a ring cavity containing laser crystals, and it was seeded by a 35 W low noise-laser. This laser went through extensive testing and refinement at the Max Planck Institute for Gravitational Physics [114] and was installed as part of LIGO's PSL.

However, due to pointing noise from the water cooling of the crystals within the HPO coupling to the differential arm motion signal, as well as one HPO being destroyed by accident, the HPO was bypassed and the LIGO detectors operated using only the 35 W laser [95]. To reach higher powers during LIGO's third observation run, instead of the HPO, a neoVAN-4S single-pass amplifier made by neoLase [115] was used. This stepped up the laser power from 35 W to 70 W [64, 116].

The next stage of development was a complete redesign of the LIGO laser. A prototype laser was constructed and tested at LIGO Livingston. This design will be installed as the new PSL for the start of LIGO's fourth observation run [95].

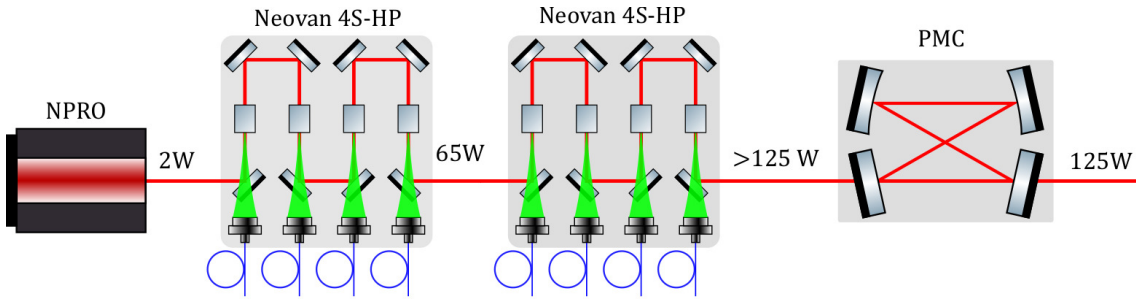


Figure 2.1: Conceptually, the PSL will be made up of four components: the NRPO, two neoVAN-4S-HP amplifiers and the PMC cavity. The NRPO provides seed light with good noise characteristics. These noise characteristics are preserved by the amplifiers, so the resulting beam will have high power and low noise. As the linewidth of the PMC  $\sim 1$  MHz, it filters away light in higher order modes and RF intensity noise so a quiet spatially pure mode can be sent to the interferometer.

## 2.2 Concept for LIGO's New Laser

LIGO will use a MOPA laser that is seeded by a *non-planar ring oscillator* (NPRO). The NPRO beam will be amplified by two neoVAN-4S-HP single-pass amplifiers [115] in series and be followed by a mode cleaner cavity to produce a low-noise, high-power laser in the fundamental mode. This concept is shown in Figure 2.1.

### 2.2.1 Non-Planar Ring Oscillators

The first element of the PSL is an NPRO [117–119]. The NPRO provides a low noise laser making it a suitable seed for a MOPA system. This is a single frequency

laser constructed from one Nd:YAG crystal which acts as both the gain medium and the cavity, thus it produces a laser with a high amount of frequency stability. The NPRO used was a Mephisto sold by Coherent [120], and it can produce 2 W of 1064 nm light.

### 2.2.2 The neoVAN-4S-HP Solid-State Amplifier

The neoVAN-4S-HP is a single-pass solid-state amplifier manufactured by Neolase. It is constructed from four Nd:YVO<sub>4</sub> crystals which are pumped by fibre coupled, low noise laser pump-diodes. It should be seeded by s-polarised light at 1064 nm. These gain mediums are in contact with a metal plate which is cooled. This keeps pointing noise low as flowing water is not directly in contact with the gain medium. As these amplifiers have low noise pump-diodes and will be seeded by an NPRO, the noise of the light produced by them should be determined by the NPRO. Results from a setup using a single neoVAN-4S-HP showed these amplifiers can be continuously operated for many tens of days [113]. A similar setup using a 35 W seed laser and two neoVAN-4S-HPs was able to generate 195 W of light [112] for nearly 80 days with no significant drops in power.

### 2.2.3 The Pre Mode Cleaner Cavity

The light transmitted by the PMC is used as the input beam for the interferometer. The PMC is locked to the fundamental mode so that the beam which is delivered to the rest of the interferometer will not contain much light in higher order

modes. This is important as the amplifiers produce light with spatial defects.

The PMC is a 2 m bow tie cavity with a *free spectral range* (FSR) of  $\sim 150$  MHz and a *full width at half maximum* (FWHM) of  $\sim 1$  MHz, thus it passively filters RF intensity noise. RF sidebands used for sensing and controlling lengths within the interferometer are provided after the PMC but before the IMC (see Figure 1.4), meaning that the IMC cannot be used to provide the required RF intensity stabilisation.

The PMC has been redesigned [121] to prevent contamination due to glue on its mirrors and to make maintaining the PMC easier. Failures of the old PMCs can be found in [122, 123]. The PMC design no longer includes a vacuum enclosure to isolate it from acoustic noise as this was found to be unnecessary.

## 2.3 Layout of the Prototype Laser System

An optical layout based on the concept described in Section 2.2 was constructed. A sketch of the layout is shown in Figure 2.2. In addition to the main beam path, there are low-power diagnostic beams after each amplifier that can be used to characterise the laser. Eventually, this laser will include the tabletop frequency stabilisation servo (TTFSS); however, at this stage of testing, the TTFSS was not installed and so this has not been included in the layout description.

The NPRO beam passes through some optics to clean up its polarisation. Light

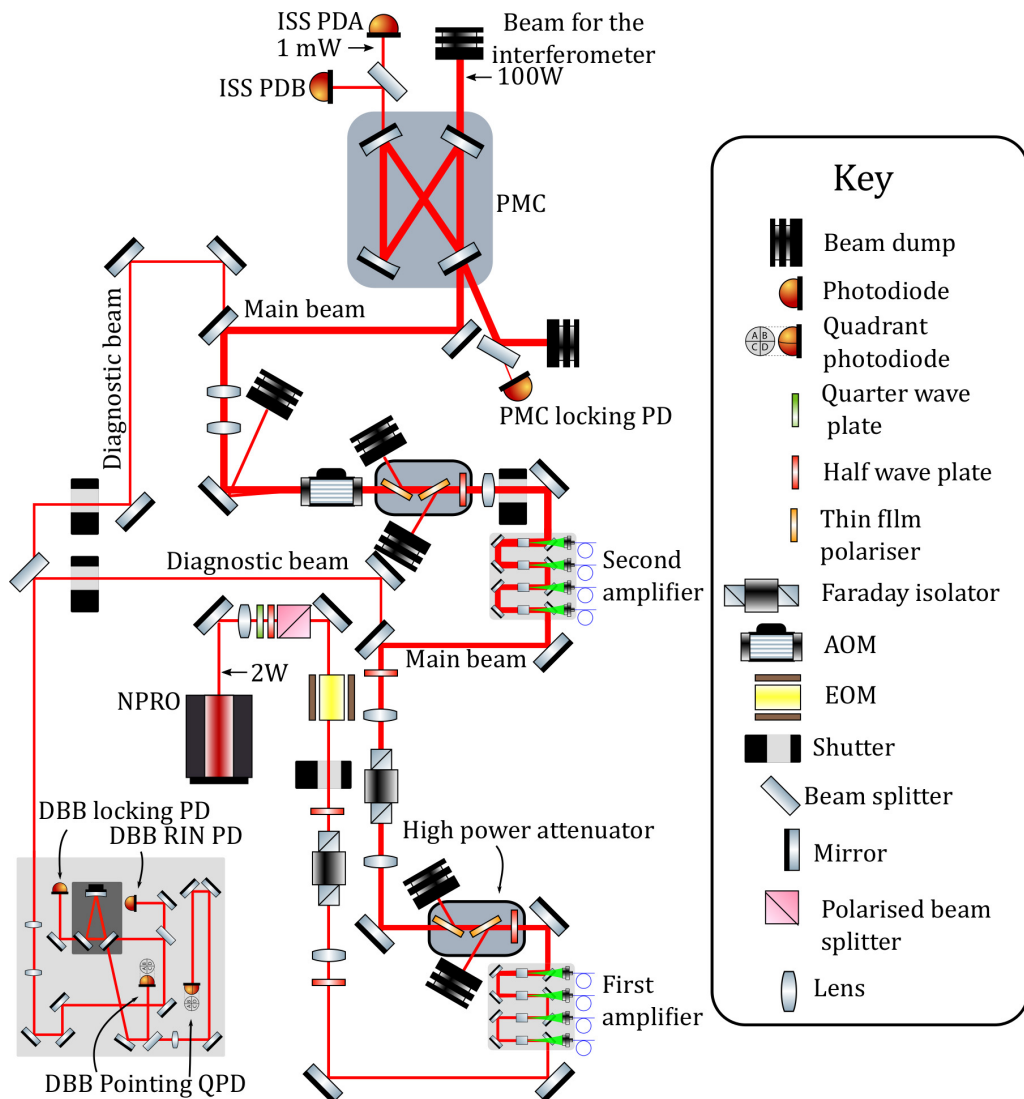


Figure 2.2: This sketch shows all the optics in the main beam path as well as the pick-off points for the diagnostic beams for the prototype of the optical layout for the PSL. After the first amplifier, the power of the laser is  $\sim 60$  W, and after the second amplifier, it is  $\sim 120$  W. While the laser is being amplitude stabilised, the throughput power of the PMC was  $\sim 100$  W. The photodiodes for stabilising the laser's intensity are called ISS PDA and PDB. Within the *diagnostic bread board* (DBB) (grey box in the bottom left), there are several photodiodes for characterising beams.

transmitted through a steering mirror is used to monitor the power of the NPRO. An *electro-optic modulator* (EOM) produces 35.5 MHz sidebands for the *Pound-Drever-Hall* (PDH) scheme used to lock the PMC. A Faraday isolator ensures light reflected back through the amplifiers does not reach the NPRO and hence damage it. The beam passes through a lens to mode match the beam to the first amplifier. Two mirrors are used to align the NPRO beam to the amplifier. A half-wave plate ensures the polarisation into the first amplifier is set correctly. These optics are shown in Figure 2.3.

After the first amplifier, the beam passes through a high-power attenuation stage, which consists of a half wave-plate and two thin film polarisers, to allow for safe set up and low power operation. When setting up this layout, the amplifiers must be run at maximum power since they exhibit significant thermal lensing. The high-power attenuators are not envisioned being used during observation runs. The light from the laser is then directed through a Faraday isolator and wave-plate before reaching the second amplifier. The mode matching lenses for the second amplifier are on either side of the Faraday isolator. Two mirrors immediately before the second amplifier are used for its alignment. The transmission through one of the steering mirrors before the second amplifier is used for monitoring the beam produced by the first amplifier. This section of the layout is shown in Figure 2.3.

After the second amplifier, the beam goes through a high-power attenuation stage before passing through an AOM. This AOM is for controlling the power of the laser. Downstream of the AOM, a pick-off beam is used to measure the properties of the laser produced by the second amplifier. Before entering the PMC, the beam is

transmitted through a thin film polariser so that the beam is set to be p-polarised. This part of the layout can be seen in Figure 2.4.

The beam produced by the second amplifier is then coupled to the PMC; this requires two mode matching lenses and two steering mirrors. There are three beams transmitted by the PMC: a high-power one, which would be sent to the interferometer, and two low-power ones for stabilising the frequency and intensity of the laser. The low-power beams are of the order 100 mW. The *intensity stabilisation servo* (ISS) inner-loop photodiodes are in a light-tight enclosure. One of the photodiodes is used as the in-loop sensor while the other is used as the out-of-loop sensor. The PMC is shown in Figure 2.5. The light reflected from the PMC is used to lock it; this path can be seen in Figure 2.4.

The DBB [124,125] is integrated into the layout via several pick-off points and can be used to monitor the status of both amplifiers. The DBB enables measurements of intensity noise, frequency noise, beam pointing noise and higher order mode content. The DBB is shown in Figure 2.6. The DBB consists of a cavity, motorised lenses, an automatic alignment system and several photodiodes. Despite having motorised lens mounts in the DBB, static mode matching lenses are required in the diagnostic beam paths. To characterise the NPRO beam, mirrors on magnetic mounts can be inserted into the layout.

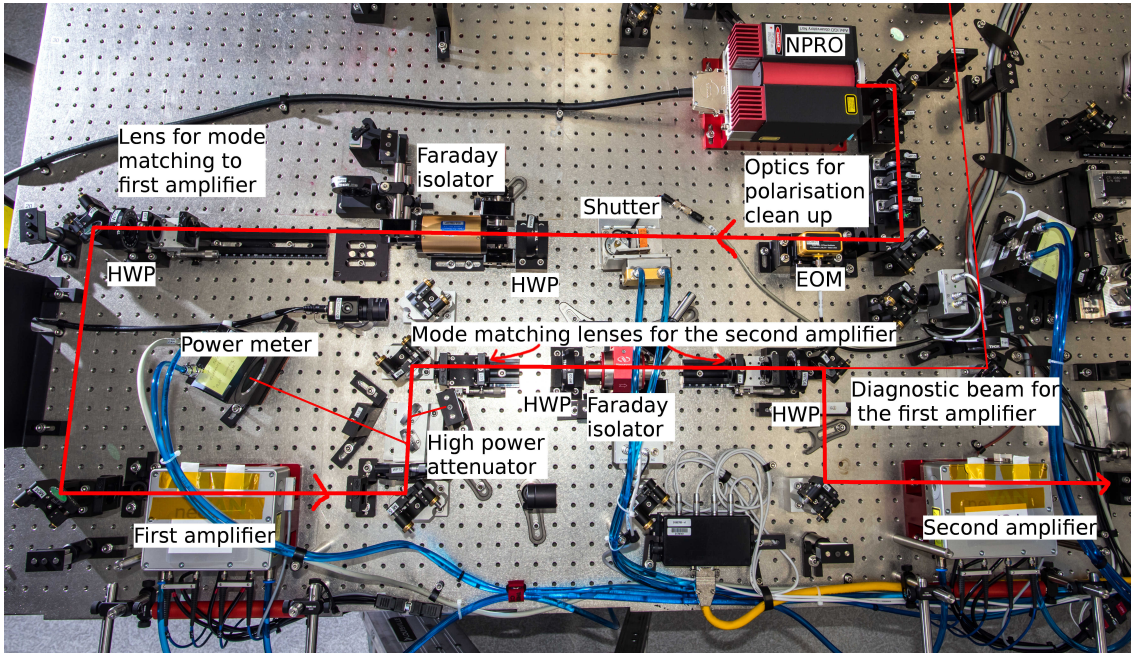


Figure 2.3: Photograph of the PSL prototype showing the beam path (red lines) from the NPRO (top right) to the second amplifier (bottom right). The beam path up to the first amplifier includes optics for setting the polarisation of the beam, an EOM, a Faraday isolator and lenses for mode matching. After the first amplifier, the beam passes through a high-power attenuator, mode matching lenses and a Faraday isolator. The first amplifier (bottom left) is monitored using a low-power pick-off beam (centre right).

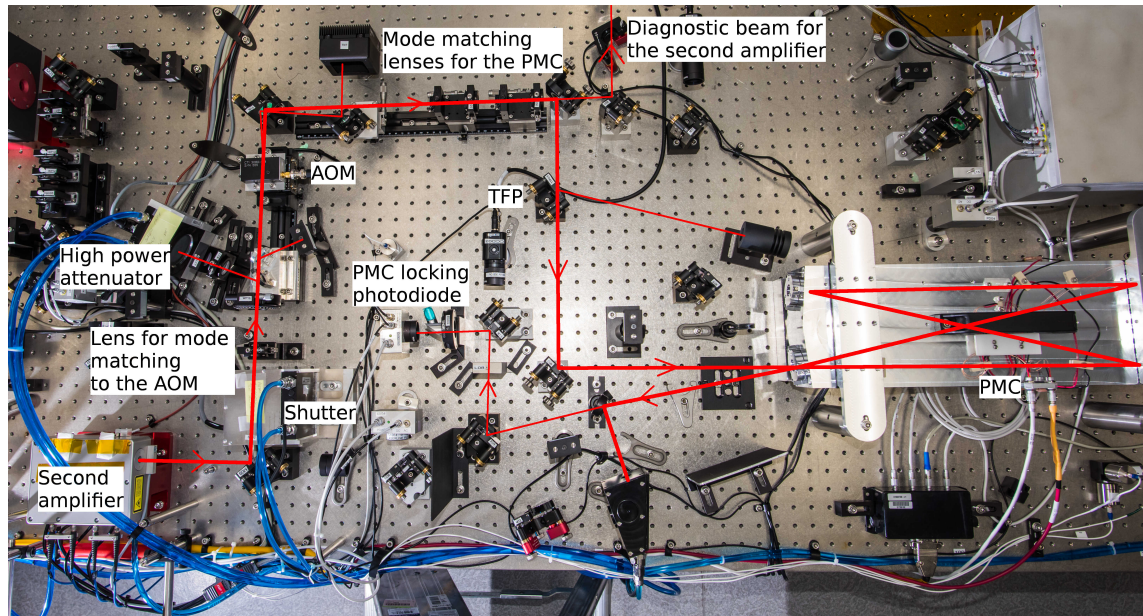


Figure 2.4: Photograph of the layout showing the beam path (red lines) from the second amplifier (bottom left) to the input of the PMC (centre right). This beam path includes a high-power attenuator, an AOM, mode matching lenses for the PMC and a thin film polariser. The PMC can be seen more clearly in Figure 2.5. The path taken by light reflected from the PMC is shown. This light is used to lock the PMC. A low-power beam for monitoring the second amplifier is obtained using the transmission through a steering mirror (centre top) for the alignment to the PMC.

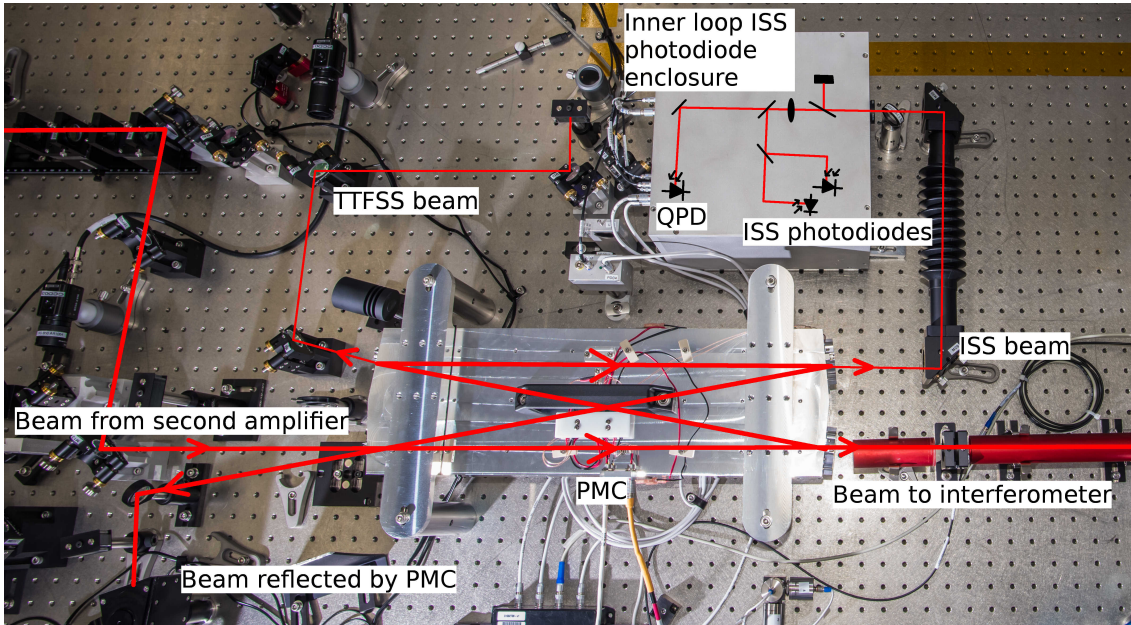


Figure 2.5: Photograph of the PMC (centre) and the inner ISS photodiode box (top right). The beam (shown in red) from the second amplifier enters the PMC. The majority of this light is sent to the interferometer. A small fraction of the light in transmission of the PMC is used to stabilise the intensity and frequency of the laser. These beams are labelled as the ISS beam and the tabletop frequency stabilisation servo beam. The ISS beam is directed into a light tight enclosure. This enclosure contains two photodiodes which are for measuring the intensity noise of the laser. One of these is an in-loop sensor; the other is an out-of-loop sensor. A quadrant photodiode (QPD) can be used to monitor the alignment of the ISS photodiodes. The reflected beam from the PMC is made up of the junk light in the beam from the second amplifier.

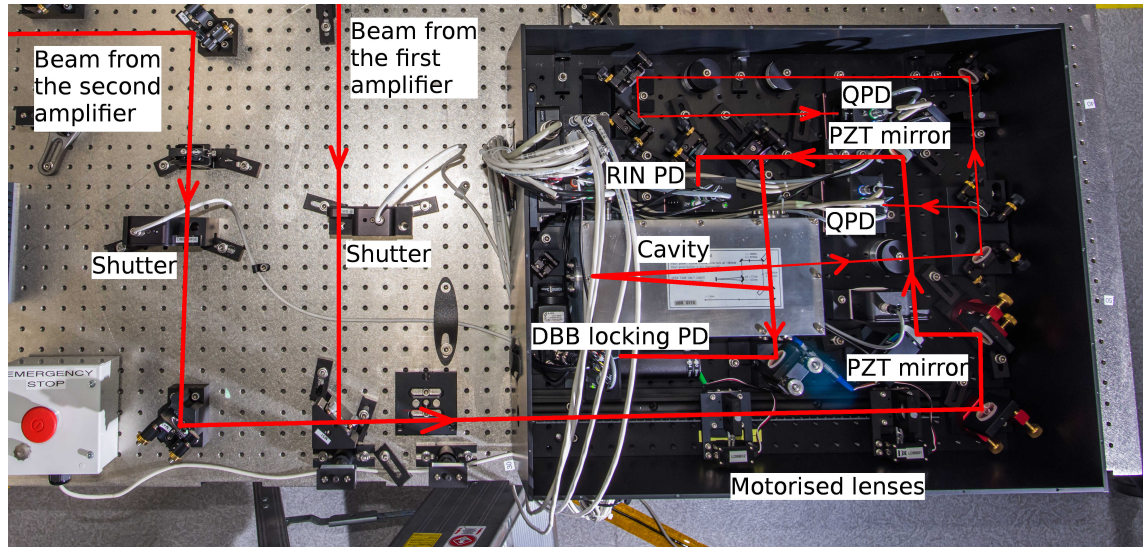


Figure 2.6: Photograph of the DBB with the beam path highlighted in red. Low power beams are used to measure properties of the laser produced by both amplifiers. The shutters control which amplifier will be characterised. The DBB contains motorised lenses and PZT mirrors so that remote mode matching and automatic alignment can be performed. The intensity noise of the beam can be measured with the *relative intensity noise* (RIN) photodiode. The DBB locking photodiode is used to lock the cavity to the beam. This photodiode is also used during mode scans to measure the higher order content of the beam. Quadrant photodiodes (QPD) separated by  $90^\circ$  of Gouy phase are used to measure the pointing noise of the incoming beam.

## 2.4 The Power Transmitted by the Pre Mode Cleaner

The PSL should deliver 125 W to the interferometer [102]. The power transmitted through the PMC is ultimately determined by two factors: the power in the beam generated by the amplifiers, and the distortion of this beam. The beam's distortion is affected by the alignment, mode matching and thermal lensing of both amplifiers. Increasing the pump-diode current increases the power that is produced by the amplifier as well as the thermal lensing. The flow rate of the coolant can be increased to mitigate thermal lensing; however, this can generate pointing noise if there is turbulence in the water cooling system.

The prototype layout was able to deliver a maximum of 111 W through the PMC during a 55 hour trial run. This is shown in Figure 2.7. The power was measured with power meters that were recently calibrated. The power emerging from the PMC dropped to 107 W during the course of the trial run, while the power incident onto it remained  $\sim 125$  W. Changes in the lab's temperature can cause slight alignment drifts, and changes in the lab's humidity can alter the properties of optical coatings. The humidity was monitored during this run as temperature and humidity track one another and the temperature sensors available were inferior to the humidity sensor. Changes in the temperature and humidity resulted in the power decreasing. As the laser will be in a controlled environment, this effect will be less severe when it is installed.

To increase the output power, the mode matching to the PMC could be improved

and the amplified beam's distortion could be reduced. Mode matching between the final amplifier and the PMC could be improved at the percent level. Increasing the flow rate would reduce the beam's distortion and may allow for higher pump-diode currents, however concerns of pointing noise meant that the flow rate was kept low. With higher flow rates, a beam with 137 W of power and a *higher order mode* (HOM) content of 4.6% was produced by the amplifiers.

To actuate on the power of the laser, some of the incident light will be 'dumped' to provide headroom for the actuator to both increase and decrease the beam's power as needed. This means that the full power will be reduced by  $\sim 10$  W when the intensity stabilisation is activated.

Long term measurements should be taken, however the results in [112] show these amplifiers can be run continuously for at least 80 days. Staff at LHO measured the input laser power dropping from 55 W to 52 W over the course of one year [1]; this was likely due to the ageing of the laser pump-diodes as well as mode mismatches resulting from changes in the thermal state of the setup.

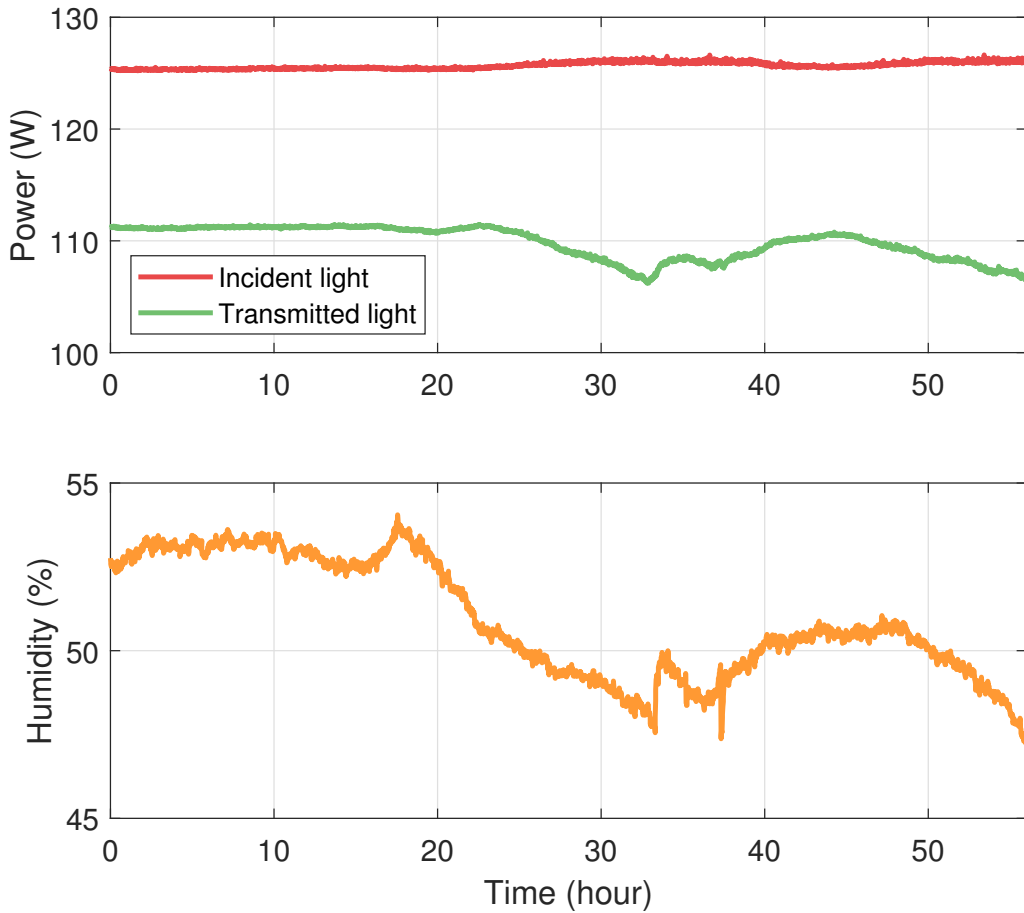


Figure 2.7: The top panel shows the power that was incident on the PMC and the power emerging from the PMC over a 55 hour trial run. The light produced by the amplifiers did not change significantly for the duration of this measurement, however the transmitted light through the PMC dropped from 111 W to, at its lowest, 107 W. This is likely due to the environmental conditions in the lab changing. The bottom panel shows the humidity of the lab. Changes in the humidity, which can be caused by a temperature change, coincide with changes in the power emerging from the PMC. This indicates that the alignment or mode matching of the laser and the PMC may be dependent on temperature due to e.g. the thermal expansion of optical mounts.

### 2.4.1 The Effect of Cooling on the Amplifier's Power and Beam Quality

As the quality of the beam emerging from an amplifier is affected by the temperature of the amplifier's head, an experiment was performed to determine a suitable operating temperature. As the Nd:YVO<sub>4</sub> crystals are cooled non-uniformly, the thermal lens is non-circular. For small amounts of thermal lensing, the beam will become slightly astigmatic. Due to the pointing noise witnessed at LHO, the flow rates in this test were set as low as possible before the power in the fundamental mode dropped significantly.

The cooling layout that was used to find a suitable amplifier head temperature to operate with is shown in part b) of Figure 2.8. The pump-diode box and amplifier head were connected in parallel, and each amplifier was on a separate cooling loop so that the amplifier head temperatures could be independently controlled. The flow rate to the first amplifier was kept high to produce a high-quality input beam for the second amplifier. The HOM content for the beam entering the second amplifier was 3.8%. The second amplifier and pump-diode box flow rate was decreased and the temperature of the pump-diode was monitored. The higher order mode content was measured with the DBB by averaging over sixty mode scans. The power of the beam was measured with a high-power power meter.

The change in beam quality and output power as a function of amplifier head temperature are shown in Figure 2.9. At 22.3°C, the HOM was  $\sim 4.5\%$  and the

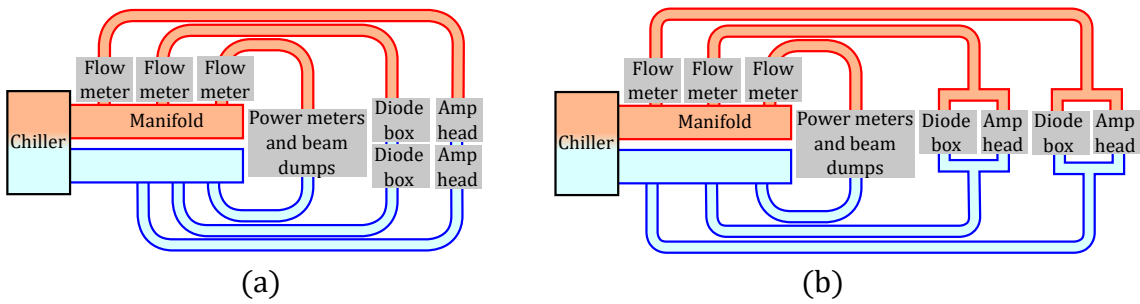


Figure 2.8: Cartoons of the water cooling layout for the prototype laser. Panel (a): The laser will be run with the amplifier heads cooled in series with each other to reduce pointing noise. Panel (b): To perform the amplifier head temperature experiment, the water cooling was arranged so that the amplifiers' head temperatures could be independently controlled.

power in the fundamental mode was  $\sim 127$  W. The change in second order mode power makes up the majority of the overall HOM power change; this is shown in Figure 2.10. This is due to the beam becoming more astigmatic as the amplifier head heats up. It was decided that the amplifier heads would be operated such that their temperature did not rise above  $\sim 27^\circ\text{C}$  to keep a high power in the fundamental mode.

For normal operation of the laser, i.e. how it will be used during observation runs, to keep the flow rate as low as possible on the table, the water cooling was set up so that the amplifiers heads were in series with each other. The pump-diode boxes were on another loop to the heads. The cooling scheme that will be used is shown in Figure 2.8. Meters which monitor the flow rate of the coolant will be placed on the return side of the system rather than the supply side. By having the flow meters on the return side, they will detect a drop in flow if there is a leak,

allowing for the water supply to be cut.

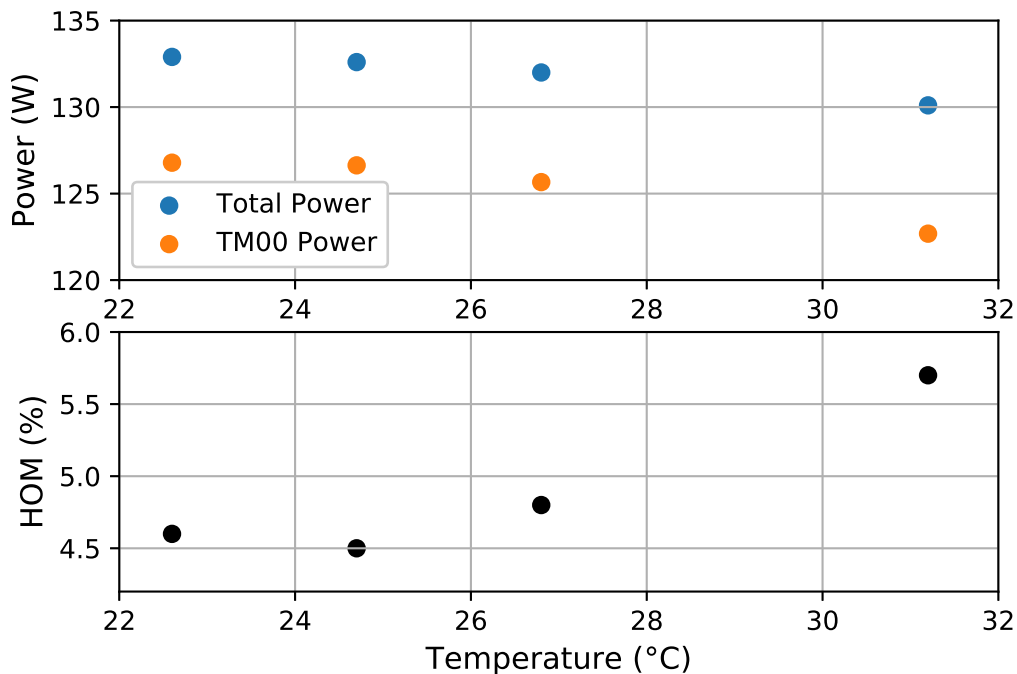


Figure 2.9: The top panel: as the second amplifier head's temperature increased, the power produced by it decreased. The bottom panel: the higher order mode content increased as the temperature of the amplifier increased. This means that the power in the fundamental mode decreased as the temperature increased due to two effects: less overall power and worse beam quality.

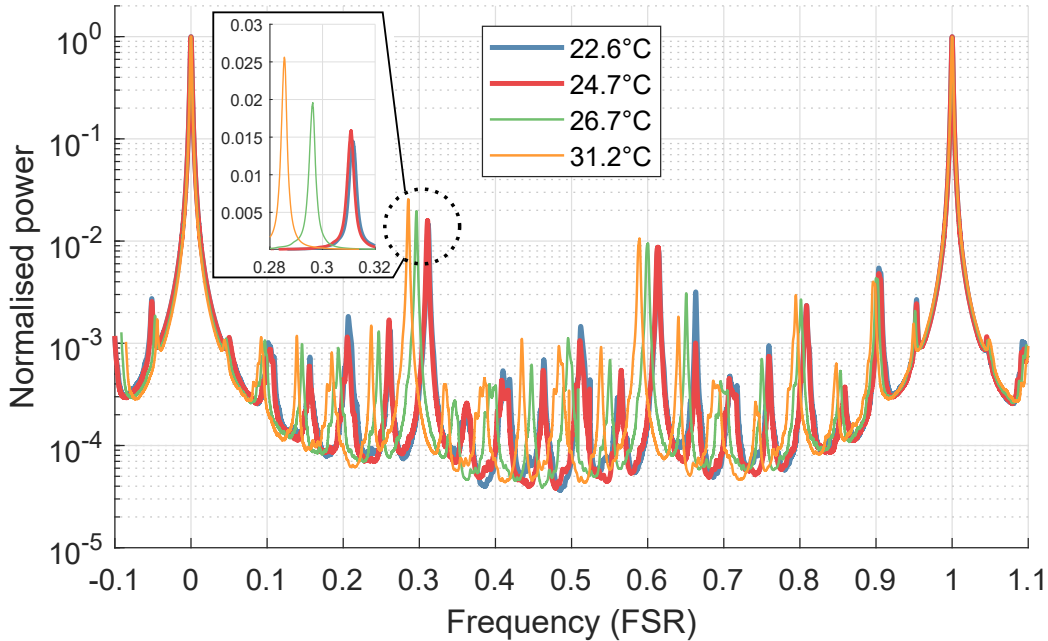


Figure 2.10: Mode scans were performed with the DBB for each amplifier head temperature. The DBB's auto-alignment system minimised the power in the first order mode. The second order mode for this cavity is located at  $\sim 0.3$  FSR; its exact location drifts due to thermal expansion of the cavity. Several percent of the beam's power is in the second and fourth order modes. As the temperature of the amplifier head changes, the second order mode content of the beam changes at the percent level. This second order mode height is shown in the inset. The second order mode changes due to the beam's astigmatism changing.

### 2.4.2 Alignment Procedure for the Amplifiers

To obtain high beam power and low HOM content, the alignment of the input beam to the amplifier needs to be optimised. The output power of the amplifier may increase at the expense of HOM content, so the beam profile and the beam power must be monitored when aligning the amplifier. Optimising the alignment to the amplifier is an iterative process; a small change in the amplifier's alignment is required with each increase in pump-diode power.

First, it was ensured that the amplifiers were switched off. This protects them against damage as well as preventing the possibility of stray light beams with several tens of watts of power being in the lab. The beam path between the NPRO and the exit of the first amplifier were inspected to make sure the beam path was clear and terminated with dumps.

Next, the NPRO was set to produce 1.3W of light. The power of the light was measured on the input side of the amplifier. The beam was roughly aligned so that the spot would hit the centre of the amplifier's input aperture using the two mirrors that immediately precede the amplifier. The power meter was placed on the exit side of the amplifier, and the input alignment was adjusted until the power emerging from the amplifier was the same as the input power. This indicates that the beam will be roughly aligned and some amplification will occur when the pump-diodes are turned on. The high-power attenuator immediately after the amplifier was set to dump all the light. The initial mode matching was based on the manufacturers

specifications, and the input light was set to s-polarisation.

The pump-diode currents were increased until the amplifier 'switched on'. This was at 2 A of current through each of the pump-diodes. Amplification begins when there is sufficient pump light to cause enough population inversion that stimulated emission occurs. At this threshold, the output power was maximised by optimising the alignment. Then, the mode matching was adjusted in tandem with correcting for misalignments caused by non-perfect centring of the beam on the lens for mode matching.

A fast low-power power meter was used to monitor the beam transmitted through the high-power attenuator. Compared to the high-power meter, the low-power meter drifted less and responded to changes in power faster. This gave quicker feedback and allowed for easier alignment.

A Wincam CCD profiler was set up to monitor the beam profile. If the amplifier is significantly misaligned and mode mismatched, the beam profile will become distorted. Large misalignment will cause the beam profile to look lopsided, and smaller misalignments will cause the beam profile to have shoulders.

Once the amplifier had been optimised for a low pump-diode current, the pump-diode current was incremented in small steps of roughly 1 A–2 A. Each time this was done, the thermal lensing increased. Due to the non-uniform way in which the heating of the Nd:YVO<sub>4</sub> crystals occurred, the input alignment and mode matching was re-optimised when the pump-diode current was increased. By going in small steps

of pump-diode current, the optimal alignment was safely achieved. The amplifier should be operated at high pump-diode currents,  $\sim 9\text{A}$ , so at low currents it was sufficient to be within 1% of optimal.

To determine when the alignment was good enough, mode scans with the DBB were performed. Due to thermal lensing, the beam will be slightly astigmatic and so optimising the mode matching from the amplifier to the DBB was difficult. When optimising the pump-diode currents, the thermal lensing changes, so the mode matching to the DBB needs to be corrected for this.

## 2.5 Intensity Stabilisation of a 100 W Beam

The free-running intensity noise of the laser exceeds the level needed for the interferometer to reach design sensitivity. Therefore, the laser must be stabilised. As actuators on the laser's intensity, a current shunt and an AOM were compared. Using the current shunt rather than the AOM enabled 10 W more power to be obtained in the beam emerging from the PMC, however the behaviour of the current shunt was highly dependent on the DC pump-diode current at 10 Hz where the laser noise requirement is most strict. If the amplifiers were required to operate under different circumstances during the course of an observation run, the current shunt may prove to be unreliable. In contrast, the AOM has proved reliable during previous observation runs. While the AOM causes the beam to have less DC power, this may not be a problem for O4 as it is unlikely that the full 125 W will be used due to point defects on the test masses [64].

### 2.5.1 The Concept and Requirements for Intensity Stabilisation Servo

The intensity noise requirement for LIGO's laser is found in [102] and reproduced in Figure 2.11. An imbalance between the powers in the arms gives rise to a laser-intensity-to-test-mass-motion coupling, so at low frequencies (0.1 Hz–10 Hz), the requirement on intensity noise is set by the motion of the test masses due to seismic vibrations; in this frequency band, the intensity noise should be low enough that the motion of the test masses is dominated by seismic noise. At 10 Hz, the laser must be stabilised to a level of  $\sim 1 \times 10^{-9}/\sqrt{\text{Hz}}$ . Above 10 Hz, the requirement on the intensity noise is relaxed as there is passive filtering of the light by the PRC. The light is passively stabilised by the PMC to reduce the intensity noise of the laser at RF.

The active intensity stabilisation of the laser is done in two stages as shown in Figure 2.12. First, the laser is stabilised by the inner-loop to a level required to lock the IMC. The light used to measure the intensity noise for the inner-loop is a low-power beam that is transmitted by the PMC. There is  $\sim 1$  mW of light in this beam, thus the laser cannot be stabilised beyond  $\sim 2 \times 10^{-8}/\sqrt{\text{Hz}}$  due to shot noise. Once the IMC is locked, a pick-off from the beam entering the interferometer is used to measure the intensity noise of the laser. This beam has enough power,  $\sim 350$  mW, to reach the noise requirement of  $1 \times 10^{-9}/\sqrt{\text{Hz}}$ . The noise of the beam entering the interferometer must be measured just after the IMC as components between the PMC and IMC can contribute to the intensity noise, and this noise is

measured with the outer-loop photodiodes.

### 2.5.2 Free-Running Noise of the Prototype Laser

To determine the open-loop gain needed for the servo to suppress the noise to the requirement, the free-running noise of the laser must be measured. The noise was measured at different points along the beam path to see the contribution that the NPRO, each amplifier and the PMC made to the total noise.

The power noise of the NPRO was measured using the DBB RIN photodiode (Figure 2.13). The NPRO had a typical noise level for this type of laser [119]. This was recorded via the *control and data system* (CDS) (see Appendix C), so the measurements near 10 kHz are affected by the anti-aliasing filter. The noise between 100 Hz and 1 kHz had features associated with the motion of the table and mirror mounts.

The power noise of the first and second amplifiers was measured using the DBB RIN photodiode (Figure 2.13). The noise was measured with a spectrum analyser rather than CDS so that measurements up to 100 kHz could be made. As the amplifiers were pumped with low noise diodes and were operating in their saturated regimes, the RIN is expected to decrease after each amplifier: when an amplifier is saturated, the amplifier will not behave linearly and instead will add a fixed input power regardless of its seed power. As expected, at frequencies above 10 kHz, the RIN after the second amplifier was less than the RIN after the first amplifier. There

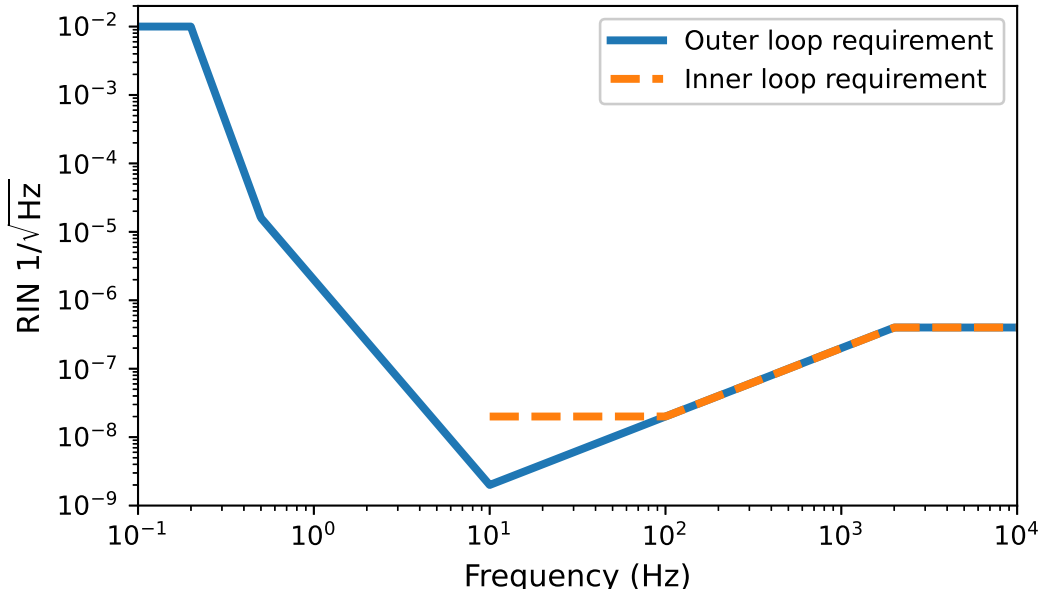


Figure 2.11: A reproduction of the intensity noise requirement from [102]. The outer-loop requirement is shown in blue and the inner-loop is shown by the dashed orange line. To lock the IMC, the inner-loop requirement must be met. Below 10 Hz, the motion of the test masses should be limited by seismic motion. An imbalance in the powers in the arm creates a coupling between laser intensity noise and differential radiation pressure noise, thus the laser's intensity needs to be stabilised such that motion induced by the laser's intensity noise is below the motion that is seismically driven. The requirement is most stringent at 10 Hz. The requirement relaxes above 10 Hz due to the PRC cavity pole. The inner-loop requirement is less extreme than the outer-loop as it is only used to stabilise the laser in the initial locking sequence.

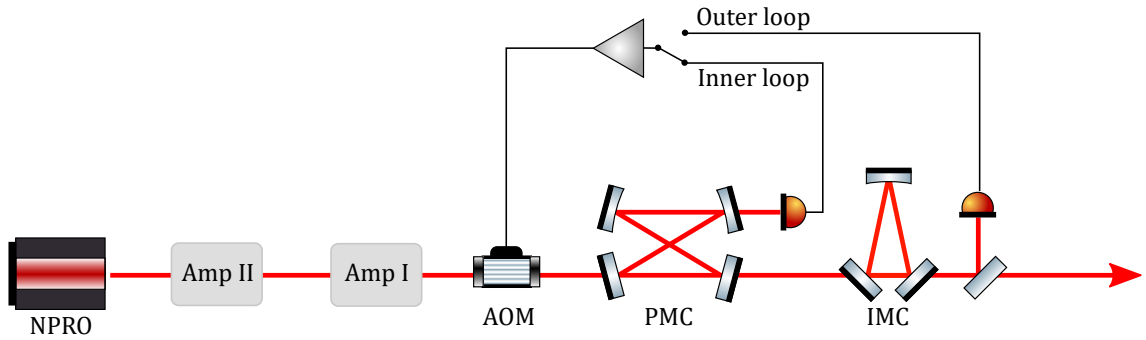


Figure 2.12: The intensity stabilisation concept involves two loops. The inner-loop is responsible for stabilising the laser so that the IMC can lock. The outer-loop is used to stabilise the laser for observation mode. The two loops sense the laser intensity noise at different points. The inner-loop uses a low-power beam,  $\sim 1$  mW, transmitted by the PMC. The outer-loop uses a higher power,  $\sim 350$  mW, pick-off from the main beam. An AOM is used to actuate on the laser's power.

was a peak at 20 Hz; this can be attributed to the air conditioning. The noise was covered in a forest of lines with 4 Hz spacing, starting from 4 Hz and continuing up to high frequencies. These lines were found to originate in the Beckhoff [126] slow-control computer which is used as an interface for the amplifiers. The laser control box needs better electrical isolation between its digital and analogue sections to remove the 4 Hz lines.

The noise of the beam emerging from the PMC was measured (Figure 2.13). The PMC introduces a length to intensity noise coupling via the offset in the PDH loop. The offset needed to remove this coupling drifted due to changing levels of RF pick-up in the servo electronics for the PMC. The coupling from length noise of the PMC to intensity noise was decreased as much as possible.

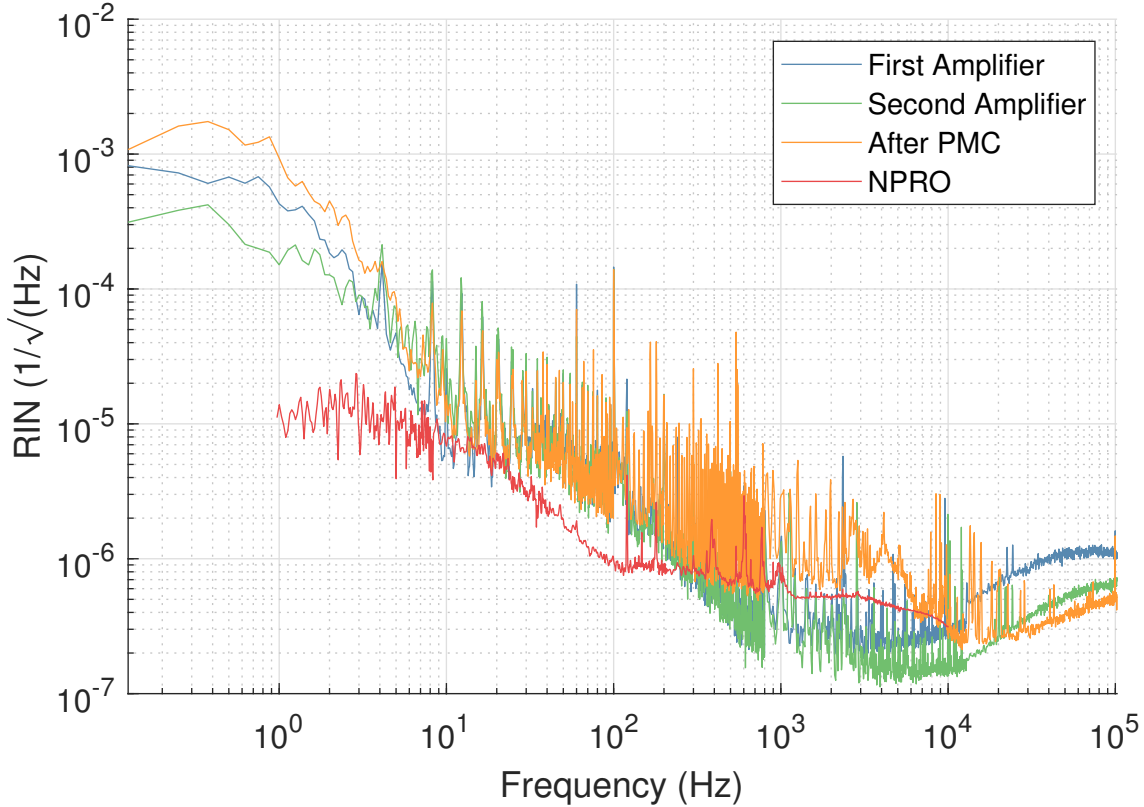


Figure 2.13: The free running noise of the NPRO and each amplifier is shown. The noise after the PMC was also measured. There is a forest of 4 Hz lines due to the Beckhoff control computer in the amplifier and PMC noise curves. Due to the non linear nature of the saturated amplifiers, at high frequencies the output beam intensity noise decreases relative to the input beam. The PMC couples length noise to intensity noise between 100 Hz and 10 kHz. This excess can be tuned away in the PDH servo.

### 2.5.3 Power Control Actuators

The actuator that was used to provide intensity stabilisation was an AOM. The use of a current shunt integrated into one of the pump-diodes in the second amplifier was also investigated. The current shunt had the potential to reduce the number of transmissive optics in the beam path and increase the total power. Despite this, the current shunt may be an unsuitable choice for stabilising LIGO's laser. The current shunt transfer function depends on the DC current; at 10 Hz it changed by  $\sim 10$  dB when the DC current was changed by  $\sim 1$  A (see Figure 2.17), and so this may make the intensity stabilisation servo unreliable if the DC pump-diode currents need to be changed over the course of an observation run.

#### 2.5.3.1 Acousto-Optic Modulator

An AOM uses acoustic waves to Bragg scatter light into higher order beams. The amount of light that is Bragg scattered depends on the intensity of the acoustic wave. The AOM used was a Crystal Technology 3080-199. An RF driver, Gooch and Housego r21080-2am-rfx, was used to control the intensity of the acoustic wave. This driver produced an 80 MHz signal whose power could be modulated. To linearise the AOM's response, an analogue multiplier *integrated circuit* (IC) (AD734) was included in the servo. By modulating the power of this signal, the power in the zeroth order beam can be controlled. The diffraction efficiency of this AOM was found to be 74%. This means that the AOM can be used for coarse and fine power adjustment. To modulate the intensity of a laser beam, some of it must always be

scattered into the first order beam. To operate linearly, the DC level of the light that is dumped was  $\sim 10\text{W}$ .

The transfer function, in relative intensity units, between the AOM control electronics to the intensity of the zeroth order beam as measured by the ISS photodiode is shown in Figure 2.15. The schematic for this measurement is shown in Figure 2.14. This transfer function is flat from 1 Hz to 100 kHz, and, as the servo's unity gain point will be between 10–100 kHz, it is worth noting that there is a phase lag of  $60^\circ$  at 100 kHz.

### 2.5.3.2 Current Shunt

Modulating the current through a laser diode will modulate the intensity of the laser. This is a standard way of implementing power control at the 10 W level [129–133]. Using a current shunt as an intensity actuator has been demonstrated in a similar system at the 100 W level [113]. The current shunt technique allows for one to have fewer transmissive high-power optics in the beam path, which potentially can reduce noise and thermal distortions in the beam. The current shunt acts linearly with a smaller DC offset compared to the AOM, therefore higher beam power can be achieved.

The amplifier's pump-diode current determines the power produced by the amplifier. By modulating the current through one of the pump-diodes, the power of the laser can be stabilised. The current shunt consists of a power MOSFET and a resistor. It diverts current from the pump-diode by pulling it through the resistor

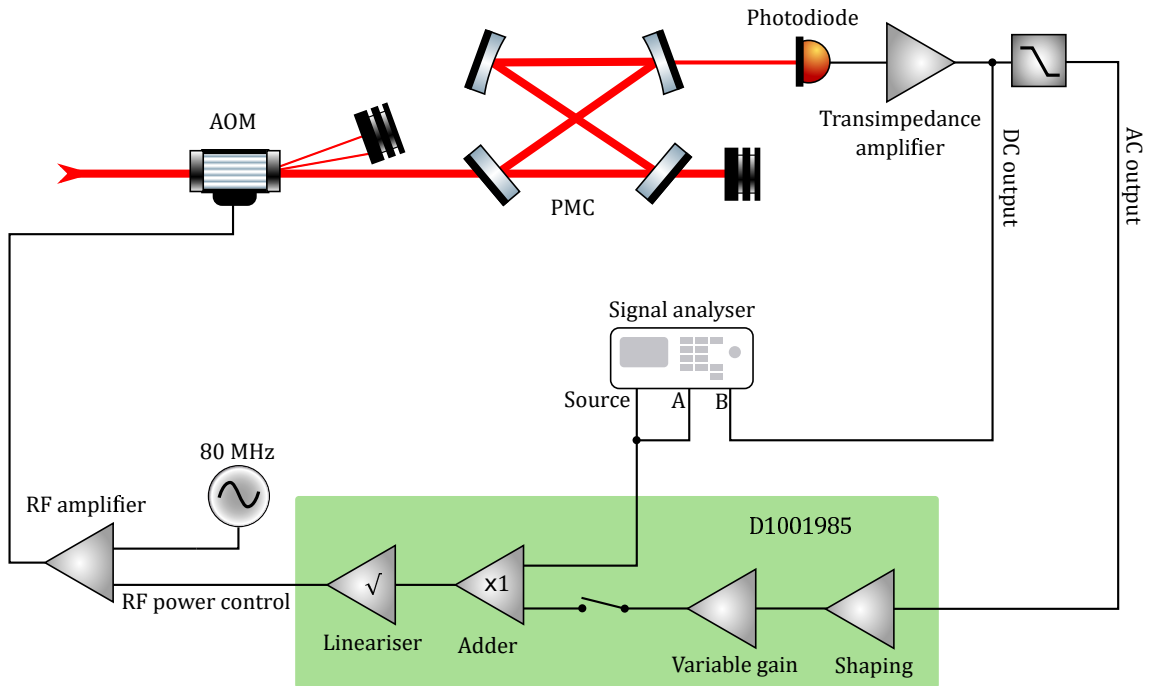


Figure 2.14: A sketch of how the AOM transfer function was measured. The components of the intensity stabilisation servo have also been shown. The PMC was locked and a signal analyser was used to perform a swept sine measurement. An IC (AD734) that performs a square root operation to an input signal was used to linearise the AOM's effect on beam power to an input signal. The transfer function was measured between the input to the lineariser and the photodiode used for the intensity stabilisation. The servo electronics are found in [127] and [128].

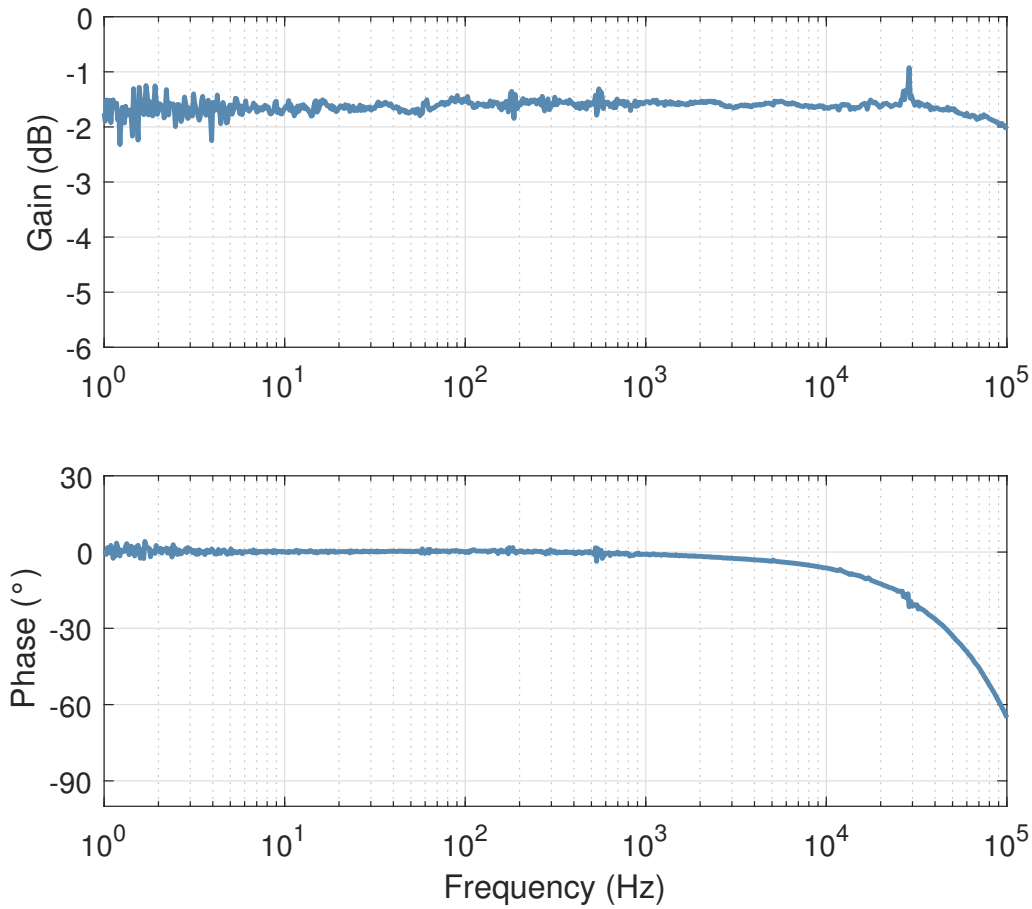


Figure 2.15: Using the layout shown in Figure 2.14, the transfer function between the input to the linearisation stage before the AOM to the light power change on the ISS photodiode was measured. The response was normalised by dividing by the DC power on the photodiode. The transfer function is flat over the region where the open-loop gain needs to be greater than one ( $\sim 10$  kHz). There is some phase lag between 10–100 kHz; this is where the unity gain point of the servo will be and so this needs to be accounted for when determining if the loop will be stable. The corner frequency of the PMC is around  $\sim 1$  MHz, so this did not affect the measurement.

instead. The current that is pulled through the resistor depends on the voltage at the gate of the MOSFET (see [134, Chapters 2 and 3]).

The transfer function between the current shunt input and the ISS photodiode in transmission of the PMC was measured for a variety of different DC pump-diode currents. This is shown, in relative intensity units, in Figure 2.17. A schematic of the measurement is shown in Figure 2.16. The transfer function was found to have significant amounts of variation in gain and phase between 1 Hz–100 kHz. Above 10 kHz the transfer function did not vary much with DC pump-diode current. This is good, as the unity gain point of the intensity stabilisation servo will be between 10 kHz–100 kHz. The AOM is a much stronger actuator than the current shunt; this can be compensated for by changing the servo electronics. It was found that the behaviour of the actuator at 10 Hz, where the servo requirement is hardest to meet, strongly depended on the DC pump-diode current.

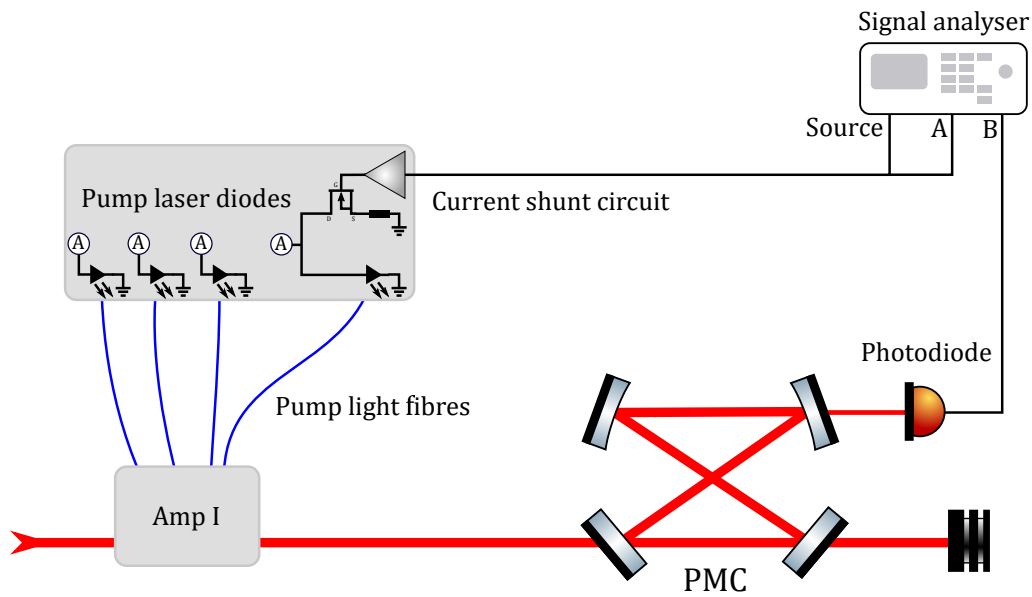


Figure 2.16: A sketch of how the current shunt transfer function was measured. The PMC was locked and a signal analyser was used to perform a swept sine measurement. The current of one of the pump-diodes in the second amplifier was modulated by applying a signal to a current shunt. The transfer function was measured between the input to the current shunt electronics and the photodiode used for the intensity stabilisation.

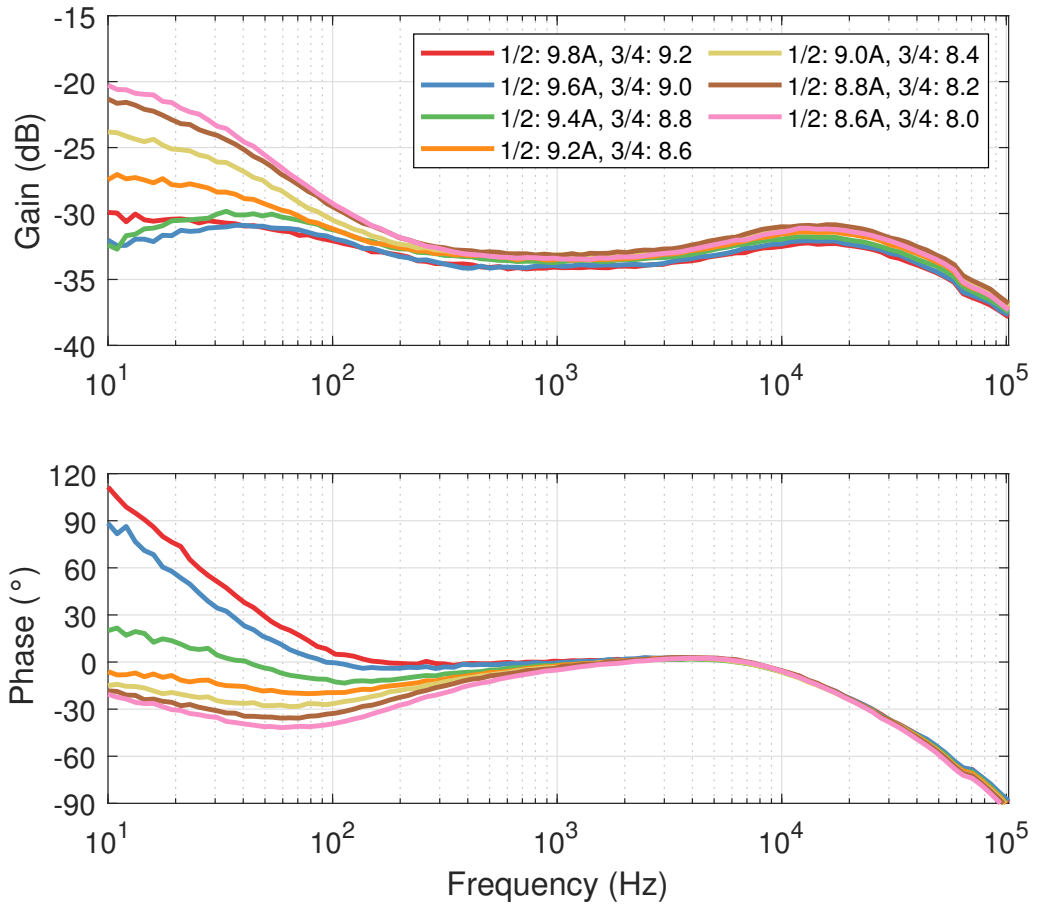


Figure 2.17: Using the layout shown in Figure 2.16, the transfer function between the current shunt input electronics and the intensity stabilisation photodiode was measured. The transfer function was normalised by dividing by the DC power on the photodiode. At 10 Hz, where the noise requirement is hardest to meet, the gain of the transfer function changes significantly depending on the pump-diode's DC current. The phase at this frequency does not matter as it is not near the unity gain point of the servo.

### 2.5.3.3 The Reason for Choosing the Acousto-optic Modulator Instead of the Current Shunt

While the current shunt offers some advantages over the AOM, it cannot reduce the power at the many tens of watts level. This is a functionality that LIGO would likely need as the detectors have never operated at full power, at present the LIGO detectors operate with between 25 W–50 W of light, due to point absorbers on the test masses.

The pump-diodes' DC currents would have to be lowered significantly to reduce the power by many tens of watts<sup>1</sup>. These amplifiers work best in their saturated regime and the RIN may be increased if the pump-diodes' currents are decreased significantly. Changing the pump-diode's DC current also changes its transfer function. Thus, setting the PSL to different DC light levels with just the amplifiers' pump diode currents would be impractical as they affect the noise of the laser and the open-loop transfer function of the servo. Additionally, there may be other circumstances in which the pump-diode currents need to be altered; the pump-diodes need to be frequently adjusted towards the end of their life-time, and the behaviour of the current shunt is not known as the pump-diode ages.

Unlike the current shunt, the AOM's response depends on the DC light level in a trivial way. While the AOM causes a decrease in total power, this downside is

---

<sup>1</sup>Alternatively, high-power attenuation optics would be required. However, one of the reasons for using a current shunt is that it would allow you to have fewer transmissive optics in the beam path, so needing to use several optics (more than just an AOM) to reduce the beam's power is not an attractive solution.

outweighed by the consistency and reliability under different operating conditions of the AOM compared to the current shunt. When the LIGO detectors are able to operate at full power, the current shunt actuator would be worth revisiting.

#### 2.5.4 Open-Loop Transfer Function of the Intensity Stabilisation Servo

The free running noise of the laser transmitted by the PMC is shown in Figure 2.13 and the requirement is shown in Figure 2.11. Based on the noise and the requirement, the unity gain point of the servo must be above 10 kHz. At 10 Hz, where the requirement is hardest to meet, the noise requirement is  $2 \times 10^{-8} \frac{1}{\sqrt{\text{Hz}}}$  and the noise is  $1 \times 10^{-5} \frac{1}{\sqrt{\text{Hz}}} - 1 \times 10^{-4} \frac{1}{\sqrt{\text{Hz}}}$ , so there needs to be at least 60 dB of open-loop gain at this frequency. If the noise of the laser was not dominated by the 4 Hz lines, the amplitude stabilisation could be achieved with a single pole low pass filter. However, this servo uses additional shaping to ensure that there is enough gain to suppress these peaks.

A sketch of the servo is shown in Figure 2.18. The servo has two circuits that add shaping; these are found built into the photodiode circuit [128] and within the rack electronics [127]. The servo model is described in detail in Section 2.5.4.1. The inner-loop ISS features two photodiodes, one for in-loop measurements and one for out-of-loop measurements. The rack electronics allow for the servo to be controlled via CDS. This gives the user the ability to turn the servo on/off, to vary the overall gain and activate extra integrators.

The transfer function of all the components in the loop apart from a unity gain summing stage, i.e. the open-loop transfer function, was measured by injecting a swept sine into the summing stage. A sketch of how this measurement was made is shown in Figure 2.18. The relationship between the signal immediately before and after the summing stage,  $a$  and  $b$ , is  $a = bH$ ; thus the ratio of these signals gives  $H$ . This method allows the loop to be closed while the measurement is made; this is useful if the laser needs to remain amplitude stabilised while the measurement is made.

For this measurement, the variable gain stage was set to 20 dB in CDS. Once the intensity stabilisation was activated, the integrators were engaged to increase the open-loop gain at low frequencies. The light transmitted through the PMC was 100 W. The open-loop transfer function was shown in Figure 2.19. The unity gain point is at 48 kHz with  $\sim 70^\circ$  of phase margin. This servo satisfies the requirements.

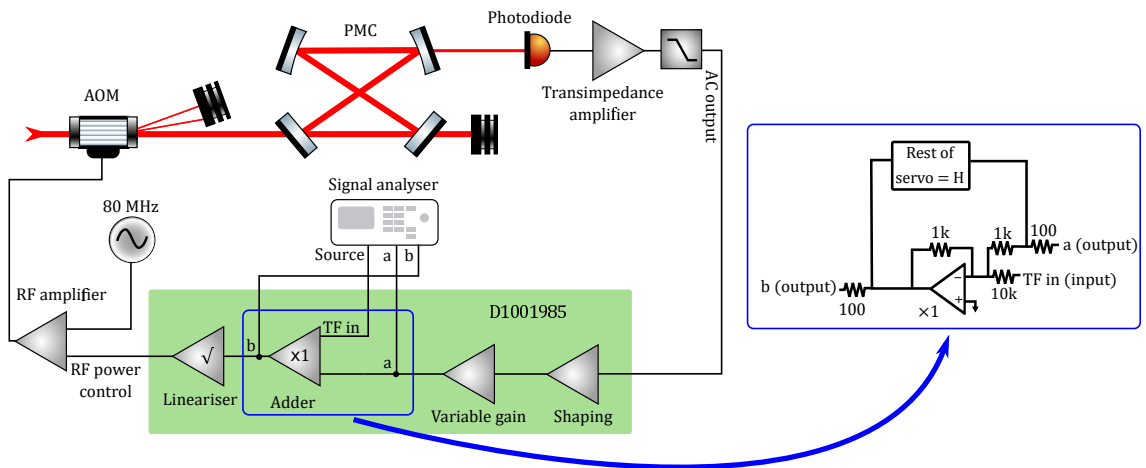


Figure 2.18: Sketch of the amplitude stabilisation servo. The components highlighted in blue have been shown in more detail. By injecting a signal into ‘TF in’ and measuring the ratio  $b/a$ , the transfer function of all the parts of the servo except for the unity summing stage,  $H$ , was measured. The measurement of the open loop transfer function with the variable gain stage set to 20 dB is shown in Figure 2.19. A block diagram of  $H$  is shown in Figure 2.20.

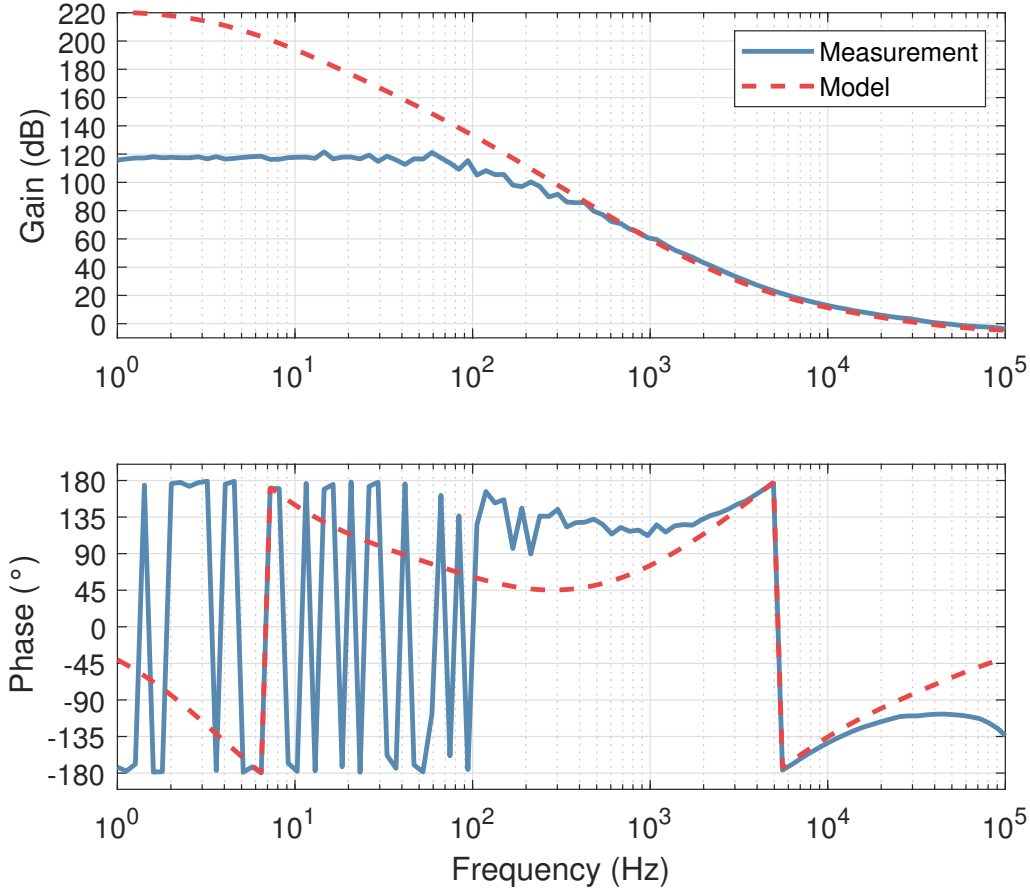


Figure 2.19: The open-loop transfer function was measured using the layout shown in Figure 2.18. The unity gain point is at 48 kHz with  $70^\circ$  of phase margin. The shaping of the servo is  $1/f$  at the unity gain point, but to achieve higher gain at low frequency, the servo has a  $1/f^3$  slope between 10 Hz—5 kHz. The measurement saturated below 100 Hz. The model and measurement do not agree well below a few kHz due to the measurement saturating.

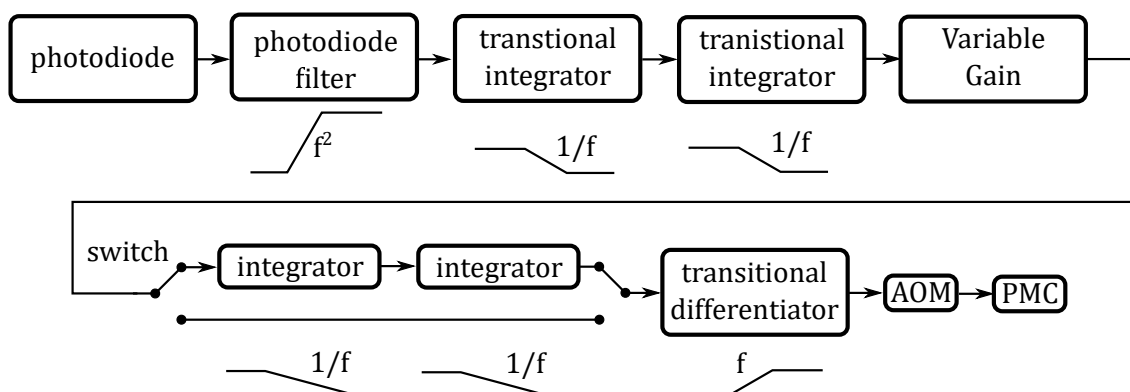


Figure 2.20: A block diagram of the components in the intensity stabilisation servo. The transfer function of each block is described in Section 2.5.4.1 and Table 2.1. Additional integrators can be activated with a digital switch. The overall gain of the servo depends on a variable gain IC and the amount of light on the photodiode. The shaping of each block is indicated below it.

#### 2.5.4.1 Model of the Open-Loop Transfer Function

To understand the behaviour of the servo at frequencies where the measurement of the open-loop gain saturated, a model is required. A block diagram of the servo's components is shown in Figure 2.20. The overall gain of the servo is determined by how much light there is on the in-loop photodiode and the setting of the variable gain. The following description puts all the gain that is distributed over all the components of the servo into one block.

The photodiode transimpedance amplifier has a low-pass corner frequency of 5.9 Hz. The photodiode signal passes through a filter which boosts its response to AC signals; this filter consists of two transitional differentiators with corner frequencies

at 0.05 Hz and 3 Hz. The rack electronics feature two transitional integrators and one transitional differentiator. The first transitional integrator has corner frequencies at 1.06 kHz and 4.83 kHz. The second transitional integrator has corner frequencies at 1.06 kHz and 4.42 kHz. The transitional differentiator has corner frequencies at 59 kHz and 2.9 MHz. Activating the extra integrator stages removes the zeros in the transitional integrators at 1.06 kHz. See Figure 2.20 for a sketch of the shape of each of these transfer functions. The AOM introduces phase lag via a delay between the input and the output of 2.5  $\mu$ s. This model is summed up in Table 2.1 and shown in Figure 2.19.

### **2.5.5 Measurement of the Intensity Stabilisation of a 100 W Beam to the Inner-Loop Requirement**

The PMC was set to transmit 100 W of intensity stabilised light. The stabilised laser noise is shown in Figure 2.21. A noise budget was created using the signal measured on the in-loop photodiode and the shot noise level of the light used to stabilise the laser. This agrees with the out of loop noise measurement above 10 Hz. Below 10 Hz, there is excess noise in the out of loop measurement compared to the noise budget. Possible sources of this noise could be scattered light or dust falling through the ISS beam. Near the unity gain point, due to the open-loop transfer function phase and gain, there is a small increase in the stabilised noise compared to the free running noise, however this is out of the frequency band of the requirement, so this is not an issue. This setup will be able to deliver at least 100 W of intensity stabilised light to the interferometer.

Component	Transfer function
Photodiode low pass	$\frac{36.945}{s+36.95}$
Photodiode filtered output	$\frac{3600(s+0.3142)^2}{(s+18.85)^2}$
Rack transitional integrator I	$\frac{0.21946(s+3.035e04)}{(s+6660)}$
Rack transitional integrator II	$\frac{0.023982(s+2.777e04)}{(s+666)}$
Rack transitional differentiator	$\frac{49.153(s+3.707e05)}{(s+1.822e07)}$
Rack additional integrators	$\frac{1 \times 10^{-8}(s+6660)^2}{(s+0.666)^2}$
AOM phase lag	$\exp(-2.5e - 06s)$
Overall gain	2.6775e10

Table 2.1: Model of the intensity stabilisation servo expressed in terms of the complex angular frequency,  $s = \omega + i\sigma$ . Base ten exponentiation is represent with ‘e’. Note that in reality the gain is distributed amongst each block; for clarity, in this model all the components have unity gain at DC and the overall DC gain factor is given. The additional integrators have been expressed as a separate block to the transitional integrators with a pole that cancels a zero in the transitional integrators; in the transfer function of this additional integrator, the zero was chosen to be below any frequency of interest and does not exist in the servo. It was included here to make modelling the servo more clear.

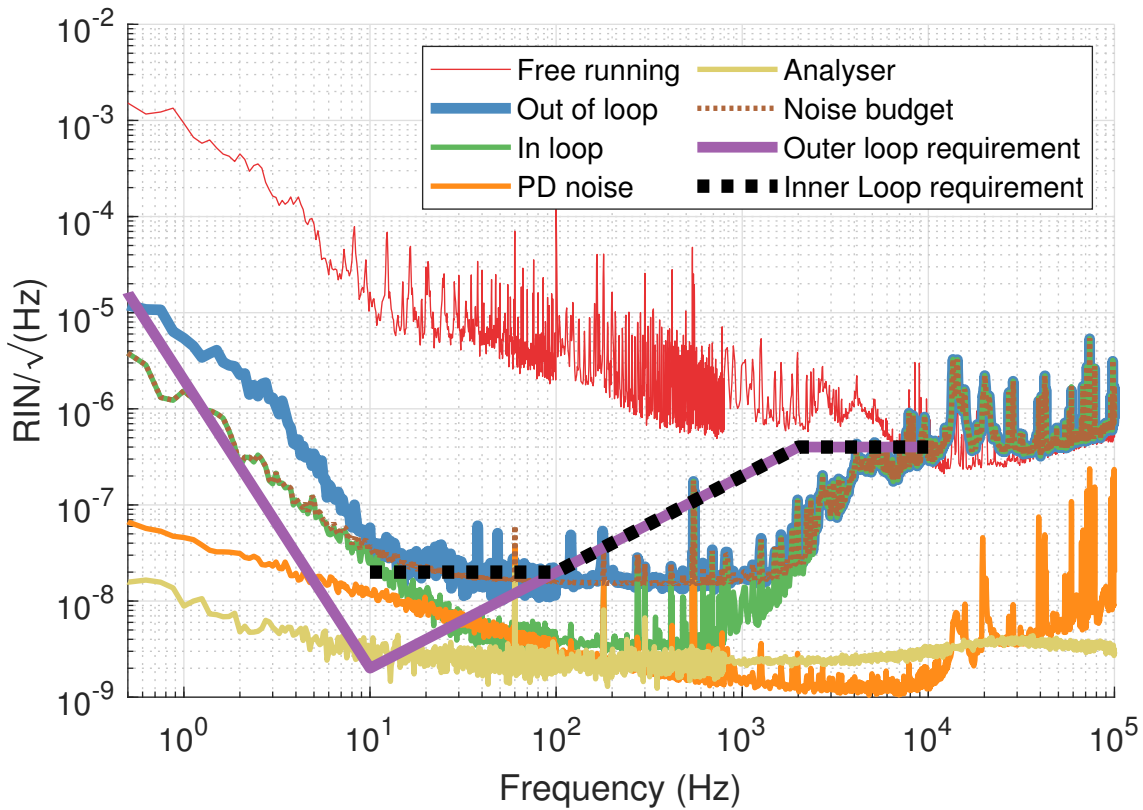


Figure 2.21: The free-running noise of the laser is shown in red. The noise of the light transmitted by the PMC is shown in blue; this meets the requirement that is shown by the dashed black line. The noise level is determined by the in-loop noise, shown in green, the shot noise and other technical noise sources; the sum of these is shown by the dotted brown line. Between 10 Hz–1 kHz, the noise of the laser is limited by shot noise. There is a discrepancy between the noise budget and the measured noise. This is likely due to dust falling through the beam or scattered light. Near the unity gain point of the servo, the noise is enhanced by the servo due to gain peaking.

## 2.6 Pointing Noise of the Beam Entering the Pre Mode Cleaner

The pointing noise witnessed at LHO is one of the reasons why single-pass amplifiers were chosen as the replacement for the HPO. Pointing noise on the beam entering the PMC manifests as intensity noise in the beam exiting the PMC since a change in beam direction can be modelled as the introduction of higher order modes. These new amplifiers are cooled in such a way that the pointing noise on the PSL beam is reduced. The pointing noise requirement is based on the transfer function of the HG10 mode between the input of the interferometer and the dark port [135].

The pointing noise was measured using the DBB and is shown in Figure 2.22. To measure pointing noise, the laser was locked to the DBB cavity. The reflected light from the cavity was made up of the fundamental mode of the cavity (some of the cavity mode leaks out) and the first order modes of the incident light associated with misalignment. The beat between these two fields can be used to determine the pointing noise of the beam; this is known as differential wavefront sensing [136].

The pointing noise can be expressed as a normalised, complex quantity  $p = \delta x/w_0 + j\delta\alpha/\Theta$ , where  $\Theta$  is half the divergence angle of the beam,  $\alpha$  is the angle of the beam,  $x$  is the beam's position and  $w_0$  is the beam's waist. The beam exiting the DBB's cavity is sensed by two quadrant photodiodes separated by  $90^\circ$  of Gouy phase so that both quadratures of  $p$  can be measured in the tangential and sagittal planes, yielding four measurements in total. The length of the cavity is modulated at 1 MHz

with a PZT, and the quadrant photodiodes are demodulated at this frequency to obtain a measurement of pointing.

While the pointing noise measurement was affected by scattering below  $\sim 200$  Hz, the pointing was measured to exceed the requirement below  $\sim 1$  kHz. To reduce the pointing noise caused by turbulence in the cooling system, the water lines should be made to have gradual bends in them. As the LIGO PSL table is in a quieter environment than this setup, an improvement will be seen when this is constructed on the PSL table.

## 2.7 Frequency Noise of the Prototype Laser

The LIGO detectors employ a multi-stage frequency stabilisation system. Ultimately, the arm cavity is used as a frequency reference since  $\delta f/f = \delta l/l$  and the LIGO arm cavities are 4 km and their length is stabilised by quadrupole suspensions. The initial stabilisation of the laser uses an ultra low expansion fused silica reference cavity located on the laser table [137]. The free-running frequency noise must be measured to design the frequency stabilisation servo. The PMC length noise,  $\delta l_{\text{PMC}}$ , is converted to a frequency noise via  $\delta f_{\text{PMC}} = f_{\text{EM}} \frac{\delta l_{\text{PMC}}}{l_{\text{PMC}}}$ , where  $f_{\text{EM}}$  is the laser's frequency and  $l_{\text{PMC}}$  is the length of the PMC.

With the stabilisation loop running, the frequency noise of the beam exiting the PMC will be determined by the frequency noise of the PMC and the frequency noise of the NPRO. The signals used to control the PMC can be converted into a

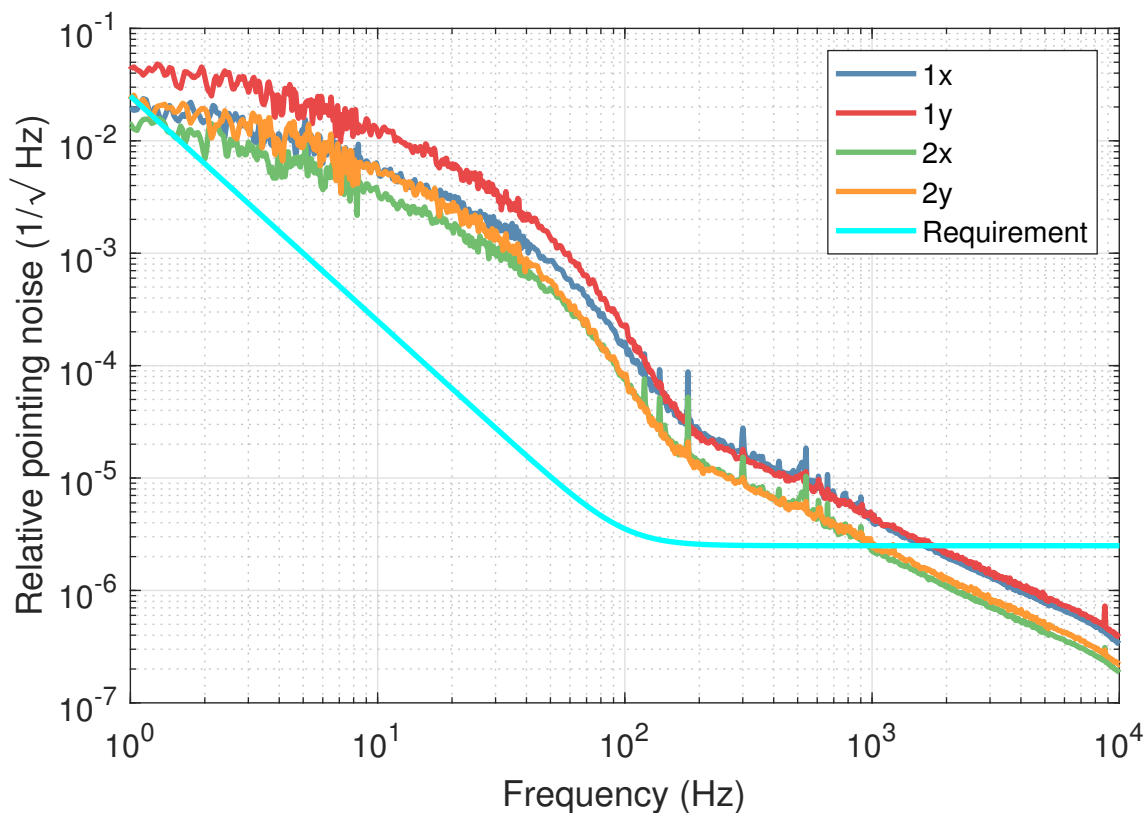


Figure 2.22: The four orthogonal relative pointing degrees of freedom, denoted by 1x, 2x, 1y and 2y, of the beam going into the PMC were measured with the DBB. The exact meaning of, say, 1x and 2x does not matter, but they must be orthogonal components of the laser’s alignment to the optical axis. For example, one orthogonal pair is the lateral shift and angular tilt of the beam with respect to the optical axis. The requirement [135] is shown in light blue. The pointing noise is above the requirement, however the lab this prototype was made in has a higher amount of environmental noise than the PSL. Measurements below 200 Hz were affected by scattering.

measurement of the system's frequency noise. The control signal which is sent to the PZT in the PMC can give the frequency noise of the system where there is sufficient open-loop gain since at these frequencies, the closed loop gain is unity. Around the unity gain point of the servo, the response of the servo needs to be factored in. Alternatively, the error signal at the mixer and the open-loop gain can be used to measure the frequency noise of the system.

The NPRO is locked to the PMC by controlling the length of the PMC. The length of the PMC is controlled with two actuators. A PZT is attached to one of the mirrors to provide fast control, and a heater which determines the thermal expansion of the PMC provides slow control. The PDH technique is used to find the difference between the cavity's frequency and the frequency of the laser. RF frequency side-bands are applied to the laser via an EOM, and the light that is reflected from the PMC is demodulated at the same frequency as the RF sidebands. When the cavity is near resonance, the demodulated signal is proportional to the difference between the laser frequency and the frequency corresponding to the cavity length. A sketch of the PMC length control servo is shown in Figure 2.23.

To see how the error signal used to lock the cavity and the open-loop transfer function gives the frequency noise, consider Figure 2.24. The difference between the laser frequency,  $a$ , and the cavity frequency,  $b$ , is obtained via the PDH technique. The PZT signal,  $c$ , is then obtained via the transfer function of the electronics and the transfer function of the optics, i.e. the frequency to voltage transfer function corresponding to the slope of the demodulated PDH signal. Combining these transfer functions gives  $G$ . First, the error signal is defined as  $c = a - b$ . Next, the control

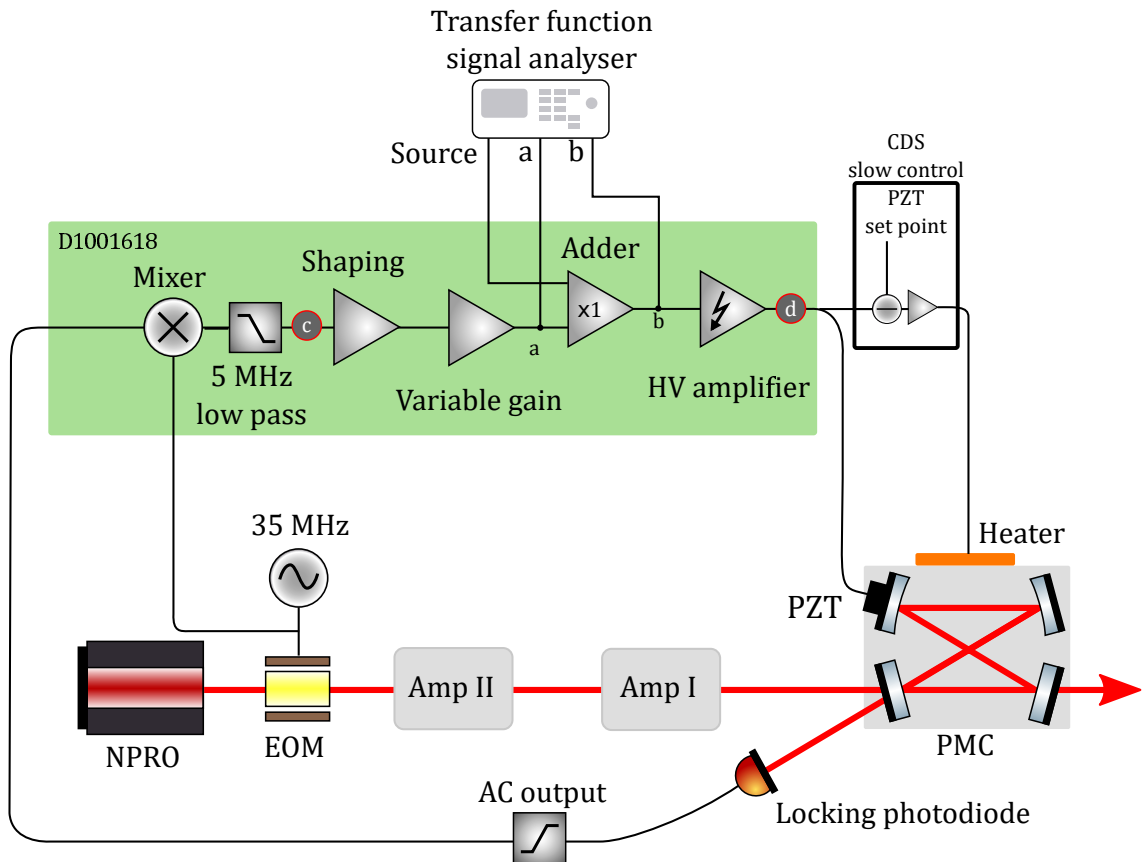


Figure 2.23: A sketch of the servo for locking the PMC. An EOM creates 35 MHz sidebands which are used to produce a PDH locking signal. A PZT controls the length of the cavity at high frequencies. A heater and a digital loop is used to provide slow control that corrects for frequency drifts associated with change in the NPRO temperature and the room temperature. This is required as otherwise the PZT would run out of range. The open-loop transfer function was measured using signals at a and b. The frequency noise was measured using the error point and control signals marked by *c* and *d*, with this notation corresponding with the notation in Figure 2.24 and Equation (2.1).

signal,  $d$ , is expressed in terms of the error signal,  $cG = d$ . Expressing the signal  $b$  in terms of  $d$  allows for signal  $a$  to be written in terms of the error signal  $c$ ,

$$a = c(1 + GH). \quad (2.1)$$

Equation (2.1) shows that to measure the frequency noise of the system,  $a$ , the error signal should be, approximately, multiplied by the open-loop transfer function,  $GH$ .

### 2.7.1 Calibrating the Mixer Signal and the PZT, and Modelling the Open Loop Transfer Function for Locking the Pre Mode Cleaner

The pole of the PMC cavity is at  $\sim 1$  MHz, so it does not affect this measurement. Thus, the transfer function representing the signal due to a difference in laser and PMC frequency (the PDH signal) to a voltage is a flat gain factor. A measurement of the difference in frequency between the PMC and NPRO and the voltage at the mixer can be obtained by measuring the slope of the PDH signal as the frequency of the cavity passes through a resonance. By driving the PZT with a ramp and simultaneously measuring the signal before and after it is demodulated, the transfer function of the optics can be obtained. Figure 2.25 shows this measurement. The time axis can be converted to frequency as the FWHM of the reflected light is determined by the optical properties of the PMC. The design value of the FWHM for the PMC is 1.19 MHz. The slope of the demodulated signal as the cavity passes

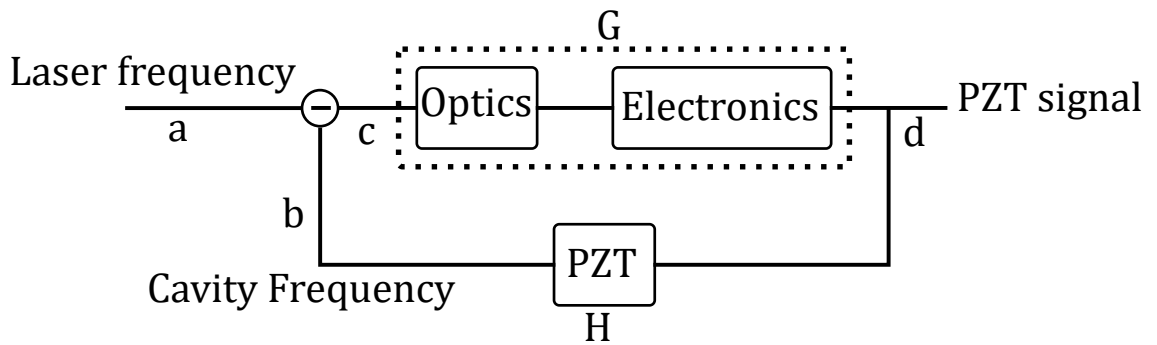


Figure 2.24: The servo can be considered as being made of three parts: the optics, the shaping electronics and the PZT. The transfer function of the optics represents how a difference in frequency between the laser and the cavity transforms into a signal after the demodulator. When at resonance and below the cavity pole, this is a flat transfer function that is proportional to the difference in frequency. Since this cavity pole is in the 1 MHz region and this measurement will only go to the kHz region, the cavity pole can be ignored. The transfer function of the electronics includes everything after the demodulator up to and including the final high-power op amp. The PZT transfer function converts a voltage to a cavity frequency. The PZT has capacitance, so a low pass filter is formed by this and the series resistor at the output of the electronics.

through the resonance can be used to give the conversion between the difference in frequency of the cavity and laser to voltage after the demodulation electronics. This factor is 0.1364 V/MHz.

A ramp was applied to the PZT and the spacing between two resonances was measured to convert the PZT voltage to the cavity frequency at low frequencies. The difference in ramp voltage between the two resonances corresponds to the FSR of the cavity. This is shown in Figure 2.26. The nominal FSR for the PMC is 148.529 MHz, so the PZT to frequency transfer function is 42.2870 MHz/V. The PZT has capacitance, so it forms a low pass filter with the series resistor at the output of the rack electronics; this must be included when modelling the servo. The corner frequency of the PZT was estimated to be at 1700 Hz. The corner frequency of the PZT drive is above the unity gain frequency of the PMC locking servo.

The measurement and model of the open-loop transfer function, i.e. the transfer functions of the optics, electronics and the PZT multiplied together, is shown in Figure 2.27. The model is within 2 dB of the measurement. A sketch of how the open-loop transfer function was measured is shown in Figure 2.23. The unity gain point of the servo was measured to be at approximately 800 Hz. The difference between the model and the measurement may be due to the use of nominal values for the properties of the PMC.

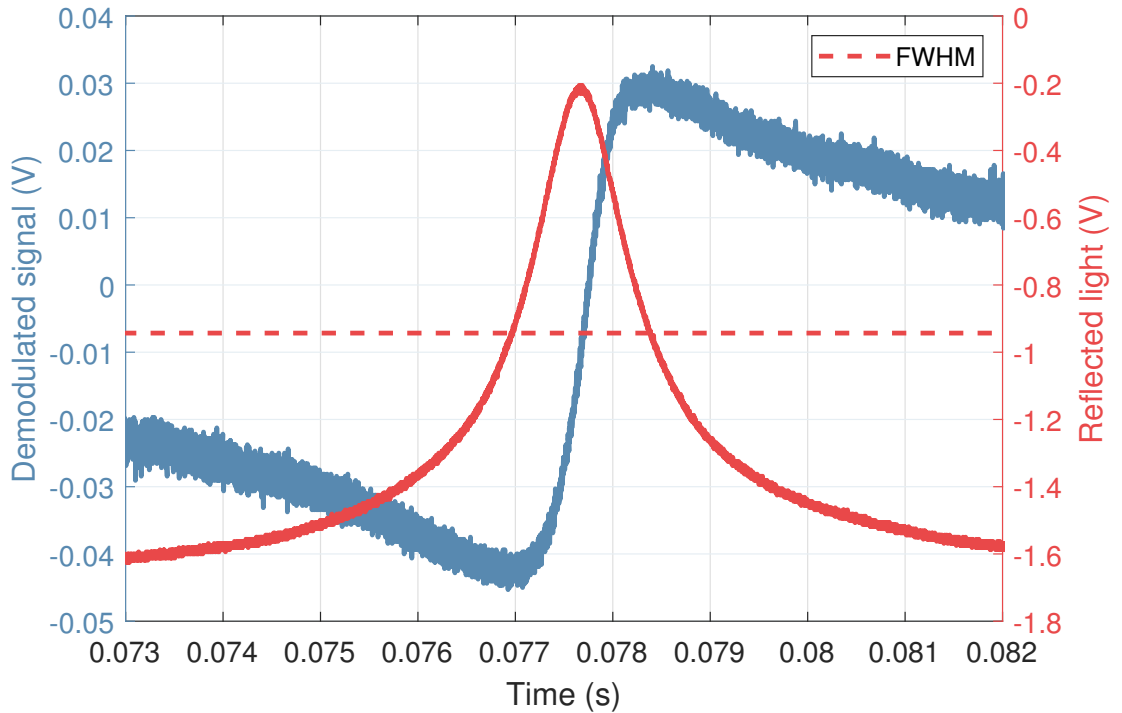


Figure 2.25: A ramp was applied to the PZT and the photodiode signal was measured before and after demodulation. The demodulated photodiode signal is shown in blue. The photodiode signal is shown in red. Around the peak of the photodiode signal, the slope of the demodulated signal gives the gain of the ‘optics’ transfer function. This can be expressed in units of V/MHz by converting the time axis to a frequency axis using the FWHM of the reflected signal as a reference frequency. The level of the FWHM is indicated by the dashed red line.

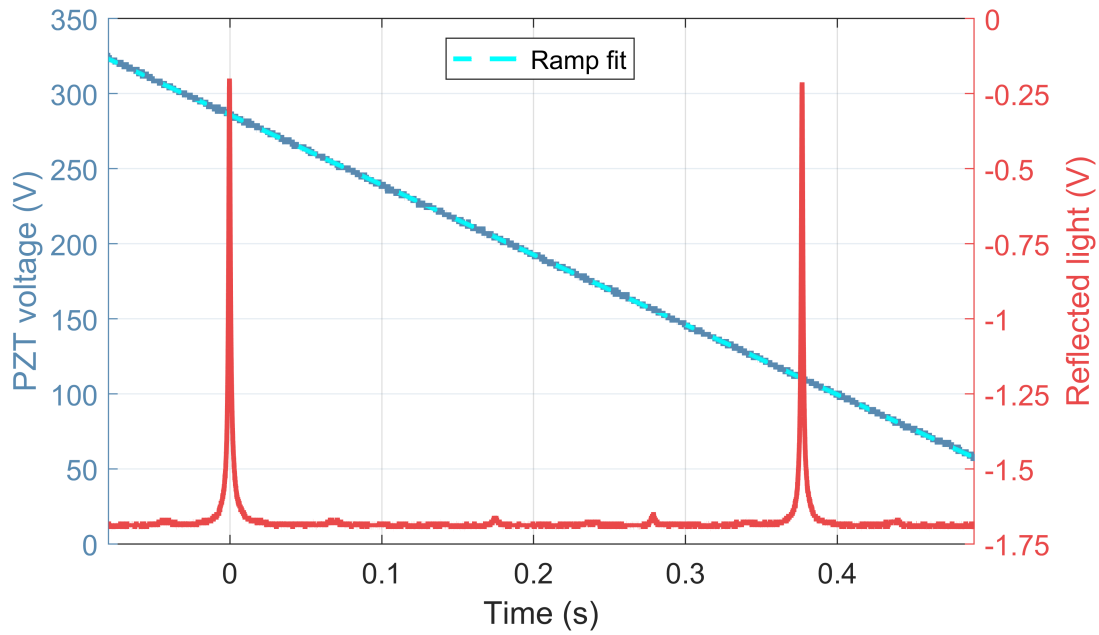


Figure 2.26: A ramp was applied to the PZT and the reflected light from the cavity was measured. The FSR of the cavity is known, so the time in this measurement can be converted to frequency using the spacing between the two peaks. This gives the PZT transfer function at low frequencies. The ramp signal is shown in blue and the reflected light is shown in red.

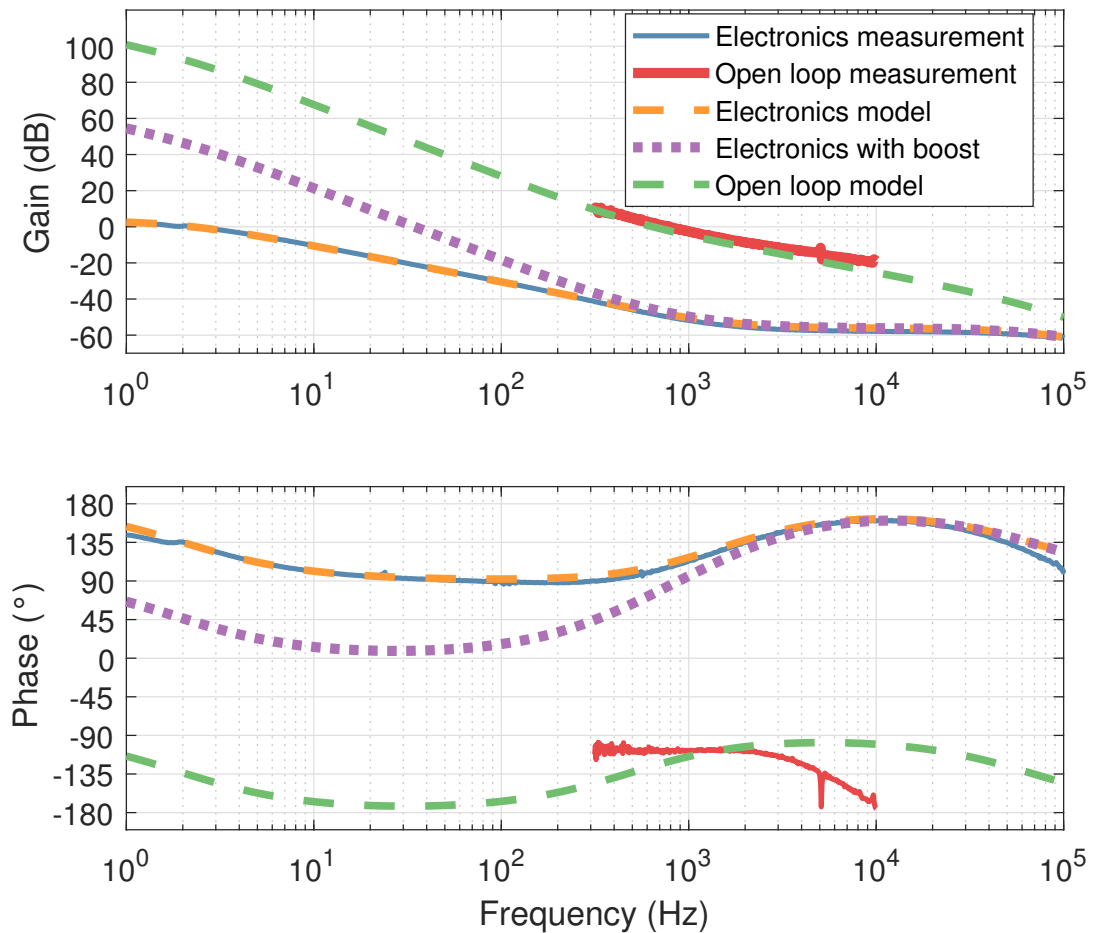


Figure 2.27: The open-loop transfer function was measured using the layout shown in Figure 2.23. This is shown in red. The transfer function of the electronics without the ‘boost’ provided by an extra integrator stage was measured and is shown in blue. The model of this is shown in orange. The boosted electronics model is shown in purple. The green line shows the expected servo gain based on the boosted electronics model and the measurements shown in Figure 2.25 and Figure 2.26. This model is within 2 dB of the measurement above the unity gain point. The PZT inducing unintended motion in the cavity as it goes through resonance may explain the phase a gain discrepancy between the model and the measurement below the unity gain point. The unity gain point was measured to be at  $\sim 800$  Hz.

### 2.7.2 Frequency Noise Measurement

The measurement of the system's frequency noise is shown in Figure 2.28. Despite imperfect calibration, this measurement provides some useful information about the frequency noise of the laser and the length noise of the PMC. As the PMC was not vacuum sealed, between 100 Hz to 1 kHz, there was a bulge in the frequency noise. It is likely that this noise will not be an issue, as LIGO never used the old PMC under vacuum. This was due to the air conditioning generating acoustic noise and length noise within the PMC, as well as non-perfect offsetting in the PDH loop.

Below the unity gain point, as the PZT response is flat, the PZT signal can be converted into frequency noise. The mixer signal and the open-loop transfer function  $c(1 + GH)$  gives the frequency noise. These two measurements are within a factor of 2 of each other. There is uncertainty in the calibration as nominal values for the optical properties of the PMC were used. The mixer signal measurement depends on the cavity's linewidth, and as this depends on the cleanliness of its mirrors, the PMC's linewidth could be different from its nominal value. Reference [138] describes measurements which could be used to accurately determine the optical properties of the PMC; however these measurements would require additional hardware.

At frequencies much above the unity gain point of the servo, a signal applied to the PZT will not be suppressed by the loop. Near the unity gain point, a signal applied to the PZT will be attenuated. A peak at 1111 Hz was used to check the calibration of the loop. The closed loop gain at 1111 Hz was modelled to be -5.2 dB,

so the peak measured at the mixer should be reduced by a factor of  $1 - 10^{-5.2/20} = 0.45$ . The peak generated at the PZT was measured at the mixer to be reduced by a factor of 0.70; the difference between the prediction and measurement would be fixed with better characterisation of the PMC.

## 2.8 Conclusion

The PSL has undergone a major redesign due to the pointing noise introduced by the cooling for the HPO. The new layout consists of an NPRO and two solid state amplifiers followed by the PMC. A prototype of this new design was constructed and tested. This layout is shown in Figure 2.2. The setup procedure was established and a cooling scheme was trialled.

The frequency noise of the beam transmitted by the PMC was investigated using signals in the PMC control loop. The laser's frequency noise was dominated by fluctuations in the optical path length of the PMC as the PMC is not shielded from acoustic vibrations. This measurement is shown in Figure 2.28.

The pointing noise was found to exceed the requirements (See Figure 2.22). To get a better measurement of this, the scattering on the DBB quadrant photodiodes needs to be reduced. A reduction in noise may be seen when the laser is commissioned as the PSL is housed in a quieter environment than the lab this prototype was made in. To reduce the pointing noise further, the flow rates being lowered will help, however this reduces the output power. To lower the pointing noise induced by

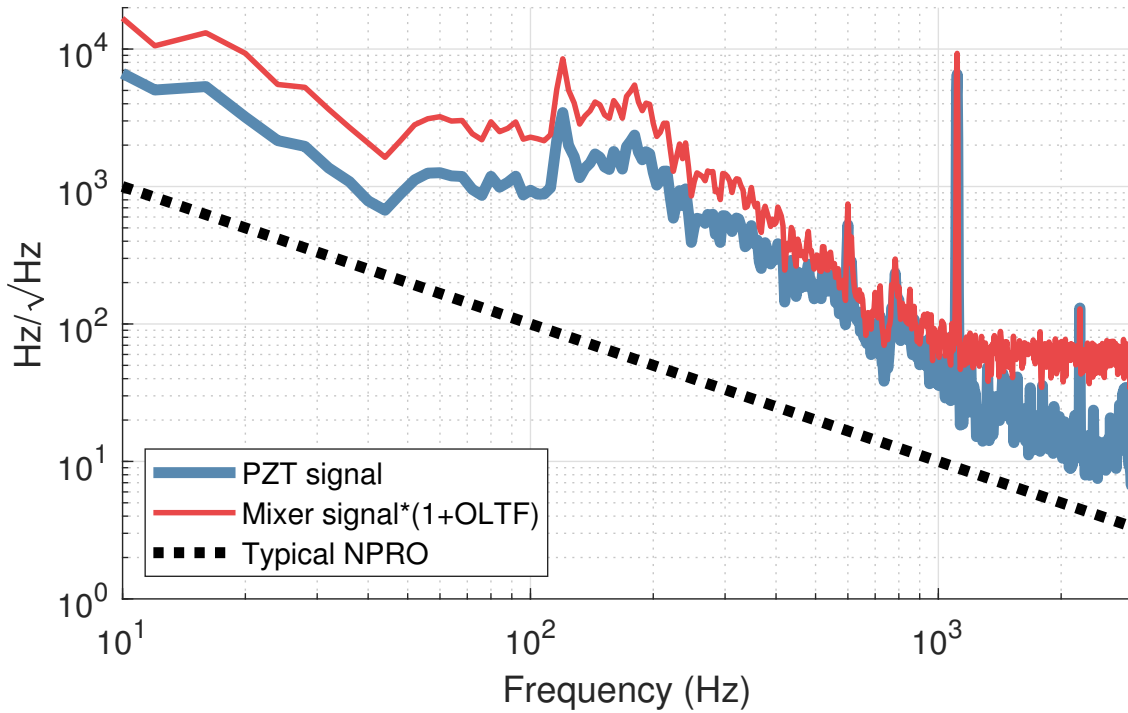


Figure 2.28: Frequency noise of the beam exiting the the pre mode cleaner. The mixer signal combined with the open-loop transfer function is shown in red. This is equivalent to the frequency noise of the system. The PZT signal should agree with this measurement below the unity gain point ( $\sim 800$  Hz). A signal was applied to the PZT at 1111 Hz. This is below the corner frequency of the PZT and above the unity gain point for the servo. This should match with the mixer signal. There is a factor of two between these two measurements. This can be attributed to imperfect calibration due to nominal parameters of the PMC being used. The typical noise expected from an NPRO is shown by the dashed black line. Between 100 Hz and 1000 Hz, there is a bulge in the frequency noise. This is likely due to acoustically driven noise of the PMC as the PMC is not vacuum sealed. This can be converted to length noise with a factor of  $\sim 10^{-14}$  m/Hz.

turbulence generated by bends in the water cooling pipes, they should be carefully laid out. Active alignment could be implemented to reduce pointing noise.

The level of power achieved with this setup will be sufficient for O4 as the usable amount of power is limited by noise couplings which arise due to point absorbers in the test masses [64]. The output power was measured over two days and was found to drop from a peak of 111 W to 107 W. This is shown in Figure 2.7. This was due to changes in the lab temperature affecting the alignment. Higher output power could be achieved if more pump-diode current and cooling is used. Additionally, to increase the power emerging from the PMC, the modematching into the PMC could be improved.

100W of intensity stabilised light was transmitted through the PMC. The free running intensity noise of the beam transmitted by the PMC was measured and the inner-loop intensity stabilisation was tested. Two actuators were considered, an AOM and a current shunt; the AOM was chosen as this offers the most flexibility in terms of loop gain and operating power. The inner-loop noise requirement was met with this setup. The stabilised noise is shown in Figure 2.21.

Future iterations of the PSL may use fibre lasers and fibre amplifiers [110, 111] as there is rapid development in this technology. These have been demonstrated at the power levels required for LIGO. Coherent power addition is another technique that can be used to obtain high beam powers (e.g. [139, 140]). When long term operation has been demonstrated, these technologies may be a viable replacement for the current laser design.



## Chapter 3

# Analysis of the Uncertainty of the Beam Parameter of the Arm Mode at the Signal Recycling Mirror

### 3.1 Introduction

A gravitational wave creates a differential signal in the arm cavities. The light containing the signal is directed to the SRC (see Section 1.4.3). This light can be contaminated with non-signal light, i.e. *junk light*, due to imperfections in the interferometer. This junk light is removed with the OMC (see Section 1.4.4), so the light emerging from the OMC will only contain the signal generated by the differential

### Chapter 3. Analysis of the Uncertainty of the Beam Parameter of the Arm Mode at the Signal Recycling Mirror

arm length change. Some of the junk light will come from mode mismatches between the arm cavities and the SRC (see Section 3.1.1), and non-optimal mode matching decreases the interferometer's sensitivity (see Section 3.1.2). The parts of the LIGO detector discussed in this chapter are shown in Figure 3.1.

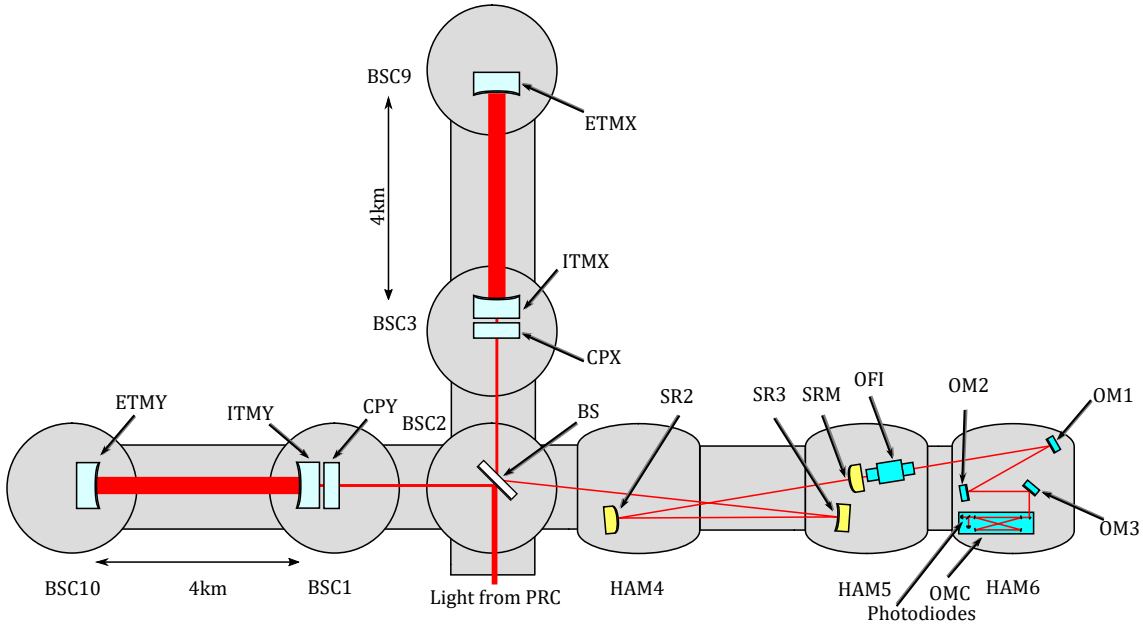


Figure 3.1: Sketch showing the parts of the aLIGO detectors discussed in this chapter. A sketch showing more of the detector is shown in Figure 1.4. The angles and lengths are exaggerated for clarity. Light from the arm cavities is incident upon the beam splitter (BS). As BS is wedged, the light going towards the SRC comes out an angle. Differential arm length signals encoded onto this light are directed towards SR3, SR2, and then the SRM. Between the SRM and the OMC, there are optics for steering and mode matching (OM1-3). Finally, to strip away junk light, the light enters the OMC. The light emerging from the OMC is detected by photodiodes.

Currently, based on the measurements reported on in Section 3.1.3, there is

significant uncertainty on the arm mode's<sup>1</sup> beam parameter at the SRM. The *active wavefront control* (AWC) within HAM6 for LIGO A+ is designed around this uncertainty (see Chapter 5).

The effect of errors in the focal length of SR3 and SR2 on the beam parameter and HOM content of the arm light at the SRM are explored in this chapter. To do this, a LIGO-like interferometer was simulated using FINESSE; this is discussed in Section 3.2 and Section 3.3. Using this simulation, the uncertainty in the beam parameter is explored (see Section 3.4).

The difference in the HOM content of the beam transmitted through the SRM between an ITM single-bounce measurement and a measurement which involves the arm cavities is discussed in Section 3.5. The effect that the interferometer being in signal recycling and RSE mode had on the HOM content of the beam as the focal length of SR3 deviated from its nominal value is also discussed in Section 3.5. Section 3.6 is a summary of the results in this chapter.

### 3.1.1 The Mode Matching Between the Arm Cavities, the Signal Recycling Cavity, and the Output Mode Cleaner

The SNR of the gravitational wave signal is directly related to the mode matching between the arm cavities, the SRC, and the OMC, so it is crucial to have accurate

---

<sup>1</sup>Strictly speaking, there is uncertainty in the beam parameter for both arms' modes at the SRM. Since the arms are almost identical, the beam parameter is essentially the same for each arm.

knowledge of the beam parameter at the SRM. The mode in the arm is well defined since the arm cavities have high finesse. Uncertainties in the *radius of curvature* (RoC) of optics in the SRC telescope (SR2 and SR3, see Figure 3.1) results in an uncertainty in the beam parameter of the arm mode at the SRM, as well as the eigenmode of the SRC. The SRC is a low finesse cavity, so a range of modes that do not match the SRC's eigenmode can be sustained within it.

Light in higher order modes will be generated if the arms are perfectly matched to the OMC but not to the SRC. There can be significant mode mismatch between the arms and the SRC and still be lots of signal-light exiting the interferometer because the SRC is a low finesse cavity ( $\sim 15$ ). If the arms are matched to the OMC but not to the SRC, then actuators for changing the mode matching between the arm and the OMC could not be used to increase the differential arm signal sensed by the photodiode after the OMC. This means the mode matching between the arm and the OMC can be optimal but the light can still contain HOM. Additionally, if the beam is astigmatic, then optimal mode matching would not correspond to perfect mode matching.

### 3.1.2 Loss due to Mode Mismatch

Loss degrades the shot noise limited sensitivity of the interferometer (see Section 1.7). It is known that  $\sim 20\%$  of the light is lost between the AS port and the readout photodiodes, as the shot noise can be compared to the expected shot noise for a given fringe slope, input power and known losses. Approximately half of the

loss is accounted for, e.g. some comes from the OFI, some comes from the OM3 pick-off; however, the other half is not fully understood, e.g. see [141]. The level of squeezing can be used to cross check the loss [142]. It is hypothesised that some of the loss which is unaccounted for may come from mode mismatch between the arm cavities and the OMC.

There are two stages of mode matching ( $\text{Arm} \rightarrow \text{SRC}$  and  $\text{SRC} \rightarrow \text{OMC}$ ), so the effect of mode mismatch is not simple; this process is known as coherent destructive modal interference [143]. To model this scenario, it is helpful to consider a Mach-Zehnder interferometer made from theoretical components (modal beam splitters) which split light into the  $\text{HG}_{00}$  and  $\text{HG}_{20} + \text{HG}_{02}$  modes (i.e the  $\text{HG}_{20+02}$  mode). HOMs are discussed in Appendix F. The amount of light transferred between the  $\text{HG}_{00}$  and  $\text{HG}_{20+02}$  mode is determined by the magnitude of the mismatch, and the phase difference between the  $\text{HG}_{00}$  and  $\text{HG}_{20+02}$  mode depends on the nature of the mismatch. An error in waist size is in-phase (real), whereas an error in waist location is out-of-phase (imaginary). In general, the mismatch introduces a complex phase. Thus, a sequence of mode mismatches can be modelled in the same way as a Mach-Zehnder interferometer. The difference in phase between the  $\text{HG}_{00}$  and  $\text{HG}_{20+02}$  mode is analogous to a difference in path length in a Mach-Zehnder interferometer. It differs from a typical Mach-Zehnder interferometer as the  $\text{HG}_{00}$  to  $\text{HG}_{20+02}$  splitting ratio is not well balanced. As the loss due to mode mismatches act coherently, the degradation of the squeezed state can be greater for loss due to mode matching than for other types of loss, e.g. the loss due to photodiodes with a quantum efficiency less than one. If the squeezer is perfectly matched to the OMC, then the mode mismatch between the squeezer and the interferometer is four times

the loss you would expect from treating a mismatch loss as a regular loss. This is explained in detail in [143, 144].

### **3.1.3 Measurements of the Mode Matching Between the Arm Cavities and the Output Mode Cleaner at the LIGO Livingston Observatory Made Between 2018–2019.**

The mode matching between the arm cavities and the OMC, and the input light to the OMC were studied at the LLO detector between 2018-2019 by on-site scientists, and these measurements are summarised in Table 3.1. These measurements contradict each other, some suggest that mode matching is near perfect, other suggest it is  $\sim 90\%$ . Only one is a direct measurement of the beam profile, which is what we want to know for the design of the AWC in HAM6 for BHD (see Chapter 5).

Techniques for determining the mode matching between the arms and the OMC include: actuating on the waist size and waist location of the beam coming from the arm and measuring what effect this has on the mode matching to the OMC; direct beam profile measurements; the application of different differential arm offsets to determine what portion of light in an OMC scan corresponds to the arm mode and what portion of the light comes from elsewhere in the interferometer (e.g. from contrast defect); and measuring a size of a signal known to originate in the arm cavities to find the optimal mode matching configuration for the interferometer. Some of these measurements were performed whilst the arm cavities were locked, and some were made when the interferometer was in *single bounce* mode, i.e. without

the arm cavities being locked.

## 3.2 Modelling Interferometers with Mode Mismatches Using FINESSE

FINESSE is software for simulating optical layouts [154, 155]. Optical layouts are modelled with components such as mirrors, lenses, and spaces. The way these components are connected is defined by nodes. FINESSE performs a nodal analysis to calculate the steady state amplitude of light fields within the optical layout, similar to how a circuit can be analysed. PyKat is a python wrapper for FINESSE which provides many quality-of-life improvements such as the ability to programmatically update and re-run simulations [156].

The light fields that are calculated in a FINESSE simulation can be outputted by using virtual detectors such as a photodiode, `pd`, or an amplitude detector, `ad`. These can be configured to detect only certain modes using the `mask` command. The `bp` detector is used for outputting the beam parameter, and the `gouy` command computes the Gouy phase accumulated along a set of spaces. These detectors were used to find the ratio of light in HOMs to light in the  $HG_{00}$  mode, the beam parameter of the arm mode that is transmitted through the SRM, and the Gouy phase accumulated along the SRC.

The beam parameters at nodes in a FINESSE simulation are determined by `cav` and `gauss` commands. The `cav` command is used for defining linear and circular

cavities. The beam parameters are found by solving for the cavity's eigenmode. Once these nodes have had a beam parameter defined at them, the components connected to them have their beam parameter calculated based on the set of linear equations that define the component. If there are more than one `cav` commands used in a simulation, the latter `cav` command overwrites the previous one. The `gauss` command executes after the `cav` commands and sets the beam parameter of the laser used in the simulation.

FINESSE can perform simulations using *Hermite-Gaussian* (HG) modes, allowing for the effects of mode mismatches to be modelled if the problem satisfies the paraxial approximation. A coupling between the HG modes happens whenever a beam described by  $q_1$  enters a segment described by  $q_2$ . This could happen if the `gauss` command used on the laser does not correspond to the eigenmode of a cavity defined by the `cav` command.

A laser beam can be modelled as a linear combination of HG modes. Ideally, an infinite number of these modes would be used in a calculation; however, since it is not feasible to simulate an infinite number of *transverse electro-magnetic* (TEM) modes, the maximum number of TEM modes needs to be defined in a FINESSE simulation. This is done using the `maxtem` command. FINESSE will calculate the coupling of the light amongst these modes. If an insufficient number of TEM modes is used in the simulation, the output will be nonsense because power from the higher order TEM modes that would be required to accurately model the optical layout will be 'aliased' into the ones defined in the simulation. When a cavity becomes unstable, FINESSE will not generate physical results since the cavity will not be

mathematically describable.

The distance between components,  $L$ , in a FINESSE simulation is defined with a macroscopic distance,  $l$ , which is modelled with the `space` command, and a microscopic distance which is modelled with the tuning parameter,  $\phi$ , belonging to components such as mirrors (`m`) and beam splitters (`bs`). The macroscopic distance  $l$  is always an integer number of wavelengths, whereas the microscopic tuning,  $\phi$ , determines the position of a component to sub-wavelength accuracy. FINESSE uses the convention that to move a mirror one wavelength, a tuning of  $4\pi$  rad is used. This is so a tuning of  $2\pi$  of a mirror in a Fabry-Perot cavity results in the cavity's round trip getting one wavelength longer. It is useful to split the total length,  $L = l + \phi$ , in this way since the  $l$  determines things like Gouy phase whereas  $\phi$  determines whether a cavity is on resonance/which mode is resonant. When simulating mode mismatches, the manual states that the command `phase 2` is required to give physically correct results.

### 3.2.1 Thin and Thick Beam Splitters

FINESSE is mature software that has been tested against analytic and experimental results. However, care needs to be taken when using `Finesse` since incorrect usage can yield erroneous results. Users will get strange results if beam splitters are modelled with just one `bs` command. In this thesis, such components are called 'thin beam splitters'. To illustrate this, two simulations of Michelson interferometers were run, one with a thin beam splitter and the other with a thick beam splitter

made up of 3 thin beam splitters and two spaces with a refractive index  $> 1$ . See Figure 3.3 for an illustration of a thick beam splitter. The FINESSE code for these simulations can be found in Appendix D.4.

For a real beam splitter, for energy to be conserved, each reflection from a dielectric coating where the refractive index is lower on the reflecting side than on the transmitting side causes a light field to gain  $180^\circ$  of phase. In a Michelson, there is one path with two of the  $\pi$  phase change reflections, while in the other path there is only one such reflection. This means when the arms have equal lengths, destructive interference occurs at the AS port. The intensity,  $I$ , at the AS port of the Michelson as a function of the tuning of one of the arm mirrors,  $\Delta\phi$ , including the FINESSE convention for phase, is

$$I = I_0 \sin^2(\Delta\phi), \quad (3.1)$$

where  $I_0$  is the input power.

The effect of using a thin beam splitter versus a thick beam splitter in a FINESSE simulation is shown in Figure 3.2. The thin beam splitter causes there to be constructive interference at the AS port for equal arm lengths, whereas Equation (3.1) shows that it should be destructive interference. Using a thick beam splitter fixes this ‘bug’, as the phase at the beam splitter is accounted for.

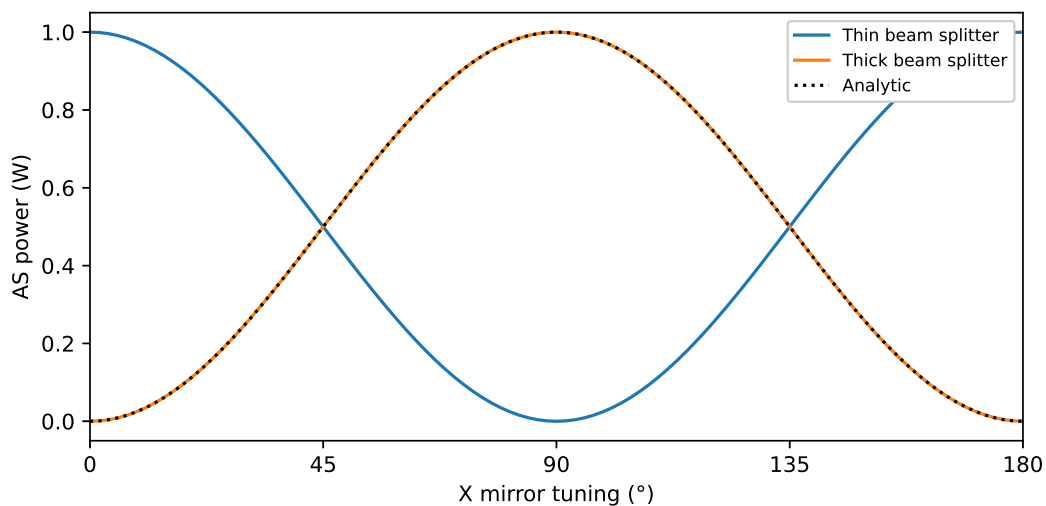


Figure 3.2: The simulation of a Michelson interferometer with a thin beam splitter is shown in blue. The same simulation was done with a thick beam splitter and this is shown in orange. The analytic behaviour of a Michelson interferometer (Equation (3.1)) is shown by the dashed black line. The tuning of one of the arm mirrors was changed and the power at the AS port was simulated. Comparing the outputs of the simulation to Equation (3.1) shows that thick beam splitters should be used.

Measurement	Description/Finding	Reference
Reflectivity of the interferometer.	There is a high amount of mode matching ( $> 99\%$ ) between the PRC and the arm cavities, so single-bounce and locked-arm measurements can be compared.	[145]
Mode matching between the arms and the OMC.	By measuring a signal that originated in the arm and adjusting the mode matching actuators between the arm and the OMC, the mode matching appears to be within a few percent of perfect.	[146, 147]
Mode scans of the light incident on the OMC.	For 10 W of input power to the interferometer, 11% of the light incident upon the OMC was in the $HG_{20+02}$ mode. For 40 W of input power, 4% of the light was in the $HG_{20+02}$ mode. Just after the interferometer lost lock, and thus was in a thermal state similar to how it would be during observation mode, the $HG_{20+02}$ content of the light incident on the OMC was estimated to be 8%.	[148–150].
Measurement of the beam profile.	A beam profiler was used to measure the size of the beam exiting the SRM. There was a 15% mismatch between this beam and the OMC mode.	[151, 152]
Measurement of the SRC's Gouy Phase	The one-way Gouy phase of the SRC was measured to be $21.3^\circ$ . It is explained in Section 3.4 how this measurement can be used to calculate the expected mode mismatch between the interferometer and the OMC to be less than 5%.	[153]

Table 3.1: Measurements made at LLO by on-site scientists of the mode matching between the interferometer and the OMC.

### 3.3 Modelling of a Michelson Interferometer with Fabry-Perot Arm Cavities and a Signal Recycling Cavity

To investigate what effect a mode-mismatch between the SRC and the arm cavities has on the HOM content of the beam transmitted through the SRM, a ‘LIGO-like’ interferometer was simulated in FINESSE. This interferometer uses two identical, design specification arm cavities. The lengths between the optics in the SRC were obtained from the Zemax model of the LLO interferometer, and the focal lengths of the optics in the SRC are the measured values for the optics used in the LLO detector. The reason for using identical arm cavities is to eliminate junk light due to mode mismatch between the arms. The OMC, IMC, and PRC were not included in this simulation as these do not affect the beam in the SRC. A schematic of the simulation is shown in Figure 3.3. The default focal lengths, transmission coefficients and spacings for this simulation are listed in Table D.7.

To perform ITM single-bounce measurements, the ETMs are misaligned. This results in the ITM having an effective power reflectivity of unity. To replicate this in FINESSE, the R for each ITM was set to 1 minus the loss of the ITM HR coating. The ETM and ITM both have 10 ppm loss. Because the mode matching between the PRC and the arms is close to 100%, this is valid.

The interferometer was set up to be in DC readout mode. The tuning of the arm

### Chapter 3. Analysis of the Uncertainty of the Beam Parameter of the Arm Mode at the Signal Recycling Mirror

mirrors was set so that there was 30 mW of light emerging from the AS port when the RoCs of the optics matched the default values. This is discussed in Section 3.3.1.

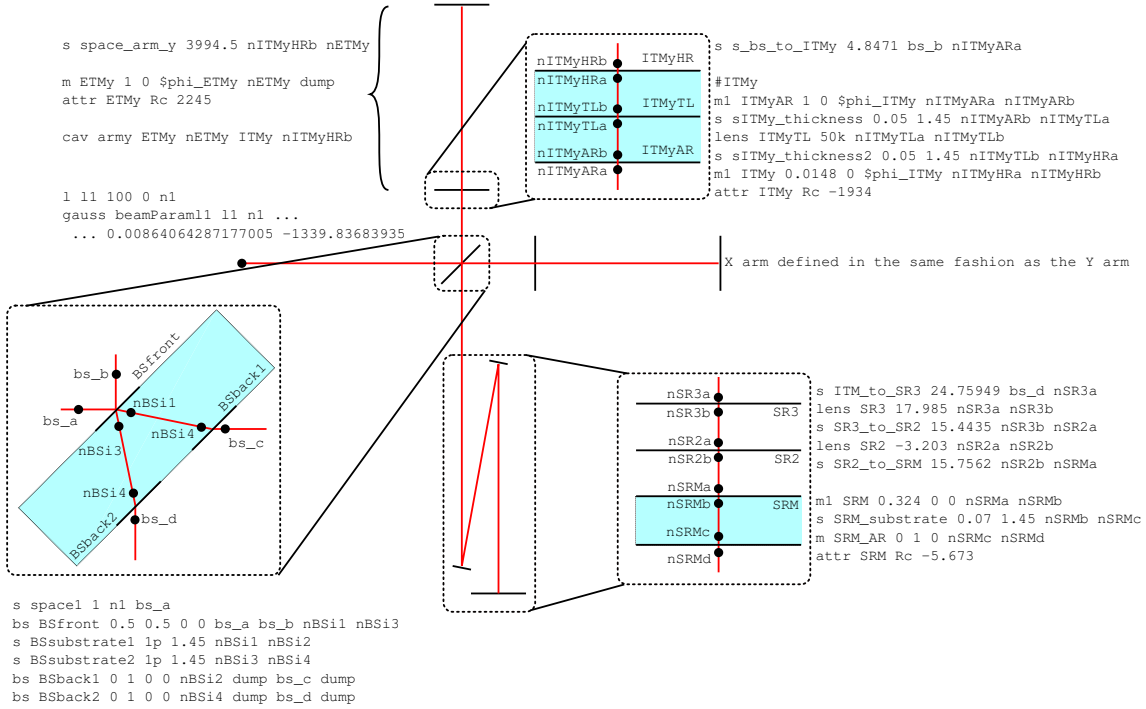


Figure 3.3: Schematic of the simulation. The dimensions of the schematic are not to scale. The laser light is shown as a red line. Black lines with red beams interacting with them correspond to components such as mirrors and lenses. Important nodes are highlighted with black dots and the associated FINESSE commands are shown nearby. Zoom-ins provide more detail for the main beam splitter, ITMy and the SRC. The elongated curled bracket highlights the arm cavity, and the text with it shows how it is implemented in FINESSE.

Geometry errors in the SRC cause couplings between the  $HG_{00}$  mode and HOM.

### 3.3. Modelling of a Michelson Interferometer with Fabry-Perot Arm Cavities and a Signal Recycling Cavity

---

There are two sorts of errors which cause mode mismatch: RoC errors and errors in the distance between each of the optics in the SRC. RoC errors are due to uncertainties in the RoC of SR3, SR2, the SRM, and unintended levels of thermal lensing in the ITM and compensation plate.

The largest geometry errors in the SRC come from RoC errors in SR3 and SR2, with both errors affecting the beam in a similar way as there is not much Gouy phase between them. Therefore, to investigate how geometry errors affect the beam transmitted through the SRM, the RoCs of SR3 and SR2 were varied.

Certain components have a small impact on the uncertainty in the beam parameter at the SRM. The thermal lensing in the ITM is assumed to have a focal length of +50 km, and it would require significant deviation, in the direction of more heating, for this lens to have a large effect. The radius of curvature of SRM is well enough known that it is not the dominant cause of junk light in the SRC. The spacings between the optics in the SRC are known to a great enough precision, less than  $\sim 1\text{mm}$ , that errors in their locations have a negligible effect.

In an interferometer with arm cavities, a small difference in the lengths between the beam splitter and the ITM for the X and Y arms, known as a Schnupp asymmetry, is required to make the interferometer controllable. For simplicity, no Schnupp asymmetry was included in this simulation. Since spaces are by default on resonance in FINESSE, no Schnupp asymmetry is needed to control the inner Michelson length in the model. The Rayleigh length of the beam at the ITM is of the order of several hundred metres. This is huge in comparison to the Schnupp asymmetry, which is

8 cm. The Schnupp asymmetry will therefore have only a small effect on the HOM content of the beam transmitted through the SRM, but since the dominant sources of HOM are RoC errors in SR3 and SR2, the behaviour of the beam in the SRC can be largely understood without it.

The beam parameter of the input laser was defined so that there was no difference between the single-bounce and the locked arm simulation. To define the beam parameter, the `gauss` command was used. In this simulation, the mode matching from the laser to the arm cavities should be perfect. The amount used was 99.99999%; this was found to be sufficient. See Appendix D for details on how  $w_0$  and  $z$  were determined for the `gauss` command used on the laser. The power of the input laser was set to 5 MW to replicate the amount of power on the main beam splitter.

The `cav` command was used to set up the arm cavities, although the `gauss` command used on the laser means the `cav` command is not required (on the fly testing showed this to be the case). A `cav` command was not used on the SRC since this forces the beam parameter at the SRM to be determined by the SRC geometry. An SRC cannot be defined in FINESSE using the `cav` command as one of the end mirrors cannot be properly defined.

The detectors for analysing the mode matching between the nominal arm mode (which matches the laser mode) and the SRC mode were `pd` and `ad` with various `mask` commands applied to them. To detect the total light, no `mask` was applied. To detect the higher order light, a `mask [pd] 0 0 0` command was used. This sets the sensitivity of the photodiode to the  $HG_{00}$  mode to 0. The mode matching is

### 3.3. Modelling of a Michelson Interferometer with Fabry-Perot Arm Cavities and a Signal Recycling Cavity

---

then determined as  $1 - \text{HOM}/\text{total light}$ . `maxtem` was set to 6 as this was sufficient to simulate the interferometer accurately while it was stable (see Figure 3.10). As a cross check, two amplitude detectors were used to detect the  $\text{HG}_{20}$  and  $\text{HG}_{02}$  modes. When plotting the power of the  $\text{HG}_{20+20}$  mode, the square of the `ad` detector output needs to be taken. The `bp` detector was used to find the beam parameter. To find the Gouy phase accumulated in the SRC by the  $\text{HG}_{00}$  mode, the `gouy` command was used.

Both signal recycling and RSE modes of operation were investigated. The tuning of the SRM determines whether the interferometer is in RSE mode or in signal recycling mode. If the interferometer has arm cavities, the SRM detuning which corresponds to RSE is  $90^\circ$  while the detuning which gives signal recycling is  $0^\circ$ . For an interferometer without arm cavities, to operate in RSE mode the SRM detuning should be set to  $0^\circ$ , while to be in signal recycling mode the detuning of the SRM should be set to  $90^\circ$ . This is because the reflected light from a cavity has an additional  $180^\circ$  compared to if it was reflecting from a mirror.

#### 3.3.1 Determining Tunings for DC readout

To maintain the same SRC finesse seen by the differential mode for each simulation, the interferometer was set up so that it was on the dark fringe, with 30 mW of light being transmitted through the SRM. This was achieved by applying a differential tuning to the ETMs for simulations with the arm cavities, and a differential tuning to the ITM for single-bounce simulations. The light transmitted through the

SRM for an interferometer with arm cavities as a function of differential ETM detuning is shown in Figure 3.4. For an interferometer without arm cavities, the power transmitted through the SRM as a function of differential ITM detuning is shown in Figure 3.5. The tunings for operating with 30 mW of light being transmitted through the SRM are shown in Table 3.2 and Table 3.3.

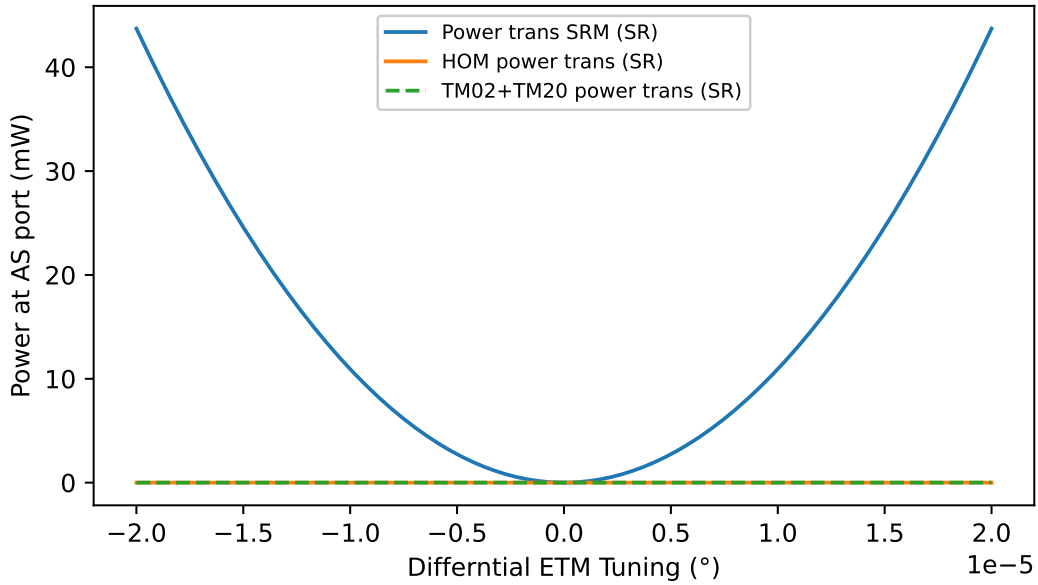


Figure 3.4: For simulations with the arm cavities, the DC offset is created by tuning the ETMs. The minimum of the dark fringe is at 0° differential ETM detuning, as shown by the blue line. A slight offset causes light to be at the AS port. This result was used to determine tunings for simulating what effect focal length errors in SR3 and SR2 have on the beam transmitted through the SRM. The orange line and dashed green line show that the beam has a negligible HOM content.

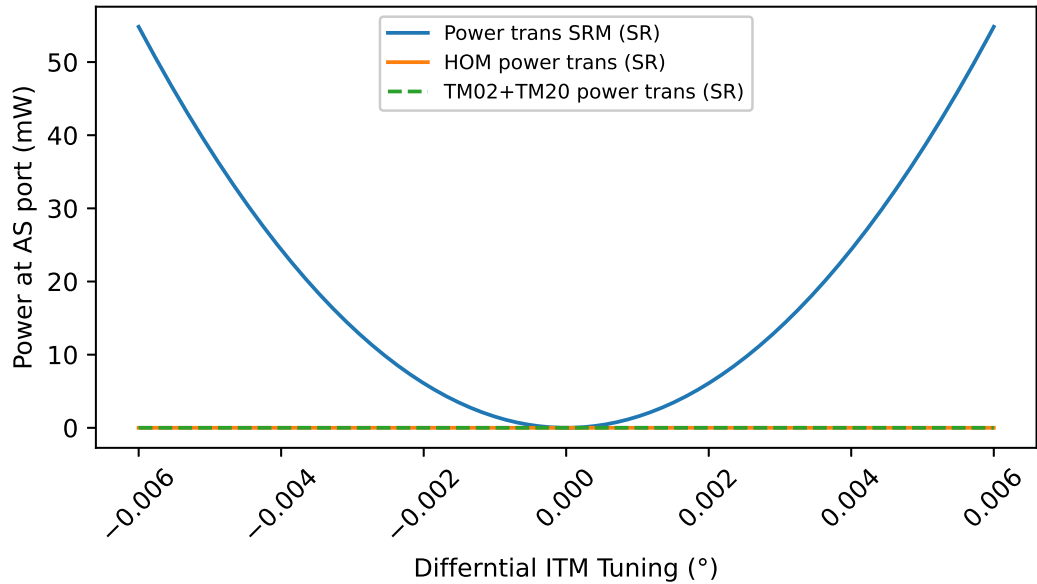


Figure 3.5: For simulations without arm cavities, i.e. single bounce simulations, the DC offset is created by tuning the ITMs. The minimum of the dark fringe is at  $0^\circ$  differential ITM detuning, as shown by the blue line. A slight offset causes light to be at the AS port. This result was used to determine tunings for simulating what effect focal length errors in SR3 and SR2 have on the beam transmitted through the SRM. The orange line and dashed green line show that the beam has a negligible HOM content.

Mirror	SRM Tuning (°)	Mirror Tuning (°)
ETM <sub>x</sub>	0	+2.76e - 06
ETM <sub>y</sub>	0	-2.76e - 06
ETM <sub>x</sub>	90	+2.64e - 05
ETM <sub>y</sub>	90	-2.64e - 05

Table 3.2: The tunings used for the arm-cavity simulation to get 30mW of light at the dark port.

Mirror	SRM Tuning (°)	Mirror Tuning (°)
ITM <sub>x</sub>	0	+0.00709
ITM <sub>y</sub>	0	-0.00709
ITM <sub>x</sub>	90	+0.00074
ITM <sub>y</sub>	90	-0.00074

Table 3.3: The tunings used for the no-arm-cavity simulation to get 30mW of light at the dark port.

## 3.4 The Beam Parameter of the Arm Mode at the Signal Recycling Mirror

The beam parameter at the SRM depends on macroscopic quantities such as the distances between mirrors and the RoC of the optics, rather than microscopic tunings. Therefore, the beam parameter is not affected by the interferometer being in RSE or signal recycling mode. To estimate the propagation of the mode from the arms to the SRM, the focal lengths of SR3 and SR2 were varied around three standard deviations of their measured values, and the effect this had on the beam transmitted through the SRM was determined with a `bp` detector.

The effect of a focal length error in SR3 and SR2 on the width and RoC of the arm mode at the SRM is shown in Figure 3.6 and Figure 3.7. These figures show that the beam parameter depends mainly on the focal length of SR3, although SR2 has a noticeable effect. When the focal lengths of SR3 and SR2 are at their nominal values, the simulated beam has a width of 2.1 mm, a RoC of  $-3.91$  m, and the Gouy phase accumulated between the ITM and the SRM is  $18.7^\circ$ . There is a slight difference between the RoC found here and the design value of  $-3.88$  m; this difference is due to the as-built focal lengths of the optics used in the SRC at LLO being different from the design values – small differences such as the 36.00 m being the nominal RoC of SR3 and  $(35.97 \pm 0.01)$  m being the measured RoC for SR3 could account for this.

Measurements of the single-bounce beam profile [152] suggests that the beam is

much larger at the SRM than the design value. This would correspond to a positive error in the focal length of SR3, as shown in Figure 3.6. If the beam were this large, it is unlikely that the SRC would be stable, as shown in Figure 3.10. The measurement of the beam width found in [152] was obtained under fairly artificial conditions, thus it may not represent the beam parameter of the arm mode when the interferometer is in observing mode. For instance, the thermal state of the interferometer was not similar to how it would be during observing mode. Additionally, [152] reports that there was difficulty in orienting the beam profiler correctly, and this leads to significant uncertainty in this measurement.

Information about the beam parameter of the arm mode can be inferred from the Gouy phase accumulated by the arm mode in the SRC. The Gouy phase as a function of focal length error in SR3 and SR2 is shown in Figure 3.8. Measurements of Gouy phase of the SRC find it to be  $22.81^\circ$  [157] and  $21.3^\circ$  [153], although the authors of [157] have low confidence in their measurement. These measurements of Gouy phase suggests that the beam at the SRM is smaller than the design value and has a lower curvature. This Gouy phase also corresponds to a similar amount of  $HG_{00}$  loss that is measured and simulated (Figure 3.13).

The Gouy phase accumulated in the SRC is almost entirely dependent on the RoC of SR3 and SR2; positioning errors of up to 1 cm of SR3 and SR2 do not affect the Gouy phase significantly. Figure 3.8 shows that it is unlikely that the Gouy phase could be  $22.81^\circ$  in a state where the arm has greater than 90% mode matching to the SRC, as the RoC of both SR3 and SR2 would have needed to have been three standard deviations from the measured value. This could be accounted

for by a much shorter thermal lens in the ITM (see Figure 3.9). The measurement of  $21.3^\circ$  of Gouy phase is plausible with the 50 km thermal lens. The single pass thermal lens was measured to be  $38.92 \mu\text{D}$ , i.e.  $\approx 25.7 \text{ km}$  [150], which corresponds to the design value and the value used in this simulation.

The focal lengths of SR3 and SR2 can be estimated from the Gouy phase measurement. A normal probability density function was used to model the uncertainties in the focal lengths of SR3 and SR2. This was combined into a 2-D normal distribution. Combinations of SR3 and SR2 that result in  $21.3^\circ$  of Gouy phase were found and the value of the 2-D normal distribution for those combinations was calculated. The maximum value of the resulting probability density function (which is normal) corresponds to the most likely combination of focal lengths for SR3 and SR2, and one standard deviation corresponds to the error. Figure 3.11 shows that the focal length of SR2 to be  $(-3.205 \pm 0.003) \text{ m}$  and the focal length of SR3 to be  $(17.971 \pm 0.002) \text{ m}$ .

The beam parameter at the SRM is determined by the focal length of SR3 and SR2, and the focal lengths of SR3 and SR2 have a probability density associated with them (see Figure 3.11). Thus, each beam width and RoC pair that was computed in this simulation also had a probability density associated with it. Based on the measurement of Gouy phase, the beam is likely to have a width of 1.84 mm and a defocus of -2.80 Dioptre. This is shown in Figure 3.12. This is a slight simplification as the beam parameter cannot be such that the Gouy phase of the cavity becomes too small (less than  $\sim 17.5^\circ$ ). The cavity will be unstable if the Gouy phase is too small, so beam widths of more than 2.25 mm are unlikely. The shape of the

Chapter 3. Analysis of the Uncertainty of the Beam Parameter of the Arm Mode at the Signal Recycling Mirror

---

distribution of the arm mode beam parameter at the SRM is driven mostly by the focal length error of SR3.

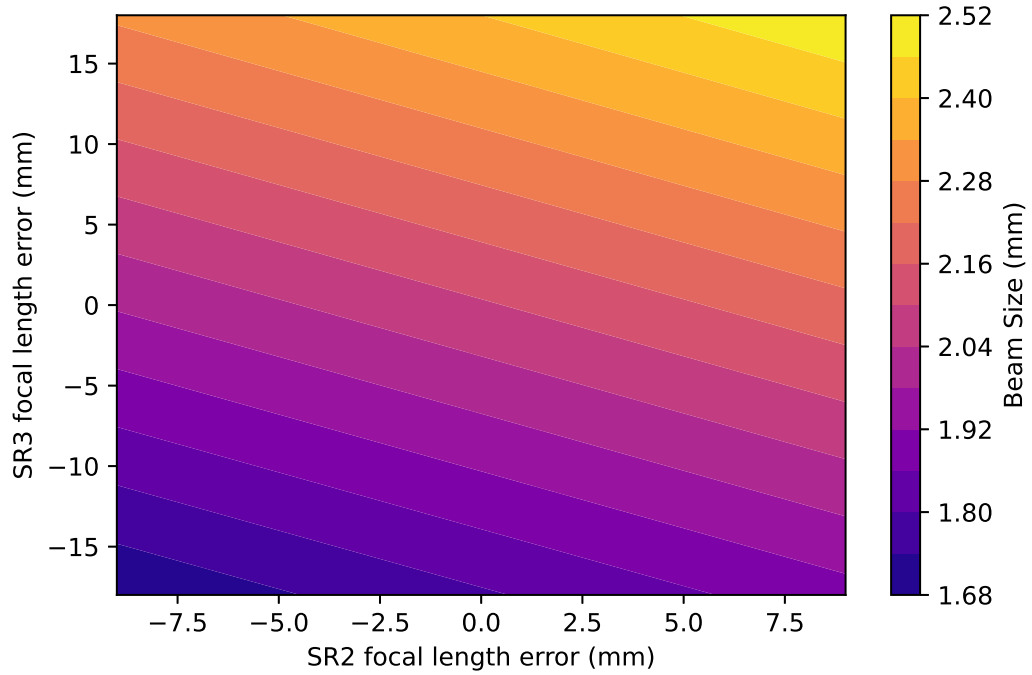


Figure 3.6: The Gaussian width of the beam that is transmitted through the SRM as a function of the error ( $\pm 3\sigma$ ) in focal length of SR3 and SR2. The Gaussian beam width is strongly dependent on SR3's focal length error, whereas SR2's focal length error is less important. When the beam size is much greater than  $\sim 2.25$  mm, the SRC is unstable (see Figure 3.10), so this area of the parameter space is unlikely to correspond to the beam at the SRM at LLO.

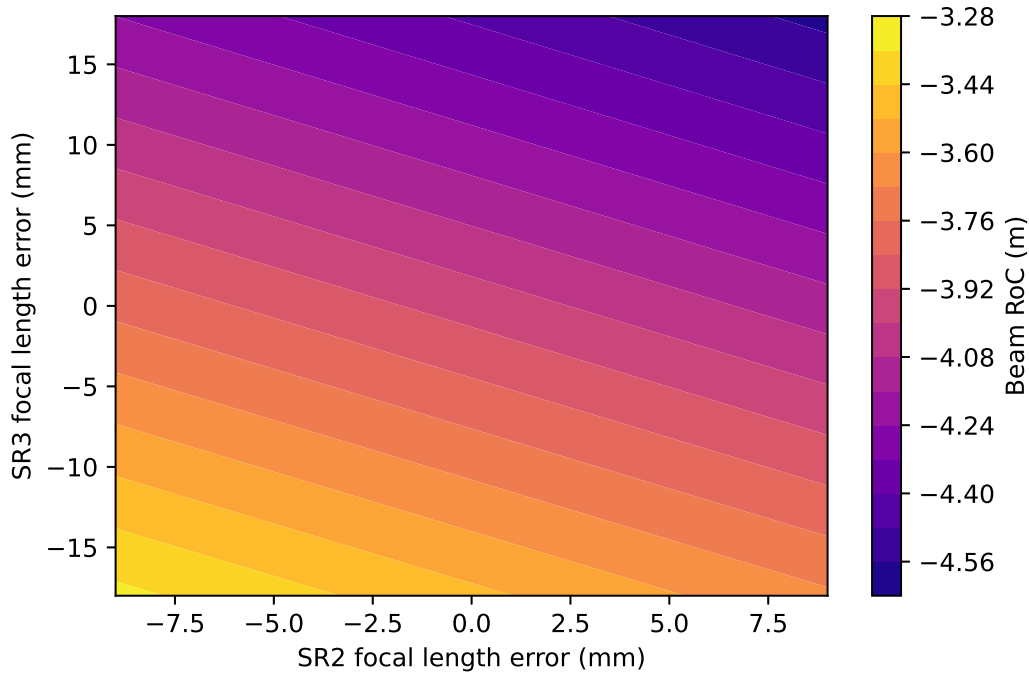


Figure 3.7: The RoC of the beam that is transmitted through the SRM as a function of the error ( $\pm 3\sigma$ ) in focal length of SR3 and SR2. If the arm cavities and the SRC are well mode matched, then the RoC of the beam transmitted through the SRM would be  $\frac{5.67\text{m}}{1.45} = 3.91\text{m}$ .

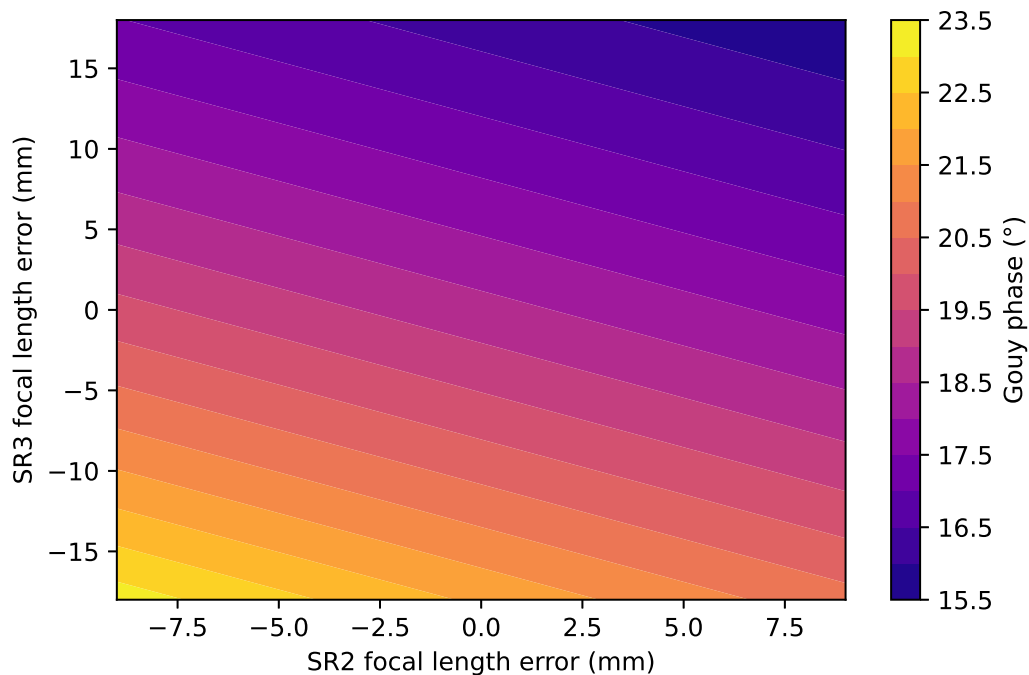


Figure 3.8: The Gouy phase between the ITMs and the SRM as a function of the error ( $\pm 3\sigma$ ) in SR3 and SR2. When the SR3 focal length error  $> 6$  mm and SR2 error is zero, the SRC is unstable (see Figure 3.10), so this area of the parameter space is unlikely to correspond to the beam at the SRM at LLO.

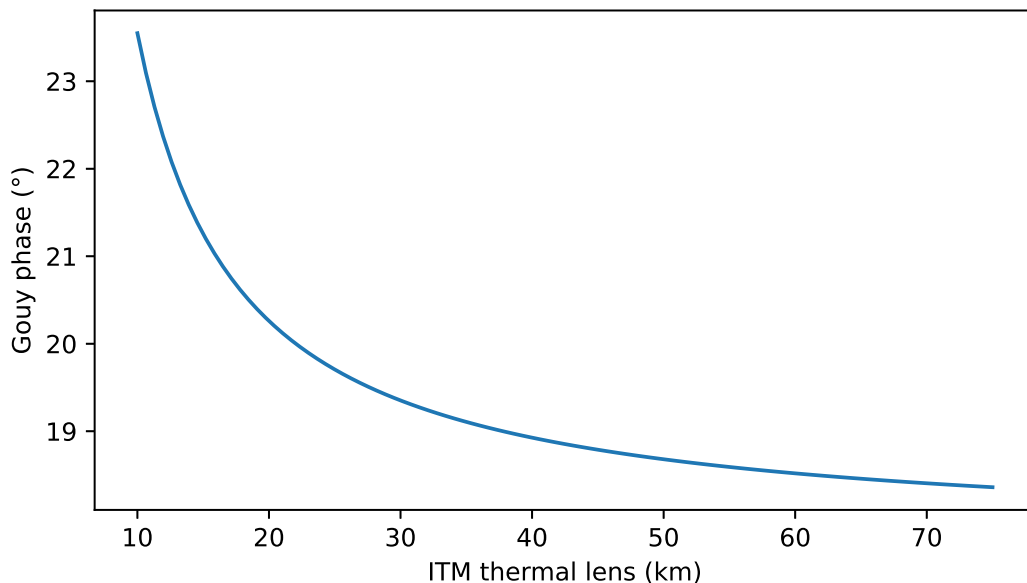


Figure 3.9: The Gouy phase between the ITMs and the SRM as a function of the thermal lens in the ITMs for the default values of SR3 and SR2. The nominal ITM thermal lens focal lengths are 50 km, and this corresponds to about 19°. More heating results in a greater thermal lens, however the LIGO detectors compensate for this with the thermal compensation system.

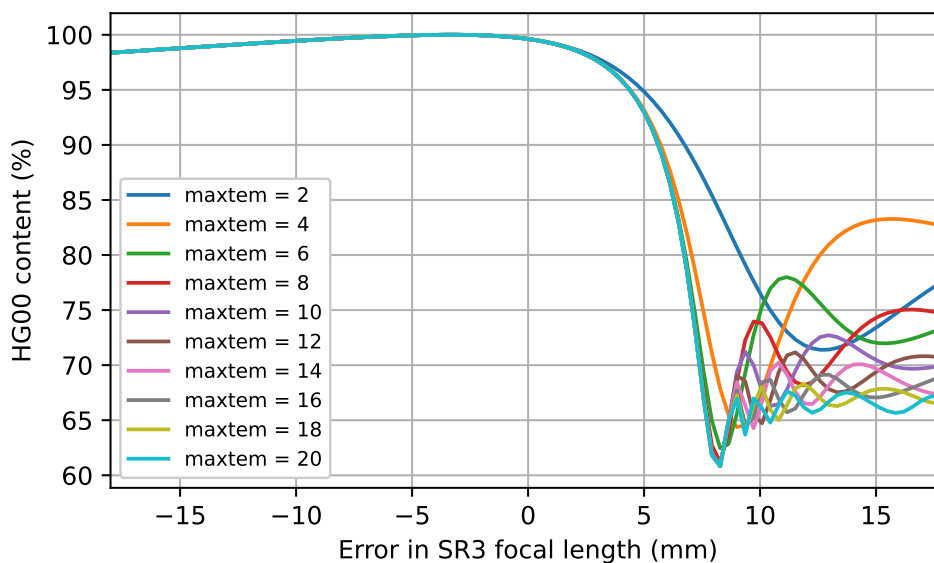


Figure 3.10: The percentage of HG<sub>00</sub> light transmitted through the SRM as a function of SR3's focal length for the Michelson interferometer with Fabry-Perot cavities in its arms was simulated. Each simulation used a different `maxtem` command. The focal length of SR3 was changed. For focal lengths with a positive error greater than 7.5 mm, the cavity becomes unstable and FINESSE does not produce reliable results. For a stable SRC, the minimum number of TEM modes needed for sub 1% accuracy is six.

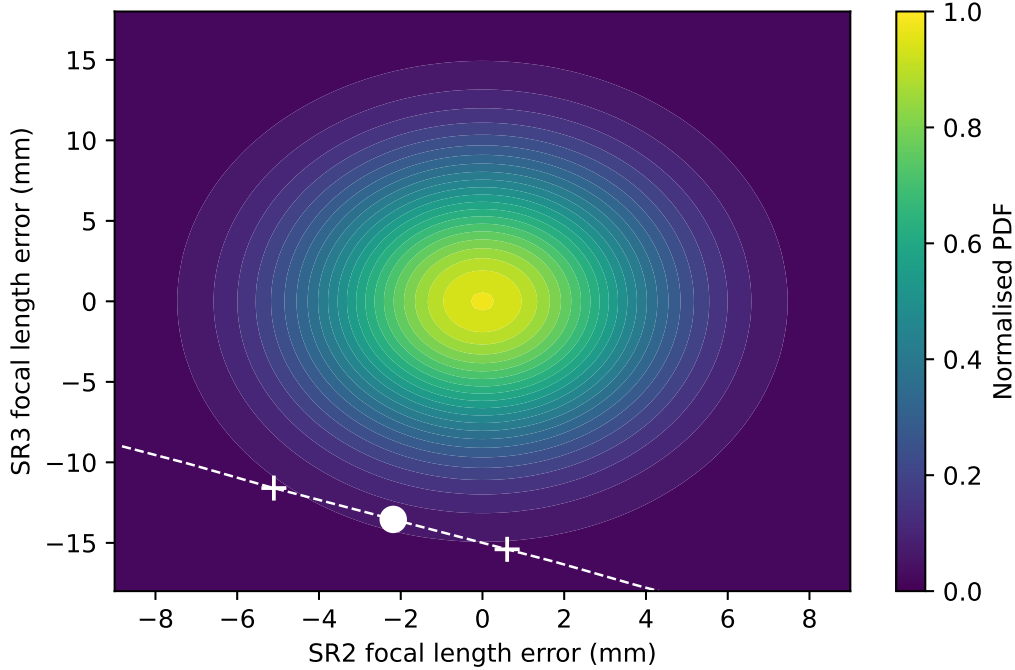


Figure 3.11: The measurement error of SR3 and SR2 follows a normal distribution. These were combined to make a 2-D normal distribution. Dark blue corresponds to the least likely combinations of SR3 and SR2, and bright yellow corresponds to the most likely. The measured Gouy phase was  $21.3^\circ$  [153]; this is indicated by the white dashed line. The white circle marks the most likely combination of SR3 and SR2 which gives  $21.3^\circ$  of Gouy phase, and the white crosses show one standard deviation from this. The white circle and crosses indicate that the focal length of SR2 is  $(-3.205 \pm 0.003)$  m and the focal length of SR3 is  $(17.971 \pm 0.002)$  m.

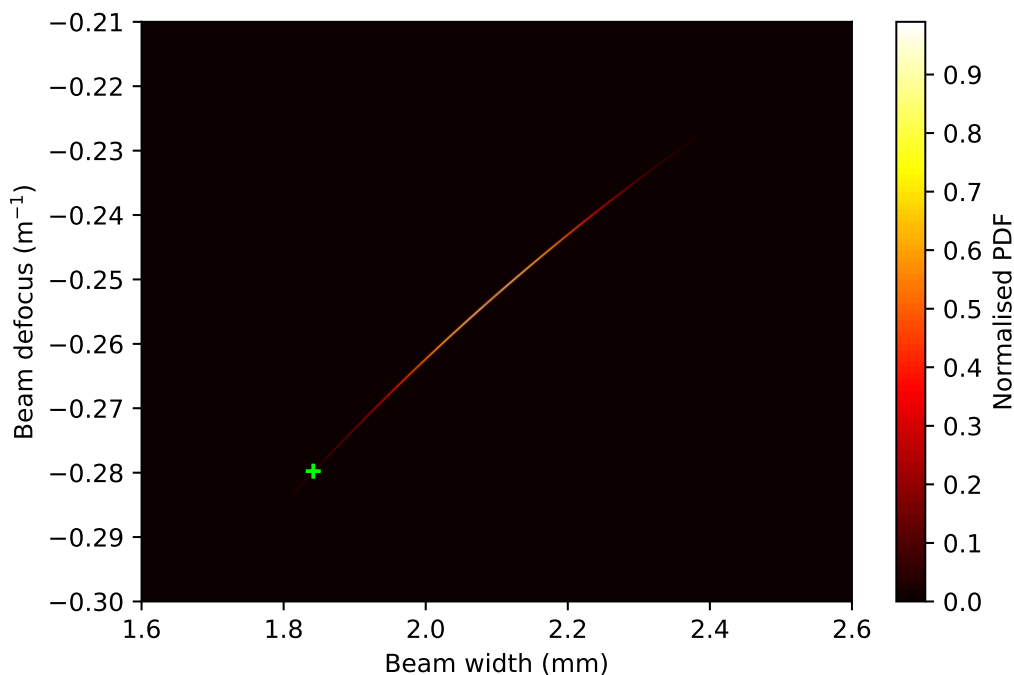


Figure 3.12: The beam parameter at the SRM was calculated for combinations of SR2 and SR3 focal lengths. The associated probability density for these combinations can be calculated (see Figure 3.11), so the probability of the beam parameter having a certain width and defocus can be calculated. The probability density for each pair of beam width and defocus is indicated with the colour bar. The mode corresponding to the measurement of  $21.3^\circ$  of Gouy phase [153] is indicated with a green cross (1.84 mm, -2.80 Dioptre). This is a simplified approach since the beam parameter cannot be such that the SRC is unstable, so certain combinations of beam width and beam defocus are not possible. Beam parameters with a width greater than  $\sim 2.25$  mm result in an unstable SRC, therefore these beams are unlikely to be present at the SRM at LLO.

### 3.5 Power Transmitted Through the Signal Recycling Mirror for a Mode Mismatch Between the Arm Cavity and the Signal Recycling Cavity

The HOM content of the beam as a function of the error in focal length in SR3 was investigated. As the arm cavities become more mismatched to the SRC, less  $\text{HG}_{00}$  mode is transmitted through the SRM. The mode mismatch can be seen in Figure 3.13. As the focal length of SR3 becomes further from its nominal value, the radius of curvature of the beam at the SRM stops matching the radius of curvature of the SRM. Since the SRC is a low finesse cavity, a significant mismatch can be tolerated before there is a large drop in the  $\text{HG}_{00}$  power transmitted. This is shown in Figure 3.13. In Figure 3.13 and Figure 3.14, it is shown that the nominal focal length of SR3, 17.985 m, is longer than optimal. When the SRC is on resonance, the peak in transmission is  $-3$  mm from the nominal focal length of SR3. This is shown by the blue and green lines in Figure 3.14.

The power of the  $\text{HG}_{00}$  light transmitted through the SRM as a function of focal length error is shown in Figure 3.14. In signal recycling mode, shown as blue and green in Figure 3.14, the transmitted power has a peak shape. This is because an error in the focal length of SR3 moves the cavity off resonance. In RSE mode, shown as red and orange in Figure 3.14, a change in focal length of SR3 does not have much effect on the amount of  $\text{HG}_{00}$  transmitted by the SRM since an anti-resonance is a much broader feature than a resonance.

### 3.5. Power Transmitted Through the Signal Recycling Mirror for a Mode Mismatch Between the Arm Cavity and the Signal Recycling Cavity

---

In a single-bounce measurement, the beam incident onto the ITM from outside the cavity is reflected straight back. This is equivalent to the reflectivity of the ITM being  $R = 1$ . When the light is resonant in the arm cavity, the ITM acts as a highly reflective mirror which applies a frequency-dependent phase shift to the light. Thus, there is no difference between a single-bounce measurement and a measurement with arm cavities at frequencies within the linewidth of the cavity. This is shown in Figure 3.13. HOM beams generated by errors in the SRC are not suppressed by the arm cavities as they are reflected by the ITM.

The ratio of the light in the  $HG_{00}$  mode versus the total light depends on the detuning of the SRM, rather than the presence of cavities in the arm. This is shown in Figure 3.13. When the light enters the arm cavities, it is reflected with an extra  $\pi$  rad phase; however, the HOMs do not enter the cavity, so they do not acquire this phase. Since the HOMs only interact with the SRC, the ratio of HOM to  $HG_{00}$  depends on the detuning of the SRM rather than whether the interferometer is in signal recycling or RSE mode. The amount of higher order mode generated in the SRC is proportional to the  $HG_{00}$  power in the SRC, so the percentage of HOM beam is dependent only on the tuning of the SRM and the focal length error of SR3.

As the SRC gets closer to being unstable, more TEM modes are required to simulate the behaviour of the cavity. The effect of using more TEM modes in the simulation is shown in Figure 3.10. For positive errors above 6 mm in the focal length of SR3, the cavity becomes unstable. It was found empirically that six TEM modes is sufficient to simulate the interferometer while it is stable. The hatched regions of Figure 3.13 and Figure 3.14 show where the simulation is not accurate.

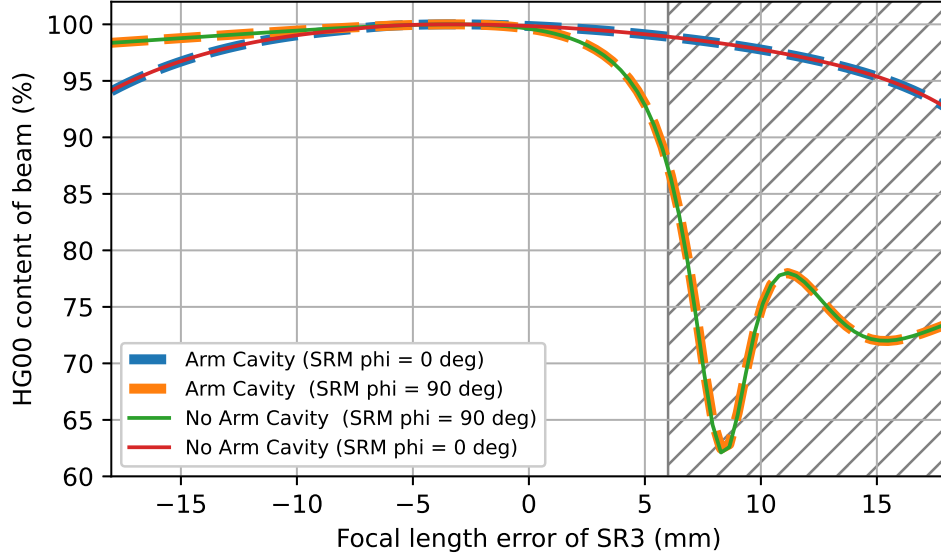


Figure 3.13: The percentage of light which is in the  $HG_{00}$  mode as the focal length of SR3 changes compared to the total light power does not depend on whether there are arm cavities. It is determined by the detuning of the SRM. The blue dashed line shows the behaviour of the beam with arm cavities present and with the SRC in signal recycling mode (SRM  $\phi = 0^\circ$ ). The red line shows how the beam changes with focal length error for a single-bounce measurement and with the SRC in RSE mode (SRM  $\phi = 90^\circ$ ). The orange dashed line corresponds to the interferometer having arm cavities and being in RSE mode (SRM  $\phi = 90^\circ$ ). The green line shows the behaviour of the beam when the interferometer is configured for a single-bounce measurement and is in signal recycling mode. The hatched region indicates where the SRC becomes unstable (see Figure 3.10), so the behaviour of the interferometer cannot be accurately simulated for these focal lengths.

### 3.5. Power Transmitted Through the Signal Recycling Mirror for a Mode Mismatch Between the Arm Cavity and the Signal Recycling Cavity

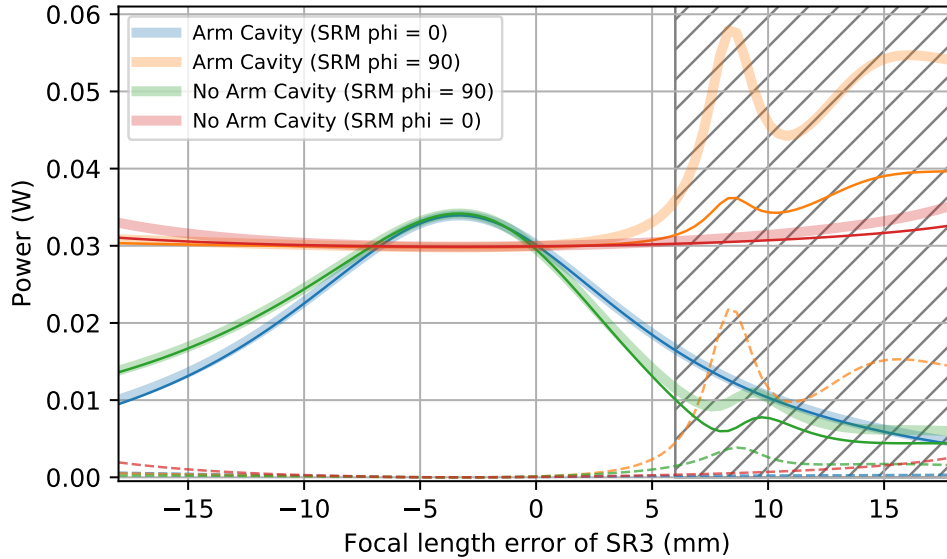


Figure 3.14: The total power transmitted through the SRM for each simulation is shown by the thick pale lines. The thin solid lines correspond to the power in the  $HG_{00}$  mode, and the thin dashed lines correspond to the power in the higher order modes. Blue lines show the behaviour when the interferometer has arm cavities and is in signal recycling mode, and the orange lines shows when it is in RSE mode. Green lines show how the power changes when the interferometer is configured for a single-bounce measurement and is in signal recycling mode, and the red line shows when its in RSE mode. The hatched region indicates where the SRC becomes unstable, and so the behaviour of the interferometer cannot be accurately simulated for these focal lengths.

### 3.5.1 Change of Finesse of the Signal Recycling Cavity

As the transmission of the SRM decreases, the finesse of the cavity increases. A FINESSE simulation was run to see the effect of increasing the power transmission of the SRM. The  $HG_{00}$  mode power decreases with lower SRM transmission slower than the power transmitted in the  $HG_{20+02}$  mode. This is shown in Figure 3.15.

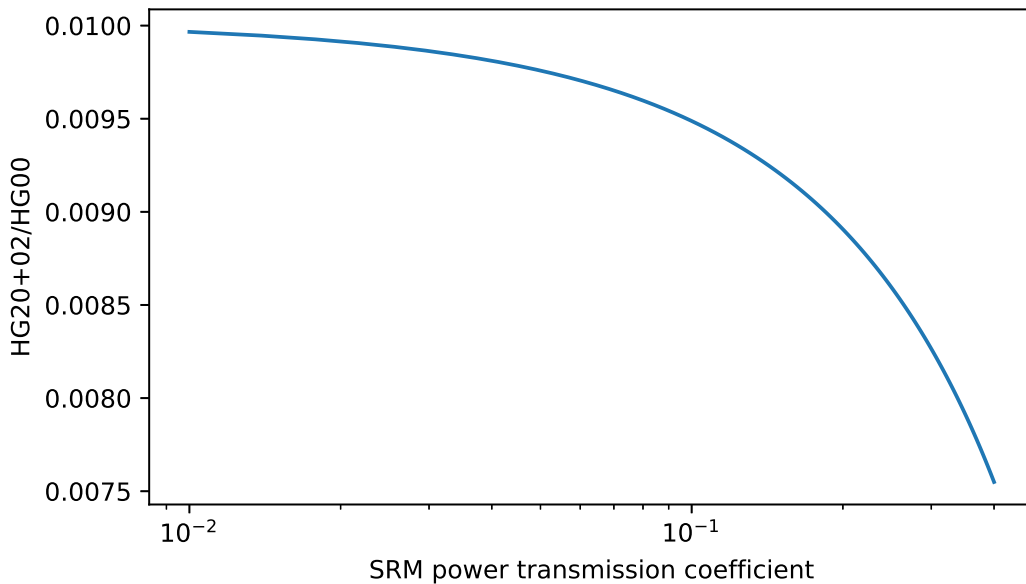


Figure 3.15: Ratio of  $HG_{20+02}$  to  $HG_{00}$  as the transmission of the SRM is increased for a mode mismatch between the arm cavities and the SRC. The interferometer is in RSE mode. A mode mismatch was introduced by setting the focal length of SR3 to be 12 mm shorter than the default amount.

## 3.6 Conclusion

The mode mismatch between the arm cavities and the SRC results in a loss mechanism whereby light is scattered from the  $\text{HG}_{00}$  mode into higher order modes. Loss in interferometers usually reduces the SNR by  $\sqrt{\text{Power}}$ , however since there are multiple points between the squeezer and the OMC where mode mismatches can happen, coherent destructive modal interference will cause the losses to have up to four times the effect they would have if it were a normal type of loss. There exists a collection of measurements which shows the arms are matched between 90% and 100% to the OMC.

FINESSE simulations were used to model mode mismatches between the arm and the SRC caused by RoC errors in SR3 and SR2. The simulation used as-built parameters for the SRC at the LLO site and design specification arm cavities. This allowed us to study the effect of non-ideal mode matching in a close to real life situation. The interferometer was modelled in signal recycling mode and RSE mode for locked-arm-cavities and single-bounce configurations.

It was found that the dependence of the ratio of  $\text{HG}_{00}$  light to the total light depends mainly on the focal length of SR3 and is not affected by the presence of arm cavities. This is because the arm cavities are well matched to the input laser. When the arm cavities are on resonance, the ITMs act as highly reflective mirrors with frequency dependent behaviour. This means if the interferometer's thermal state remains the same, there is no difference in HOM content of the beam

transmitted through the SRM between a single-bounce measurement and an arm-cavity measurement.

The ratio of HOM to  $HG_{00}$  for the beam emerging from the SRM depends on the detuning of the SRM, although it does not depend on whether the interferometer is in signal recycling mode or RSE mode. As HOMs do not enter the arm cavities, they cannot distinguish between the signal recycling and RSE modes of operation. When the SRC is on resonance, it is much more sensitive to an error in SR3's focal length than when the SRC is anti-resonant. The light is less sensitive to an error in the focal length of SR2.

The uncertainty in the beam parameter of the arm mode at the SRM and the eigenmode of the SRC is driven by the uncertainty in SR3. This is shown in Figure 3.6 and Figure 3.7. The single pass Gouy phase of the SRC for different combinations of SR3 and SR2 was simulated; this is shown in Figure 3.8. The Gouy phase acquired in a single pass of the SRC was measured to be  $(21.3 \pm 0.3)^\circ$ , so it can be inferred that the focal length of SR2 is  $(-3.205 \pm 0.003)$  m and the focal length of SR3 is  $(17.971 \pm 0.002)$  m. This is shown in Figure 3.11. These values of focal length would result in the arm mode having a width of 1.8 mm and a defocus of  $-0.28 \text{ m}^{-1}$  immediately after it is transmitted through the SRM, and there would be a few percent HOM in OMC scans (see Figure 3.12).

Future work could involve using a heater to change the focal length of SR3 and measuring the effect this has on the Gouy phase accumulated in the SRC. This measurement could be used to validate the model of the geometric properties of

the SRC. As the lengths between all the optics is well known, and the focal length of the ITMs is well known, the squeezer beam could be used to gain information about the RoCs of SR3 and SR2. This would be done by setting up a single-bounce measurement. Having greater confidence in the beam parameter of the arm mode at the SRM would be of great benefit for the design of future upgrades, such as balanced homodyne detection (see Chapter 4 and Chapter 5), to the LIGO detectors.



## Chapter 4

# Balanced Homodyne Detection for LIGO A+

A major change between the aLIGO and LIGO A+ detectors will be the replacement of DC readout (see Section 4.1.1) with BHD. The motivations for implementing BHD into the LIGO detectors are described in Section 4.1; the key reason is: that if the detectors are to reach their design sensitivity, they require BHD. In contrast to DC readout, the LO and signal do not follow the same optical path in a BHD scheme; the consequence of this is the phase of the LO beam needs to be stable. The stability requirement of the LO's phase is discussed in Section 4.2. Figure 4.2 is a sketch of the LO's beam path. The proposed BHD layout is discussed in Chapter 5.

## 4.1 The Principles of and Motivations for Balanced Homodyne Detection

BHD is a method of measuring the information encoded in any quadrature of a signal beam (see e.g. [47, Section 2]); thus, BHD forms a key part of many quantum optics experiments (e.g. [69, 70, 158]). In a BHD readout scheme, the signal beam is set up to interfere with a LO beam with the same optical frequency on a beam splitter, and the interference is measured with photodiodes at the beam splitter's output ports. A sketch of a BHD readout is shown in Figure 4.1.

The LO beam has a larger power than the signal beam, and the power of the LO is chosen to bring the quantum noise above the noise floor of the photodiode and its preamplifier. An arbitrary quadrature of the signal beam can be measured by correctly setting the relative phase between the LO and signal beams. This phase is known as the *homodyne angle*. If the two photocurrents are balanced, subtracting them results in a measurement which is proportional to the selected quadrature of the signal beam. Additionally, the subtraction results in the removal of the classical intensity noise of the LO from the measurement. BHD is mathematically described in Section 4.1.2.

The LIGO A+ detectors need to use frequency-dependent squeezing to reach their design sensitivities. To do this, the homodyne angle must be  $90^\circ$ . There is a low amount of tolerance on the homodyne angle,  $(90 \pm 1)^\circ$ , before the quantum noise is significantly degraded [159], and the current readout method (see Section 4.1.1)

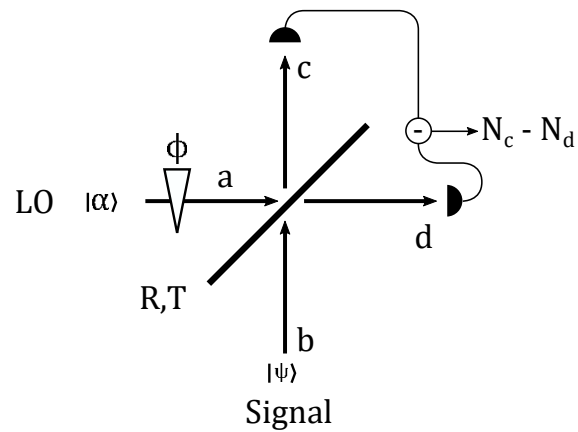


Figure 4.1: A coherent state  $|\alpha\rangle$ , enters port  $a$  of a beam splitter. A signal  $|\Psi\rangle$  enters port  $b$ . These two beams interfere, resulting in photons being detected at the  $c$  and  $d$  ports. The two photocurrents are subtracted, and the signal that is produced is proportional to an arbitrary quadrature of the state  $|\Psi\rangle$ ; the difference in the signals at the  $c$  and  $d$  ports is given by Equation (4.7). The quadrature of the state  $|\Psi\rangle$  that is observed depends on the homodyne angle,  $\phi$ .

does not offer sufficient control over the homodyne angle. For aLIGO, the homodyne angle is around  $10^\circ$  away from the phase quadrature [160]. Currently, the squeezing angle is set to be at the same angle as the readout quadrature [67]; the preference would be to set the readout quadrature to the squeezing angle, as then there would be more control over the quantum noise of the detector i.e. you wouldn't be forced to use a squeezing angle that was bad for radiation pressure effects, for example. The effect that controlling the squeezing angle has on the quantum noise floor has been demonstrated at LLO [70]. However, [70] used a diagnostic BHD setup which was too noisy to allow gravitational wave detections.

#### 4.1.1 Alternatives to Balanced Homodyne Detection

The current detection scheme is known as DC readout [40]; this is a form of homodyne detection. A differential offset in the arm lengths produces the LO in DC readout; the size of the LO can be set with the differential offset in the length of the arms, and the homodyne angle can be set with the differential arm power [161]. DC readout has some key positive outcomes, such as there being no phase noise between the LO and the signal, and the LO and signal being perfectly aligned and mode matched to each other. However, while theoretically the homodyne angle can be set, due to different amounts of loss in each arm, the homodyne angle is not a free parameter. The inability to tune the homodyne angle increased the detector's quantum noise <sup>1</sup>.

---

<sup>1</sup>This increase was buried under the classical noise floor; however, this noise was in a frequency band where the LIGO detectors are designed to be quantum noise limited.

The first generation of detectors used heterodyne readout (e.g. [162]). Heterodyne readout involves a modulation-demodulation scheme whereby the signal is beat with a RF LO to a frequency where technical noise is no longer a concern. It is then demodulated at the same modulation frequency to recover the original signal. This method comes with the draw back that the shot noise is enhanced by the modulation-demodulation process [163]. Heterodyne detection is described in more detail in the final paragraph of Section 6.1.

### 4.1.2 Quantum Mechanical Description of Balanced Homodyne Detection

To understand how BHD can be used to detect quantum states of light, it is useful to mathematically express light and interference in terms of quantum mechanics. From the two-photon formalism of light (see Section 1.5), the general quadrature operator,  $\hat{\mathbf{X}}_\phi$  can be obtained,

$$\hat{\mathbf{X}}_\phi = \hat{\mathbf{X}} \cos \phi + \hat{\mathbf{Y}} \sin \phi, \quad (4.1)$$

where  $\phi$  is the homodyne angle. By setting the homodyne angle, one can sense an arbitrary combination of the phase and amplitude of a light field.

Consider the interference of a LO field,  $\hat{a}$ , and a signal field,  $\hat{b}$ , on a 50:50 beam splitter. The resulting fields,  $\hat{c}$  and  $\hat{d}$ , are detected on two photodiodes. This is

shown in Figure 4.1. The photocurrents are proportional to

$$\begin{aligned}\hat{\mathbf{N}}_c &= \hat{c}^\dagger \hat{c} = \left( \sqrt{R} \hat{a}^\dagger + \sqrt{T} \hat{b}^\dagger \right) \left( \sqrt{R} \hat{a} + \sqrt{T} \hat{b} \right), \\ &= R \hat{a}^\dagger \hat{a} + T \hat{b}^\dagger \hat{b} + \sqrt{RT} (\hat{a}^\dagger \hat{b} + \hat{b}^\dagger \hat{a}),\end{aligned}\quad (4.2)$$

$$\hat{\mathbf{N}}_d = \hat{d}^\dagger \hat{d} = T \hat{a}^\dagger \hat{a} + R \hat{b}^\dagger \hat{b} - \sqrt{RT} (\hat{a}^\dagger \hat{b} + \hat{b}^\dagger \hat{a}).\quad (4.3)$$

As the beam splitter is 50:50,  $R = T = 1/2$ . This results in the difference in the photocurrents being proportional to

$$\hat{\mathbf{N}}_c - \hat{\mathbf{N}}_d = \hat{a}^\dagger \hat{b} + \hat{b}^\dagger \hat{a}.\quad (4.4)$$

The operators  $\hat{a}$  and  $\hat{b}$  can be written as  $\hat{a} = \alpha + a$  and  $\hat{b} = \beta + b$  to separate quantum behaviours (denoted with  $a$  and  $b$ ) and classical behaviours (denoted with  $\alpha$  and  $\beta$ ) [164]. Furthermore, the phase between the signal field and the LO field can be expressed in terms of the homodyne angle with  $\hat{b} \rightarrow \hat{b} \exp(i\phi)$ . If the higher order term containing  $ab$  is neglected, Equation (4.4) can be written as

$$\hat{\mathbf{N}}_c - \hat{\mathbf{N}}_d = 2\alpha\beta \cos \phi + 2\alpha \mathbf{X}_{-\phi}^b + 2\beta \mathbf{X}_\phi^a.\quad (4.5)$$

The variance,  $\sqrt{V(X)} = \Delta X$ , of this measurement would then be

$$V(\hat{\mathbf{N}}_c - \hat{\mathbf{N}}_d) = 4\alpha^2 V(\mathbf{X}_{-\phi}^b) + 4\beta^2 V(\mathbf{X}_\phi^a).\quad (4.6)$$

If the LO is much stronger than the signal field,  $\alpha \gg \beta$ , then the measurement is

$$\hat{\mathbf{N}}_c - \hat{\mathbf{N}}_d = 2\alpha\beta \cos \phi + 2\alpha \mathbf{X}_{-\phi}^b.\quad (4.7)$$

This shows that the difference between the two photocurrents will result in the quadrature of the  $b$  field that is set by the homodyne angle to be measured. The noise of this measurement will be strongly dependent on the power of the  $a$  field if it is much larger than the  $b$  field.

### 4.1.3 Other Motivations for Implementing Balanced Homodyne Detection in LIGO A+

Different gravitational wave sources carry their information in different frequency bands, and the detector may be optimised to reflect this [59, 79, 165, 166]. For instance, BNS signals continue to higher frequencies than BBH signals, so it may be of interest to optimise the detector around higher frequencies to improve our understanding of the properties of BNS systems. To optimise the sensitivity of the interferometer to different sources, the detector's noise would need shaping. To do this, BHD can be used alongside other upgrades (e.g [27, 59]).

More advanced upgrades, e.g. converting the detectors to speedmeters (see Chapter 1.6 or [59]), could alter the detector's quantum noise substantially; this would also rely on the implementation of BHD. These changes to the interferometer are non-trivial and would require significant redesign of many parts of the layout, so the implementation of BHD for A+ does not necessarily correspond to a suitable BHD system for one of these more advanced interferometer configurations. However, BHD for A+ would provide experience with implementing BHD on a large-scale interferometer, which would help when considering how to realise these more novel

interferometer configurations.

BHD has some benefits over DC readout relating to the reduction of the DC light emerging from the AS port [161]. With a lower amount of DC light at the AS port, the coupling between the SRC length and the gravitational wave signal will be reduced<sup>2</sup>. Additionally, there will be less scattering from the septum window between HAM5 and HAM6<sup>3</sup>.

## 4.2 The Local Oscillator Path

Phase noise arises due to phase fluctuations in the LO beam being indistinguishable from phase fluctuations in the signal beam. A gravitational wave produces a phase modulated signal in the signal beam, and the LO field phase is modulated by the motion of the mirrors in the LO path. When these beams are combined, it is the phase difference between the two fields that produces a signal, so the phase noise of the LO path must be low enough for the signal generated by the interference of the LO and signal beams to be due to the phase modulation of the signal beam.

The layout for the optics which combine the LO and signal beam is shown in Figure 4.2. The LO will be picked off from the power recycling cavity and guided by

---

<sup>2</sup>The dominant coupling due to the power entering the SRC can be intuitively understood by considering a Fabry-Perot cavity with a slight tuning offset. A DC offset in the cavity's will give rise to a linear coupling between the cavity's length and the power transmitted by the cavity which scales with the size of the DC offset. The second route by which SRC length noise may couple to the signal is via optical springs between the SRC and arm cavities [167].

<sup>3</sup>Strictly speaking, the scattering from the septum window is not a property of DC readout as the window could be removed. However, this window is crucial for the maintenance of the interferometer.

one steering mirror, BHDM1, to the BHD combining beam splitter, BHDBS2. The signal beam will exit the OFI and be steered by one mirror, OM0, onto BHDBS2. OM0 and BHDM1 will be used to align the beams so they overlap on BHDBS2. The angle of BHDBS2 will be used to make the LO and signal beams overlap in the far field. Two lenses are used for mode matching the LO beam to the signal beam.

To acquire a LO with low frequency and intensity noise, the LO will be picked off from a point within the interferometer. The two ways of obtaining a LO beam considered were a beam picked off from the main beam splitter's AR coating (BSAR) or the beam transmitted through PR2 (POP) [168]. The determining factor in choice of pick-off point was the effect of backscatter on the interferometer's strain sensitivity. The POP port was chosen as it is far superior to the BSAR choice at all frequencies and scatter phases. This is because backscattered light from the BSAR enters only one arm, thus making it a differential effect. Any backscatter that enters the POP port is common-mode, and therefore the differential arm signal is far less sensitive to this source of backscatter.

### 4.2.1 The Local Oscillator Path Length Stability Requirement

The first step is to express the A+ sensitivity curve in units of  $\text{rad}/\sqrt{\text{Hz}}$ . This requires the A+ sensitivity curve to be deconvolved with the linear response function of the interferometer. The signal generated by the differential motion of the ETMs is low-passed by the coupled SRC-arm cavity, so the linear response function can be

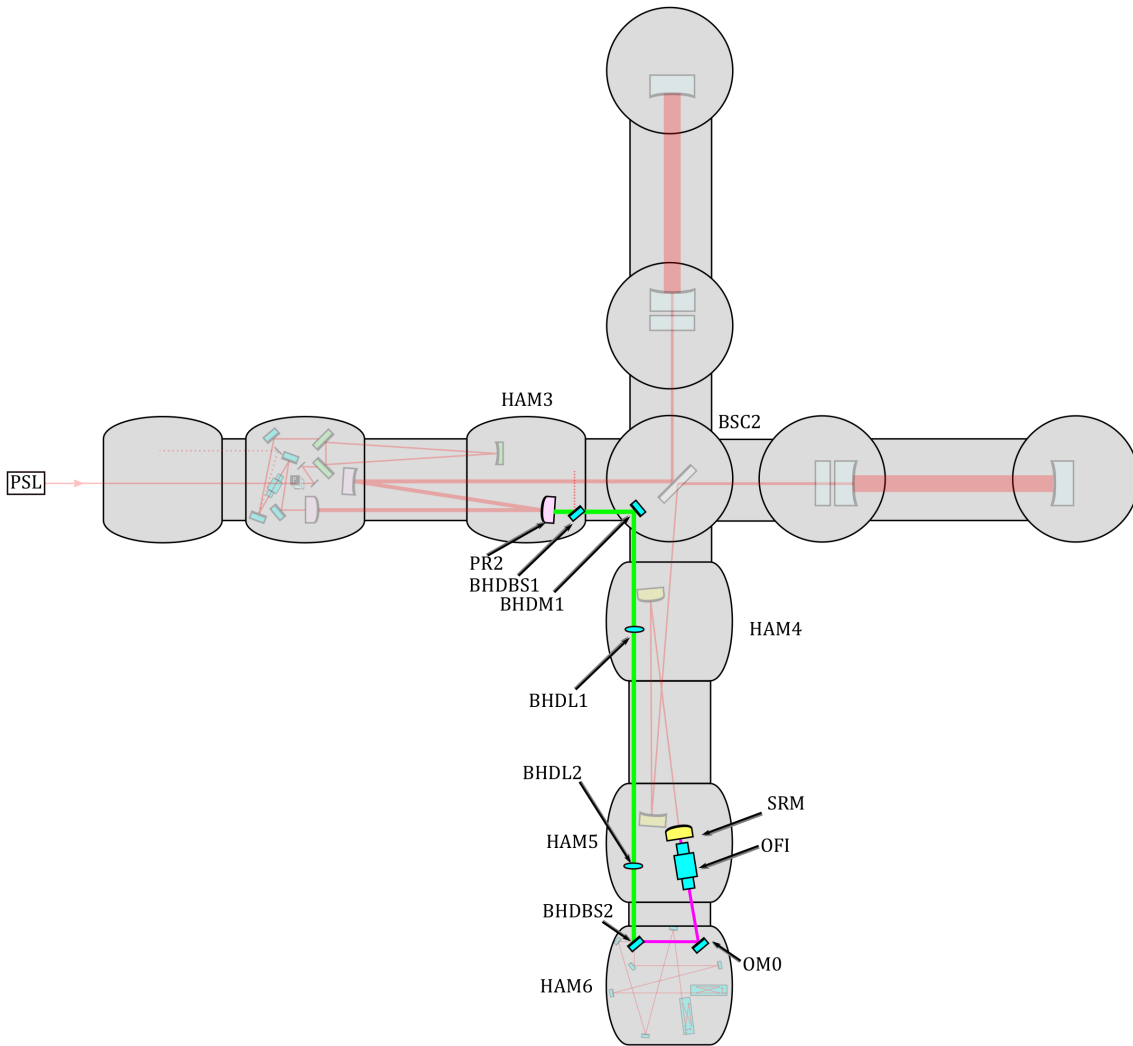


Figure 4.2: Sketch of the LO (green) and signal (pink) beam paths in relation to other parts of the interferometer (see Figure 1.4 and Section 1.9). The LO beam emerges from PR2. Some of this light is used to control the interferometer, so BHDBS1 is needed to split the light. BHD1 directs the LO onto BHDBS2. The signal beam emerges from the SRM. It passes through the OFI and is reflected by OM0. The signal combines with the LO on BHDBS2. The layout of the optics in HAM6 is shown in Figure 5.1.

written as

$$H(f) = \frac{H_0}{1 - if/f_c}, \quad (4.8)$$

where  $H_0$  is a gain factor,  $f$  is the frequency and  $f_c$  is the corner frequency of the SRC-arm cavity. For the LIGO detectors,  $f_c = 380$  Hz [167]. This linear response function does not include optical spring effects, but these are small and not important for this calculation.

$H_0$  can be calculated by dividing the phase noise of the signal beam,  $\Delta\phi_{\text{sig}}$ , by the product of the A+ sensitivity curve (see Figure 1.3) and  $1/(1 - if/f_c)$  at a frequency where the detector will be shot noise limited. Care needs to be taken to avoid double counting the squeezing; the signal beam will be squeezed in the phase quadrature, but as the A+ sensitivity curve includes squeezing, the squeezing factor can be omitted from the phase noise associated with the signal beam in this calculation.

From Equation (1.10), the relationship between the phase of the signal beam  $\phi_{\text{sig}}$  and its power  $P_{\text{sig}}$  can be written as

$$\Delta\phi_{\text{sig}} = \sqrt{\frac{h\nu}{4P_{\text{sig}}}} \quad (4.9)$$

where  $h$  is Planck's constant and  $\nu$  is the frequency of the light. For A+,  $P_{\text{sig}} = 5$  mW. The linear response function is shown in Figure 4.3. To express the A+ sensitivity curve in units of  $\text{rad}/\sqrt{\text{Hz}}$ , the sensitivity curve should be divided by the linear response function shown in Figure 4.3.

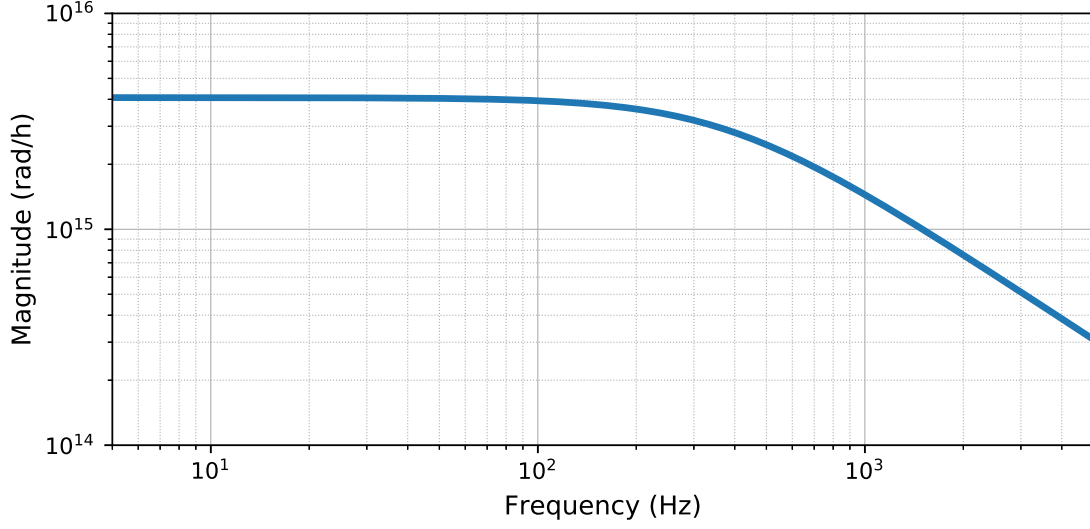


Figure 4.3: The linear response function between strain and signal, expressed in units of radians/gravitational wave strain, at the AS port. The corner frequency at  $\approx 380$  Hz comes from the pole of the coupled SRC-arm cavity.

The next step is to use the equations for interference at a beam splitter to convert a change in phase between the LO and signal beam into a change in power of the combined beams that exit the beam splitter. When the LO and signal beams interfere at BHSBS2, the exiting beams have power  $P_c$  and  $P_d$ . These are given by

$$P_c = \left| \frac{1}{\sqrt{2}} E_{\text{sig}} e^{i\omega t} + \frac{1}{\sqrt{2}} E_{\text{LO}} e^{i\omega t + \phi} \right|^2 = \frac{|E_{\text{sig}}|^2}{2} + \frac{|E_{\text{LO}}|^2}{2} + |E_{\text{sig}} E_{\text{LO}}^\dagger| \cos(\phi) \quad (4.10)$$

and

$$P_d = \left| \frac{1}{\sqrt{2}} E_{\text{sig}} e^{i\omega t} - \frac{1}{\sqrt{2}} E_{\text{LO}} e^{i\omega t + \phi} \right|^2 = \frac{|E_{\text{sig}}|^2}{2} + \frac{|E_{\text{LO}}|^2}{2} - |E_{\text{sig}} E_{\text{LO}}^\dagger| \cos(\phi), \quad (4.11)$$

where  $E_{\text{sig}}$  and  $E_{\text{LO}}$  are the complex field amplitudes of the signal and LO beams

expressed in units such that  $E^*E$  gives the power of the beam;  $\omega$  is the laser frequency;  $t$  is time and  $\phi$  is the homodyne angle. The power of the LO beam will be  $P_{\text{LO}} = 100 \text{ mW}$ . Note, the signal carrying light will be detected on four photodiodes (two at the output of each OMC), and this power is compatible with the discussion of a photodiode's requirements in Section 6.1.

The difference in  $P_c$  and  $P_d$  signals gives the BHD signal,

$$P = 2|E_{\text{sig}}E_{\text{LO}}^\dagger| \cos(\phi). \quad (4.12)$$

Differentiating with respect to  $\phi$  gives the relationship between a change in power of the interfered beams and a change in phase between the LO and signal beams,

$$dP = -2|E_{\text{sig}}E_{\text{LO}}^\dagger| \sin(\phi)d\phi. \quad (4.13)$$

Since the homodyne angle is  $90^\circ$ , this becomes

$$dP = -2|E_{\text{sig}}E_{\text{LO}}^\dagger|d\phi. \quad (4.14)$$

Using Equation (4.14), the phase noise requirement for the local oscillator can be expressed in units of  $\text{rad}/\sqrt{\text{Hz}}$ . This is shown in Figure 4.4. This requirement was also derived in [168, 169] and [170]; however, these calculations all differ from each other by factors of  $\sim 1$ . This can be explained by differences in the assumed power of the local oscillator.

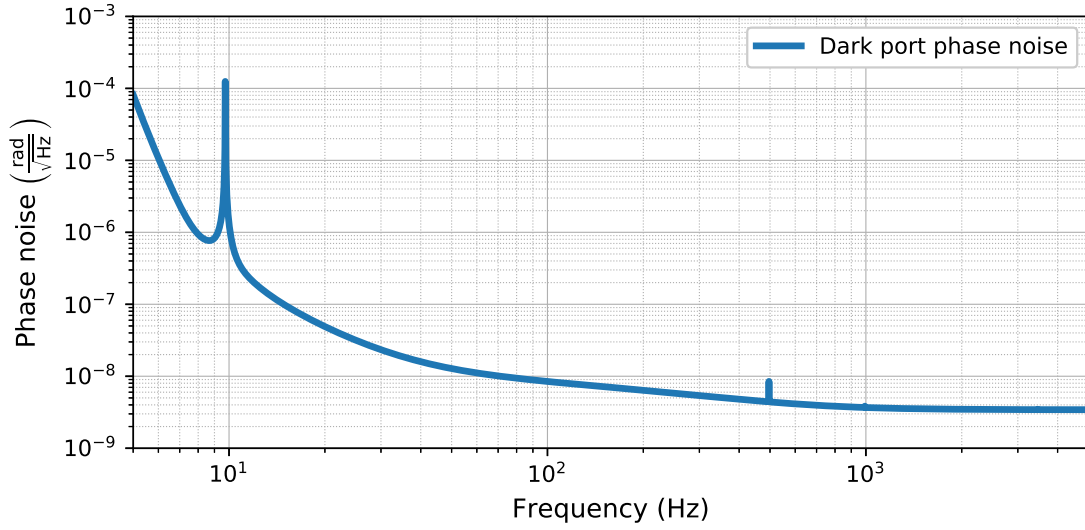


Figure 4.4: The sensitivity curve for the A+ detectors expressed in units of  $\text{rad}/\sqrt{\text{Hz}}$ . At frequencies above 1 kHz, the noise is flat ( $3.4 \times 10^{-5} \text{ rad}/\sqrt{\text{Hz}}$ ) as it is dominated by shot noise. At lower frequencies, the noise is increased relative to shot noise due to radiation pressure, coating thermal noise and other noise sources. At 5 Hz, the noise is  $8 \times 10^{-5} \text{ rad}/\sqrt{\text{Hz}}$ .

To express phase in terms of optical path length, the phase should to be multiplied by  $\lambda_{\text{EM}}/(2\pi)$ . The relationship between the optical path length noise,  $n_p$ , and the motion requirement for the optics,  $n_o$ , assumes that there will be two mirrors at  $45^\circ$  which are used to steer the AS and LO beams. As the optics reflect at  $45^\circ$ , the path length change due to the optic's motion is multiplied by  $\sqrt{2}$ .

The beams are combined on a beam splitter, and the motion of this beam splitter needs to be counted twice. Figure 4.6 illustrates this. The relationship between

optical path length,  $n_p$ , and the motion of each optic,  $n_o$ , is

$$n_p = 10 \times \sqrt{(\sqrt{2}n_o)^2 + (\sqrt{2}n_o)^2 + 2 \times (\sqrt{2}n_o)^2}. \quad (4.15)$$

Since there are many uncorrelated sources of noise in the LIGO detectors, a factor of 10 is used as a safety margin.

Multiplying the phase noise shown in Figure 4.4 by  $\lambda_{\text{EM}}/(2\pi \times 10\sqrt{8})$  gives the upper limit tolerable for the longitudinal motion of the optics. This is shown in Figure 4.5. To determine the amount of isolation required, the typical motion of the optical table needs to be compared to the motion requirement for the optics; see references [171, 172] for details on this. This led to triple suspensions, known as HAM relay triple suspensions, being used to passively isolate the optics in the local oscillator and signal beam paths.

## 4.3 Conclusion

One of the major changes to the LIGO detectors for A+ will be the implementation of BHD. BHD is needed for the LIGO detectors to meet their sensitivity target as frequency dependent squeezing requires the homodyne angle to be a free parameter.

A sketch of how the signal and LO will be combined is shown in Figure 4.2. We derived the relative path length stability requirement for the LO and signal beams, and the requirement is shown in Figure 4.5. The local oscillator's phase

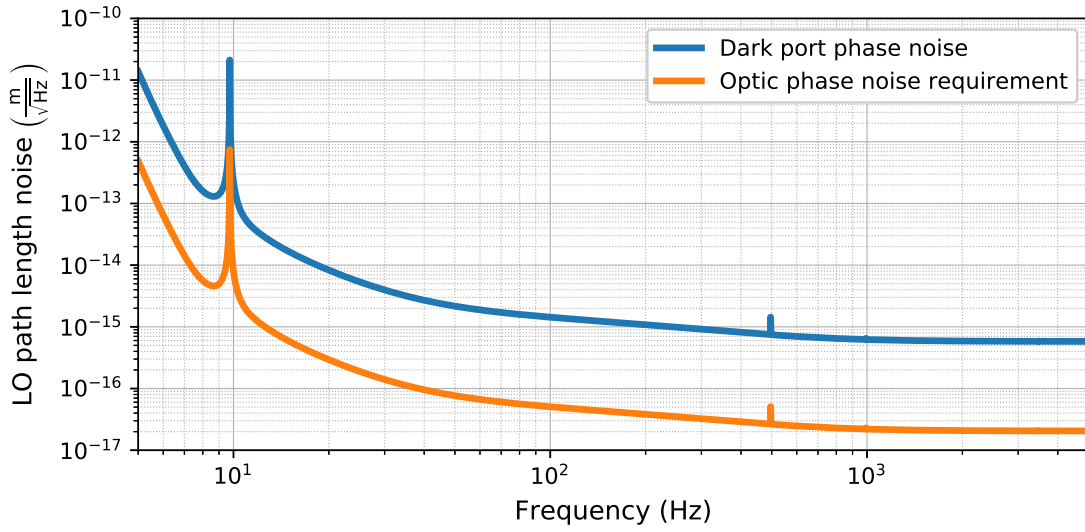


Figure 4.5: The sensitivity curve for A+ sets the limit on the amount of path length noise that is acceptable between the AS and LO beams. The blue line shows the sensitivity curve in units of path length noise between the AS and LO beams, and the orange line shows the longitudinal motion requirement for the optics which combine the LO and signal beam. At 5 Hz, the longitudinal motion requirement for the optics is  $4.9 \times 10^{-13} \text{ m}/\sqrt{\text{Hz}}$ .

noise requirement led to HAM relay triple suspensions being chosen to steer the LO and signal beams onto the combining beam splitter.

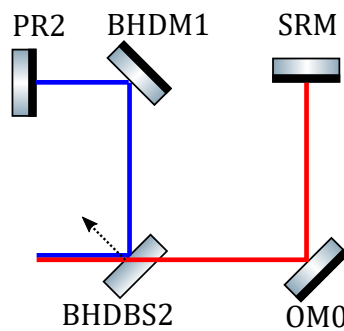


Figure 4.6: A sketch of the LO and signal beam paths. The LO beam path is shown in blue, and the signal beam is shown in red. The dashed arrow indicates the direction that the recombining beam splitter, BHDBS2, may move in. If BHDBS2 moves in this way, the phase of the signal beam has increased while the phase of the LO beam has decreased at the point where the signal and LO beams combine. This means that the recombination beam splitter motion needs to be counted twice in calculations of the phase noise requirement.



# Chapter 5

## Analysis of the Active Wavefront Control for the Balanced Homodyne Detector for LIGO A+

Fundamentally, the optical layout in HAM6 must combine the signal beam and the LO beam and sense the combined beams to form a BHD. The location of HAM6 with respect to the rest of the interferometer is shown in Figure 1.4. As loss, such as that caused by mode mismatch, in the interferometer's readout will degrade its sensitivity, and as there is uncertainty in the interferometer's beam parameter, it is vital that the AWC can correct for possible mode mismatches between the interferometer and the OMCs so that loss due to mode mismatch is minimal.

In this chapter, the effectiveness of the AWC is analysed. Figure 5.7 shows the range of modes at the SRM which can be corrected for such that the target for loss due to mode mismatch for A+ can be met. Other aspects of this layout and its requirements outside the scope of this thesis can be found in [173, 174].

## 5.1 The Optics for Mode Matching the Interferometer and the Output Mode Cleaners

The design of the optical layout within HAM6 that is being taken forward<sup>1</sup> is shown in Figure 5.1. The properties of this layout are summarised in Table 5.1. The two beam paths after the beam splitter upon which the signal and LO beams are combined (BHDBS2) are called A and B. The mirrors OMA1, OMB1, OMA2 and OMB2 will be referred to as OMx1 and OMx2 as it is not important to make a distinction between the A and B paths when considering mode matching. The A/B paths are terminated by OMCA/B.

The AWC in HAM6 has two functions: it will be used to correct for errors in the interferometer's beam parameter at the SRM, e.g. due to thermal effects or errors in the RoC of the optics in the SRC, and to correct for geometry errors within HAM6 such that the mode matching between the arm mode and the OMC is maximised [174]. As mentioned in Section 3.1.2, the loss in sensitivity from mode mismatch can be four times greater than a simpler source of loss (e.g. photodiode

---

<sup>1</sup>As of January 2021, millimetre scale changes have been made which do not affect the analysis in this chapter.

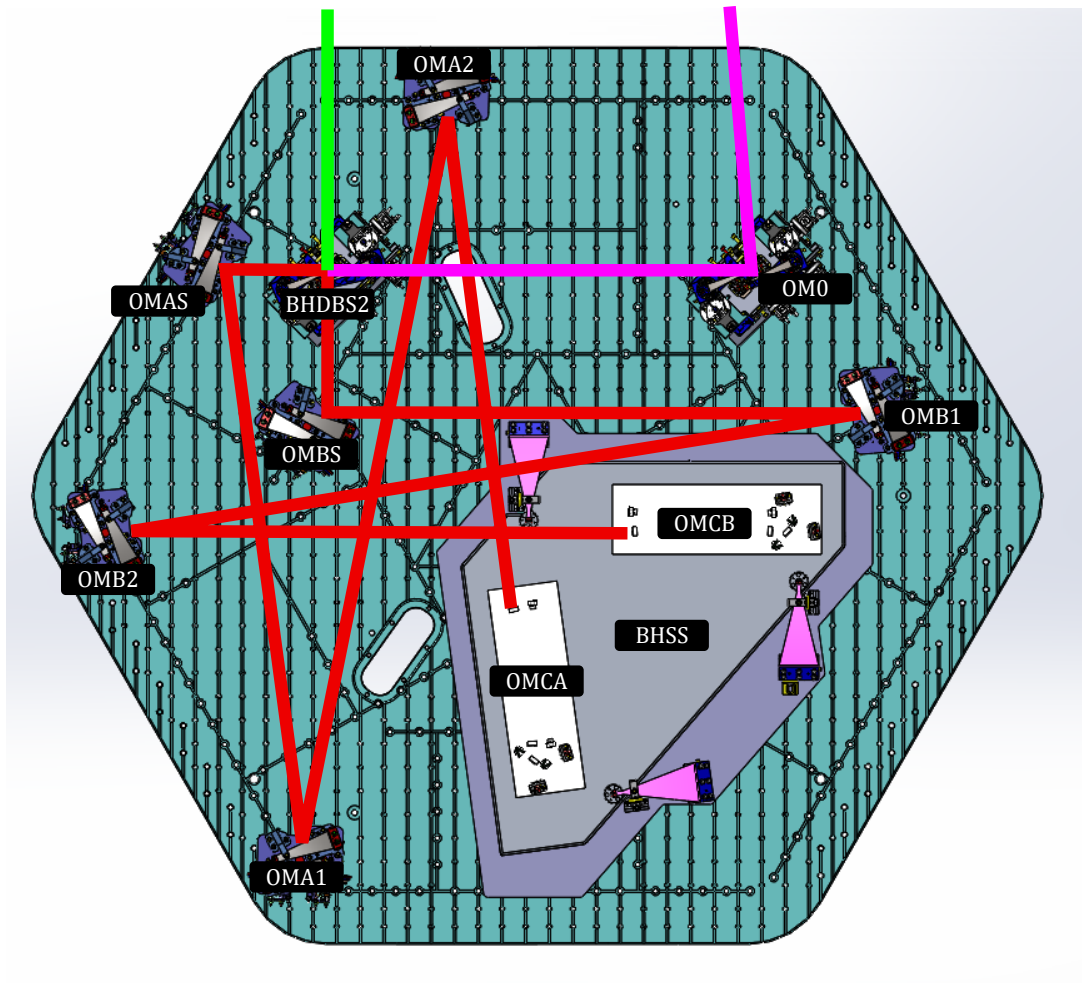


Figure 5.1: The LO beam enters HAM6 directly above BHDBS2 (north side), and it is highlighted in green. The signal beam enters HAM6 directly above OM0 (north side), and it is highlighted in pink. The signal beam is steered by OM0 onto BHDBS2 where it is combined with the LO. The two combined beams are shown in red. These are incident upon a mirror used for steering (OMxS), and then upon two curved mirrors (OMx1 and OMx2). The beams enter the OMCs, which are seismically isolated by the BHSS (the large triangular component). The spacings for these components are given in Table 5.1.

quantum efficiency) due to coherent destructive modal interference [143]. Active mirrors, called *suspended active matching stages* (SAMS), will be used to correct for mode mismatch; they will provide a range of at least  $\pm 50$  mD of optical power [175].

The optical layout in HAM6 must mode match the nominal SRM and OMC modes. The OMC waist size is  $485 \mu\text{m}$  [57]. As discussed in Chapter 3, the beam parameter at the SRM is expected to differ from its nominal value of  $q_{\text{SRM}} = (-3.55 + 1.09i) \text{ m}$  [176]. It is described in Chapter 3 how geometry errors in the SRC cause the arm cavity and the SRC to be mismatched. From this, a set of modes which may be present at the SRM was calculated. The design of the layout within HAM6 is based on the nominal beam parameters, and the set of modes shown in Figure 3.12 was taken into consideration when analysing the pros and cons of different candidate layouts since they may have been more or less robust to beam parameter errors at the SRM.

Three optics provide mode matching between the mode at the SRM and the OMC mode. The output Faraday isolator, located in HAM5, will feature a lens which is for making the Gouy phase between the two SAMS, OMx1 and OMx2, closer to  $45^\circ$ , thus making them closer to being orthogonal<sup>2</sup>. The optimal choice in power for the OFI lens, OMx1 and OMx2 is shown in Figure 5.2. With the layout shown in Figure 5.1, it is possible to achieve  $42^\circ$  of Gouy phase separation between OMx1 and OMx2. Other layouts could provide exactly  $45^\circ$  of Gouy phase separation; however, this layout offers practical benefits over the other considered

---

<sup>2</sup>An adaptive optic was considered for the OFI lens, however concerns over the OFI assembly heating resulted in this idea being discarded.

designs that outweigh an additional  $3^\circ$  of Gouy phase separation between OMx1 and OMx2 mainly in relation to the suspended platform (BHSS) upon which the OMCs are located. This layout also provides good Gouy phase separation for alignment control as there is  $> 80^\circ$  between OMxS and OMx2. The mode matching between the interferometer and the OMCs will be open-loop, i.e the mode matching will be optimised manually, however having near-orthogonal separation of the actuators for mode matching will make this process easier.

As astigmatism degrades the mode matching, it can contribute to the loss in the readout of the interferometer. Astigmatism arises when a beam reflects from a surface with a non-zero angle of incidence; the amount of astigmatism introduced to the beam depends on the beam's curvature and the curvature of the reflecting surface. As the beam in this layout has a relatively low radius of curvature at each mirror, the dominant source of astigmatism is the mirrors (for a comprehensive description of astigmatism see [177]). For this layout, the astigmatic loss was calculated to be less than 0.05%; see Appendix G for detail in this type of calculation. The astigmatic loss is plotted as a function of angle in Figure 5.3; as the beam will have low curvature, the loss only becomes significant when the angle of incidence is above  $10^\circ$ . Table 5.2 summarises the loss budget for the HAM6 layout, and a loss of less than 0.05% is negligible compared to the loss expected from other components.

The Gaussian width and Gouy phase of the beam as a function of position along the optical axis is shown in Figure 5.4. Significant points along the optical axis are also shown in this figure. The size of the beam at the final optic for mode matching

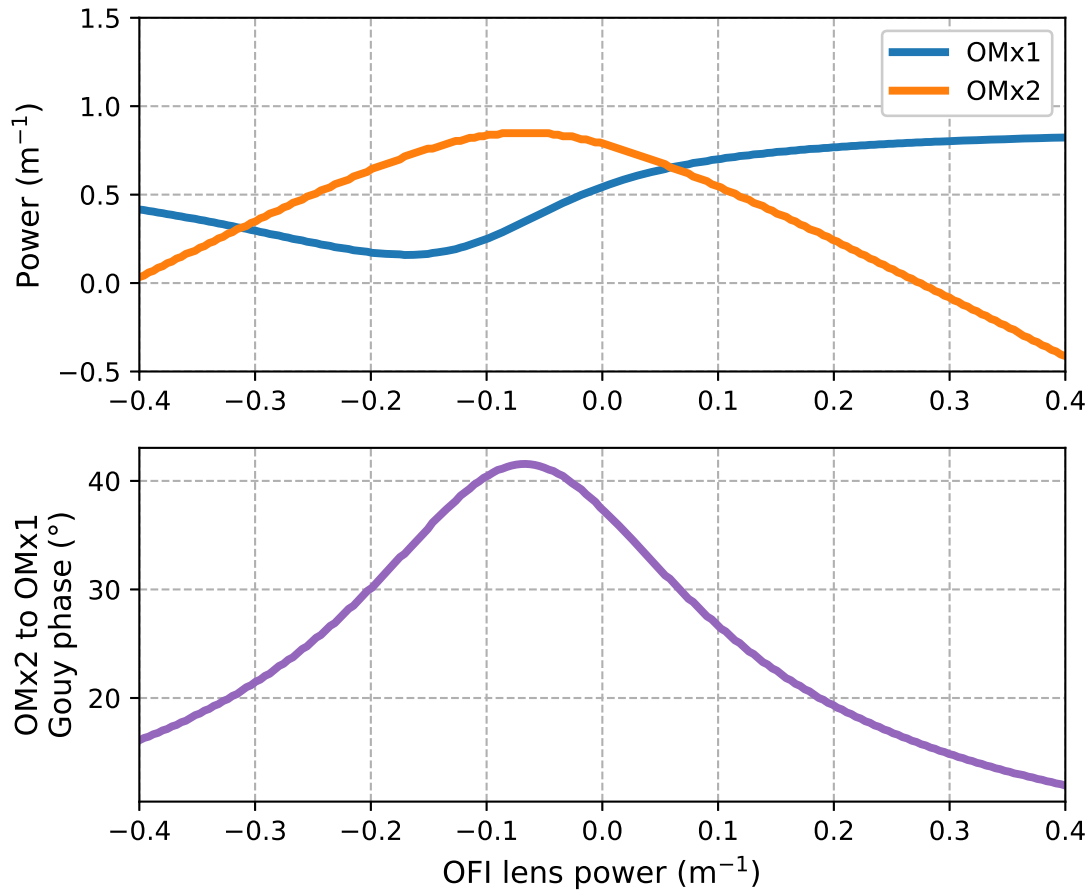


Figure 5.2: Top panel: the power of the OFI lens power affects the combination of OMx1 and OMx2 powers that is required for 100% mode matching. Bottom panel: the best choice for the OFI lens is where the Gouy phase separation between OMx1 and OMx2 is closest to  $45^\circ$ , as this means OMx1 and OMx2 are as close to being orthogonal as possible. The most Gouy phase separation between OMx1 and OMx2 achievable with this layout is  $42^\circ$ .

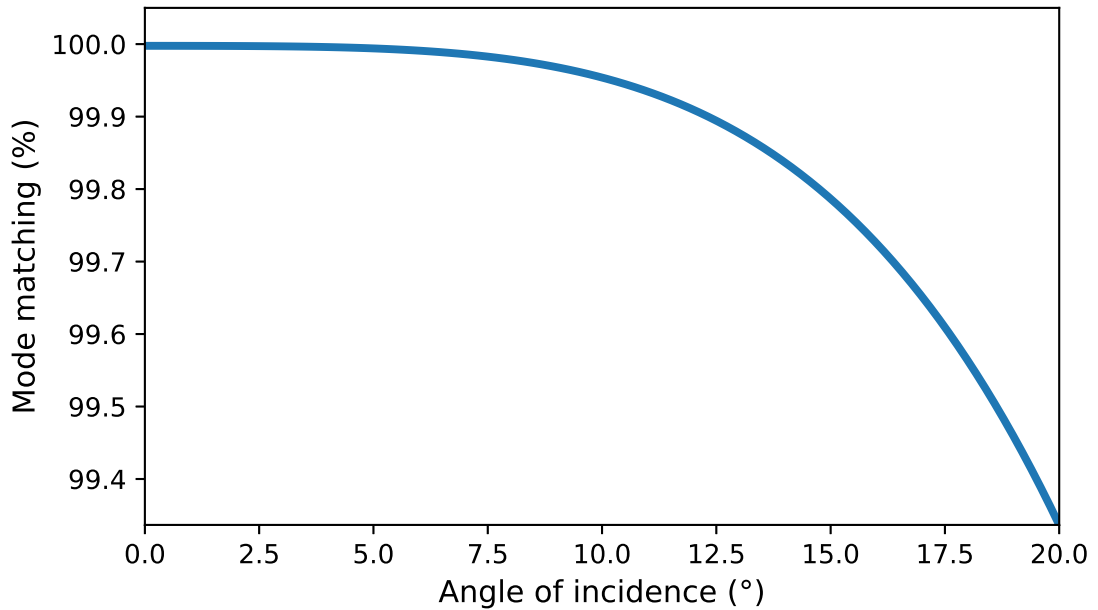


Figure 5.3: Astigmatism is a source of loss. When designing the layout shown in Figure 5.1, the angle of incidence for the curved mirrors was altered to explore how sensitive it was to astigmatism. Using Equation (5.2), the loss was computed. This effect is negligible up to 10°. Above 10°, loss due to astigmatism starts to become significant compared to the losses summarised in Table 5.2.

Chapter 5. Analysis of the Active Wavefront Control for the Balanced Homodyne Detector for LIGO A+

Optic	Power (1/m)	Focal length (m)	RoC (m)
OFI lens	-0.066	-15.068	-
OMx1	-0.350	-2.855	-5.709 (concave)
OMx2	-0.847	-1.180	-2.360 (concave)

Space Name	Optical Path Length (mm)
SRM to OFI lens	1120
OFI lens to HAM6 table edge	720
HAM6 table edge to OM0	500
OM0 to BHDBS2	946
BHDBS2 to OMxS	Path A: 225, Path B: 315
OMxS to OMx1	Path A: 1240, Path B: 1150
OMx1 to OMx2	1590
OMx2 to OMCx waist	1220

Parameter	Value
SRM Complex Beam Parameter	$q_{\text{SRM}} = (-3.55 + 1.09i) \text{ m}$
OMC waist	485 $\mu\text{m}$
OMx1 to OMx2 Gouy phase	42°
OMxS to OMx2 Gouy phase	Path A: 85°, Path B: 81°
OMx1 and OMx2 angle of incidence	A: 9.7°, B: 4.9°

Table 5.1: Mechanical and optical properties of the LIGO A+ HAM6 layout.

matches the size of the target mode, as the size of the beam cannot be changed at a mirror's surface.

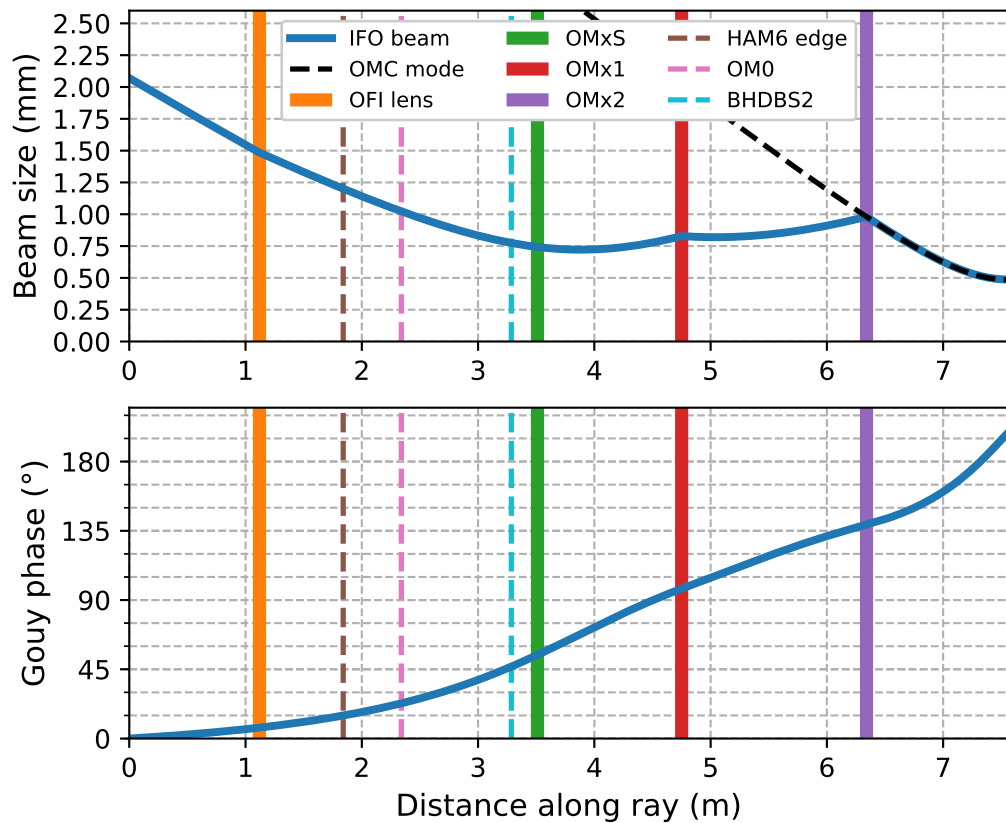


Figure 5.4: The top panel shows the radius of the beam as it travels from the SRM ( $z = 0$ ) to the waist of the OMC. Significant points along the axis are marked with vertical lines. Less significant, but useful, reference points are marked by dashed vertical lines. The bottom panel shows the Gouy phase shift accumulated by the beam as it propagates along the optical axis.

HAM6 loss Source	Target for O5
OMC throughput loss	< 2%
OM3 transmission (or equivalent) for sensing	1–2%
Photodiode quantum efficiency	1%
Mode mismatch to the OMC	< 2% (as low as possible)
Any other optical loss	< 1%

Table 5.2: Target for losses in HAM6. Reproduced from [178].

## 5.2 Method for Visualising the Effectiveness of Systems with Active Optics for Mode Mismatching

As described in Section 5.1 and Chapter 3, it is expected that there will be some mismatch between the arm mode and the OMC. To visualise the effectiveness of the AWC provided by the layout’s active optics, it is useful to consider a 2D space representing Gaussian beams. The region of this space which contains modes that can be matched to  $>98\%$  by the AWC and a distribution of modes that those optics may have to correct for can be compared to gain insight into the effectiveness of the layout.

The proposed layout in Section 5.1 can mode match the majority of beam parameters one would expect to be present at the SRM based on uncertainties in the RoC of the optics within the SRC. Despite this good coverage, measurements from LLO show that the beam parameter may fall outside the region of *waist-defocus* (WS) space which can be compensated for by the layout. If this were the case, the static RoC of the SAMS would need to be changed.

### 5.2.1 A Description of Mode Matching in Terms of Hermite-Gaussian Modes

Beams which are mode matched have identical beam parameters, i.e. they have the same sized waist and their waists are at the same position along the optical axis. Small mode mismatches can be modelled as light scattering from the beam's, or cavity's, fundamental mode into its  $HG_{20}$  and  $HG_{02}$  modes (i.e the  $HG_{20+02}$  mode). If a cavity is designed such that the fundamental mode will be resonant while the  $HG_{20+02}$  mode will be reflected, the effect of mode mismatch between the cavity and a signal carrying beam is to decrease the signal light that is transmitted by the cavity since some of the signal carrying light will be scattered into the reflected  $HG_{20+02}$  mode. Sensing the  $HG_{20+02}$  mode therefore gives a measure of the mode matching between two modes. As the  $HG_{20+02}$  mode acquire  $2\phi$  Gouy phase compared to the fundamental mode, where  $\phi$  is the Gouy phase acquired by the fundamental mode, spacing beam curvature actuators at  $45^\circ$  of Gouy phase apart provides an orthogonal basis for control over mode matching [136].

### 5.2.2 Calculating Mode Matching Using The Gaussian Beam Parameter

Two perfectly mode matched beams will have identical beam parameters at the same point along the optical axis. The overlap integral between two fields,  $E_1$  and

$E_2$ ,

$$\mathcal{M} = \frac{|\int_A E_1^* E_2 dA|}{\int_A |E_1|^2 dA \int_A |E_2|^2 dA}, \quad (5.1)$$

can be used to determine the amount of mode matching,  $\mathcal{M}$ , between two astigmatic modes. Solving this integral gives

$$\mathcal{M} = \frac{\sqrt{(q_{x1} - q_{x1}^*)(q_{y1} - q_{y1}^*)(q_{x2} - q_{x2}^*)(q_{y2} - q_{y2}^*)}}{|q_{x2} - q_{x1}^*||q_{y2} - q_{y1}^*|}, \quad (5.2)$$

where  $q_{x1,x2,y1,y2}$  are the beam parameters of the electric fields  $E_{1,2}$  in the tangential and sagittal planes. This is derived in Appendix G. The solution to Equation (5.2) is always  $0 < \mathcal{M} \leq 1$ . Alternatively, mode matching may be computed in terms of the amplitude of the higher order modes relative to the fundamental mode [179]. The mode matching can be calculated at any point along the optical axis of the layout because mode matching must be preserved throughout it; however, it makes sense to calculate the mode matching in a physically significant plane such as the input plane, a plane containing a curved optic or the plane containing the waist of the target beam.

### 5.2.3 Waist-Defocus Phase Space Visualisations

A Gaussian beam can be described by its beam size,  $w$ , and defocus,  $S$  [180]. A WS phase space representation plots a Gaussian beam in terms of these two parameters. The effect of focussing elements on Gaussian beams can be clearly seen in this representation of them. Because a curved mirror can only change the curvature of a beam, at the mirror's surface the beams before and after reflection

must have the same size. The process of a Gaussian beam, described by  $q_1(S_1, w_1)$ , being reflected from a mirror with power  $S_m$  to produce a new Gaussian beam,  $q_2$ , can be written as

$$\frac{1}{q_2} = S_m + \frac{1}{q_1} = (S_m + S_1) - i \frac{\lambda}{\pi w_1^2}. \quad (5.3)$$

From Equation (5.3) it can be seen that a mode moves in the  $S$  direction when it reflects from a curved mirror. This representation of Gaussian beams has the advantage of showing the beam in terms of intuitive quantities. The downside to this representation is as the beam propagates through the layout, the path that is traced through the WS space by the mode is fairly complicated.

There are two other ways that a beam parameter could be graphically represented. Since  $q$  is a complex number, it could be represented in terms of its real and imaginary components. This makes seeing the effect of propagation straight forward, but the effect of a focussing element is harder to visualise. Alternatively, plotting  $1/q$  in terms of  $\lambda/\pi w^2$  and  $S$  produces plots where the effect of focussing elements and propagation are easy to visualise [181, p.680]. Curved mirrors and lenses result in a change in defocus, and propagated modes follow circular paths. As these figures are being used to visualise mode matching and the effect of actuators on the beam size (rather than  $\lambda/\pi w^2$ ) and defocus, the WS representation was chosen. One could express the beam parameter in terms of natural units by dividing the beam size by the beam's minimum waist size,  $w_0$ , and the defocus by the inverse of the beam's Rayleigh range,  $1/z_R$ .

To illustrate how actuators move a mode in WS space, consider two lenses with

variable power separated by  $45^\circ$  of Gouy phase, thus making them orthogonal. In a WS space, the orthogonality of two actuators can be seen by the angle between the two vectors that represent each actuation. Figure 5.5 is a sketch of the WS space representation for a simple optical layout consisting of two active lenses separated by  $45^\circ$  of Gouy phase.

It is useful to plot contours of the mode overlap in the WS space between a mode and a target mode. Note that these contours can only tell you about the overlap between a mode and the target mode; the mode matching between two arbitrary modes can not be deduced from these contours [180]. For example, two modes may be mismatched by the same amount from the target in orthogonal directions in WS space. They cannot be perfectly mode matched as these two modes are different from each other.

#### **5.2.4 Visualising how the Active Optics for Mode Matching Expand the Area of Waist-Defocus Space Representing Acceptable Input Modes**

To visualise the effectiveness of the actuation provided by the active elements of the HAM6 layout, the region of the WS space at the SRM from which the target mode matching space can be achieved was computed. To do this, first the ring of modes in WS space that is 98% mode matched to the OMC after reflection from the second active mirror, OMx2, was considered. If OMx2 had a static radius of curvature, the effect of OMx2 would be to move the ring vertically in the WS plane.

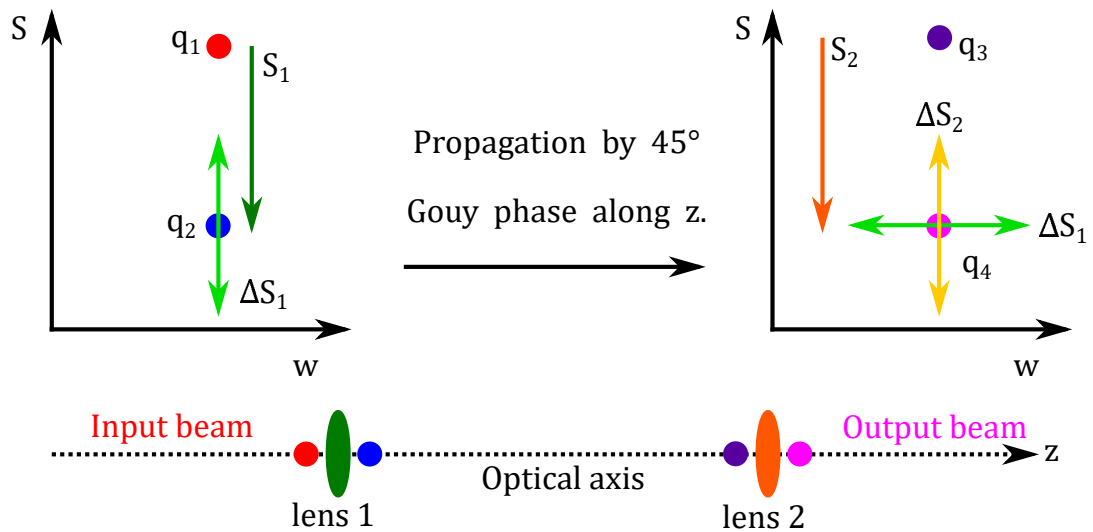


Figure 5.5: Sketches of the WS representation for a Gaussian beam interacting with different parts of a simple optical layout consisting of two active lenses with powers  $S_{1,2} \pm \Delta S_{1,2}$ . The left-hand axes shows the WS plane at Lens 1. The input beam,  $q_1$ , is indicated by a red dot, and the effect of the lens on  $q_1$  is shown by the dark green arrow  $S_1$ . This results in a new mode  $q_2$  which is shown as a blue dot. A light green arrow indicates the actuation of Lens 1. The right-hand axes shows the WS plane at Lens 2. The input mode at Lens 2,  $q_3$ , is shown as a purple dot, and the output mode,  $q_4$ , is shown as a pink dot. The static and dynamic power of Lens 2 is indicated by the orange and yellow lines. As Lens 1 and Lens 2 are separated by  $45^\circ$  of Gouy phase, the actuation provided by Lens 1 results in a change in the beam parameter which is orthogonal to the actuation provided by Lens 2, provided that the actuations are small enough. Beneath the two WS space diagrams is a sketch of the optical axis and the location of the modes.

However, the ring can also be stretched in the  $S$  direction as OMx2's RoC can be changed. This can be seen, crudely, by applying  $S_{\text{OMx2}} \pm \Delta S$  to the original  $> 98\%$  mode matching ring to produce two new rings separated by  $2\Delta S$ .

To generate the region from which the target region can be reached by OMx2, the target region should be cut by a line which intersects the ring at the extrema of the beam size. To maximise the amount of WS space covered by the actuator, the upper target region should have  $+\Delta S$  applied to it whereas for the lower region the actuation should be  $-\Delta S$ . This results in a region of WS space which is larger than the initial target region. All modes in the new region can be at least  $98\%$  mode matched to the OMC. The new region was then propagated to the first mirror, OMx1, where the same procedure can be applied to further expand the region. This process is shown in Figure 5.6.

The modes from the SRM that can be matched to the target are shown in Figure 5.7. To visualise how successful the layout is at handling the likely modes from the interferometer (i.e. the set of modes investigated in Chapter 3), the interferometer modes were compared to the region of WS space containing modes which can be corrected such that they meet the  $> 98\%$  mode matching requirement. It was found that majority of likely modes will be covered by the layout as the modes near the edge of the interferometer mode continuum are more unlikely to occur than the ones near the centre; however, measurements of the SRC's Gouy phase at LLO can be used to infer the beam parameter at the SRM, and this mode would fall outside of the region of WS space which can be compensated for by the AWC. Its worth noting that the modes at the yellow end of the continuum shown in Figure 5.7 may

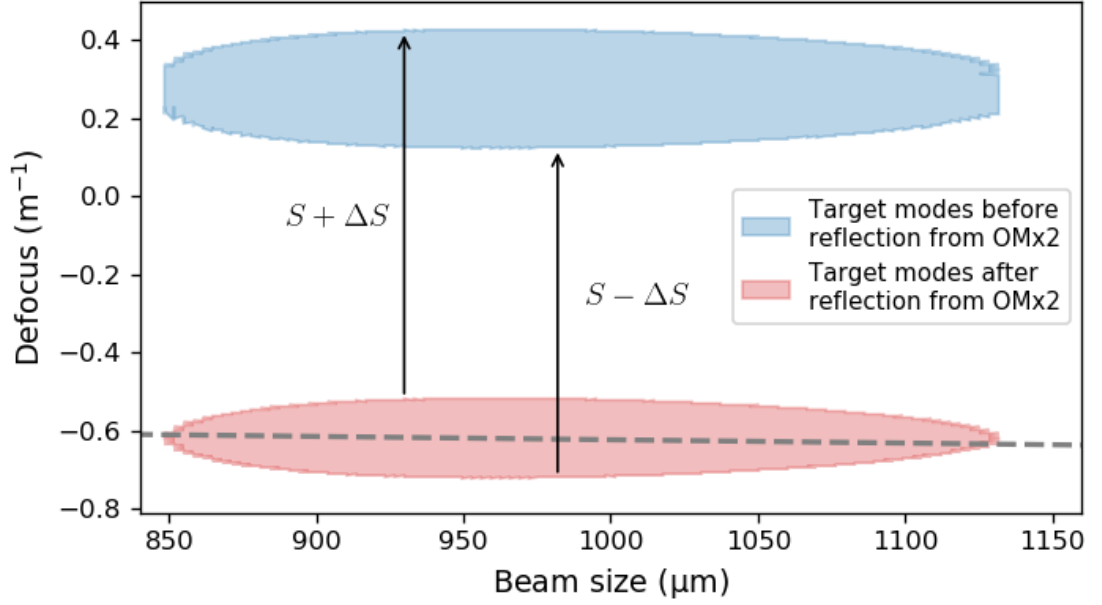


Figure 5.6: The WS space at the OMx2 plane. The effect of OMx2 in the plane of OMx2 is to move a mode vertically in WS space. After reflection from OMx2, a mode should be at least 98% mode matched to the OMC as there are no further active mode matching elements in the layout of HAM6. Such modes are shown by the red region. The blue region represents modes which can be reached from the red region by either  $S_{\text{OMx2}} \pm \Delta S$ , and was constructed by applying transformations to the modes in the red region. The red region was split into two parts, ‘upper’ and ‘lower’, indicated by the dashed line that connects the two extremes in width of the region. To create the lower edge of the blue region, modes in the lower edge of the red region had the transformation corresponding to a mirror power of  $S_{\text{OMx2}} - \Delta S$  applied to them. To construct the upper edge of the blue region, the upper edge of the red region had the transformation corresponding to a mirror power of  $S_{\text{OMx2}} + \Delta S$  applied to them.

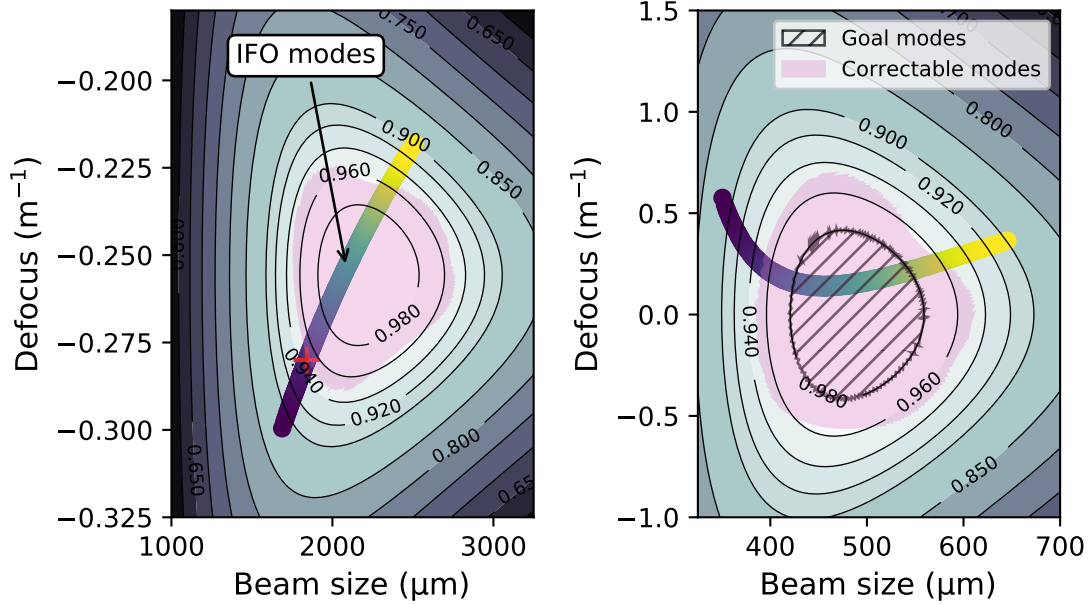


Figure 5.7: The region of WS space covered by the AWC in HAM6 for the layout discussed in Section 5.1. Left panel: the set of modes that is expected to be present at the SRM, as described in Chapter 3, is shown by the purple-blue-green-yellow curve. The pink region shows which modes can be corrected for so that 98% mode matching is achieved. The contours indicate the mode matching between a mode  $(W, S)$  and the OMC mode. The red cross indicates the mode size that can be inferred from measurements of the SRC’s Gouy phase at LLO. Right panel: this shows the same modes as the left panel, except they have been transformed by the optical layout to the plane of the OMC waist. Modes within the pink region can be actuated on so they move to the goal region, which is indicated with a hatched area.

not be physical as they correspond to an unstable SRC.

The shape of the pink region in Figure 5.7 is nominal; when the HAM6 layout is constructed the pink region's shape will be altered by geometric errors in OMx1 and OMx2. Nevertheless, Figure 5.7 is encouraging since it shows that the actuation provided by OMx1 and OMx2 is highly tolerant to mode matching errors generated by errors in the SRC.

### 5.2.5 Optimising Waist-Defocus Space Coverage in Favour of Expected Mode Errors

The majority of the uncertainty in the interferometer's beam parameter comes from the uncertainty in SR3's RoC (see Figures 3.6 and 3.7). Ideally, one would correct for this by actuating on the RoC of SR3. While there is no hardware that can actuate on the RoC of SR3 strongly enough, one could configure the AWC within HAM6 such that it is biased for correcting the errors in the interferometer's beam parameter caused by the error in SR3.

By reducing the orthogonality of the AWC actuators, more range can be obtained for one of the beam's properties, e.g. the size of its waist. A Gouy phase separation  $\sim 30^\circ$  offers a compromise between orthogonality versus actuation range for errors in one of the beam parameter's dimensions; for a given Gouy phase, a set of static optical powers can be obtained from Figure 5.2 for the OFI lens, OMx1 and OMx2 that gives perfect mode matching between the interferometer's nominal

beam parameter and the OMCs. However, layouts with less Gouy phase separation between OMx1 and OMx2 also have less Gouy phase separation between the mirrors for aligning the interferometer to the OMCs, so this idea was ultimately rejected.

### 5.3 Conclusion

The proposed layout for HAM6 was presented in Section 5.1. The optical properties of this layout were investigated. By selecting the right combination of optics for mode matching, near orthogonal control of the mode matching and alignment between the interferometer and the OMC can be achieved.

The effect that the AWC had on the region of WS space that contains modes which satisfy the  $> 98\%$  mode matching requirement was investigated. WS diagrams were used to represent how robust the layout is to initial mode mismatch. Figure 5.7 shows the amount of WS space that the AWC could correct for. The AWC covers a wide range of possible modes that may emerge from the interferometer, and the static defocus of the SAMS can be changed, so it is highly likely that the AWC in HAM6 will give optimal mode matching between the interferometer and the OMC.

## Chapter 6

# Characterisation of Photodiodes for Detecting $2\mu\text{m}$ Light

As discussed in Section 1.8, a new photodiode technology may be needed for the third generation of ground-based gravitational wave detectors. Quantum efficiency, power handling and dark noise are three important properties for a photodiode that would be used in a gravitational wave detector, so the requirements for such a photodiode are explored in Section 6.1. Extended InGaAs photodiodes can be sensitive to  $2\mu\text{m}$  light; however, for the reasons explained in Section 6.2, fabrication of an extended InGaAs photodiode that meets the requirements set out in Section 6.1 is challenging. The properties of off-the-shelf extended InGaAs photodiodes were measured under different reverse biases to investigate whether they met the requirements. As well as extended InGaAs, InSb is sensitive to  $2\mu\text{m}$  light, so the properties of an InSb

detector are explored in Section 6.8.

## 6.1 Quantum Efficiency, Power Handling and Dark Noise Requirements for Photodiodes in a Gravitational Wave Detector

The photodiodes used in a gravitational wave interferometer should have a quantum efficiency of at least 99%, as described in [178], because loss within the interferometer decreases its SNR, as it diminishes the level to which the signal light can be squeezed (see Equation 1.18). High quantum efficiency is required to detect the target of  $\sim 10$  dB of squeezed light that future gravitational wave detectors will use [90, 93, 94].<sup>1</sup>

In some applications, lost light can be compensated for by increasing the gain of the photodiode circuit. However this method would not work in a gravitational wave detector. Vacuum noise would pollute the quantum state due to the loss introduced in the photon-to-electron conversion process that happens within non-ideal photodiodes.

Current gravitational wave detectors run with light of  $\sim 10$  mW at the output (e.g. [58]) to ensure that the junk light from other modes is a small portion of the

---

<sup>1</sup>Avalanche photodiodes can be operated to have a quantum efficiency much greater than one. However, an avalanche photodiode will suffer from noise introduced by the fluctuations in its gain factor and loss relating to the heat generated in the avalanche process.

### 6.1. Quantum Efficiency, Power Handling and Dark Noise Requirements for Photodiodes in a Gravitational Wave Detector

---

total signal (see Section 1.4.4). For the remainder of this chapter, as  $q\lambda_{\text{EM}}/hc$  is of the order unity, the requirement for a photodiode is that it should be able to produce  $\sim 10$  mA of photocurrent without saturating.

Photodiodes for gravitational wave detectors should have low  $1/f$  dark noise so that the interferometers are limited by quantum noise in their detection bands. Third generation ground based gravitational wave detectors are designed to be quantum noise limited down to about 10 Hz [89, 90, 94], so the  $1/f$  noise must be sufficiently far below the shot noise of the photocurrent above 10 Hz. For a 10 mA photocurrent, the shot noise is  $6 \times 10^{-11}$  A/ $\sqrt{\text{Hz}}$ . Below 10 Hz, other rapidly rising sources of noise are predicted to limit the sensitivity of the Einstein Telescope and Cosmic Explorer.

The  $1/f$  noise could, in principle, be avoided by using heterodyne detection. However, a conventional heterodyne detection scheme would increase the shot noise level of the signal [163, 182, 183]. Although an optimal choice of modulation-demodulation waveform can recover the SNR by increasing the signal [163], the benefits of using squeezed light would be lost because the shot noise would be enhanced compared to homodyne readout, as vacuum noise at frequencies that do not contain signal would enter into the measurement. However, it has been proposed that the increase in noise associated with heterodyne readout could be avoided by using a broadband squeezer [184], although the feasibility of implementing this in a gravitational wave detector has yet to be experimentally demonstrated. Even with heterodyne readout, the quantum efficiency and linearity requirements remain severe.

## 6.2 What is an Extended InGaAs Photodiode?

The performance of an extended InGaAs photodiode depends substantially on the number of defects within it. A basic explanation of how photodiodes work, how these defects arise, and how these defects affect the photodiode is given in this section. More details on the semiconductor physics of diodes and photodiodes can be found in many textbooks e.g. [185, 186].

The basic physics of a PIN photodiode can be qualitatively understood by considering a simpler pn junction. A pn junction consists of two types of semiconductor: p-doped and n-doped. These regions have ions which are in fixed positions and charge carriers, known as majority charge carriers, which are free to move. Holes are the majority charge carriers in the p-doped region, and the ions are negatively charged (acceptors). In the n-doped region, electrons are free to move, and the ions are positively charged (donors). In equilibrium, the number of holes is equal to the number of electrons. The free charge carriers will diffuse across the interface between the p-doped and n-doped region. This causes the p-doped and n-doped regions to become charged. This results in a region of the pn junction where there are no free electrons and holes. This is known as the depletion region.

If a photon is absorbed by a pn junction, a free electron-hole pair is generated. A photon may be absorbed by the pn junction if its energy is large enough to move an electron from the valence band into the conduction band. If the photon is absorbed within the depletion region of the photodiode, the electron and hole are separated

due to the electric field, and a current is generated in the circuit connected to the photodiode. However, if a photon is absorbed outside the depletion region, then the electron-hole pair will have a large chance of recombining and not contributing to the current in the circuit.

The relationship between quantum efficiency,  $\eta$ , light power,  $P_{EM}$ , and photocurrent,  $I_p$  is given by

$$I_p = \eta \frac{q\lambda_{EM}}{hc} P_{EM}, \quad (6.1)$$

where  $\lambda_{EM}$  is the wavelength of the light,  $h$  is Planck's constant and  $c$  is the speed of light.

To widen the depletion region, an external voltage can be used. When a reverse bias is applied to the photodiode, there is a larger electric field at the interface between the p-doped and n-doped region; thus, the depletion region is widened, and hence applying a reverse bias to a photodiode increases the volume of the photodiode in which absorbed photons will generate photocurrent.

To further increase the width of the depletion region, a layer of intrinsic semiconductor can be used to separate the p-doped and n-doped regions. An intrinsic semiconductor has no doping, and the number of electrons equals the number of holes within it. As the intrinsic region physically separates p-doped and n-doped regions, a larger volume of the photodiode will be depleted of charge carriers due to the electric field within the photodiode. Additionally, the capacitance of the photodiode will be decreased. The thickness of the depletion region of a photodiode

should be several times larger than the semiconductors absorption length so that a high proportion of the photons incident on the photodiode are absorbed.

InGaAs is a widely used semiconductor for making photodiodes. InGaAs needs to be grown on a substrate. To combine two types of semiconductor, they must have similar lattice constants and share the same lattice structure; this is known as lattice matching. Typically, the indium content of InGaAs is around 53%, this is signified with the chemical formula  $\text{In}_{0.53}\text{Ga}_{0.47}\text{As}$ , so that the InGaAs can be lattice matched to an InP substrate<sup>2</sup>. With this amount of indium, the InGaAs photodiode will suffer from few lattice mismatch defects, and the photodiodes created can be of high quality.

Normally, InGaAs photodiodes are sensitive up to wavelengths around 1.6  $\mu\text{m}$ , but longer wavelength sensitivity can be achieved by increasing the indium content of the photodiode (e.g. [187–189]). As mentioned in Section 1.8, these photodiodes are often called extended, and they can be sensitive for wavelengths up to 3  $\mu\text{m}$ . To absorb 2  $\mu\text{m}$  photons, the indium content needs to be at least 70%. One of the key issues faced when creating an extended InGaAs photodiode is the strain induced by the lattice mismatch between the InGaAs and the InP substrate [190] as this introduces defects.

Defects caused by the strain between the InGaAs and InP layers of the photodiode generate excess noise, dark current and reduce its quantum efficiency [191]. The

---

<sup>2</sup>Ge is sometimes used as a substrate. This will be lattice matched for InGaAs with an In content of around 10%; this corresponds to the bandgap being similar to the energy of a 1  $\mu\text{m}$  photon.

photodiode can be made thinner to reduce this strain. The critical thickness, i.e. the thickness above which strain degrades the crystal, for extended InGaAs is of the order 0.1 nm [190] whereas the absorption coefficient (of the order of  $10^4 \text{cm}^{-1}$  [188]) requires the photodiode to be several microns thick for it to have the high quantum efficiency that is required for the detection of gravitational waves (see Section 6.1). Therefore, it is highly likely that such a thick extended InGaAs photodiode will have defects. Additionally, because InGaAs is not a good conductor of heat, a thicker photodiode can exhibit reduced power handling [192].

These defects manifest as abrupt changes in the crystal structure known as misfit dislocations (e.g. [193, 194]). The resulting undesirable states in the bandgap that charge carriers can occupy, known as trap states, give rise to a generation-recombination dark current [195]; thus, defects are a source of  $1/f$  noise in extended InGaAs (see [196] for a description of  $1/f$  noise in semiconductors). Defects cause there to be more free charge carriers in the InGaAs. This leads to the depletion region becoming smaller, thus defects cause the quantum efficiency to be decreased [197]. For indium doping levels other than 53%, buffer layers of InGaAs between the absorbing layer and the substrate can be used to mitigate the lattice mismatch [195]. The number of defects depends on the growth conditions of the photodiode, and by improving them, the dark noise of a photodiode made from extended InGaAs can be reduced by orders of magnitude [189].

An anti-reflection coating can be used to increase the quantum efficiency of a photodiode. For example,  $\text{In}_{0.7}\text{Ga}_{0.3}\text{As}$  has a bandgap which is equal to the energy of a  $2 \mu\text{m}$  photon, and it has a refractive index,  $n$ , of approximately 3.7 at this

wavelength. Assuming a single quarter-wave layer was to be applied, the film would need a refractive index of  $n_f = \sqrt{3.7}$  and be  $\sim 250$  nm thick. The idea of using this anti reflective coating as a passivation layer – a passive material designed for protecting the semiconductor from the environment – is presented in [198]. Some manufacturers create a range of photodiodes with different spectral responses by changing the anti-reflective coating rather than by changing the photodiode’s indium content [80].

The dark noise and dark current of a photodiode have several contributors. In low bias regimes, the dark current is driven by the diffusion of minority carriers [197, 199]. However, the thermally driven generation-recombination of electron/hole pairs drives the  $1/f$  dark noise at low bias [196]. In other words, dark current and dark noise are created via different mechanisms. Therefore, the dark current does not predict the dark noise; however, as both increase with higher levels of defects, a photodiode with a high dark current will tend to have a high dark noise. When the bias exceeds a certain threshold, electrons can tunnel across the junction, leading to a substantial increase in dark current; the bias corresponding to this tunnelling threshold is typically of the order of 1 V in extended InGaAs photodiodes.

The noise spectral density,  $i_n$ , of a photocurrent can be modelled as

$$i_n = \sqrt{2qi + \frac{4k_B T}{R_{PD}} + \left(\frac{A}{f^\beta}\right)^2}. \quad (6.2)$$

The first term under the square-root,  $2qi$ , is the term associated with the shot noise of a current  $i$ . The second term,  $\frac{4k_B T}{R_{PD}}$ , is the term related to the Johnson-Nyquist noise

due to the shunt resistance of the photodiode,  $R_{PD}$ ; this term can become significant when the shunt resistance is low, as it is in some extended InGaAs photodiodes, and microwatt levels of light are being detected. The final term is an empirical relationship known as Hooge's law [196];  $A$  is the characteristic noise level and  $\beta$  is usually  $0.5 \pm 0.1$ , thus leading to a  $1/f$  power spectrum.

## 6.3 Selection of Off-the-shelf Extended InGaAs Photodiodes

The dark current and dark noise were characterised in a selection of commercially available photodiodes. The photodiodes that were tested and their properties according to their datasheets<sup>3</sup> are listed in Table 6.1. The quantum efficiency as a function of bias was measured for one of the photodiodes, the FD10D, and the saturation limits of the FD10s, IG22x1000S4i, IG24x500S4i and IG26x500S4i photodiodes were investigated. The dark current and dark noise were measured for each model of photodiode.

With no reverse bias<sup>4</sup>, the typical quantum efficiency of these photodiodes is 80%;

---

<sup>3</sup>Datasheets often quote the noise equivalent power (NEP) of a photodiode. The NEP is the noise spectral density of the dark current generated by the photodiode divided by its responsivity. While the NEP for a photodiode may seem sufficiently low, it does not capture the behaviour of the photodiode at illumination levels of several milliwatts where a bias is needed to ensure the photodiode does not saturate. Additionally, the noise of these photodiodes is not flat (see Appendix A), so the NEP should be specified as a function of frequency. Furthermore, the noise and responsivity are both functions of reverse bias, so the NEP is a function of bias. Another quantity related to the NEP is the specific detectivity; this incorporates the area and bandwidth of the photodiode with the NEP.

<sup>4</sup>Usually, the operating conditions of the photodiode is stated in the photodiode's datasheet when a parameter is given; however, there is no information on what reverse bias gives the respon-

this is far below the target of greater than 99%. However, the quantum efficiency of a photodiode can be improved by increasing the bias voltage (see Section 6.4). The photodiodes listed in Table 6.1 are sold with protective windows, and these windows reflect a significant amount of light. These windows should be removed in experiments requiring high quantum efficiency.

InGaAs photodiodes are highly sensitive to *electro-static discharge* (ESD) damage. At every stage of handling, precautions were taken to ensure that they were not damaged. These included: wearing antistatic wristbands and removing nitrile gloves when necessary, working on grounded worktops, and storing the photodiodes in antistatic foam within an antistatic box.

## 6.4 The Effect of Reverse Bias on the Quantum Efficiency of an Extended InGaAs Photodiode

The relationship between the reverse bias and quantum efficiency of an extended InGaAs photodiode, the FD10D, was investigated. The FD10D was chosen for this experiment as one had been used in an experiment to do with squeezed light at 2 $\mu$ m [84]. The two types of measurement used are described in Section 6.4.1. A clear motivation for increasing the reverse bias of an extended InGaAs photodiode is shown in Figure 6.2.

---

sivity in the FD10D's datasheet.

6.4. The Effect of Reverse Bias on the Quantum Efficiency of an Extended InGaAs Photodiode

---

Photodiode	Peak quantum efficiency (%)	Cut-off wavelength <sup>a</sup> ( $\mu\text{m}$ )	Diameter (mm)	Datasheet
FD10D	80 <sup>b</sup>	2.5	1	[200]
G12183-010k	77 <sup>b</sup>	2.5	1	[201]
G12183-005k	77 <sup>b</sup>	2.5	0.5	[201]
IG26x500S4i	86 <sup>c</sup>	2.5	0.5	[202]
IG24x500S4i	84 <sup>c</sup>	2.4	0.5	[203]
IG22x1000S4i	91 <sup>d</sup>	2.2	1.0	[204]
G12182-005k	84 <sup>e</sup>	2.1	0.5	[205]
G12182-010k	84 <sup>e</sup>	2.1	1.0	[205]

<sup>a</sup>  $\lambda_{\text{EM}}$  at which the quantum efficiency = 50%    <sup>b</sup>  $\lambda_{\text{EM}} = 1.9\mu\text{m}$     <sup>c</sup>  $\lambda_{\text{EM}} = 2.0\mu\text{m}$   
<sup>d</sup>  $\lambda_{\text{EM}} = 1.7\mu\text{m}$     <sup>e</sup>  $\lambda_{\text{EM}} = 1.6\mu\text{m}$

Table 6.1: Information from the datasheets of the photodiodes that were tested. Note that none of the photodiodes has a quantum efficiency of at least 99%, however measurements of dark noise and dark current and investigations into their optimal operating conditions are still of interest. This choice of photodiodes covers a range of manufacturers, sizes and cut-off wavelengths.

### 6.4.1 Method

To measure the effect that changing the reverse bias voltage has on the quantum efficiency of a photodiode, two approaches were used. It is straightforward to determine the change in quantum efficiency by measuring the photocurrent as a function of reverse bias. Alternatively, one can modulate the bias and measure the modulation in the photocurrent. If the quantum efficiency,  $\eta$ , depends on the reverse bias of the photodiode, modulating the reverse bias,  $V_B$ , at a frequency  $f$  will result in  $\eta$  modulating at  $f$  and so the measurement will be of  $\Delta\eta/\Delta V_B$ . The input modulation  $\Delta V_{\text{in}} = \Delta V_B$  and the output modulation is  $\Delta V_{\text{out}} \cos \theta = \Delta\eta V_{\text{TIA}}(V_B)$ , where  $V_{\text{TIA}}(V_B)$  is the DC signal from the photodiode and  $\theta$  is the phase between the input and output modulation. The quantum efficiency should be independent of frequency if the photodiode is operating in a time-independent, linear fashion and so the two types of measurement should yield the same outcome.

To prove that the increase in signal was a result of the photodiode's quantum efficiency increasing and there were no non-linear mechanisms by which photocurrent was generated, the shot noise level of the photocurrent was measured. This measurement required a sufficiently quiet photodiode circuit and an amplitude stabilised laser.

To measure photocurrent with sufficient SNR, a transimpedance amplifier with electronic noise 25 times below the shot noise level of the expected signal (10 mA) photocurrent was used. This circuit is shown in Appendix B.2. The circuit allowed

#### 6.4. The Effect of Reverse Bias on the Quantum Efficiency of an Extended InGaAs Photodiode

---

for the reverse bias of the photodiode to be set externally via a low-passed bench-top power supply. The low-pass filter had two poles at 16 Hz.

The optical layout is shown in Figure 6.1. A laser with a power of 50 mW and a wavelength of 1.55  $\mu\text{m}$  (Pure Photonics PPCL300) was used to illuminate the FD10D, the device under test. Results at 1.55  $\mu\text{m}$  can be extended up to 2  $\mu\text{m}$ . The dependence of a photodiodes responsivity on wavelength is largely to do with the anti-reflection coating on the photodiode's window; the quantum efficiency tends to be uniform over a band of wavelengths which includes 1.55  $\mu\text{m}$  and 2  $\mu\text{m}$  (see e.g. [206]).

The light from the laser was split by a 50:50 beam splitter so that a suitable amount could be used to amplitude stabilise the laser. The in-loop photodiode used to sense the laser's power was a high-performance InGaAs photodiode (C3061GH). The laser was amplitude stabilised by actuating on the current of the laser's pump-diode. The amplitude stabilisation servo had sufficient gain so that the in-loop noise was below the level of shot noise of a 10 mA photocurrent, so the servo could stabilise the light sufficiently that shot noise limited measurements could be made on the out-of-loop photodiode. With this apparatus, shot noise limited measurements could be made above 1 kHz. A half waveplate and polarising beam splitter were used to adjust the power level of the light incident on the FD10D, and a lens was used to set the beam's Gaussian width to sizes up to the width of the photodiode.

As the FD10D has a diameter of 1 mm, the laser beam could not have a width larger than 330  $\mu\text{m}$  for there to be  $< 1\%$  loss due to clipping. For the reasons

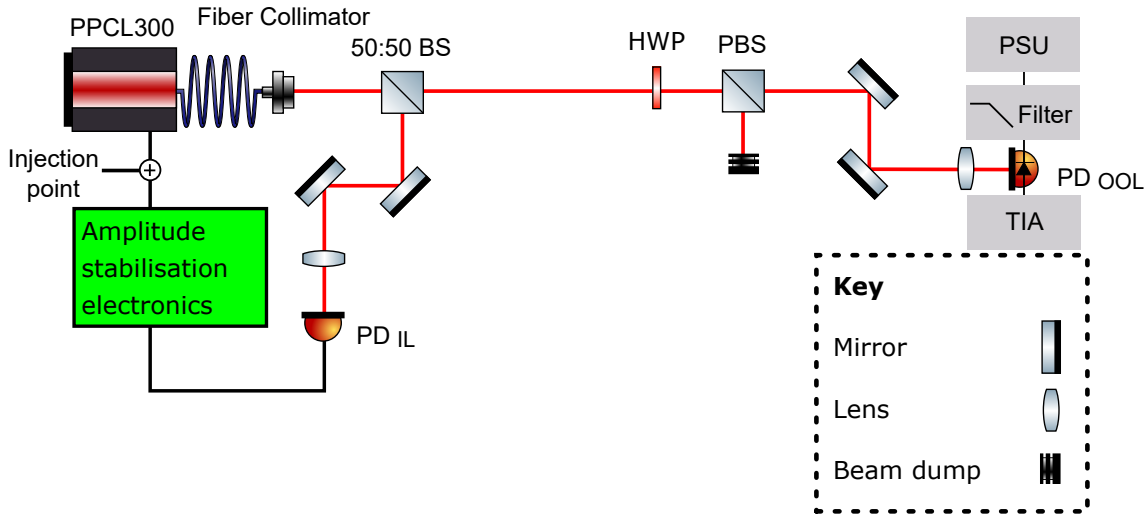


Figure 6.1: Optical layout used for measuring the effect that increasing the reverse bias of a photodiode had on its quantum efficiency and saturation limit. The out-of-loop photodiode,  $PD_{OOL}$ , was the photodiode under test (FD10D). A 1.55  $\mu$ m laser was used to assess the optical properties of the photodiode. A combination of half wave plate (HWP) and polarised beam splitter (PBS) allowed for the power of the beam to be set, and a lens was used to set the size of the beam on the photodiode under test. Amplitude stabilised light was needed to ensure the increase in photocurrent seen when the bias was increased was due to an improvement in quantum efficiency. The photodiode circuit (TIA) (see Appendix B.2) allowed for shot noise limited measurements of current around 10 mA and for the bias to be selected. The calibration signal was added onto the amplitude stabilisation error signal.

#### 6.4. The Effect of Reverse Bias on the Quantum Efficiency of an Extended InGaAs Photodiode

---

stated in Section 6.1, the FD10D was tested at a power level of  $\sim 10$  mW. The methods in this section were used to measure relative increases in quantum efficiency; measurements of absolute quantum efficiency require a calibrated power meter. A method of measuring the absolute quantum efficiency of a photodiode with squeezed light is presented in [207].

The photodiode was biased such that the dark noise was sufficiently low (see Section 6.5 for details), and the noise of the photocurrent was compared to the level expected for shot noise. The expected level of noise,  $n$ , in units of  $\text{A}/\sqrt{\text{Hz}}$ , is given by

$$n = \sqrt{2qI_{\text{OOL}} + 2qI_{\text{IL}} + n_{\text{IL dark}}^2 + n_{\text{OOL dark}}^2 + n_{\text{loop}}^2 + n_{\text{analyser}}^2}. \quad (6.3)$$

The first two terms under the square root represent the shot noise of the current produced by the in-loop and out-of-loop photodiodes,  $n_{\text{OOL/IL dark}}$  is the dark noise of the out-of-loop photodiode and in-loop photodiode,  $n_{\text{loop}}$  is the electronic noise of the loop and  $n_{\text{analyser}}$  is the noise of the analyser. The noise contribution of each component in Equation (6.3) can be expressed in terms of current by multiplying them by the appropriate transfer function.

The light from the laser was amplitude modulated at 1111 Hz by adding a signal to the laser's pump-diode error signal (see Figure 6.1). This modulation was used to calibrate the measurements of noise as the relative intensity of this peak was known and could be checked against the signal measured by the high-performing in-loop photodiode. By tracking the height of an intensity modulation in the light for a series of powers up to 16 mW, the saturation limit of the photodiode was investigated. A

similar type of measurement is reported in [208].

### 6.4.2 Results

The effect of increasing the reverse bias on the quantum efficiency of the FD10D is shown in Figure 6.2. For all beam intensities which the photodiode was exposed to, the increase in quantum efficiency was  $\sim 15\%$  as the reverse bias went from 0V to 1.8V, the stated maximum reverse bias in the FD10D's datasheet. There may be a saturation related effect at the 1% level: beams with a lower intensity experienced a greater increase in  $\eta$  than beams with a higher intensity. This could be explained by the quantum efficiency not being uniform over the photodiode – the spatial dependence of  $\eta$  can be crater-like with  $\eta$  being greatest at the edges of the photodiode (this can be seen in Figure 5 of reference [206]). The difference between the DC and AC response is described by a non-linear process. These effects are small, and Figure 6.2 gives a clear incentive to increase the bias voltage to improve the quantum efficiency of the FD10D.

Figure 6.3 shows the noise of the photocurrent when the photodiode was biased with 0.6V. As Equation 6.3 matches the measured noise, the increase in photocurrent at a reverse bias voltage of 0.6V is, without doubt, an increase in quantum efficiency.

At 0.6V reverse bias, for DC photocurrent ranging from 7.5 mA to 15.5 mA, the calibration peak and the noise level of the photocurrent were measured to ensure the photodiode was not saturating. Over this range there was a 2% change in the

## 6.4. The Effect of Reverse Bias on the Quantum Efficiency of an Extended InGaAs Photodiode

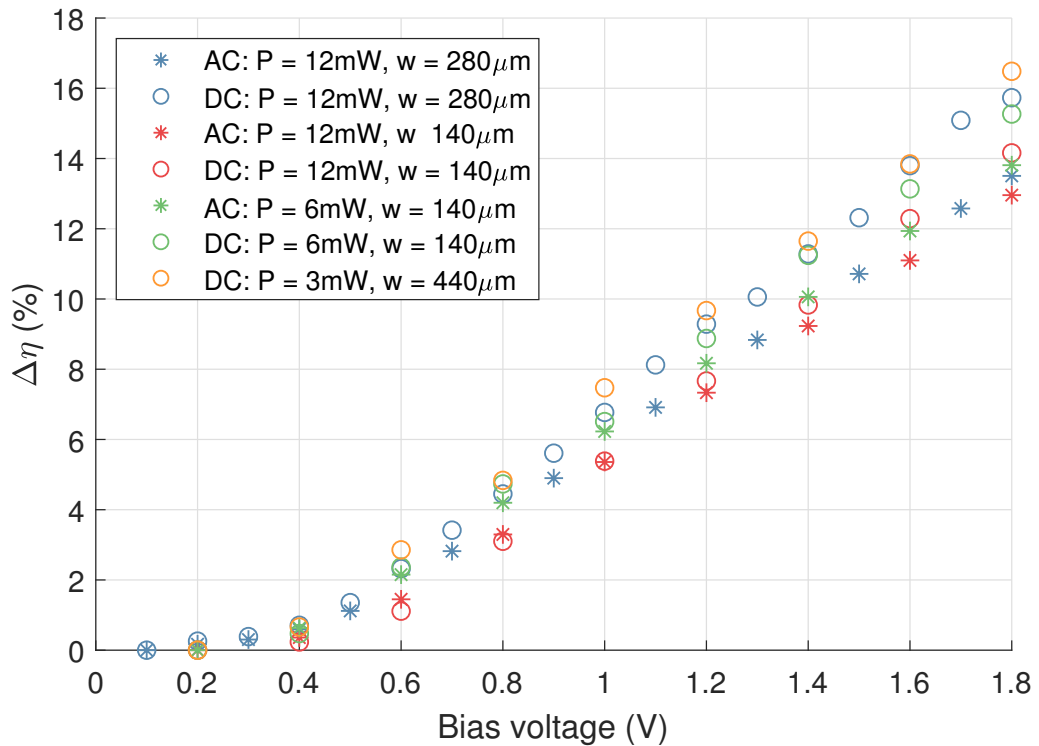


Figure 6.2: The FD10D’s quantum efficiency depends on its reverse bias; the increase in quantum efficiency was  $(15 \pm 1)\%$  when the bias was increased to the maximum value specified in its datasheet. Two types of measurement were used to determine the increase in quantum efficiency as the bias was increased. The first method was to measure the photocurrent with a voltmeter as the bias was increased, and the corresponding results are shown as circles (‘DC’). The second method involved modulating the bias and measuring the resulting modulation in the photocurrent, i.e. an AC measurement, and these are shown by the star markers. Each set of measurements was done with a different intensity by changing either the beam’s width or power. Further detail on both methods is given in Section 6.4.1.

ratio between the DC and AC measurement, this is shown in Figure 6.4. The SNR of this measurement is limited to the 1% level due to the difference between the calibration peak and the level of shot noise, so there was no sign of the photodiode saturating.

By measuring the photocurrent, the power of the incoming light and the power of the light reflected by the FD10D's window, at 0.6 V reverse bias, its quantum efficiency was measured to be 70%. It was assumed that no light was absorbed by the window. This was calibrated using two independent power meters. There is a significant amount of light reflected by the FD10D's window; if the window was not removed, at 0.6 V reverse bias the quantum efficiency would be 60%.

## 6.5 Dark Current and Dark Noise in Extended InGaAs Photodiodes

Following the observation that both dark noise and quantum efficiency both increase with reverse bias, there is a compromise to be made between quantum efficiency and dark noise. A maximum reverse bias voltage that balanced quantum efficiency and noise was found for each photodiode listed in Table 6.1. See Section 6.4.2 for details on the dependence of quantum efficiency on reverse bias. The dark noise of the photodiode should be below the shot noise level of the detected light. For the reasons discussed in Section 6.1, the shot noise of a 10 mA photocurrent,  $6 \times 10^{-11} \text{ A}/\sqrt{\text{Hz}}$ , was used as a benchmark for the photodiodes' dark noise at a frequency of 10 Hz.

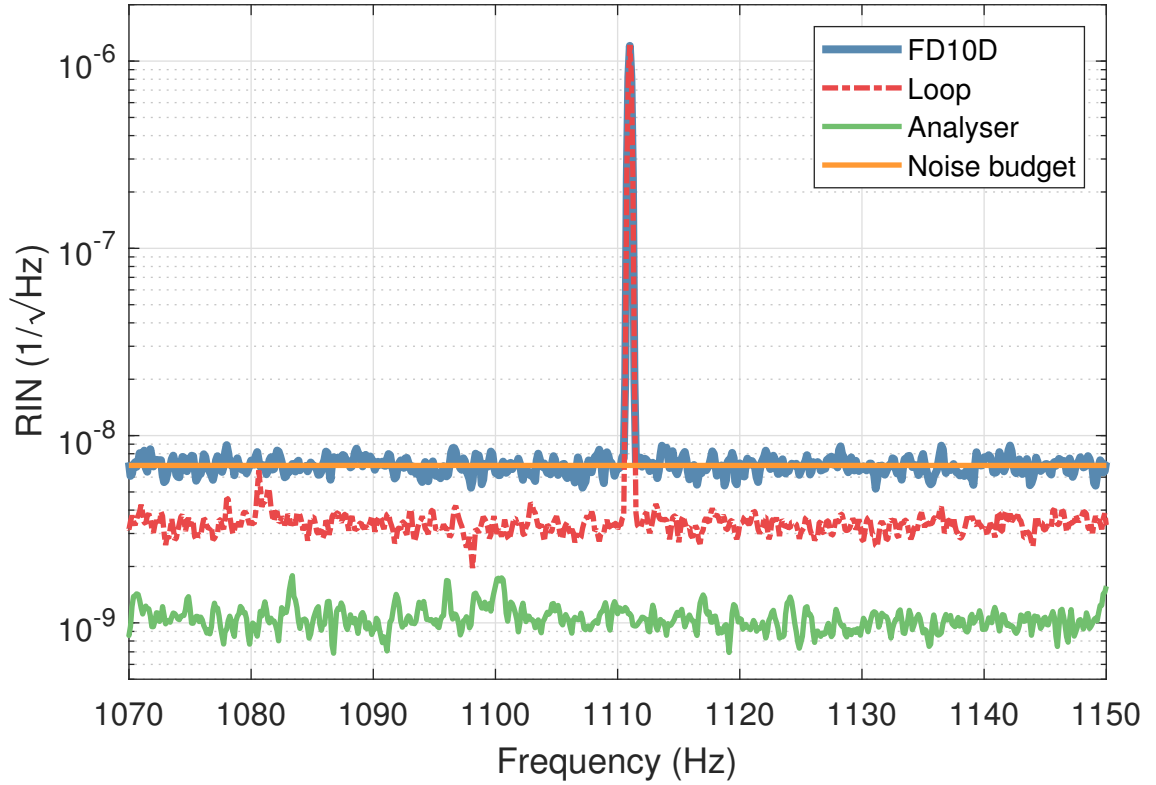


Figure 6.3: The bias of the FD10D was set to 0.6 V, and it was exposed to 15 mW of 1.55  $\mu\text{m}$  light. 15 mA of photocurrent was generated. The noise of the photocurrent produced by the FD10D (blue line) corresponds to the level predicted by Equation 6.3 (orange line) meaning that the increase in photocurrent can only be explained by an increase in quantum efficiency. The 1111 Hz signal was used to calibrate the measurement as this modulation also could be measured on the high-performance in-loop photodiode.

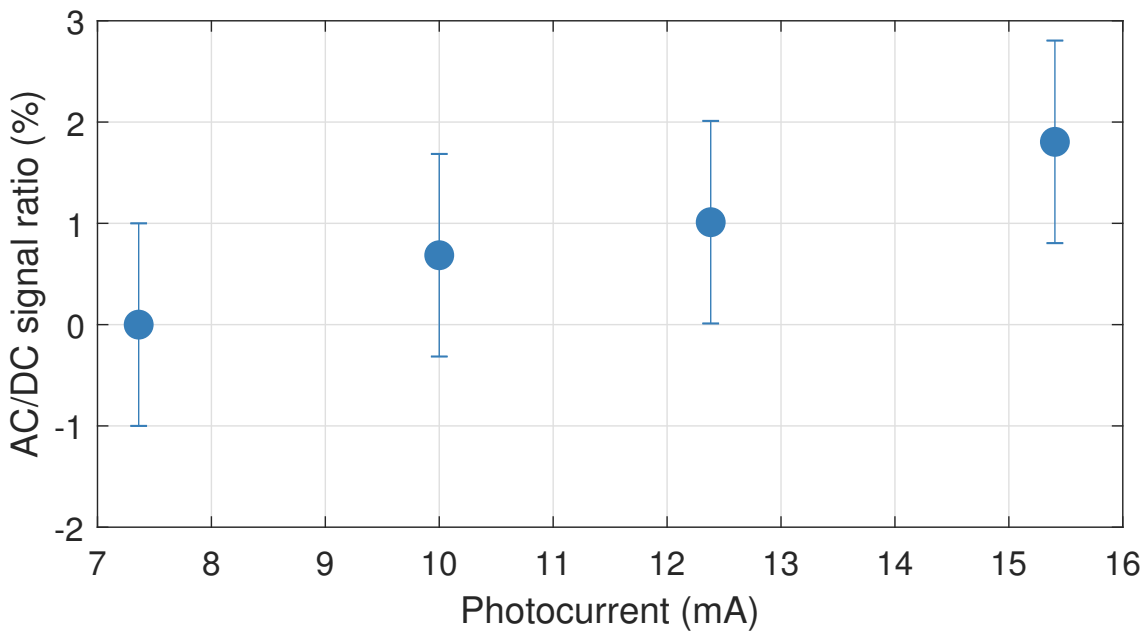


Figure 6.4: The bias of the FD10D was set to 0.6 V, and it was exposed to a series of different power levels to check at what photocurrent the photodiode would saturate at. This was done by measuring the height of the calibration peak; if this peak decreased in size relative to the DC signal then this would indicate the photodiode was saturating. This peak could only be measured to within 1%, and so the FD10D showed no sign of saturation under these conditions.

Low dark currents were expected, so a transimpedance amplifier with higher gain than in Section 6.4 was used. This circuit, shown in Appendix B.1, could measure current noise of at least  $0.2 \text{ pA}/\sqrt{\text{Hz}}$  between 10 Hz–1000 Hz.

The photodiodes were placed in a light tight box while the measurements were being made. Measurements of the dark noise of photodiodes at room temperature are reported in Section 6.5.1. As the dark noise of a photodiode depends on its temperature, an experiment was performed to explore this dependency (see Section 6.5.2).

### 6.5.1 The Dependence of Dark Noise and Dark Current on Reverse Bias in Extended InGaAs Photodiodes

The dark noise of the FD10D as a function of reverse bias was measured in a lab with a stable temperature of  $\sim 21^\circ\text{C}$ . The dark noise of the FD10D is shown in Figure 6.5. The dark noise for the rest of the photodiodes listed in Table 6.1 can be found in Appendix A.1. The dark noise at 10 Hz and the dark current as a function of bias for each photodiode is shown in Figure 6.6. The noise at 10 Hz was determined by either reading the value from the corresponding graph in Appendix A.1 or by fitting a  $1/f^\beta$  slope to the data and inferring the noise from the fitted line. Not all photodiodes had a simple noise spectrum; however, usually, the spectrum would fall as  $1/f^{0.5}$ .

When there were duplicate photodiodes to choose from, the superior photodiode

was selected for characterisation. This was done by measuring the dark noise of the photodiodes under their maximum reverse bias and choosing the one with the lower noise. There can be a significant variation in quality within a batch of photodiodes. It is shown in Figure 6.7 that there was a difference of two orders of magnitude in the dark noise between two nominally identical photodiodes. This could be due to the photodiodes having significantly different numbers of defects or because the worse one was damaged prior to purchase.

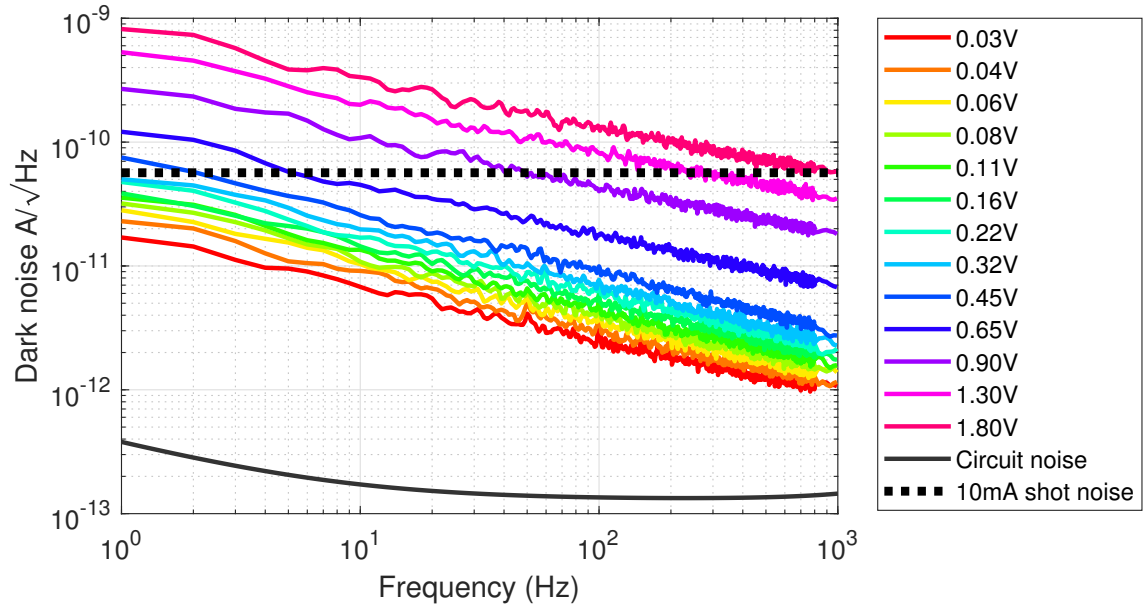


Figure 6.5: The dark noise of the FD10D increases as its reverse bias is increased. Above 0.6 V, the dark noise of the FD10D would limit the noise of a 10 mA current above 10 Hz. As the noise spectral densities have no knees, the function  $A/f^\beta$  can be fitted to the data. See Appendix A.1 for the dark noise spectra of other photodiodes. Below 0.9 V reverse bias, the spectra fall as  $f^{-0.45}$  and above 0.9 V bias the spectra fall as  $f^{-0.4}$ . The values for  $\beta$  are typical for ‘ $1/f$ ’ noise [196]. The dark noise at 10 Hz for each reverse bias is shown in Figure 6.6 alongside the results for the other photodiodes that were tested.

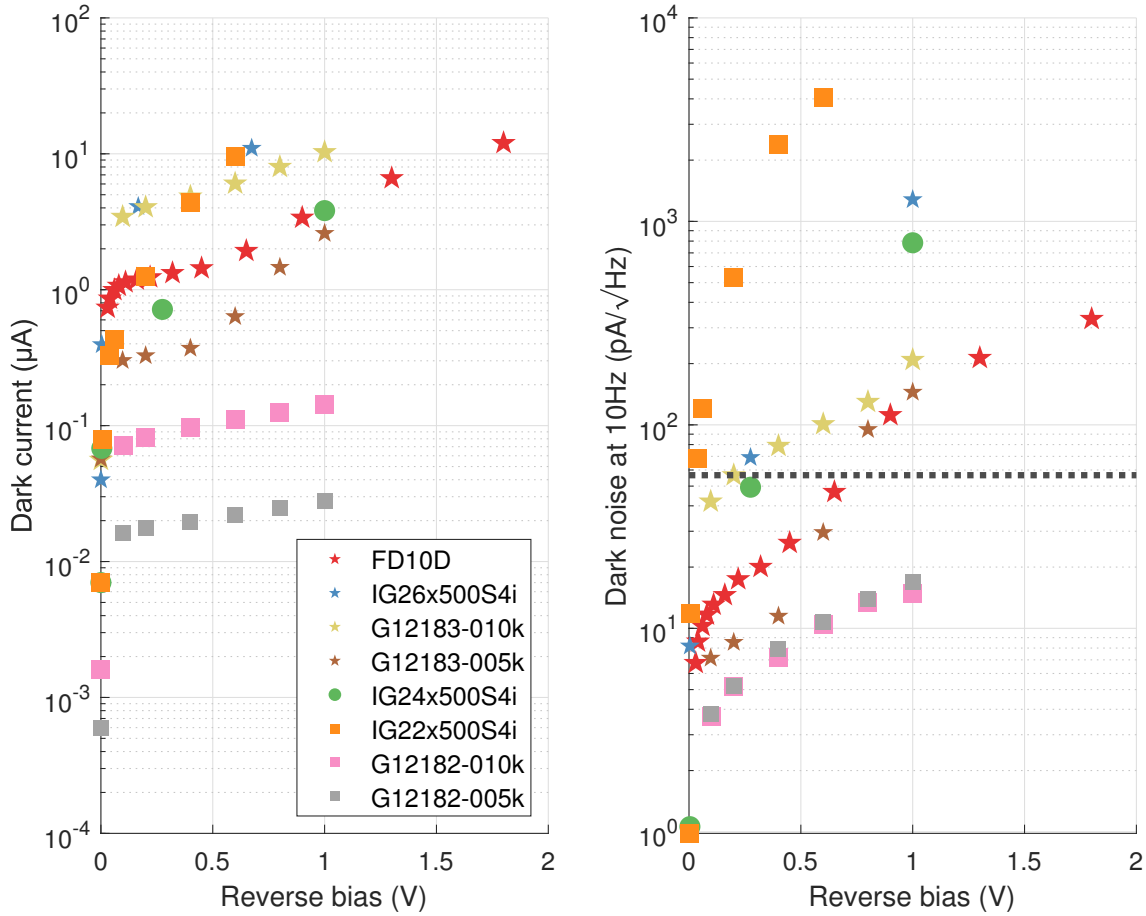


Figure 6.6: Left panel: the dark current for each photodiode was measured. Photodiodes of a similar cut-off wavelength share the same marker shape. The 1 mm photodiodes have larger markers than the 0.5 mm photodiodes. See Table 6.1 for information about the size and cut-off wavelength for each photodiode. Right panel: the dark noise at 10 Hz for each photodiode. The dashed line indicates the shot noise for a 10 mA current. The data used to create these plots are shown in Appendix A.1.

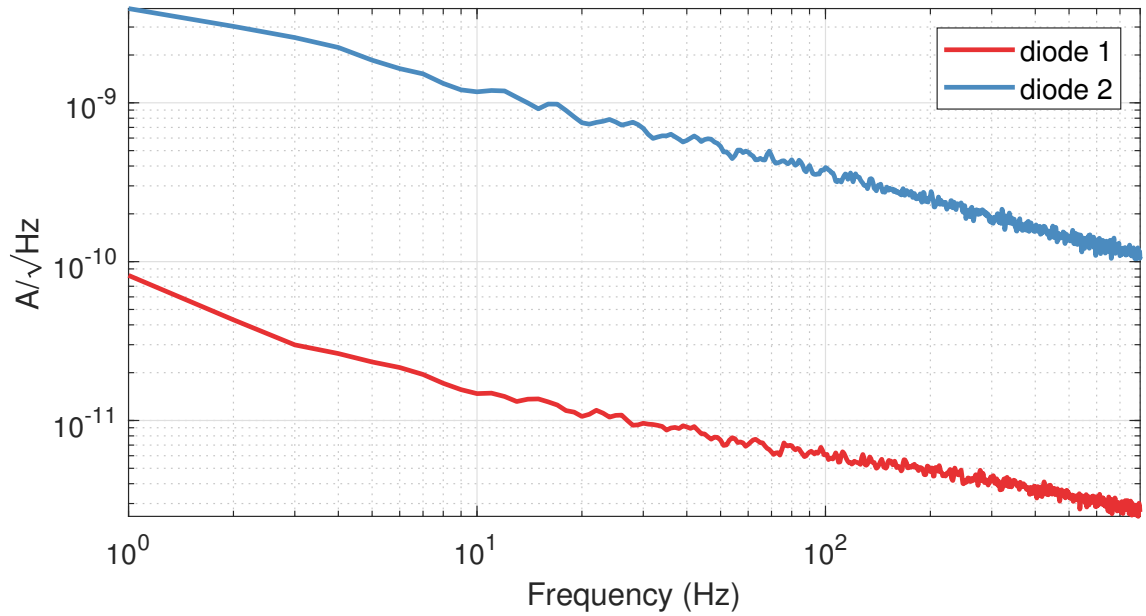


Figure 6.7: The difference in dark noise between two nominally identical photodiodes (g12182-010k) under the same operating conditions (room temperature at 1 V bias). Photodiode 1 performs nearly 100 times better than photodiode 2. For the duration of this experiment, the photodiodes were handled with suitable ESD precautions. This difference in noise may be explained by differing numbers of defects or by ESD damage prior to purchase.

### 6.5.2 The Dependence of Dark Noise and Dark Current on Temperature in Extended InGaAs Photodiodes

The lowest temperature that InGaAs photodiodes can be safely operated at typically is  $-40^{\circ}\text{C}$ , so the dark noise of the photodiodes listed in Table 6.1 was measured at a range of temperatures from  $-40^{\circ}\text{C}$  to  $30^{\circ}\text{C}$  at the maximum reverse bias specified in their datasheets. The photodiodes were glued to an aluminium block with ICEoxford cryo-varnish [209]. The temperature of the block was controlled with power resistors and a copper rod inserted into a liquid nitrogen bath. The block is shown in Figure 6.8. A computer-controlled power supply (Tenma 72-2540) was connected to the power resistors. A pt1000 temperature sensor and a multimeter (Keithley 2000), configured to make a four-wire resistance measurement, were used to measure the temperature of the block. LabVIEW was used to perform the proportional–integral–derivative calculation for temperature control of the photodiode. This program measured the temperature of the block and calculated the required voltage at which to set the power supply for the block to reach the requested temperature.

The dark noise at 10 Hz and the dark current for each photodiode is shown in Figure 6.9. The individual dark noise spectra for each photodiode at each temperature is shown in Appendix A.2. Except for the IG24x500S4i, the dark noise and dark current for each photodiode fell exponentially, as expected [199], as the photodiode was cooled.

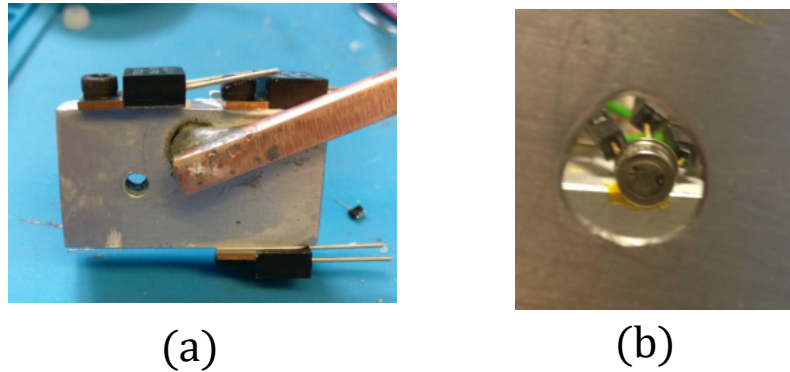


Figure 6.8: (a) The photodiode was affixed to this aluminium block. The power resistors provided heating to the block and the copper rod provided a thermal link between the liquid nitrogen bath and the block. (b) A photodiode glued with ICEoxford cryo-varnish to the block such that a considerable proportion of the photodiode was in contact with it.

The IG24x500S4i had an unexpected knee-like feature in its spectrum. Above 10 Hz, the dark noise fell as the IG24x500S4i was cooled, however below 10 Hz the noise spectra were bunched together and had a weak dependence on temperature.

## 6.6 The Saturation Limit of the IG22x1000S4i, IG24x500S4i and IG26x500S4i

The IG22x1000S4i, IG24x500 and IG26x500 were found to saturate at low power if they were biased with low enough voltage such that their dark noise was below the target. The change in the height of the calibration peak relative to the DC photocurrent was measured (see Section 6.4.1 for detail); this is shown in Figure 6.10. If the ratio between the photocurrent and the size of the calibration modulation decreases

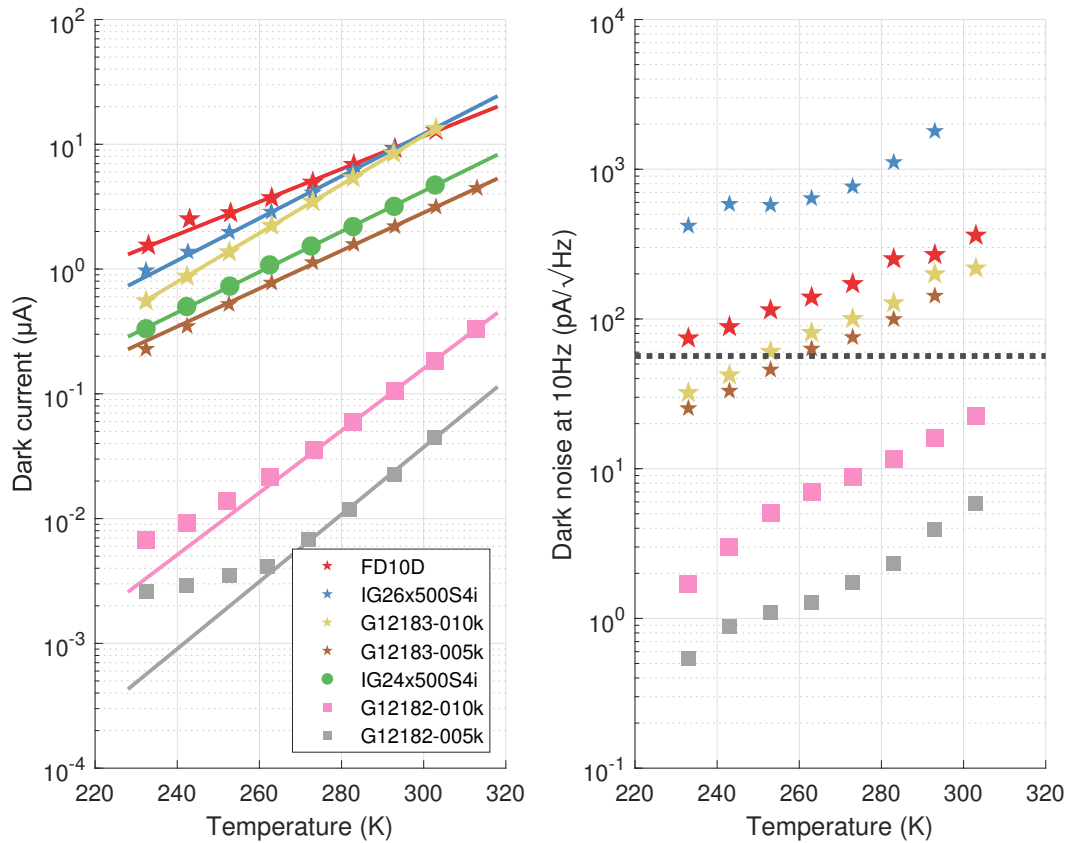


Figure 6.9: Left panel: the dark current for each photodiode at their maximum datasheet-specified reverse bias as a function of temperature. The measurement of the DC dark current approached the resolution of the multimeter around 1 nA. Exponentials were fitted to the data. Photodiodes with similar cut-off wavelengths share marker shapes, and 1 mm photodiodes have larger markers than the 0.5 mm ones. See Table 6.1 for information about the size and cut-off wavelength for each photodiode. Right panel: the dark noise of each photodiode was measured as a function of temperature. The black dashed line indicates the shot noise level for a 10 mA current. At 10 Hz, the measurements for the IG24x500S4i did not change much as the temperature changed because there was a knee around this frequency (see Figure A.13); the noise of the IG24x500S4i was 600 – 700 pA/ $\sqrt{\text{Hz}}$  at 10 Hz.

as the photocurrent increases, this indicates that the photodiode is saturating.

## 6.7 Excess Noise in the IG24x500S4i

The noise of a 1.3 mA photocurrent produced by the IG24x500S4i exceeded shot noise over a 100 Hz bandwidth around the 1111 kHz calibration modulation by a factor of 1.8. This is shown in Figure 6.11. Although 0.25 mA is already far below the photocurrent requirement described in Section 6.1, the noise was measured at 0.25 mA, and it exceeded the predicted amount by a factor of 1.2. The apparatus used and calibration method are described in Section 6.4.

Since excess broadband noise was observed, there was concern of bias voltage noise coupling to the photocurrent via the photodiode's impedance. Thus, a noise projection measurement was made. For a description of noise projection measurements, see [210]. The transfer function between the voltage at the anode of the photodiode and the output of the transimpedance amplifier was measured while 1 mA of photocurrent was being generated by the photodiode. A calibration modulation was applied to the bias voltage, and the noise at the anode of the photodiode and the noise at the output of the transimpedance amplifier were simultaneously measured. Using this method, 42.5 dB of bias voltage noise was subtracted from the measurement; however, this did not reduce the excess broadband noise. This is shown in Figure 6.12.

The equation of a diode contains a variable called the *ideality factor*. If the

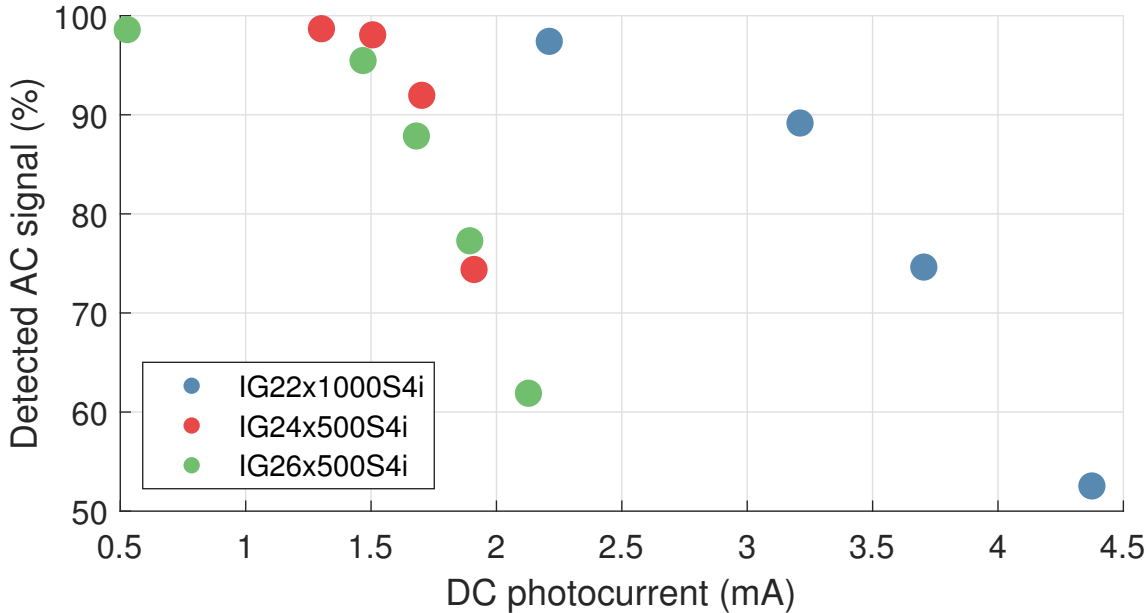


Figure 6.10: The saturation limits of the IG22x1000S4i, IG24x500S4i and IG26x500S4i photodiodes were measured. The photodiodes were biased so that their noise at 10 Hz was equal to the shot noise of a 10 mA current. The IG24x500S4i and IG26x500S4i were exposed to a beam with a  $3\sigma$  width of 220  $\mu$ m and the IG22x1000S4i was exposed to a beam with a  $3\sigma$  width of 1000  $\mu$ m. The size of the light modulation of known size was tracked as the DC photocurrent was increased. As the photodiodes saturated, the relative size of the AC signal decreased. The uncertainty in these measurements was  $\pm 1\%$ . These photodiodes had low saturation limits compared to the FD10D, which showed no signs of saturation up to 16.5 mA (see Figure 6.4).

ideality factor differs significantly from unity, additional behaviour that was not described in Section 6.2 may be occurring within the photodiode. Thus, the ideality factor of the IG24x500S4i was investigated. The equation for the I-V curve of a photodiode is

$$I = I_p + I_s \left( \exp \left( -\frac{qV_b}{nk_B T} \right) - 1 \right), \quad (6.4)$$

where  $I_p$  is the photocurrent,  $I_s$  is the saturation current of the photodiode,  $q$  is the charge of the electron,  $V_b$  is the bias of the photodiode,  $n$  is the ideality factor,  $k_B$  is Boltzmann's constant and  $T$  is the temperature of the photodiode. The current flowing through the photodiode as a function of forward bias was measured and is shown in Figure 6.13. The SciPy python function `scipy.optimize.curve_fit` was used to do an unweighted fit of the data to Equation 6.4. The photodiode was found to have  $n \sim 1$ . The  $I_p$  term in Equation 6.4 was checked by shining light onto the photodiode. This is shown in Figure 6.14.

The source of this excess noise is still unclear: the photodiode was not saturating as the calibration signal was the right level relative to the DC photocurrent, a noise projection measurement showed that the bias voltage noise was not the source of the excess photocurrent noise, and a measurement of the ideality factor was used to determine if the photodiode behaved as an ideal photodiode would. The noise cannot be explained by the Johnson-Nyquist noise of the shunt resistance of the photodiode.

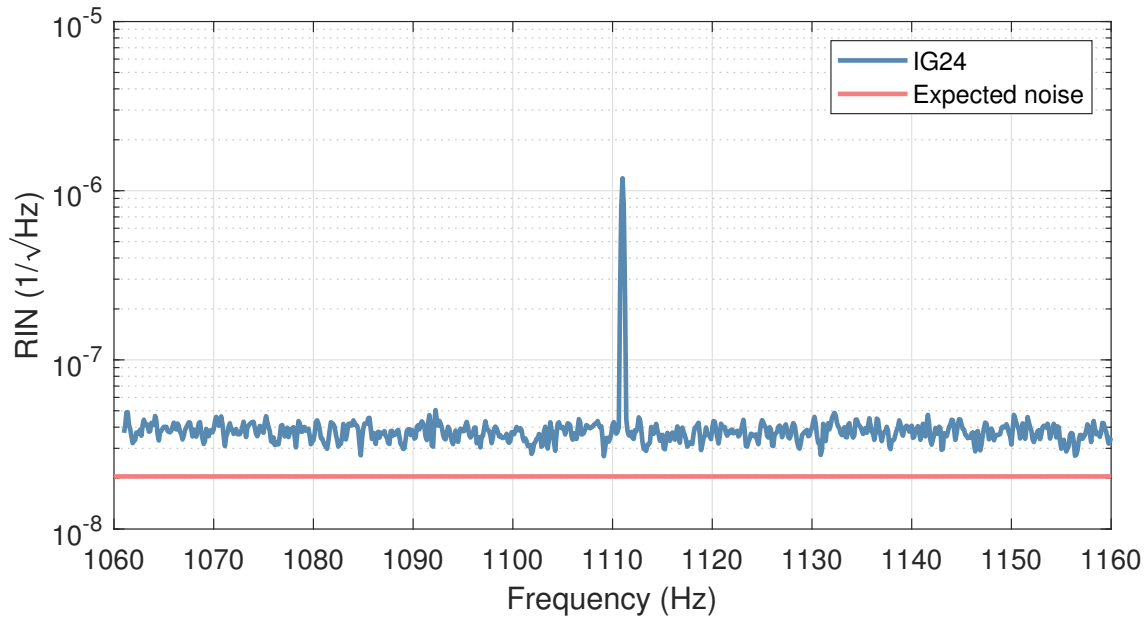


Figure 6.11: The noise of a 1.3 mA photocurrent made by the IG24x500S4i (blue) exceeded the expected amount (red) based on Equation 6.3 by a factor of 1.84. Note that the height of the 1111 Hz peak cannot be expressed in terms of amplitude spectral density units; however, this peak was measured to be the right level, so this beam was not saturating the photodiode.

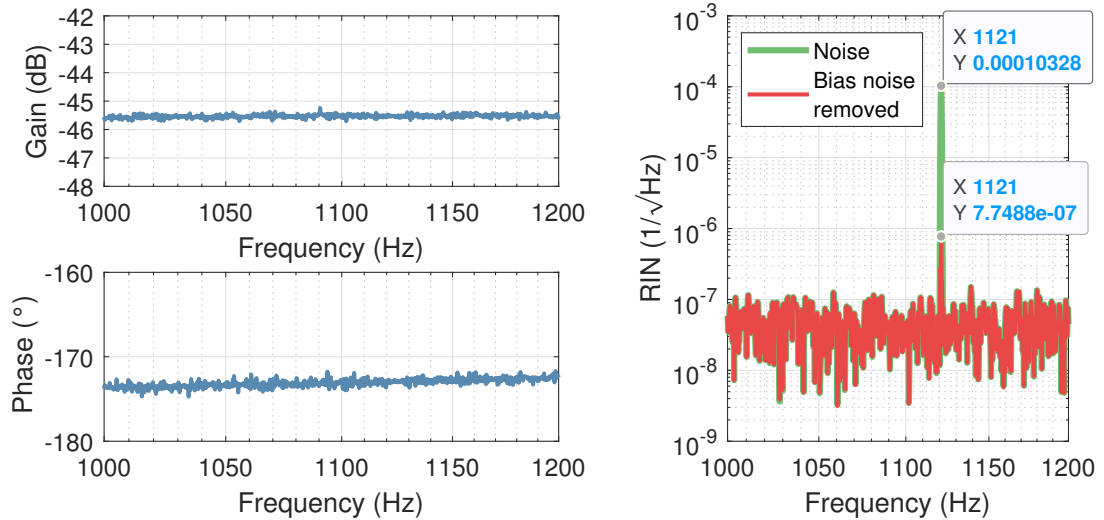


Figure 6.12: A noise projection measurement was performed to determine if the excess noise in the photocurrent produced by the IG24x500S4i (see Figure 6.11) was due to bias noise. The Bode plot of the transfer function between the photodiode’s cathode and the output of the transimpedance amplifier when the photodiode was producing 1.3 mA of photocurrent is shown in the left-hand panels. The effect of subtracting bias noise from the signal at the output of the transimpedance amplifier is shown in the right-hand panel. The peak at 1121 Hz was a modulation applied to the photodiode’s cathode; 42.5 dB of this signal was removed by using the noise projection technique, and this is approximately the amount expected from the measured transfer function (45.5 dB at 1121 Hz). However, the level of the broadband noise remained unchanged thus indicating that the excess noise witnessed in the photocurrent produced by the IG24x500S4i was not due to bias noise.

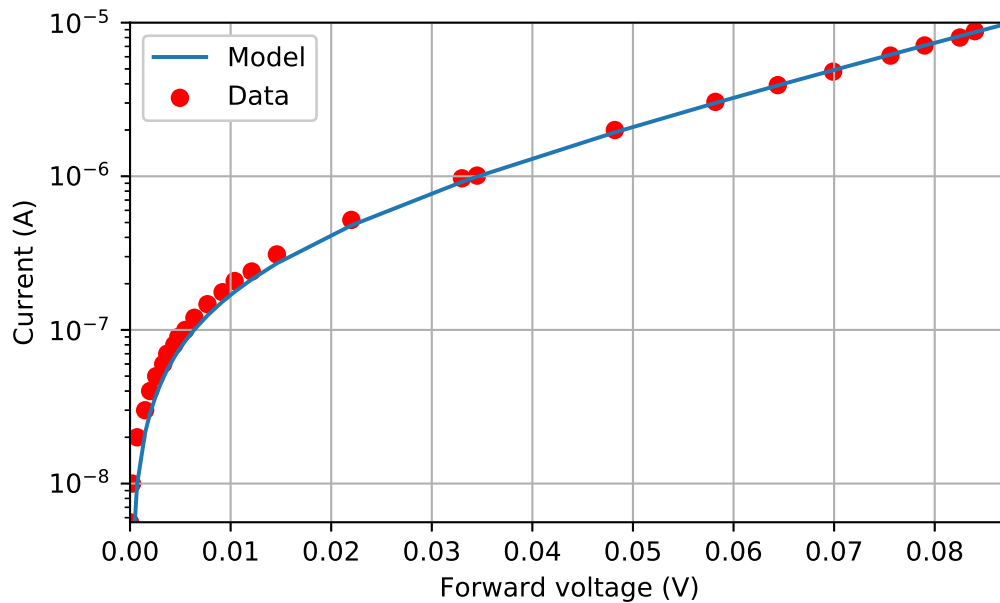


Figure 6.13: To investigate reasons why there was excess noise in the photocurrent produced by the IG24x500S4i, its ideality factor was measured (red points). Equation 6.4 was used to do an unweighted fit to the data ( $I_0 = (360 \pm 10)$  nA and  $n = 1.02 \pm 0.01$ ). The random error in this measurement is  $\sim 1\%$ , however a systematic error due to contact potential affected the data below 0.02 V . The IG24x500S4i was found to be close to ideal because  $n$  was close to unity and so this does not provide clues to the source of excess noise in the photocurrent.

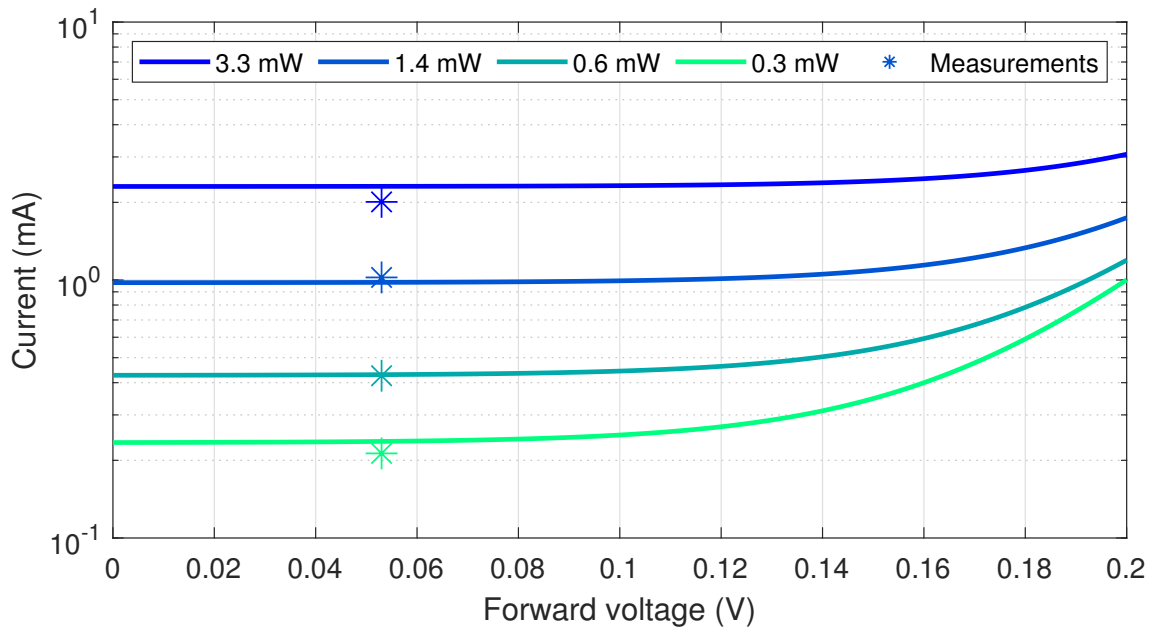


Figure 6.14: Light was shone onto the photodiode and the current produced at 0.05 V forward bias was recorded. These measurements are shown by the star shaped markers. Based on the model obtained from the data shown in Figure 6.13, the current flowing through the photodiode was predicted (shown by the lines). The model and the measurements are in good agreement with each other for 1.4 mW and 0.6 mW. The 0.3 mW measurement may have been affected by low frequency drifts in the electronics. The photodiode may have been saturating for the 3.3 mW measurement.

## 6.8 Noise Properties of an InSb Detector

InSb photodetectors are sensitive to light with wavelengths between 1  $\mu$ m – 5  $\mu$ m, and they have been used by the infra-red astronomy community (e.g. [211]). InSb detectors have near unity quantum efficiency above 2.5  $\mu$ m, and below 2.5  $\mu$ m, their quantum efficiency can exceed unity due to multi-electron processes [212]. Because InSb detectors are sensitive to light with wavelengths up to 5 $\mu$ m, they may need shielding from heat sources if they were used in a gravitational wave interferometer. While a quantum efficiency greater than unity does not necessarily correspond to worse noise performance, multi-electron processes can convert some of the detected photon energy to heat, i.e. introduce a loss mechanism.

The noise of the photocurrent produced by a Hamamatsu P5968 [213] detector was measured. The transimpedance amplifier used to measure the photocurrent is shown in Section B.1. InSb detectors must be operated at low temperatures, so liquid nitrogen was used to cool the photodiode to 77 K. The detector was characterised by covering its aperture with a low emissivity material (aluminium foil) which was at room temperature. The P5968's window lets light between 1.5  $\mu$ m – 5.3  $\mu$ m pass. The viewing angle of the detector was 60°; based on the solid angle covered by the material as seen by the detector, the expected level of thermal radiation that would be detected could be calculated. The expected photocurrent due to the aluminium foil was 5.5  $\mu$ A. The DC current from the device was measured to be 5.3  $\mu$ A, so the photocurrent can be explained by the thermal radiation of the aluminium foil. The results from this test are shown in Figure 6.15. This corresponds to the device

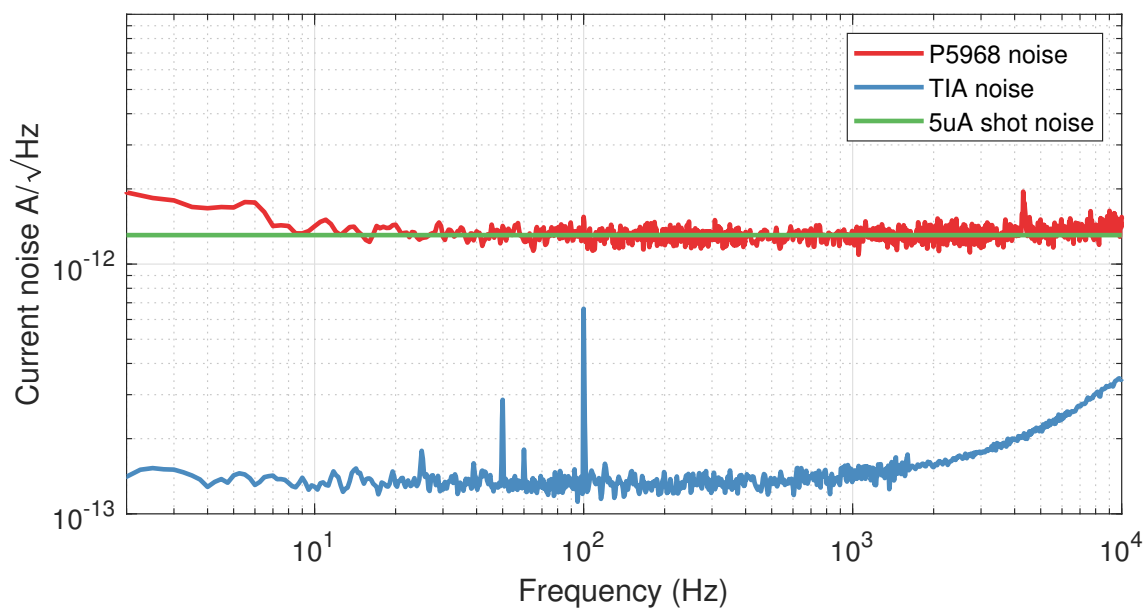


Figure 6.15: The P5968 InSb detector had its cathode grounded, and the noise of the photocurrent due to the blackbody radiation produced by room temperature aluminium was measured (red). The expected level of photocurrent was calculated to be  $5.5 \mu\text{A}$  and the measured photocurrent was  $5.3 \mu\text{A}$ . The noise of the photocurrent corresponds to shot noise (green). The noise of the transimpedance amplifier (blue) is well below the shot noise of the photocurrent.

having a quantum efficiency of  $\sim 90\%$ .

The behaviour of the P5968 under a reverse bias was investigated as the quantum efficiency of InSb photodetectors depends strongly on the reverse bias for wavelengths of  $1.55 \mu\text{m}$  [214]. A reverse bias was applied to the device, and the P5968 exhibited  $1/f$  noise. The full data are shown in Section A.3. Above  $0.2 \text{ V}$  reverse bias, the noise of the photocurrent became susceptible to bias voltage as shown in Figure 6.16. At low frequency, the noise is dominated by  $1/f$  noise, and this effect

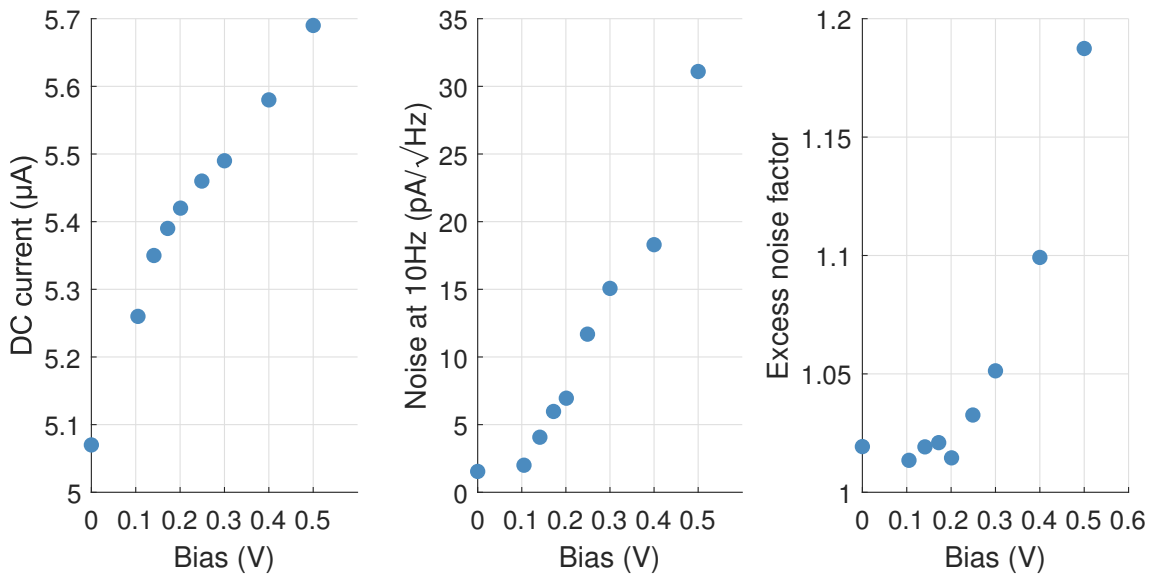


Figure 6.16: Left panel: the DC dark current of the P5968 as a function of bias. Middle panel:  $1/f$  noise rose as the bias of the P5968 was increased (see Figure A.15). Right panel: At a frequency where  $1/f$  was not present, the noise of the photocurrent was measured. The excess noise factor is the multiplicative factor that the shot noise corresponding to the DC photocurrent needs to be multiplied by to get the noise level that was measured.

depends strongly on bias. There is excess white noise that rises with reverse bias, however this depends less strongly on the reverse bias than the  $1/f$  noise does.

## 6.9 Discussion

None of the photodiodes tested in this chapter would meet the requirements described in Section 6.1 because the quantum efficiency is specified in all of their datasheets to be below 99%. Communication with four commercial manufacturers of extended InGaAs photodiodes suggest that there is no off-the-shelf photodiode capable of meeting the requirements set out in Section 6.1 [80–83]; the results in Section 6.4 and Section 6.5 support this and give insights into the best possible operating conditions for an off-the-shelf extended InGaAs photodiode. As discussed in Section 6.2, high quality extended InGaAs photodiodes are difficult to fabricate because of the lattice mismatch between the InGaAs and the InP substrate.

As only two copies of most photodiodes were available for testing, batch-level statistics cannot be obtained from these results. For instance, the FD10D reported on in this chapter has lower dark noise than the G12183-010k; however, this does not tell one if FD10Ds are generally better than G12183-010ks. Due to the nature of semiconductors with high amounts of strain, inter and intra wafer variability is expected. For example, there was a factor of  $\sim 100$  between the dark noise of the two G12182-010ks that were tested (see Figure 6.7). Whether this is due to their manufacturing or how they were handled prior to purchase is unclear, however this result shows that it may be worth buying several extended InGaAs photodiodes and selecting the best ones from them. Additionally, the results only cover seven different models of extended InGaAs photodiode, and it is possible that another photodiode manufacturer will have better performing photodiodes than the ones tested in this

chapter.

The effect that biasing an extended InGaAs photodiode can have on its quantum efficiency is shown in Section 6.4. The quantum efficiency of the FD10D was increased by 15% when its bias was set to its maximum value. This increase in quantum efficiency occurs because the depletion region of the FD10D was made larger by applying a reverse bias, and because the electron-hole pairs that are excited by the incoming photons spend less time within the depletion region when the bias is larger, thus they have a smaller chance of recombining with another hole/electron. This motivates using as large a bias as possible as the quantum efficiency of a photodiode can be greatly increased by doing this.

The high dark noise associated with the bias found in the IG24x500S4i and IG26x500S4i photodiodes (see Section 6.6) meant that they had to be operated with a low bias if they were to produce shot noise limited photocurrent at frequencies above 10 Hz. This resulted in them having a low saturation level, see Figure 6.10. To avoid this saturation limit, one could split the beam and use an array of photodiodes to detect the light. However, due to each photodiode in the array contributing the same amount of dark noise, each photodiode would need to have less dark noise compared to the case where all the light was detected on one photodiode<sup>5</sup>. Instead, better performing photodiodes could be used; for example, the FD10D showed no signs of saturation, see Figure 6.4, when operating with a bias that fulfilled the noise criteria.

---

<sup>5</sup>If dark noise is the limiting factor, splitting the light onto an array of  $k$  photodiodes makes the SNR a factor of  $\sqrt{k}$  worse. As electronic noise adds in quadrature, the SNR would be  $S/\sqrt{kn}$ , where  $n$  is the noise of an individual photodiode.

Applying a reverse bias to a photodiode reduces its capacitance, however the few hundred picofarads of capacitance that photodiodes have at low bias voltage is a manageable amount around which to design a transimpedance amplifier for a DC readout or BHD scheme (see Chapter 7). For instance, the photodiode circuit used in Section 6.4 (see Appendix B.2) has a large enough bandwidth for a photodiode used in gravitational wave interferometer and was quiet enough to be limited by the shot noise of a 10 mA photocurrent over a bandwidth relevant in ground-based gravitational wave detection.

While the dark current does not depend strongly on the reverse bias when the bias is below the tunnelling threshold, the dark noise of every photodiode increased as its reverse bias increased. Although photodiodes with higher dark current tended to have higher dark noise, the dark noise could not be predicted from the dark current. For instance, the FD10D had a larger dark current but lower noise than the IG24x500S4i. The dark current tended to be greater in larger photodiodes; this is due to larger photodiodes being more likely to have a greater number of defects as well as them having more edge-related current. However, the IG24x500S4i and IG26x500S4i photodiodes had higher dark noise than the FD10D despite them being smaller than the FD10D.

As the dark current and dark noise of a photodiode increases exponentially with temperature, the dark noise of a photodiode can be significantly reduced by cooling it. Extended InGaAs photodiodes can be purchased with thermoelectric coolers. Once the quantum efficiency and dark noise problems surrounding extended InGaAs photodiodes have been solved, the integration of such a photodiode into a vacuum

system could be investigated.

## 6.10 Conclusion

Extended InGaAs photodiodes are widely available detectors that can be used to sense 2  $\mu$ m light; however, off-the-shelf detectors do not fulfil the requirements of a photodiode that can be used in a gravitational wave detector. In particular, this is due to them not having a large enough quantum efficiency, and this leads to a relative increase in the shot noise of the detected light.

It is technically challenging to create extended InGaAs photodiodes with high quantum efficiency due to the lattice mismatch between the InP substrate and the InGaAs. While the depletion region of a photodiode can be made larger by running the photodiode with a reverse bias, the dark noise of an extended InGaAs photodiode increases when reverse biased. Measurements of the dark noise as a function of reverse bias (see Figure 6.6) and temperature (see Figure 6.9) were made to find the operating conditions which balance quantum efficiency and dark noise.

To overcome the manufacturing challenges associated with creating extended InGaAs photodiodes, a wafer would need to be commissioned. Increases in quantum efficiency can be obtained by coating the photodiodes in an anti-reflective film; however, the primary challenge of creating high quantum efficiency photodiodes is making them thick enough while keeping their defect level low. Reference [215] shows results from a photodiode with 95% quantum efficiency and a cut-off wavelength of

2.4  $\mu\text{m}$ , however due to the exponential dependence of absorption on thickness, it is still a significant challenge to reach 99% quantum efficiency. Future work may include investigating the growth conditions for extended InGaAs photodiodes.

Alternative photodiode materials could be used to detect 2  $\mu\text{m}$  light, and a range of cryogenic photodetectors have been used in infrared telescopes. We investigated an InSb detector (see Section 6.8) as InSb detectors can have near unity quantum efficiency above 2.5  $\mu\text{m}$ , however its characteristics at 2  $\mu\text{m}$  are still unclear. To investigate these, the device's window would need removing and a 2  $\mu\text{m}$  laser with several milliwatts of power would be needed because the device was not sufficiently sensitive to the laser that was available. HgCdTe is another material used to detect infrared light, and HgCdTe detectors under development by colleagues [216] could be used to make a photodiode with at least 99% quantum efficiency at 2  $\mu\text{m}$  as HgCdTe does not suffer from strain related issues; however, the optimal growth conditions for these devices has not been established, and the linearity and dark noise of such HgCdTe photodiodes is unknown.



# Chapter 7

## Shot Noise Calibration

### Measurements Based on a

### Mach-Zehnder Interferometer

Measurements of shot noise within a Mach-Zehnder interferometer were made to demonstrate that currents measured by the transimpedance amplifiers developed for some of the experiments in Chapter 6 can be linked to the wavelength of light. As a Mach-Zehnder interferometer was used, this experiment is topologically similar to a Michelson interferometer with a balanced homodyne detection scheme. A shot noise limited measurement was made in-air, and this is reported in Section 7.1.

Section 7.2 is a description of an attempt to perform this measurement in-vacuum

so that shot noise could be measured at lower frequencies, however due to scattered light, this was unsuccessful. With this apparatus, the servo required to control a suspended BHD was investigated, the effect of scattered light was measured and modelled, and the effect of misalignment on the size of a signal in a BHD scheme was investigated.

## 7.1 Shot Noise in a Mach-Zehnder Interferometer

A sketch of a Mach-Zehnder interferometer is shown in Figure 7.1. At the second beam splitter, two beams are combined to produce an interference pattern that depends on the relative phase between the two beams. This is analogous to an interferometer that uses balanced homodyne detection. In an interferometer with a balanced homodyne detection scheme, the two beams are called the signal and local oscillator, and the relative phase between the two beams ideally represents the motion of the ETMs.

The signal measured by each photodiode can be described by Equation (4.14). The shot noise of this measurement depended on the total power in the signal and LO beams, and because the power of the LO beam,  $P_{LO}$ , was much greater than the power of the signal beam,  $P_{sig}$ , the amplitude spectral density associated with the shot noise,  $n_z$ , of the detected light can be expressed in units of  $m/\sqrt{\text{Hz}}$  by

$$n_z = \sqrt{\frac{2hc\lambda}{16\pi^2 P_{sig}}}. \quad (7.1)$$

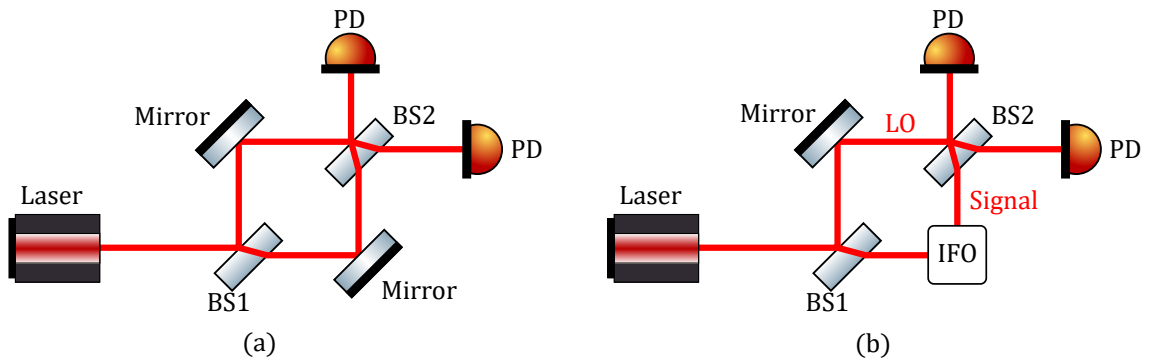


Figure 7.1: (a) Sketch of a Mach-Zehnder interferometer. The interference at BS2 depends on the difference in the phase of the two beams after BS1. (b) Sketch of an interferometer (IFO) with a balanced homodyne detection scheme. The IFO could be, for instance, a Michelson interferometer. The IFO adds a phase modulation to the signal beam, and this results in an intensity modulation in the combined beams after BS2. In essence, (b) is similar to (a).

The noise,  $n_z$ , can be interpreted as the detected relative motion between the two mirrors in the Mach-Zehnder interferometer.

### 7.1.1 Apparatus for the In-Air Mach-Zehnder.

The in-air Mach-Zehnder is shown in Figure 7.2 and Figure 7.3. It was constructed from highly stable, rigid mounts to keep the noise due to the vibration of the mounts low. The Mach-Zehnder was mounted on a thick aluminium baseplate which was isolated from the optical table by rubber dampeners. The Mach-Zehnder was acoustically shielded with a plastic box of a  $\sim 1$  mm thickness. A half-wave plate and polarised beam splitter were used to control the power entering the Mach-Zehnder and the polarisation of the light entering the Mach-Zehnder.

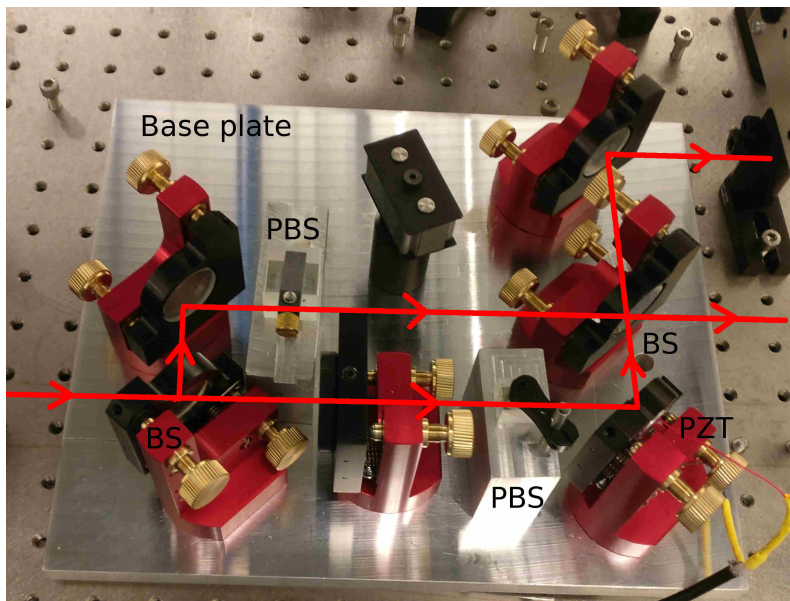


Figure 7.2: Photograph of the Mach-Zehnder baseplate. The polarising beam splitters were part of an earlier design; they were removed when the measurements with this apparatus were made.

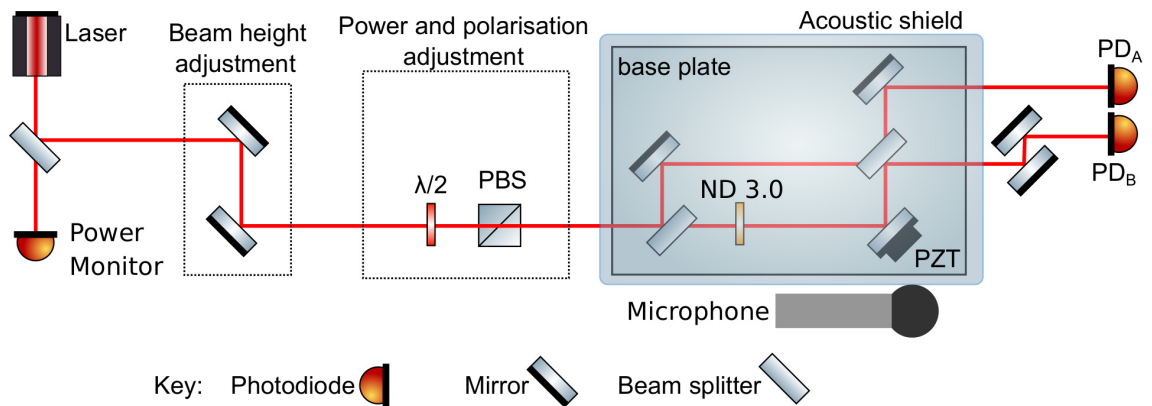


Figure 7.3: Sketch of the optical layout for the in-air Mach-Zehnder interferometer. The laser was generated by an NPRO. The power of the laser was monitored using a photodiode immediately after the laser. The beam's power and polarisation were controlled with a half wave plate and polarising beam splitter (PBS). The Mach-Zehnder was mounted on a baseplate, and it was acoustically shielded by a plastic box and rubber feet. The splitting ratio of BS2 was measured to be 50:50. A *neutral density* (ND) filter was used to decrease the power in one of the paths within the Mach-Zehnder.

The reflectivity,  $R$  and transmissivity,  $T$ , of the beam splitter on which the beams were recombined was measured to be  $0.50 \pm 0.01$ . To replicate a situation analogous to a balanced homodyne detection scheme, the power in one arm was attenuated with an ND filter. The optical density of the ND filter was found by measuring the ingoing and outgoing beam's power with the two photodiode for detecting the light exiting the Mach-Zehnder,  $PD_A$  and  $PD_B$ ; this was done by blocking the upper path and measuring the signal with and without the ND filter. The ND filter decreased the power in the signal arm by a factor of 232.

The signals from the photodiodes were measured using the same design of transimpedance amplifier as in the experiment in Section 6.4. This design gives sufficient SNR to make shot noise limited measurements for currents of  $\sim 20$  nA. The design of this amplifier is shown in Appendix B.2. The response of this photodiode circuit is flat at all frequencies of interest and is 390 V/W at DC.

The signals from the photodiodes were recorded with CDS (see Appendix C). Voltages that are measured with CDS are quantised by *analogue-to-digital converters* (ADCs). Each quantum is called a *count*. The voltages are recorded as 16 bit integers, and the peak-to-peak voltage that the ADC can record is 20 V, so the relationship between the input voltage to CDS and a count is  $20/(65536)$ . CDS features an anti-aliasing filter which affects measurements above 9 kHz. The response of the anti-aliasing filter can be seen in Figure C.2.

Cables are susceptible to common-mode noise that arises due to pickup. To avoid this problem, the signals were sent differentially to CDS. Send-receive circuits

were constructed with the THAT Corporation range of IC. A by-product of using these send-receive circuits was the signals from the photodiodes were multiplied by a factor of two.

To keep the measured signal above the digitisation noise inherent to the ADCs used in CDS, whitening filters are required. CDS noise is shown in Figure C.2. A whitening circuit boosts the AC components of a signal while keeping the DC level of the signal small enough as to not saturate CDS's ADCs. A dewatering filter is a digital filter whose transfer function is the reciprocal of the whitening filter's transfer function. For this photodiode circuit, the level of shot noise due to 20 mW of light is  $\sim 3 \times 10^{-8} \text{ V}/\sqrt{\text{Hz}}$  and the noise of CDS above  $\sim 10 \text{ Hz}$  is  $\sim 2 \times 10^{-6} \text{ V}/\sqrt{\text{Hz}}$  (See Figure C.2), so the whitening filter needs to boost the photodiode signal by  $\sim 40 \text{ dB}$ . The transfer function of the electronics for sending, receiving and whitening the photodiode signal is shown in Figure 7.4.

A servo was required to lock the Mach-Zehnder so that the light detected on both photodiodes was within 1% of each other, i.e. to within 1% of a fringe, to ensure sufficient linearity. The circuit diagram for the servo is shown in Figure 7.5. The phase between the two beams was actuated on with by moving one of the corner mirrors with a PZT. The error signal was obtained by subtracting the signals from the two photodiodes. The error signal was low pass filtered, and the corner frequency of the low pass filter was at 1 Hz. The PZT needed to be driven with a high voltage ( $\sim 100 \text{ V}$ ), so a high voltage op amp (OPA454) was used in the final stage of the servo electronics. The PZT had a capacitance, so the output of the OPA454 was followed by a resistor to prevent the op amp oscillating. This corresponded to an

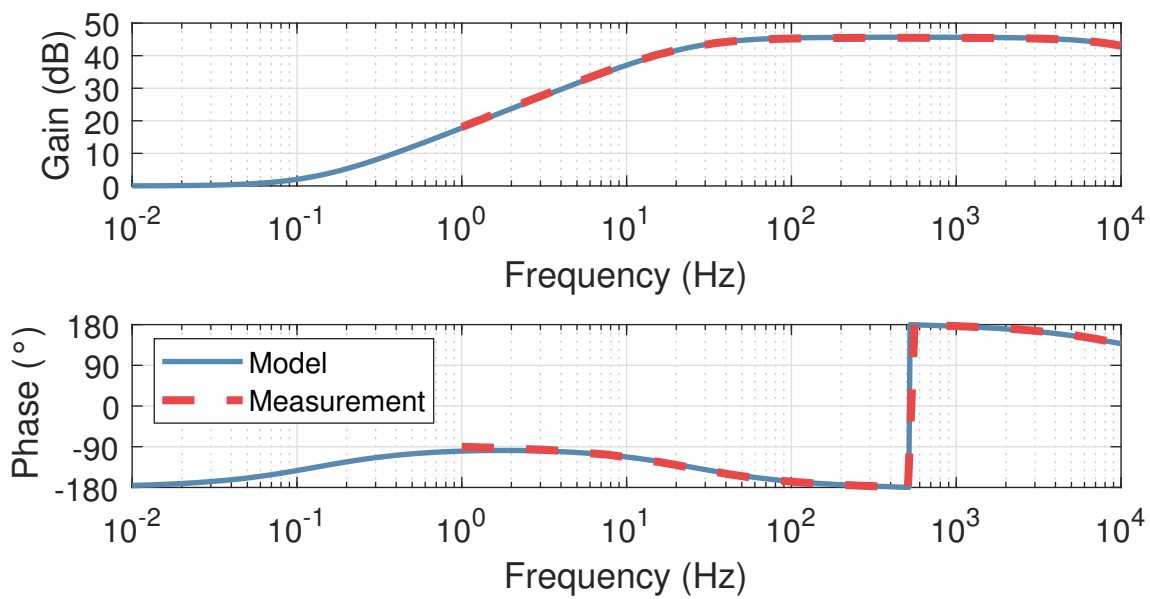


Figure 7.4: The transfer function of the electronics for the whitening the photodiode signal was modelled and measured. This gave the desired level of SNR to make shot noise limited measurements above  $\sim 200$  Hz.

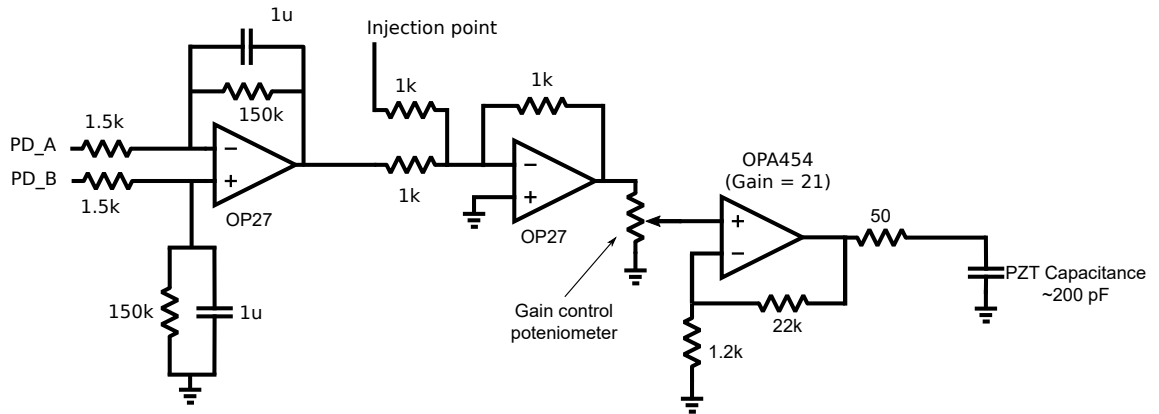


Figure 7.5: Circuit diagram for the electronics used to keep the in-air Mach-Zehnder locked to the middle of a fringe. The inputs PD\_A and PD\_B connect to two identical transimpedance amplifiers (see Appendix B.2). The first stage subtracts the signals from the photodiodes and provides a 1 Hz roll-off. The second stage allowed for a signal to be applied to the PZT. The final stage boosted the signal to around 100V. The final resistor was used to prevent the OPA454 oscillating when driving the PZT, as the PZT is a capacitive load.

additional corner frequency in the servo at  $\sim 8$  kHz. The overall gain of the servo was set with a potentiometer such that the unity gain frequency was in the stable range below 8 kHz. A way of injecting signals onto the PZT was included in the servo.

### 7.1.2 Calibration

The signal measured at the photodiodes can be calibrated in terms of the difference in path length between the two arms by applying a ramp signal to the PZT. Ramping the PZT causes the Mach-Zehnder to be driven over multiple fringes. The

ramp signal and the photodiode signals were recorded on an oscilloscope. The difference in the photodiode signals was then plotted against the measured ramp signal. One period of this signal corresponds to one wavelength, so fitting a sinusoid to the data and finding its gradient around where the subtracted photodiode signal is 0 V gives one the photodiode signal to path length conversion. This is shown in Figure 7.6. This measurement was affected by high frequency uncorrelated noise and by the quantisation of voltages recorded by the oscilloscope.

Alternatively, one can calibrate the differential path length signal by measuring the power in the two beams while they are not interfering (see Equation (4.14)). The power of the LO beam was measured to be  $(20.3 \pm 0.1)$  mW. Without the ND filter, the power of the signal beam was measured to be  $(18.3 \pm 0.1)$  mW, so with the ND filter it would be 78  $\mu$ W. The conversion between photocurrent and power was made using the responsivity found in the photodiode's (C30665) datasheet [217]. This calibration is shown in Figure 7.6, and it agrees with the calibration obtained via ramping the PZT voltage to within 10%.

### 7.1.3 Measurement of Shot Noise

The Mach-Zehnder was locked, and the difference between the photodiode signals was measured. To demonstrate that the difference in the photodiode signals depended on the differential path length of the Mach-Zehnder, a modulation at 6033 Hz was applied to the PZT. The amplitude spectral density of the difference in the photodiode signals is shown in Figure 7.7. The signal was calibrated using

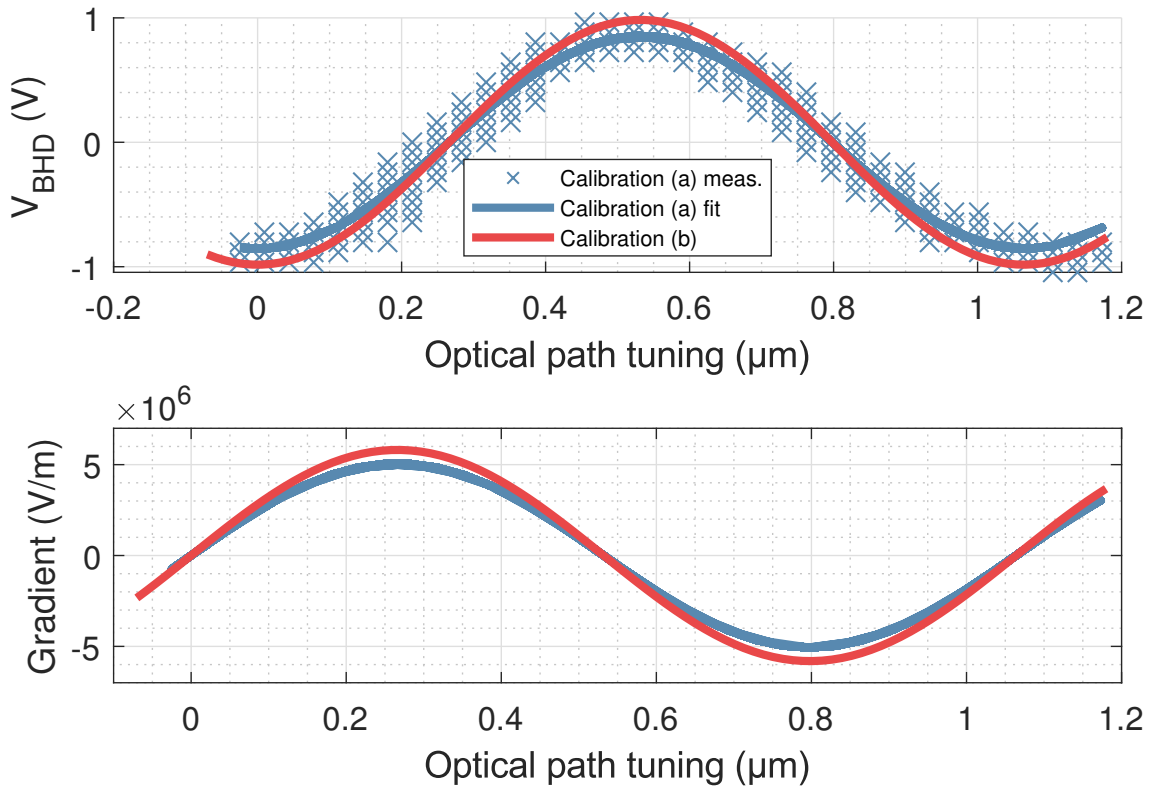


Figure 7.6: There are two ways of calibrating the differential photodiode signal that will be generated by a change in optical path length between the two paths in the Mach-Zehnder. Method (a) is to measure a ramp signal that is applied to the PZT while simultaneously measuring the photodiode signals. The measurement of this is shown by the blue crosses, and the fit to this data is shown by the blue line. Method (b) is to measure the power in the local oscillator and signal beams when they are not interfering. From this, Equation (4.14) can be used to find the response of the Mach-Zehnder. This is shown by the red line. Thus, the blue and red data are independent of each other. The two calibrations agree to within 10%. The gradient of  $V_{\text{BHD}}$  is used to get the conversion factor for a change in beam power to a change in differential path length.

the ramp technique described in Section 7.1.2. The dashed red line indicates the noise predicted by Equation 7.1, and at frequencies free of noise due to acoustic vibrations and scattered light, this matches the measured noise to within 5%. Thus, the measurement was limited by shot noise.

Below 1 kHz, scattered light and frequency noise of the laser may have affected the measurement. The laser's frequency noise can couple to the measurement via imbalances in the Mach-Zehnder's path lengths. A pessimistic imbalance of  $\Delta x = 1$  mm was assumed. The frequency noise of the laser was modelled as typical NPRO noise ( $n_f(f) = 1 \times 10^4 / f \frac{\text{Hz}}{\sqrt{\text{Hz}}}$  [119]), and the associated spectrum that would appear in the differential signal,  $x_f(f)$ , was calculated with  $x_f(f) = \Delta x \times n_f / f_{\text{EM}}$ , where  $f_{\text{EM}}$  is the laser's frequency.

Every interface which light is incident upon produces scattered light, and scattered light can be a source of noise. Scattered light that is reflected from a surface which is moving will be phase modulated, and if the scattered light interferes with the signal beam on the photodiode, these phase modulations will be converted into intensity modulations and thus will contribute to the photocurrent. To estimate the noise that is due to scattered light, a phase modulated signal,  $A \exp\left(\frac{\omega_m}{\Omega} \sin(\Omega t)\right)$ , was fit to the data. The frequency at which the scattering surface is moving is known as the modulation frequency, and this is represented by  $\Omega$ . The amount by which the frequency is changed by, represented by  $\omega_m / \Omega$ , is known as the modulation index. For more information, see reference [44].

A likely source of motion is the air-con, and this drives modulations at 20 Hz, so

## 7.2. Noise in an In-Vacuum Mach-Zehnder Interferometer and the Effect of Misalignment Between the Local Oscillator and Signal Beam

$\Omega = 2\pi \times 20 \text{ rad s}^{-1}$ . From Figure 7.8, one can see that  $\omega_m \sim 2\pi \times 1000 \text{ rad s}^{-1}$ . By computing the power spectrum in terms of relative intensity units and integrating over the frequency, and dividing by two<sup>1</sup>, one can estimate the squared amplitude of scattered light relative to the DC light power (see e.g. [218]). For this experiment, 300 fW of scattered light could explain a significant amount of the noise below 1 kHz.

The measurement of shot noise reinforces the measurements made in Chapter 6. The power of the light was measured using the same range of InGaAs photodiodes in both experiments, and the measurement of shot noise in the Mach-Zehnder links the power of light and photocurrents to the position of a mirror, so analogies between the results in Chapter 6 and shot noise in an interferometer can be made.

## 7.2 Noise in an In-Vacuum Mach-Zehnder Interferometer and the Effect of Misalignment Between the Local Oscillator and Signal Beam

To measure shot noise in an interferometer at frequencies around 100 Hz, the frequency band of interest in a gravitational wave detector, suspended optics are used in vacuum to reduce acoustic and seismic noise. There was an opportunity to perform the experiment from Section 7.1 in-vacuum with left-over apparatus built by others for a previous experiment [219]. The photodiode circuits used in this experiment were, however, made by the author. Ultimately, scattered light

---

<sup>1</sup>The modulating term in the interference between the LO field,  $E_{\text{LO}}$ , and the scattered light field,  $E_s$ , is from the cross-terms of  $(E_s + E_{\text{LO}}^*)(E_s^* + E_{\text{LO}})$ .

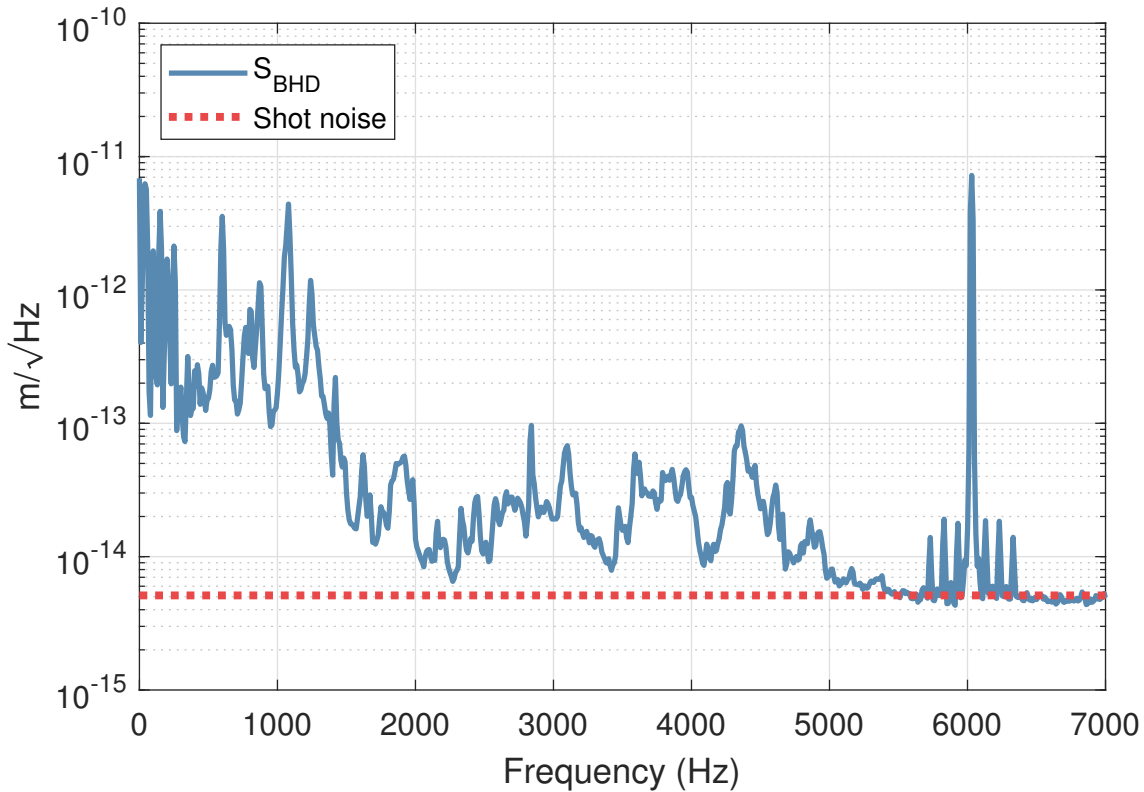


Figure 7.7: The amplitude spectral density of the difference between the two photodiodes' signals ( $S_{\text{BHD}}$ ) is shown in blue. The peak at 6033 Hz was injected to demonstrate this measurement corresponds to differential arm length modulations. The expected shot noise is based on Equation (7.1), and this is shown by the dashed red line. The noise measured at frequencies above 5500 Hz is within 5% of the expected shot noise. Below 5500 Hz, acoustic noise limited the Mach-Zehnder's sensitivity. Above 7000 Hz, the data was affected by the anti-aliasing filter in CDS. This plot is for emphasising the shot noise limit of the measurement in metres; for an analysis of the noise due to scattered light, see Figure 7.8.

7.2. Noise in an In-Vacuum Mach-Zehnder Interferometer and the Effect of Misalignment Between the Local Oscillator and Signal Beam

---

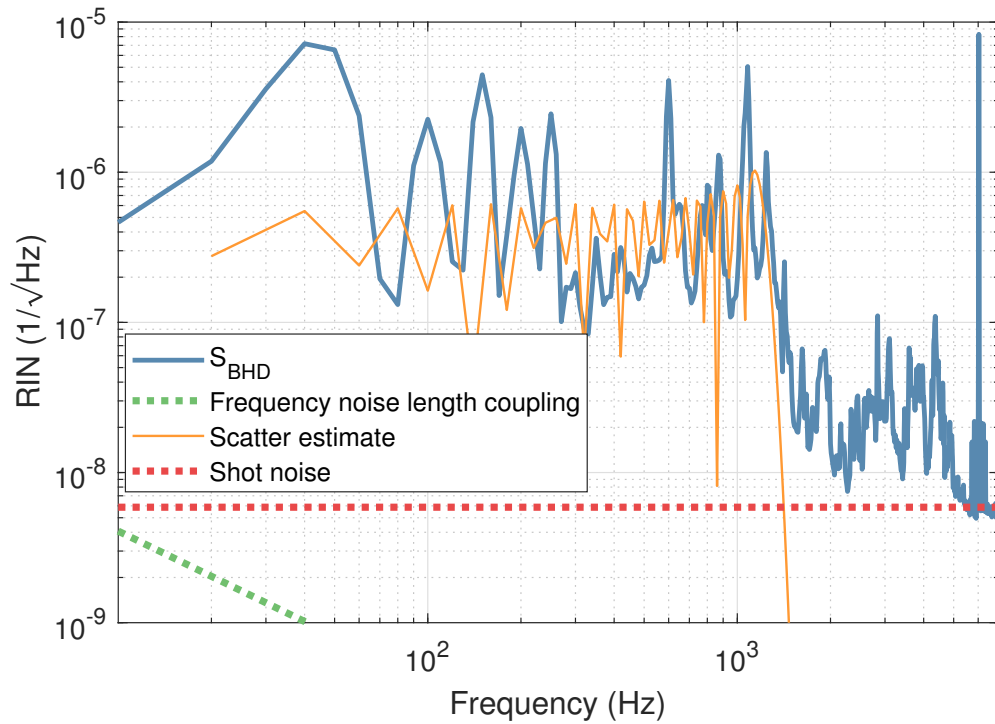


Figure 7.8: The amplitude spectral density of the difference between the two photodiodes' signals ( $S_{\text{BHD}}$ ) is shown in blue. The frequency noise that couples via a difference in path lengths between the two arms was estimated, and this is shown in green. The estimated spectrum due to 300 fW of scattered light is shown in yellow.

interfering with the light detected by the photodiodes meant that shot noise could not be measured at any frequency. However, this apparatus was used to explore the effect of misalignment between the local oscillator and the signal beam.

### 7.2.1 Apparatus for the In-Vacuum Mach-Zehnder

The Mach-Zehnder was constructed in a vacuum system which was pumped down to 1 mbar to provide adequate acoustic isolation. An NPRO was used to provide the laser light. A sketch of the layout is shown in Figure 7.9, and photographs of the equipment are shown in Figure 7.10.

The input steering mirrors, corner mirrors and input beam splitter of the Mach-Zehnder were housed in identical suspensions. These suspensions were double pendulums with masses of 75 g separated by wires with lengths of 100 mm (top to middle mass) and 150 mm (middle to bottom mass). This resulted in them having longitudinal resonances around  $\sim 1$  Hz. The rigid body modes of the suspension were reduced with eddy-current dampers on the upper mass of the suspension. More detail on these suspensions can be found in [220, Chapter 5]. The angles of incidence were controlled with CDS.

The balanced homodyne detector platform was a suspended assembly that included the recombination beam splitter, steering mirrors for the recombined beams and photodiodes. The transimpedance amplifiers for the photodiode signals were the same as the ones used in the in-air experiment (see Appendix B.2).

7.2. Noise in an In-Vacuum Mach-Zehnder Interferometer and the Effect of Misalignment Between the Local Oscillator and Signal Beam

---

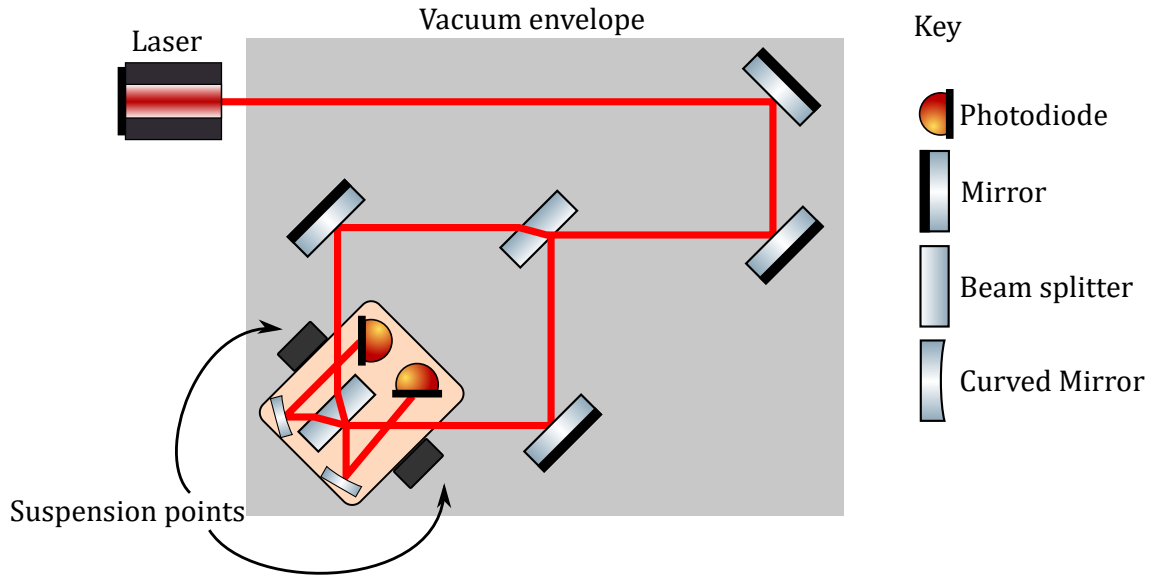
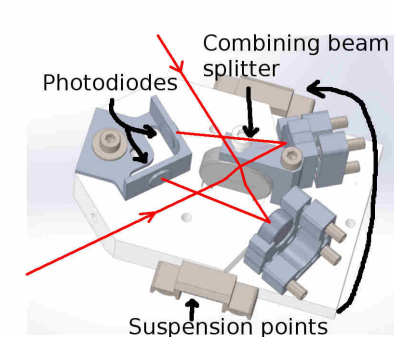


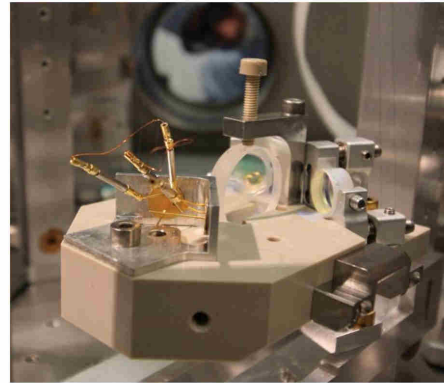
Figure 7.9: Sketch of the in-vacuum Mach-Zehnder. Laser light entered the vacuum system and was steered by suspended optics into a Mach-Zehnder interferometer. The first beam splitter and the two corner mirrors were in identical suspensions. The suspensions are described in Section 7.2.1. The beam splitter for recombining the beam was part of a larger suspended assembly which also included steering mirrors and the photodiodes. Photographs of the components are shown in Figure 7.10. The mirrors and the beam splitter were suspended with identical suspensions, and the recombining beam splitter was part of a larger assembly.



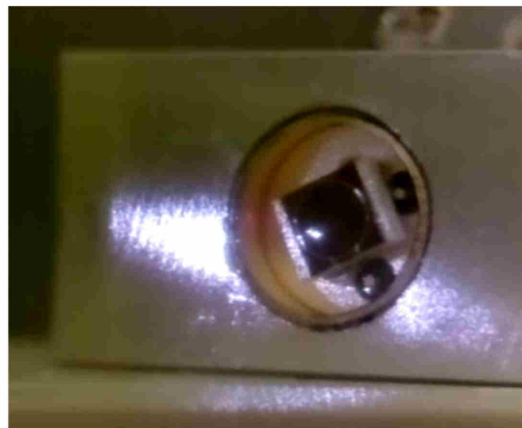
Suspended mirror



BHD PlatformCAD



BHD Platform



Scattered light on photodiode

Figure 7.10: Photographs of the components used for the in-vacuum Mach-Zehnder. The scattered light originated from the uncoated back faces of the curved steering mirrors on the balanced homodyne detector platform. The design of the suspended mirrors is discussed in [220, Chapter 5]. The photograph of the suspension was used by courtesy of Jan-Simon Hennig.

### 7.2.2 Calibration and Locking of the In-Vacuum Mach-Zehnder

To lock the Mach-Zehnder, its differential arm length needed to be controlled below the main resonance of the suspensions ( $\sim 1$  Hz) because the optics moved on the order of one wavelength at these frequencies. There were many modes per suspension<sup>2</sup> that coupled to the longitudinal signal around 30 Hz because of the design of the balanced homodyne detector platform. The optical bench moved a large amount at frequencies near 30 Hz due to insufficient seismic isolation, thus the combination of this and the design of the balanced homodyne detector platform meant the differential arm length noise was at a similar level at  $\sim 30$  Hz as it was at  $\sim 1$  Hz. Additionally, scattered light caused there to be a high amount of noise in the error signal.

To lock the Mach-Zehnder's differential arm length, one of the suspended corner mirrors was actuated on with a magnet and coil. The coil acted on a magnet glued to the bottom stage of the pendulum, therefore the actuator's strength fell as  $1/f^2$  above the suspension's resonance. Thus, to control both the 1 Hz motion and the 30 Hz motion, the coil would need to drive a large signal at 1 Hz, as well as one that was 1000 times greater at  $\sim 30$  Hz.

Because of the steep roll-off of the actuator, the servo could not control the 30 Hz features and 1 Hz features as a servo with that bandwidth would saturate on the 30 Hz components i.e. it would use up all the available electronic range and

---

<sup>2</sup>For a two stage suspension, you can have two modes for each of: longitudinal, pitch, yaw, roll, vertical and sideways.

the *digital-to-analogue converters* (DACs) would saturate. Therefore the unity gain point had to be kept well below 30 Hz such that residual feedback at 30 Hz did not lead to saturation.

The transfer function of the servo is shown in Figure 7.12, and a sketch of the servo is shown in Figure 7.11. The servo consists of five logical blocks: the coil-driven suspended mirror, the ‘optical transfer function’ that represents a change in differential arm length and a change in the power of the recombined beams, the photodiode circuit, the analogue to digital/digital to analogue converters, and the digital filtering. As before, whitening and dewhitening was needed. The transfer function of the suspension was simulated using the model developed in [220] and the digital filters just add shaping. Therefore, to calibrate the loop, the conversion factors for the electronics and optics were measured; this is summarised in Table 7.1.

By injecting and measuring a signal across a unity gain block in the digital part of the servo (see Figure 7.11), as the ratio of the two signals gives the closed-loop gain, the model’s calibration was independently measured. This is shown in Figure 7.12. This calibration ties up to within 0.1 dB. Therefore, the unity gain point of the servo was at 5.5 Hz with 15° of phase margin.

### 7.2.3 Measurement of the Differential Arm Signal

With the servo described in Section 7.2.2, the in-vacuum Mach-Zehnder was locked. The differential arm motion’s spectral density is shown in Figure 7.13. The

7.2. Noise in an In-Vacuum Mach-Zehnder Interferometer and the Effect of Misalignment Between the Local Oscillator and Signal Beam

---

Component	Transfer function	unit
CDS ADC converter	3.3	count/mV
CDS DAC converter	0.31	mV/count
Send/receive	2	V/V
Coil driver	1.0	mA/V
Coil	10	mN/A
Suspension	$H(f)$	m/N
Mach-Zehnder	665000	$\lambda/m$
Fringe to counts	79000	count/ $\lambda$
Digital filtering	$G(f)$	count/count

Table 7.1: Elements of the in-vacuum servo and their transfer functions. The suspension transfer function,  $H(f)$ , was obtained by simulation, obtaining the digital filter's transfer function is trivial, the coil's force per current was calculated using a Mathematica script developed by Mark Barton, the rest of the transfer functions were directly measured. These values were used to produce the servo model shown in Figure 7.11.

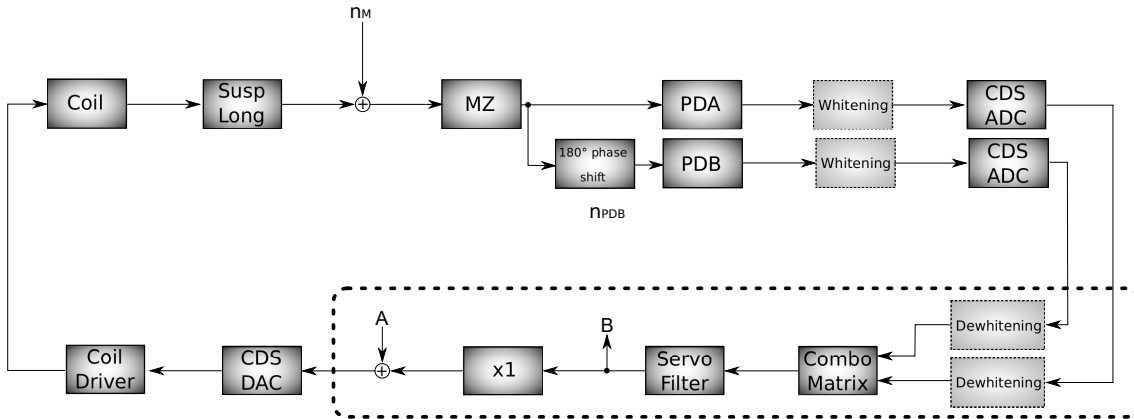


Figure 7.11: Flow diagram showing each block of the servo used to lock the in-vacuum Mach-Zehnder. The digital part of the servo is shown in the dashed area. The injection point A and measurement point B were used to calibrate the servo (see Figure 7.12) are around a times one block. The mirrors motion that the servo must correct for is represented by the signal  $n_M$ . The information about the Mach-Zehnder differential arm length is encoded by two signals that are  $180^\circ$  out of phase. The whitening and dewhitening filters are paler as these do not affect the gain of the loop.

7.2. Noise in an In-Vacuum Mach-Zehnder Interferometer and the Effect of Misalignment Between the Local Oscillator and Signal Beam

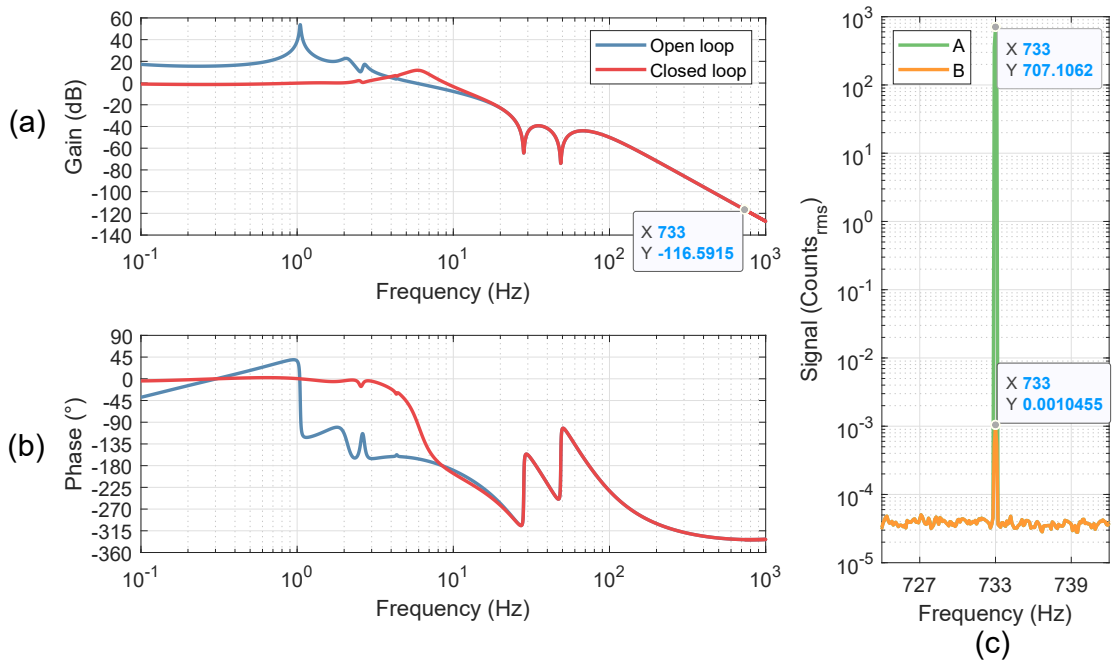


Figure 7.12: Panel (a) and panel (b) show the servo’s open and closed-loop transfer function. This was calibrated using the factors from 7.1. Panel (c) shows a measurement where a signal was injected at point A in the servo and measured at point B (see Figure 7.11); these two points are separated by a unity gain block, and so the ratio of these signals represents the closed-loop transfer function of the servo. These measurements are in agreement with the model to within 0.1 dB.

curved mirrors used to guide the beam onto the photodiodes did not have an AR coating on their back face, and this caused a large amount of scattered light (see Figure 7.10). To estimate the amount of scattered light interfering with the local oscillator, the same analysis as in Section 7.1.3 was performed. The modulation frequency was approximately 1 Hz and the modulation depth was approximately 36. From this, the power of the scattered light was estimated to be  $\sim 20 \mu\text{W}$ .

#### 7.2.4 The Effect of Misalignment on the Size of a Signal in an Interferometer

The in-vacuum apparatus was used to verify that an angular misalignment,  $\theta$ , will cause the signal,  $S_{\text{sig}}$ , to drop from its maximum value,  $S_0$ , as

$$S_{\text{sig}} = S_0 e^{-((\theta - \theta_0)/\theta_c)^2}, \quad (7.2)$$

where  $\theta_c = \sqrt{2}\lambda_{\text{EM}}/\pi w_0$  is the characteristic angle of a beam with waist  $w_0$ . As the apparatus was not perfectly aligned initially,  $\theta_0$  is included as an offset. This effect is derived in e.g. [221].

Misalignments were made by applying a signal from CDS to one of the corner suspensions. The counts to angle factor was measured by applying the largest possible angle offset that CDS could provide and measuring the distance the beam moved, a few millimetres, over a distance of the order a metre. The beam's waist was known to be  $460 \mu\text{m}$ .

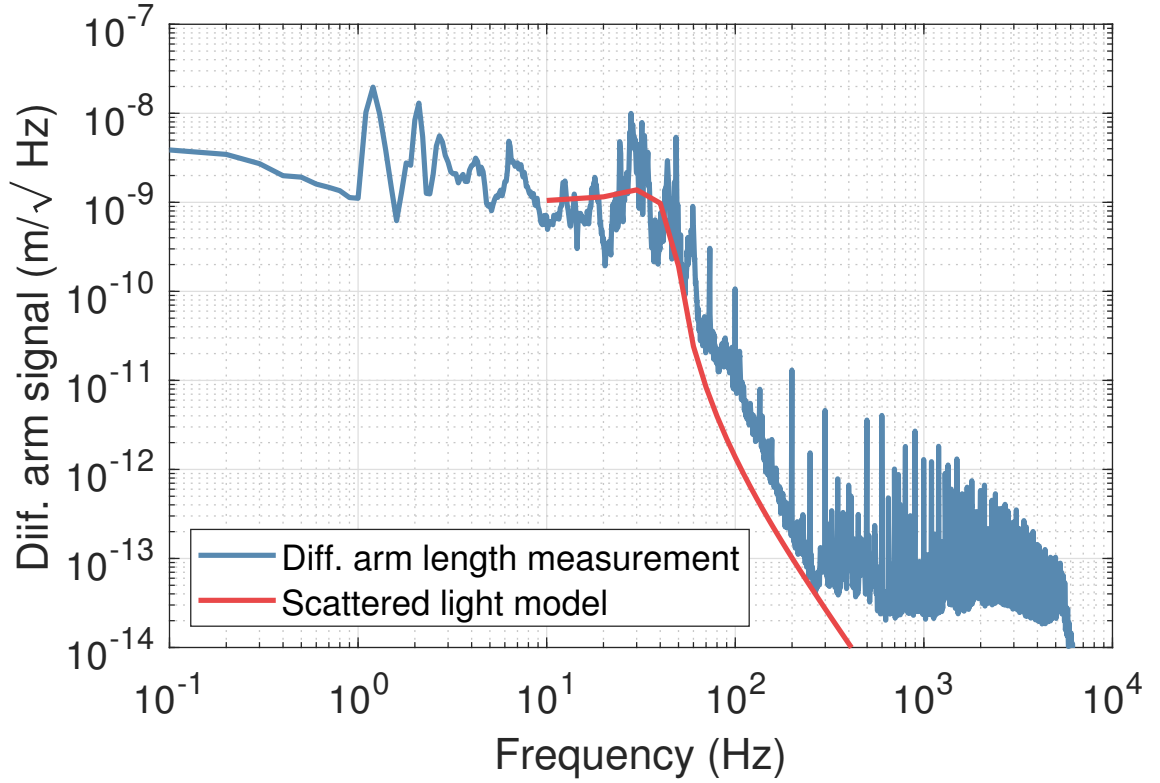


Figure 7.13: Scattering caused there to be a high level of noise in the differential arm length signal. Many peaks related to the balanced homodyne detector suspension can be seen around 30 Hz, and this motion generated phase modulations in the scattered light. The noise was caused by the interference between the scattered light and the signal-carrying light on the photodiodes. The power of the scattered light was estimated to be  $\sim 20 \mu\text{W}$ . For this measurement, shot noise would have been at  $\sim 10^{-15} \text{ m}/\sqrt{\text{Hz}}$ .

A differential arm signal was generated and the resulting photodiode signal was measured for a range of angular misalignments. This result is shown in Figure 7.14. To prevent noise at nearby frequencies from leaking into the measurement, a narrow frequency resolution was required (0.2 Hz). Around ten averages were used to measure the signal size at each misalignment. The variance of these averages was large and this is represented by the error bars shown in Figure 7.14.

A weighted non-linear least squares regression function (MATLAB's `nlinfit`) was used to fit the data to Equation 7.2, with each point weighted with  $1/\text{error}^2$ . The resulting fit parameters were  $S_0 = (6.9 \pm 0.3) \times 10^{-3}$  counts and  $\theta_0 = (0.46 \pm 0.02)$  mrad. The covariance between  $S_0$  and  $\theta_0$  was  $\sigma_{S_0, \theta_0} = 2.4 \times 10^{-9}$ , and the reduced  $\chi^2$  statistic was 3.07. Thus, the data are consistent with Equation (7.2).

### 7.3 Conclusion

The experiment reported on in this Chapter was in support of the work in Chapter 6 to do with photodiodes and the work on BHD in Chapter 4 and Chapter 5. The shot noise of a current measured with the transimpedance amplifier used in Chapter 6 was experimentally related to the displacement of a mirror in an interferometer. The measurement of shot noise is shown in Figure 7.7.

The experiment was tried in-vacuum with the aim of making shot noise limited measurements at lower frequencies so that the electronics could be calibrated in the frequency band of interest for ground-based gravitational wave detection. Due to

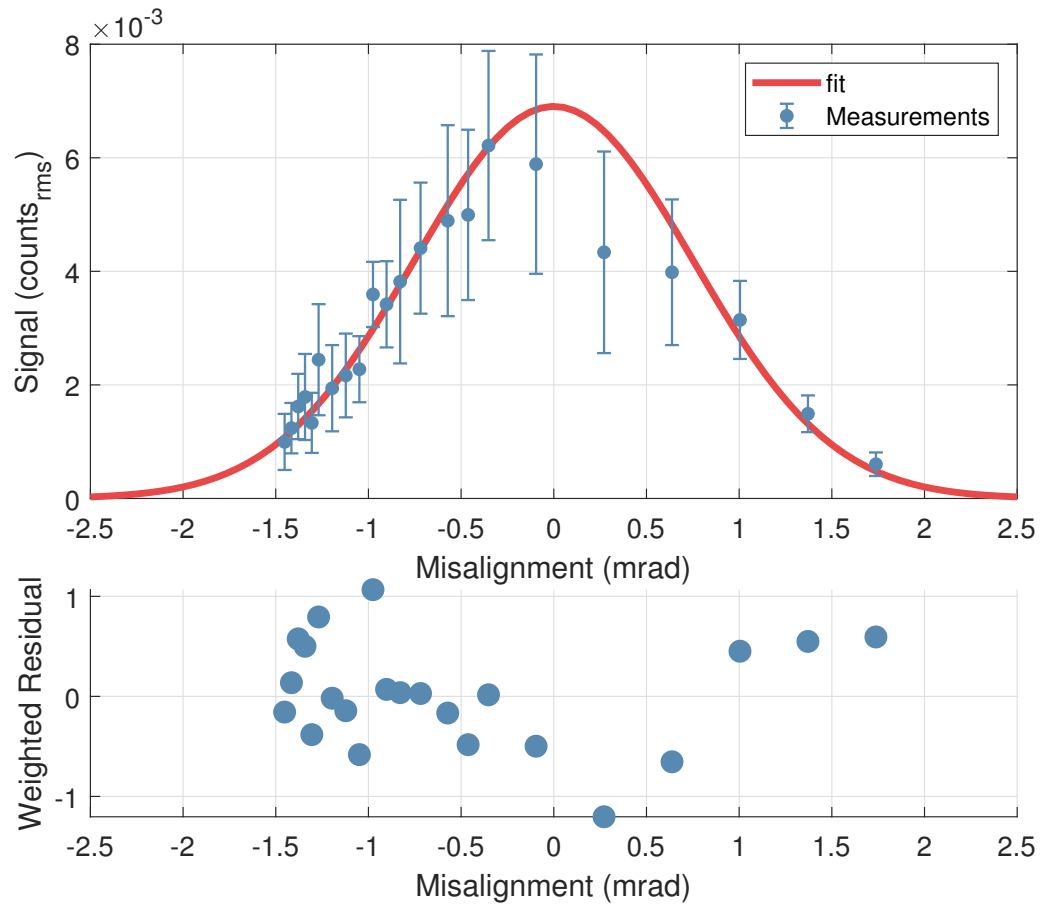


Figure 7.14: Top panel: As the Mach-Zehnder was misaligned, the signal due to the differential arm length modulation decreased. The blue points show the measured signal as a function of misalignment. The data was fit to Equation (7.2), and this is shown in red. Bottom panel: the weighted residuals of the measurements to the fit show no pattern, indicating that the model used was appropriate.

the unexpected amounts of scattering and excessive motion of the suspended optics, this was not possible. However, the in-vacuum experiment highlighted problems that may occur due to scattered light in the design of BHD or any similar interferometer. This noise was analysed in terms of the amplitude of the scattered light and the rate of change of phase of the light. This apparatus was used to gain an insight into the feedback loops required to control suspensions, and an investigation was carried out to confirm models of loss due to misalignment in interferometers/BHD.

# Chapter 8

## Conclusion

As described in Chapter 1, gravitational wave detections are made with extremely sensitive interferometers. In this thesis, technologies that will help current and future gravitational wave detectors reach their target sensitivities were analysed and characterised.

The LIGO detectors are designed to use a 125 W laser; however, the current laser can only produce  $\sim 70$  W of light. To increase the maximum power that can be delivered to the interferometers for LIGO's fourth observation run, the new lasers will use two single-pass amplifiers. In Chapter 2, the prototype for this laser was characterised. With this laser,  $\sim 100$  W of amplitude stabilised light in the HG00 mode was generated. As the pointing noise of this prototype was shown to exceed LIGO's requirement, sources of pointing noise, such as turbulence in the laser's

water-cooling system, must be kept minimal when it is commissioned to be part of the interferometer.

Two actuators for stabilising the amplitude of the prototype laser's power were investigated. These were an AOM and a current shunt on one of the pump diodes in one of the amplifiers. Because the operators of the interferometers will need to have control over the input laser power, the AOM was chosen to be the actuator used to stabilise the amplitude of the laser as it was found to behave consistently over a wider range of power.

Balanced homodyne detection is a crucial part of the upgrade from advanced LIGO to LIGO A+ since the homodyne angle must be a free parameter if the detectors are to reach the planned quantum noise by using squeezed light. The fundamentals of balanced homodyne detection and the phase noise requirement for the local oscillator were discussed in Chapter 4.

To preserve a squeezed state of light, it is essential that there is minimal loss within the detector. As part of the balanced homodyne detector upgrade for LIGO A+, active wavefront control will be used to minimise the loss due to mode mismatch between the interferometer's arm mode and the output mode cleaners. To tackle this problem, the range of interferometer arm modes that the active wavefront control will have to mode match was determined by simulation. This is described in Chapter 3. The dominant source of uncertainty in the mode emerging from the SRM comes from the uncertainty in the radius of curvatures for the optics within the SRC. The probability of a mode exiting the SRM was determined by the probability

---

of the optics within the SRC having the radii of curvature required to produce the beam. Combining this with measurements of the Gouy phase of the LLO SRC, the beam exiting the SRM was inferred to be 1.84 mm in width and to have a defocus of  $-2.80$  Dioptre.

With a set of likely modes that the adaptive optics for mode matching would need to correct for, the robustness of the active wavefront control for the balanced homodyne detector to a mode mismatch was determined. This is explored in Chapter 5. With the pessimistic assumption that the range of the active optics will be  $\pm 50$  mD, it was found that most of the likely beams that could emerge from the SRM are covered by the proposed design for the active wavefront control.

Future cryogenic ground-based gravitational wave detectors may use either  $1.5 \mu\text{m}$  or  $2 \mu\text{m}$  light. For  $1.5 \mu\text{m}$  light, photodetectors that have high quantum efficiency, high linearity, and low noise already exist. However, this may not be the case for  $2 \mu\text{m}$ . Previous experiments have been limited by the extended InGaAs photodiodes used in them. The strained nature of extended InGaAs photodiodes leads to a degradation in their performance, thus it was important to carry out the experiments described in Chapter 6 to determine if suitable extended InGaAs photodiodes already exist or whether additional research into either extended InGaAs or other photodiode technology is needed.

It was found that off-the-shelf extended InGaAs photodiodes do not meet the requirements of a third-generation ground-based interferometer under any operating conditions because their quantum efficiencies are too low. To create an InGaAs

photodiode with a high quantum efficiency, its thickness must be greater than its critical thickness and the number of defects in it must be low. This is technically challenging to achieve. The quantum efficiency of extended InGaAs photodiodes can be improved by reverse biasing them; however, when reverse biased, extended InGaAs photodiodes will exhibit  $1/f$  dark noise.

The  $1/f$  noise arises due to the generation-recombination current associated with the strain-induced defects in the extended InGaAs photodiode. The dark noise for a selection of extended InGaAs photodiodes as a function of bias and temperature was shown in Chapter 6. If biased with the maximum value stated in their datasheets, the  $1/f$  noise produced by the photodiodes would exceed the typical shot noise of the light detected by the photodiode. As expected, cooling the photodiodes caused the dark noise to be exponentially reduced.

In conclusion, if developments in mirror substrates and coatings favour interferometers using  $2\ \mu\text{m}$  light rather than  $1.5\ \mu\text{m}$  light, further research into the design and the optimal growth conditions of extended InGaAs is needed. Alternatively, similar research into other semiconductors that are sensitive to  $2\ \mu\text{m}$  light would need to be carried out.

# Appendix A

## Dark Noise Spectra of Photodiodes

The spectra in this appendix were measured for the experiments reported on in Chapter 6.

### A.1 Dark Noise as a Function of Reverse Bias

The dark noise as a function of bias for each photodiode in Table 6.1 was measured at room temperature (21°C). The results shown in this section were used to create Figure 6.6. In each figure, the shot noise of the benchmark 10 mA current is shown by a dashed line.

Appendix A. Dark Noise Spectra of Photodiodes

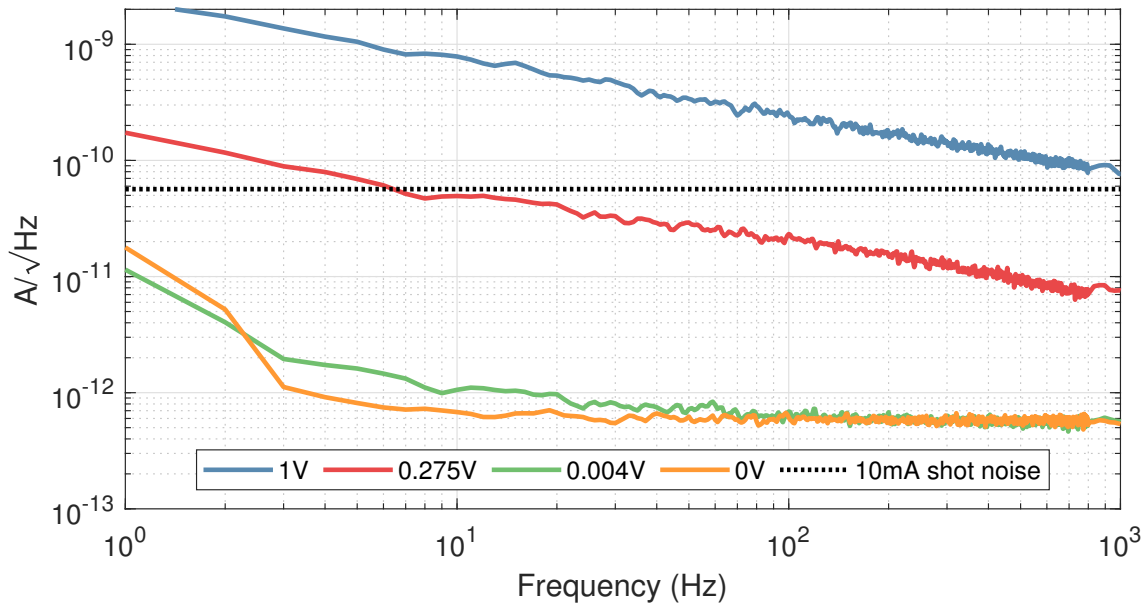


Figure A.1: Dark noise of the IG24x500S4i at 21°C for a series of reverse biases.

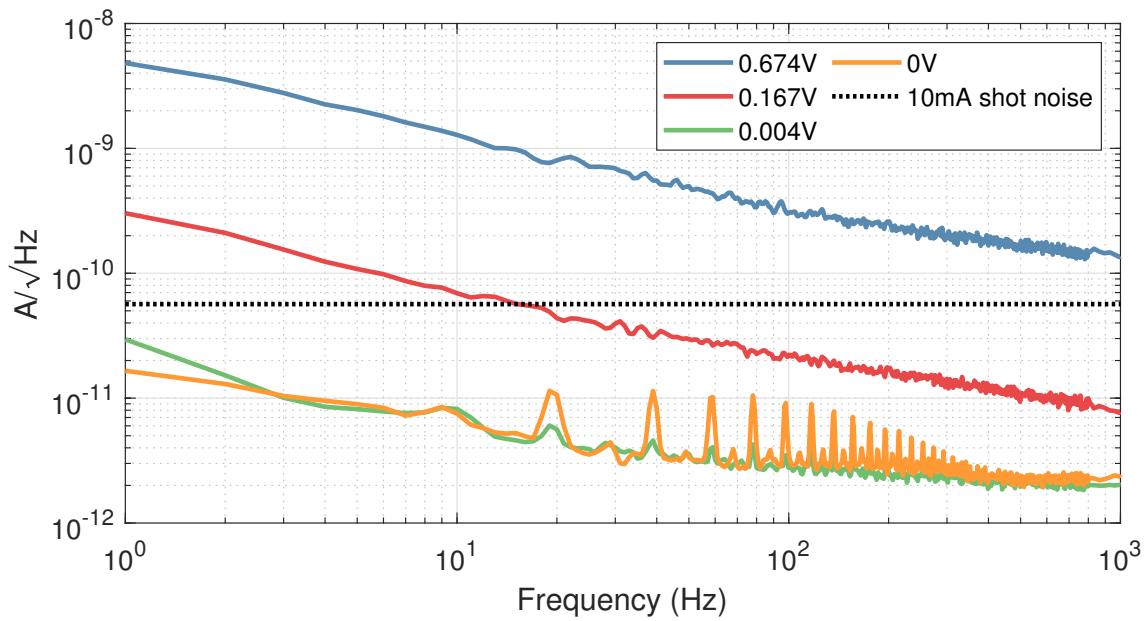


Figure A.2: Dark noise of the IG26x500S4i at 21°C for a series of reverse biases.

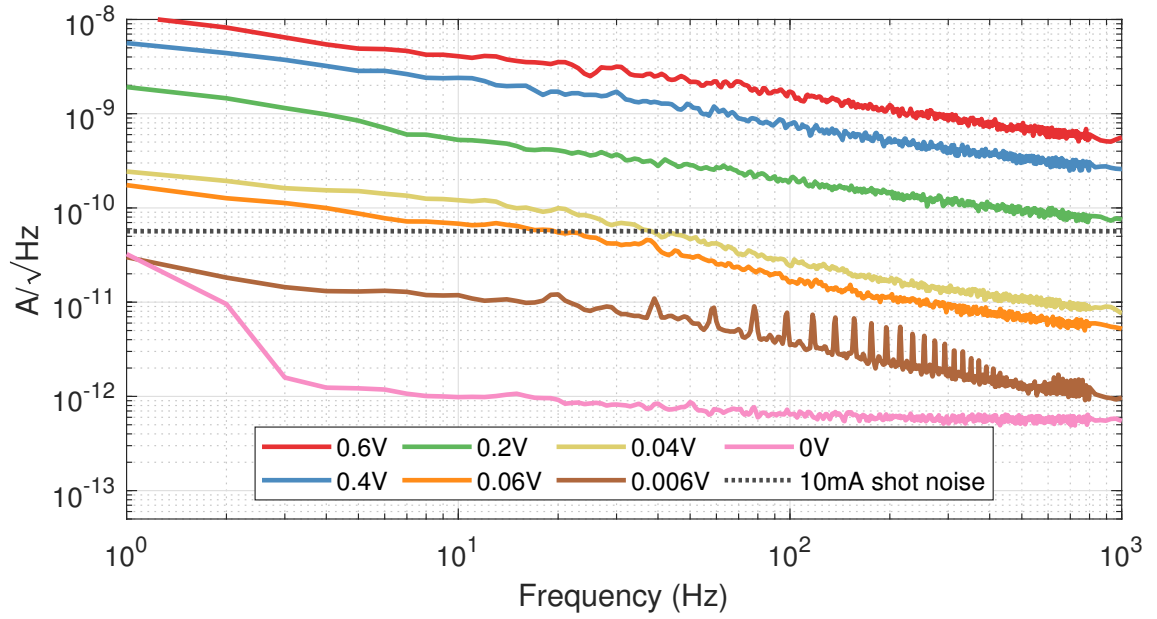


Figure A.3: Dark noise of the IG22x1000S4i at 21°C for a series of reverse biases.

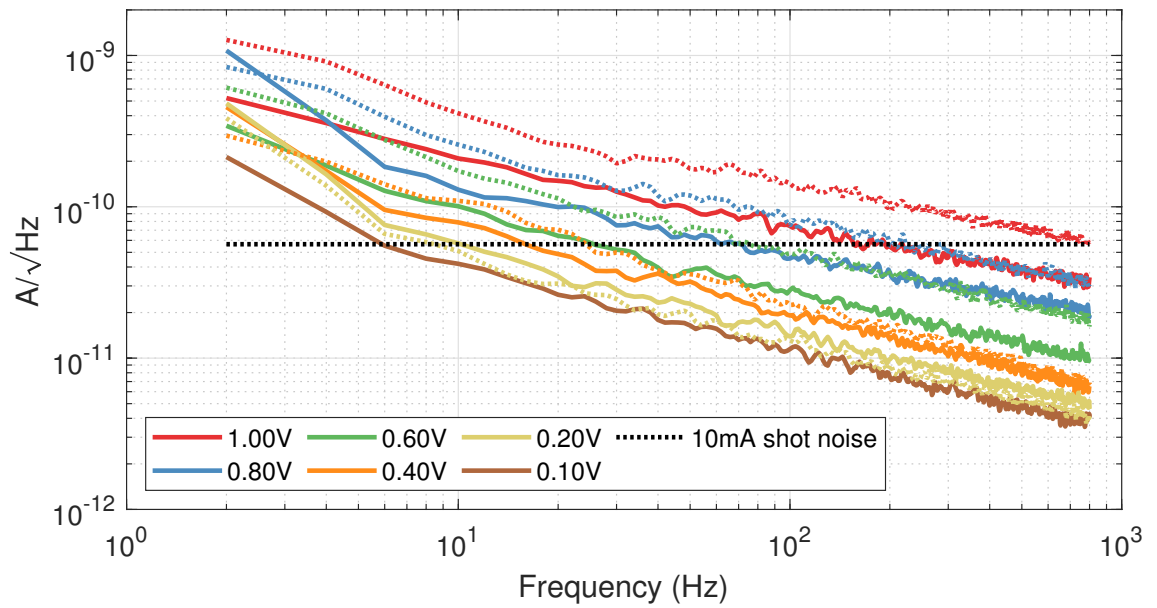


Figure A.4: Dark noise of the G12183-010k at 21°C for a series of reverse biases.

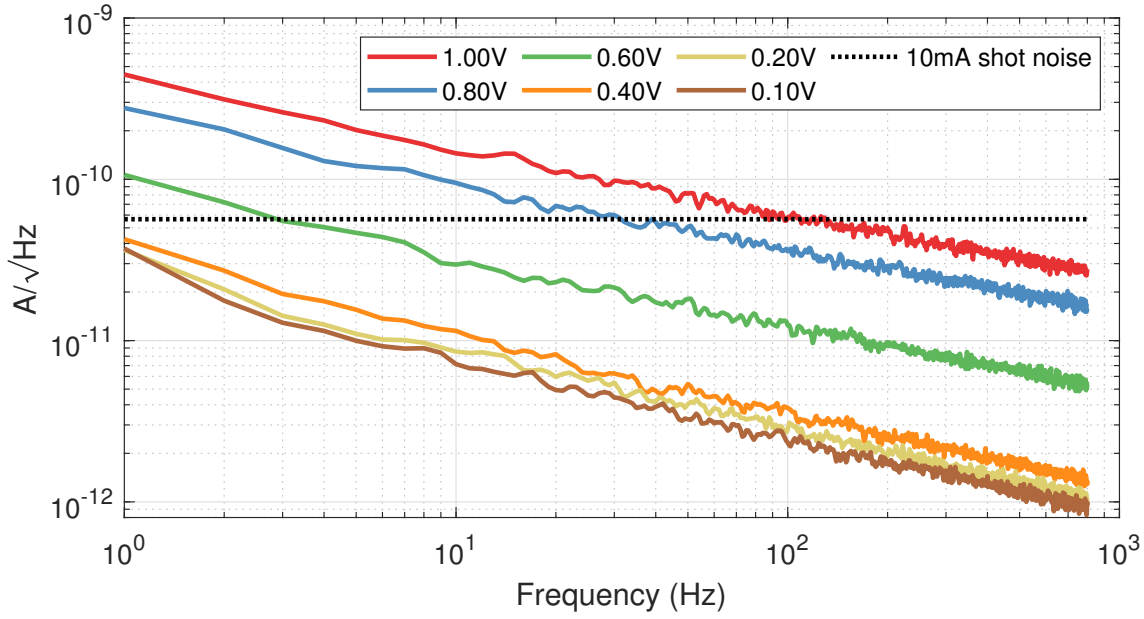


Figure A.5: Dark noise of the G12183-005k at 21°C for a series of reverse biases.

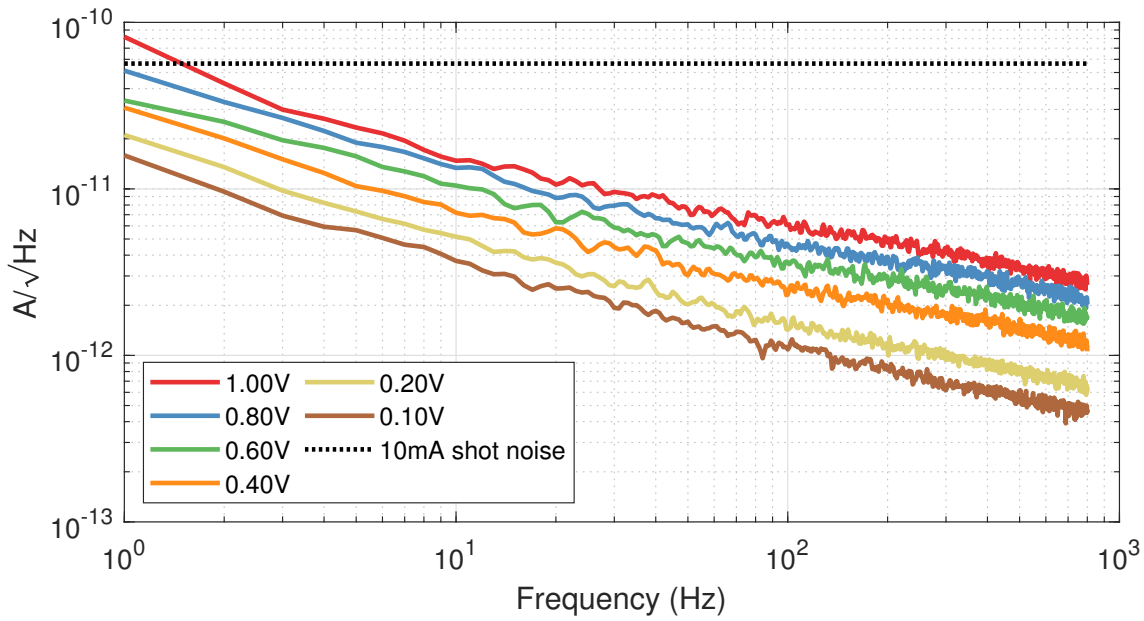


Figure A.6: Dark noise of the G12182-010k at 21°C for a series of reverse biases.

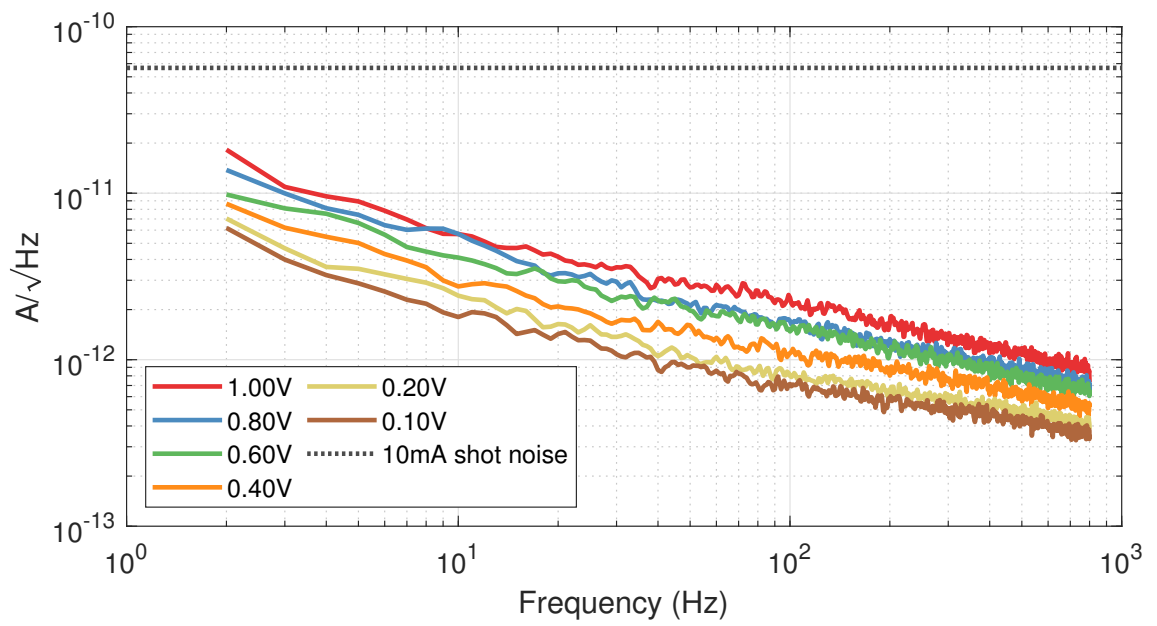


Figure A.7: Dark noise of the G12182-005k at 21°C for a series of reverse biases.

## A.2 Dark Noise as a Function of Temperature

The dark noise as a function of temperature for each photodiode in Table 6.1 was measured at the maximum reverse bias stated in its datasheet. These photodiodes had a damage threshold of  $-40^{\circ}\text{C}$ , so the noise was measured between  $-40^{\circ}\text{C}$  and  $30^{\circ}\text{C}$ . The results shown in this section were used to create Figure 6.6. The shot noise of the benchmark 10 mA current is shown by the dashed line.

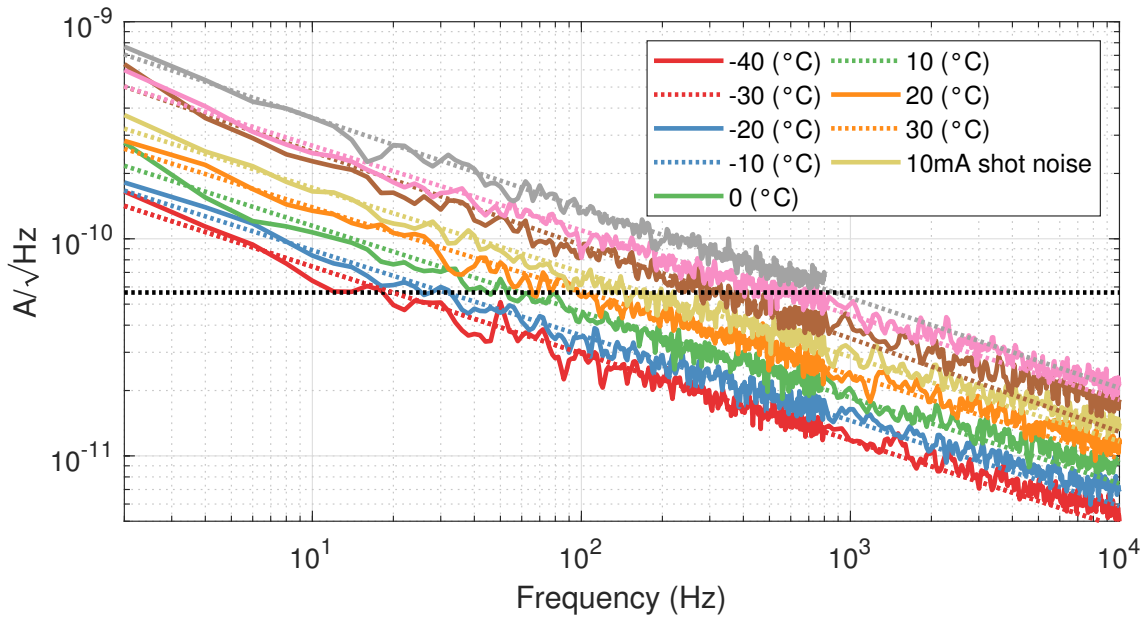


Figure A.8: The dependence of dark noise on temperature for the FD10D at 1.8V reverse bias. The measured spectra are shown with solid lines and the fits of the measurements are shown with dashed lines.

A.2. Dark Noise as a Function of Temperature

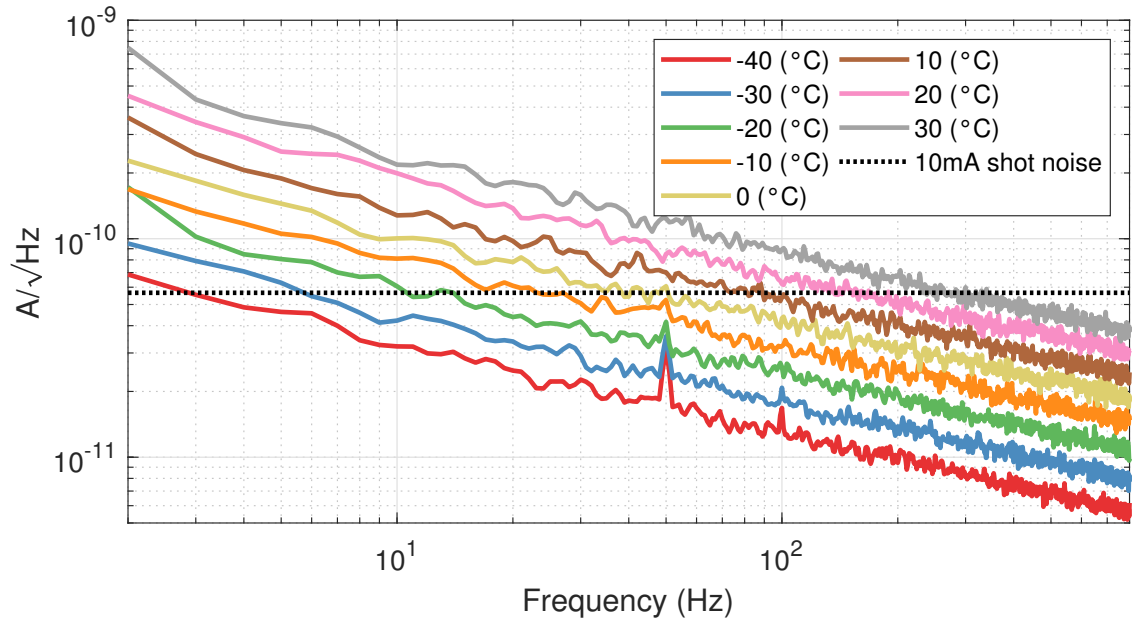


Figure A.9: The dependence of dark noise on temperature for the G12183-010k at 1.0V reverse bias.

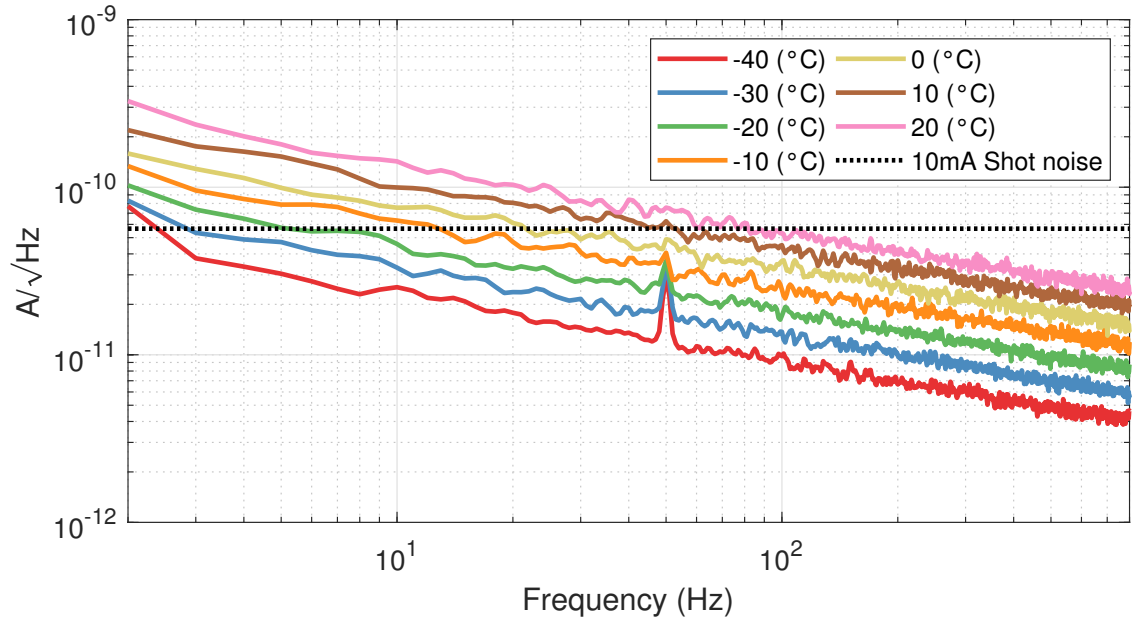


Figure A.10: The dependence of dark noise on temperature for the G12183-005k at 1.0V reverse bias.

Appendix A. Dark Noise Spectra of Photodiodes

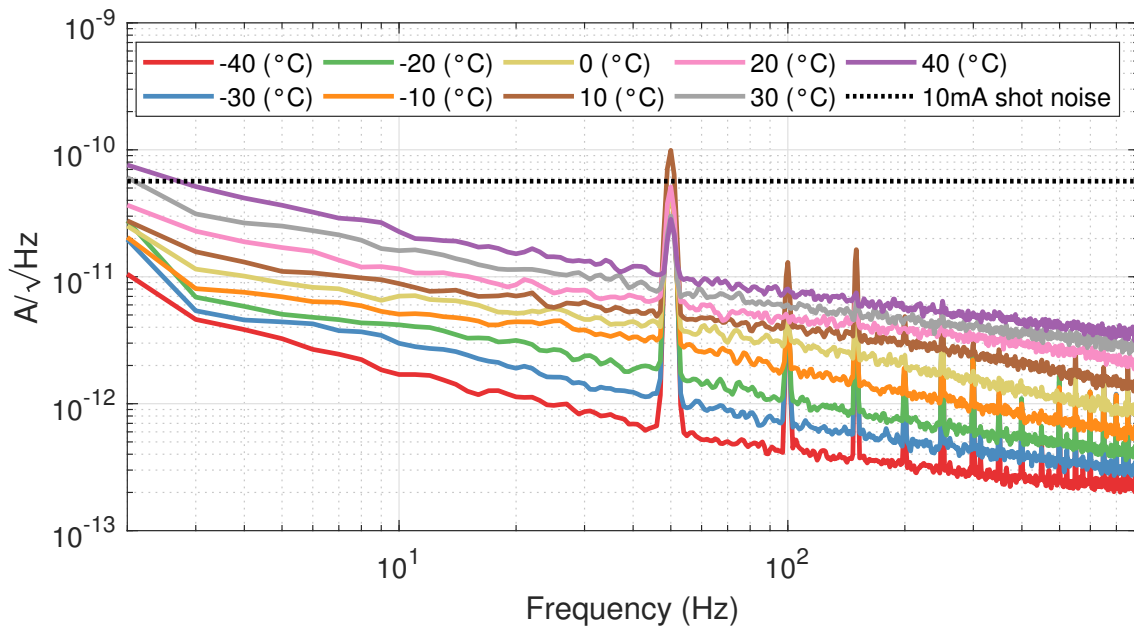


Figure A.11: The dependence of dark noise on temperature for the G12182-010k at 1.0V reverse bias.

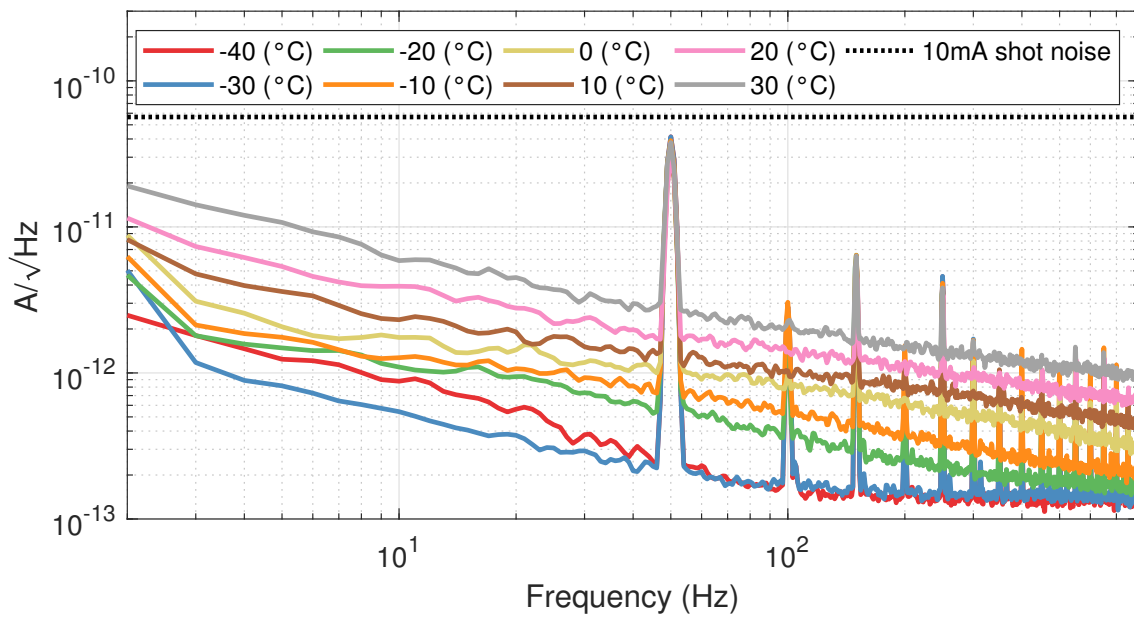


Figure A.12: The dependence of dark noise on temperature for the G12182-005k at 1.0V reverse bias.

A.2. Dark Noise as a Function of Temperature

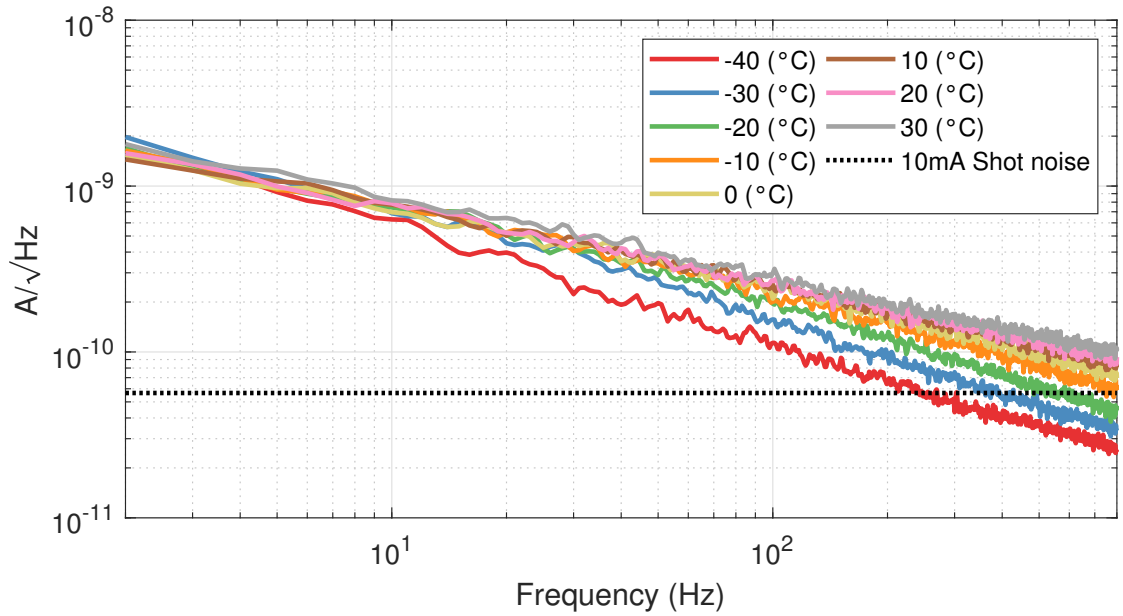


Figure A.13: The dependence of dark noise on temperature for the IG24x500S4i at 1.0V reverse bias.

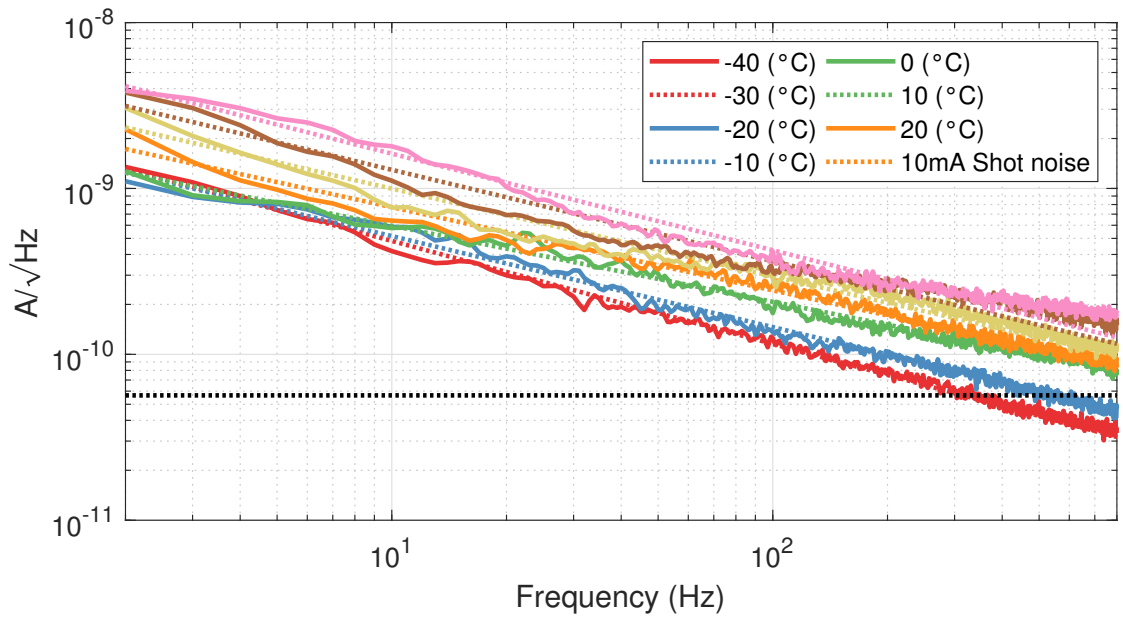


Figure A.14: The dependence of dark noise on temperature for the IG26x500S4i at 1.0V reverse bias.

### A.3 Noise of a Photocurrent Generated by an InSb Detector as a Function of Bias

The noise of the photocurrent produced by the P5968 when its field of view was covered by room temperature aluminium for a series of reverse biases is shown in Figure A.15. This data was used to produce the plots shown in Figure 6.16.

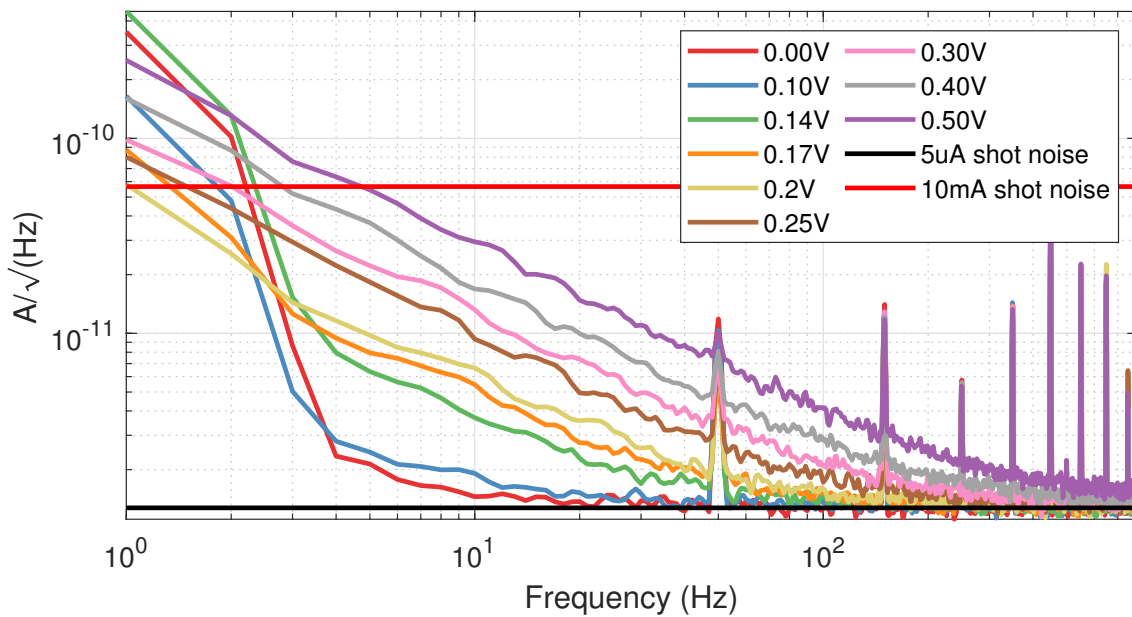


Figure A.15: The noise of the photocurrent produced by the P5968 as a function of bias. The photocurrent due to thermal radiation was expected to be  $5\ \mu\text{A}$ , and the noise of the photocurrent made by the P5986 at sufficiently low bias reaches the expected shot noise for this current. The benchmark noise corresponding to a  $10\ \text{mA}$  photocurrent is also shown.

# Appendix B

## Photodiode Circuits

Throughout the work reported on in this thesis, several designs of photodiode circuit were used to make sufficiently low noise measurements of photocurrents. For many of the experiments, it was necessary to measure a photocurrent's DC component, noise spectral density, and the size of calibration modulations in the photocurrent. Thus, the frequency response and noise characteristics of the photodiode circuits needed to be known.

## B.1 A Transimpedance Amplifier for Measuring the Dark Noise of Photodiodes

A circuit which allowed for the reverse bias to be set and for the easy exchange of photodiodes was constructed. The photodiodes were connected to the circuit using pin header style connectors. To measure small amounts of current noise, a transimpedance amplifier with a large gain is needed. As the dark current for these photodiodes was expected to be of the order of  $1\ \mu\text{A}$ , the gain of the transimpedance amplifier was chosen to be  $1 \times 10^6$  so that signals of the order  $1\ \text{V}$  would be produced, and so a  $1\ \text{M}\Omega$  resistor was used in the feedback path.

The input noise of an op amp depends on its input current noise, input voltage noise and the Johnson-Nyquist noise of the feedback resistor (e.g. [134, Figure 8.58]). In this application, as the current noise that is to be measured is small and the feedback resistor is large, a TL071, a JFET style op amp with low input current noise, was selected, and this selection of op amp allowed the transimpedance amplifier to beat the noise requirement by a factor of several hundred (see Figure B.6). As the photodiode has capacitance and the op amp has finite bandwidth, a  $2.2\ \text{pF}$  capacitor in parallel with the feedback resistor was needed to keep the circuit stable.

Several methods of providing the reverse bias were tested. The first of these derived the reverse bias from a LM7815 regulator in combination with a variable resistor configured as a potential divider; this circuit is shown in Figure B.1. A similar circuit which was used in later experiments is shown in Figure B.2.

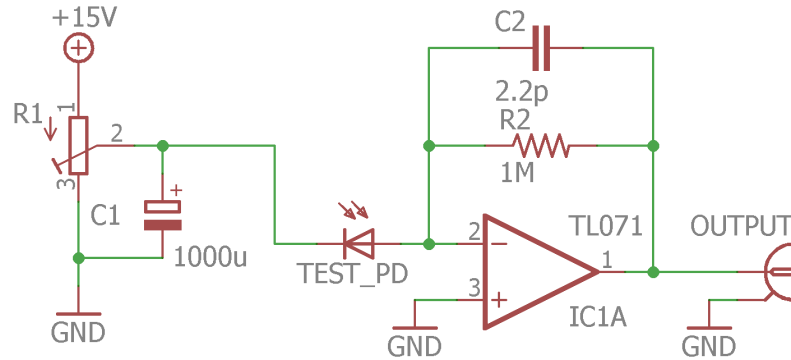


Figure B.1: The circuit used to measure the dark noise of photodiodes, represented by TEST\_PD, under different reverse biases. The transimpedance amplifier has a  $1\text{ M}\Omega$  resistor (R2) in parallel with a  $2.2\text{ pF}$  capacitor (C2) in the feedback path of the TL071 op amp. The reverse bias was generated by a potentiometer (R1) connected to an LM7815 voltage regulator. This voltage was low passed using C1. Note that the low pass corner frequency depends on the setting of R1.

To verify that this was a sufficiently quiet reverse bias voltage source that does not contaminate the measurements with noise, an ultra-quiet reverse bias reference was used to crosscheck a measurement; this circuit is shown in Figure B.2. By filtering the voltage made by a reference voltage IC (AD587JNZ), this circuit provided a reverse bias with  $5\text{ nV}/\sqrt{\text{Hz}}$  at  $10\text{ Hz}$ . The reverse bias of the FD10D was set to  $1\text{ V}$  in both circuits. In this circuit, the photodiode was soldered into it with minimal distance between the photodiode and the transimpedance amplifier. Figure B.4 shows that the regulator-potentiometer reverse bias voltage source is sufficiently quiet.

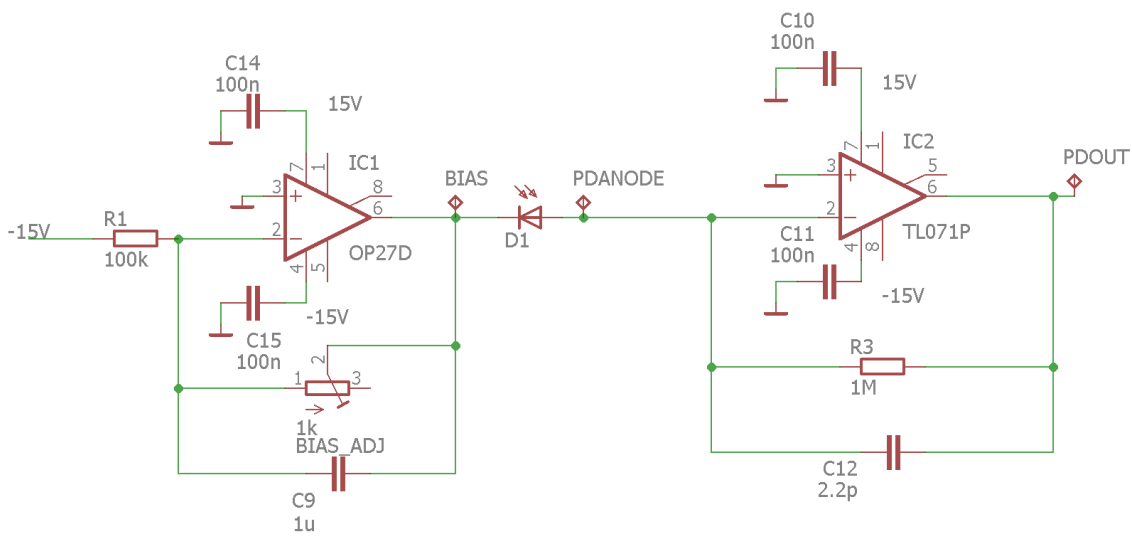


Figure B.2: The circuit used to measure the dark noise of photodiodes. The transimpedance amplifier used is identical to the one shown in Figure B.1. The reverse bias voltage was controlled with the potentiometer BIAS\_ADJ, and the reverse bias voltage was generated using an OP27 op amp (OP27D) with a gain less than one.

## B.1. A Transimpedance Amplifier for Measuring the Dark Noise of Photodiodes

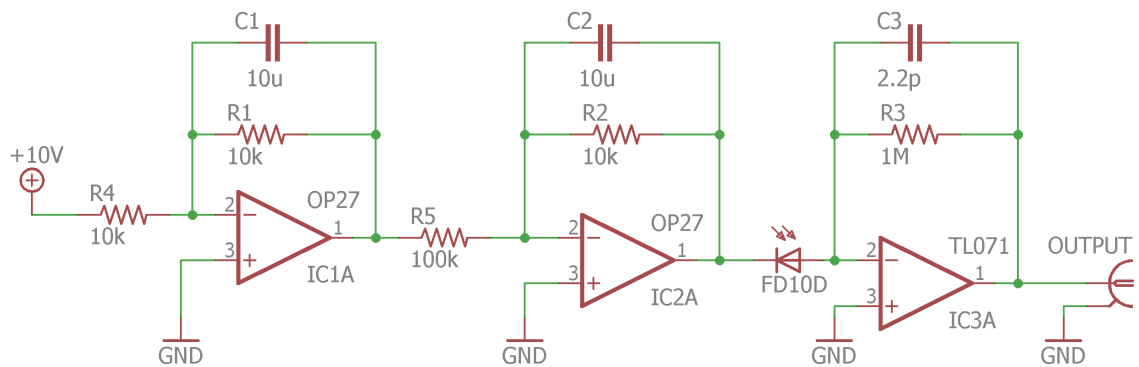


Figure B.3: The circuit used to check that reverse bias voltage noise was not contaminating dark noise measurements. To reach  $5 \text{ nV}/\sqrt{\text{Hz}}$  at 10 Hz, a 10V low noise reference IC (AD587JNZ) was used to generate the reverse bias. The output of this IC was filtered by two low pass filters. The transimpedance amplifier used is identical to the one shown in Figure B.1

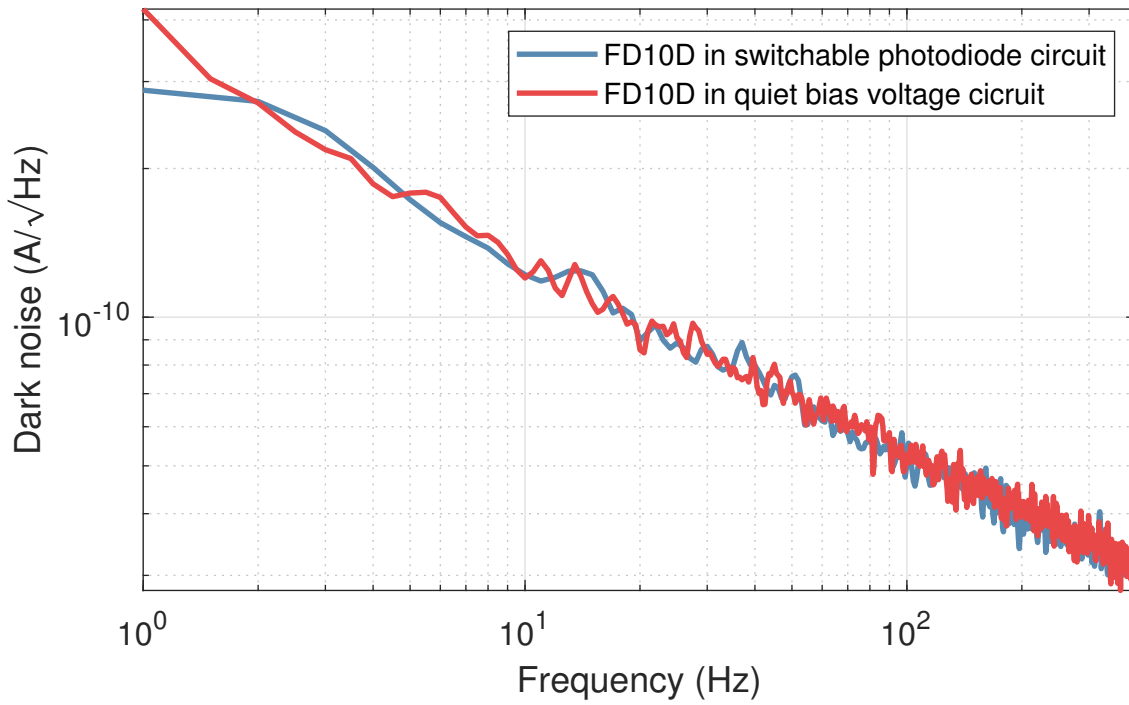


Figure B.4: The FD10D was biased with 1 V in the circuits shown in Figure B.1 and Figure B.3. The low-noise fixed-bias circuit and the circuit with a settable-bias gave the same results, so we can be confident that the circuits shown in Figures B.1 and B.3 will produce measurements that are not contaminated by reverse bias noise or noise due to how the photodiode is connected to the circuit.

### B.1.1 Transfer Function

The transfer function of the transimpedance amplifier shown in Figure B.1 was measured under a variety of different physical constructions as this circuit's behaviour can be affected by stray capacitance. The measurements of these transfer functions are shown in Figure B.5. When constructed from strip board and with the photodiode's anode and cathode cables near each other, there was of the order 10 pF of stray capacitance, i.e. it was as if the circuit had an extra 10 pF capacitor between the inverting input of the op amp and ground. By making this circuit on a prototyping board with less stray capacitance between the strips and by keeping the photodiode anode and cathode wires from forming a capacitor, the stray capacitance was reduced. The measurement matches the LISO (see Section B.3) simulation of this circuit. This was cross-checked using the MATLAB function described in Section B.4.

### B.1.2 Noise Measurement

The dark noise of the circuits described in Section B.1 is shown in Figure B.6. The shot noise of a typical photocurrent in a gravitational wave detector is several hundred times larger than the noise of this circuit. To measure the noise of the transimpedance amplifier, instead of a photodiode, a 470 pF capacitor was connected between the inverting input of the op amp and ground.

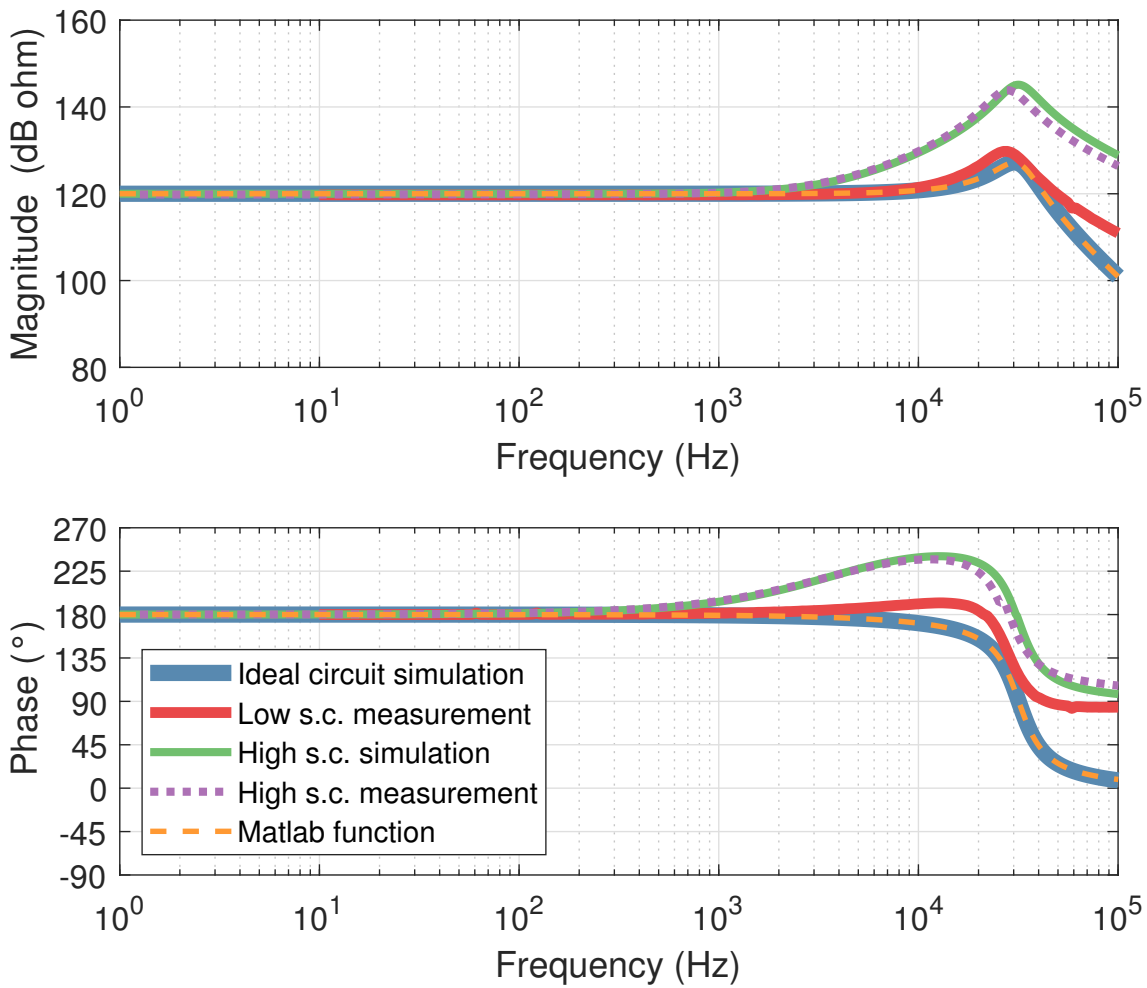


Figure B.5: The transfer function between a current into the inverting input of the transimpedance amplifier design shown in Figure B.1, Figure B.2 and Figure B.3 was measured and simulated using LISO. A MATLAB function (see Section B.4) was used to check the measurement and the simulation. This circuit is sensitive to stray capacitance (s.c.) at the inverting input of the TL071. The stray capacitance was reduced by changing the physical layout of the circuit.

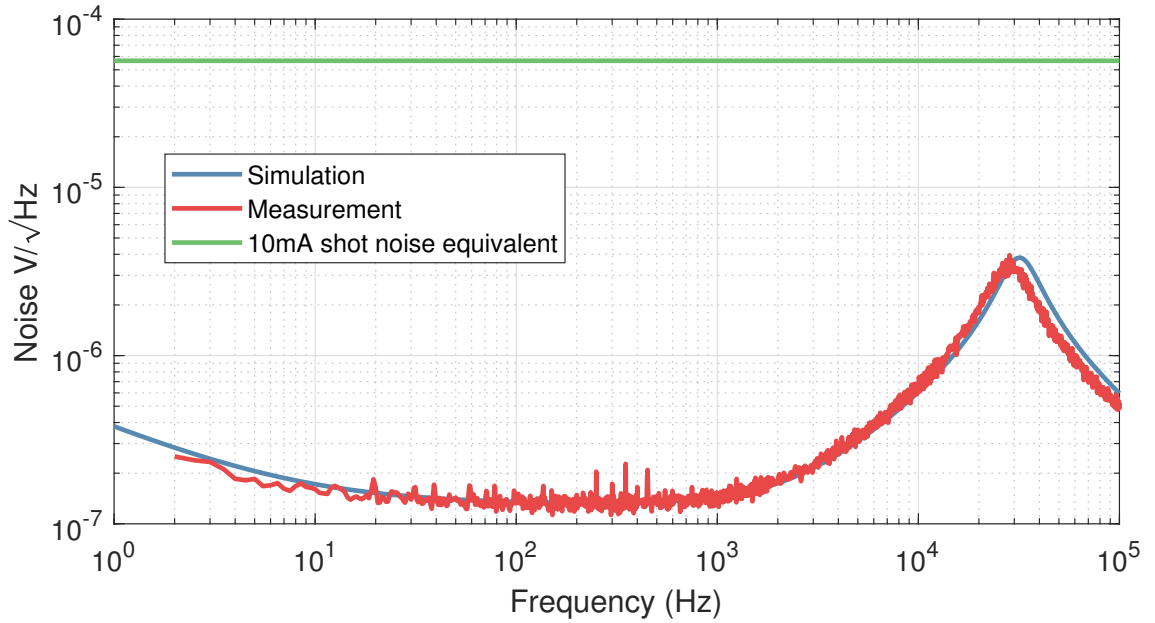


Figure B.6: At low frequencies, the noise of the transimpedance amplifier shown in Figure B.1, Figure B.2 and Figure B.3 is dominated by the low frequency voltage noise of the TL071. Above 10 Hz, the noise of the circuit is dominated by the Johnson-Nyquist noise of the feedback resistor. At 30 kHz, the impedance of the feedback network causes a noise peak.

## B.2 A Transimpedance Amplifier for Making Shot Noise limited Measurements of 10 mA Photocurrents

A photodiode circuit with electronic noise  $\sim 25$  times lower than the shot noise of a 10 mA current at frequencies between 100 Hz to several MHz is shown in Figure B.7. Below 100 Hz, the noise rises as  $1/f$ , and it equals the shot noise of a 10 mA current at 0.1 Hz. The noise for this circuit is shown in Figure B.8 and the transfer function is shown in Figure B.9. While Figure B.7 is specific to the experiment described in Section 6.4, the design of the transimpedance part of this circuit (the AD797 and accompanying parts) was also used in Chapter 7.

The AD797 [222] is a low-noise, high-speed op amp. Without feedback, the AD797 has a higher output impedance than most common types of op amp. As the AD797 is a fast device, the datasheet warns that consideration must be given to the interaction between the output impedance and a capacitive load to ground, including via the feedback network and the input network. As photodiodes have capacitance, care needs to be taken in designing transimpedance amplifiers that use AD797s. To avoid oscillations in similar circuits to the one shown in Figure B.7, the feedback capacitor may need a resistor in series with it (see [222, p.14]); however, in the circuit shown in Figure B.7, one was not required. Even so, if the photodiode is not biased or has a large area, this circuit may oscillate at a frequency between 10 MHz–100 MHz due to the capacitance of the photodiode. Every time a version

## B.2. A Transimpedance Amplifier for Making Shot Noise limited Measurements of 10 mA Photocurrents

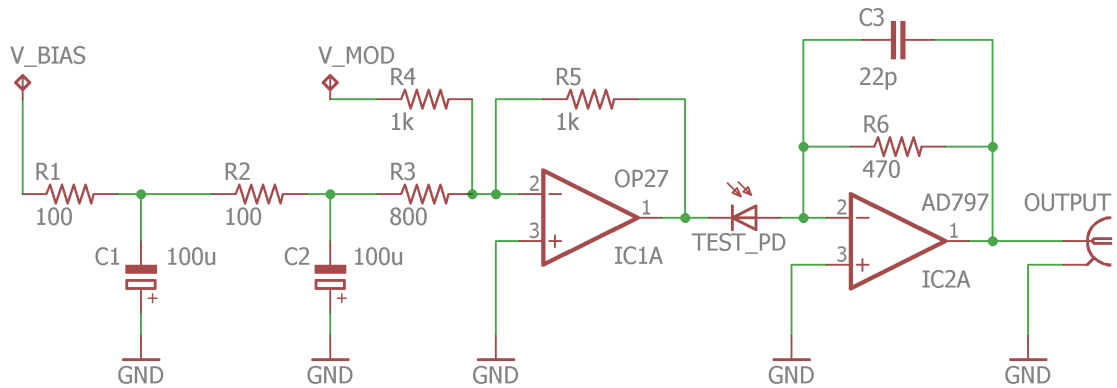


Figure B.7: The AD797 stage of the circuit (right) is a transimpedance amplifier for measuring the shot noise of 10 mA photocurrents. The left-hand stage of the circuit is used to provide the reverse bias for the photodiode. One input of this stage is a low-pass filter with two poles at 16 Hz. A bench-top power supply would be connected to this input ( $V\_BIAS$ ). The other input, ( $V\_MOD$ ), was used to provide a modulation to the reverse bias voltage.

of this circuit was made, an oscilloscope was used to check for such oscillations, as LISO does not model this behaviour.

For convenience, the circuit shown in Figure B.7 allowed for the reverse bias to be externally set. A DC reverse bias was created with a bench-top power supply, and low passed with a filter that had two poles at 16 Hz. An AC component could be added onto the reverse bias with an op amp configured to sum two input voltages.

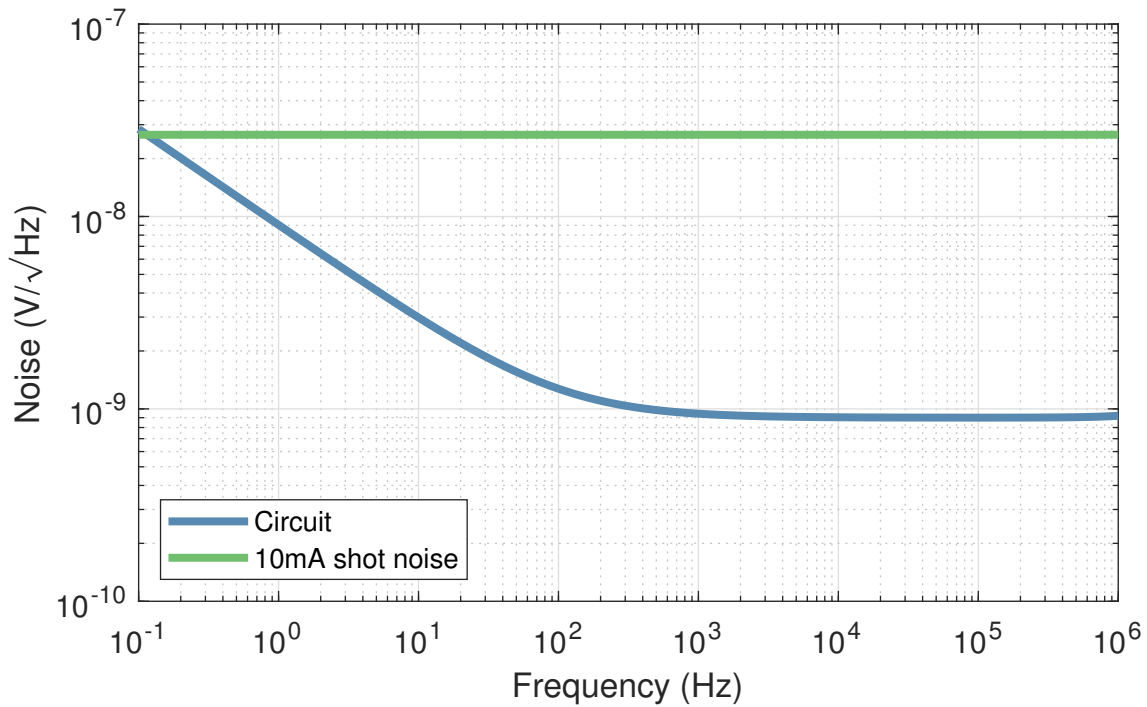


Figure B.8: LISO simulation of the noise of the circuit used for measuring photocurrents of  $\sim 10$  mA. This circuit is shown in Figure B.7. Note that the simulation may not be accurate above 1 MHz due to the unusually high output impedance of the AD797 and the capacitive load to ground.

B.2. A Transimpedance Amplifier for Making Shot Noise limited Measurements of  
10 mA Photocurrents

---

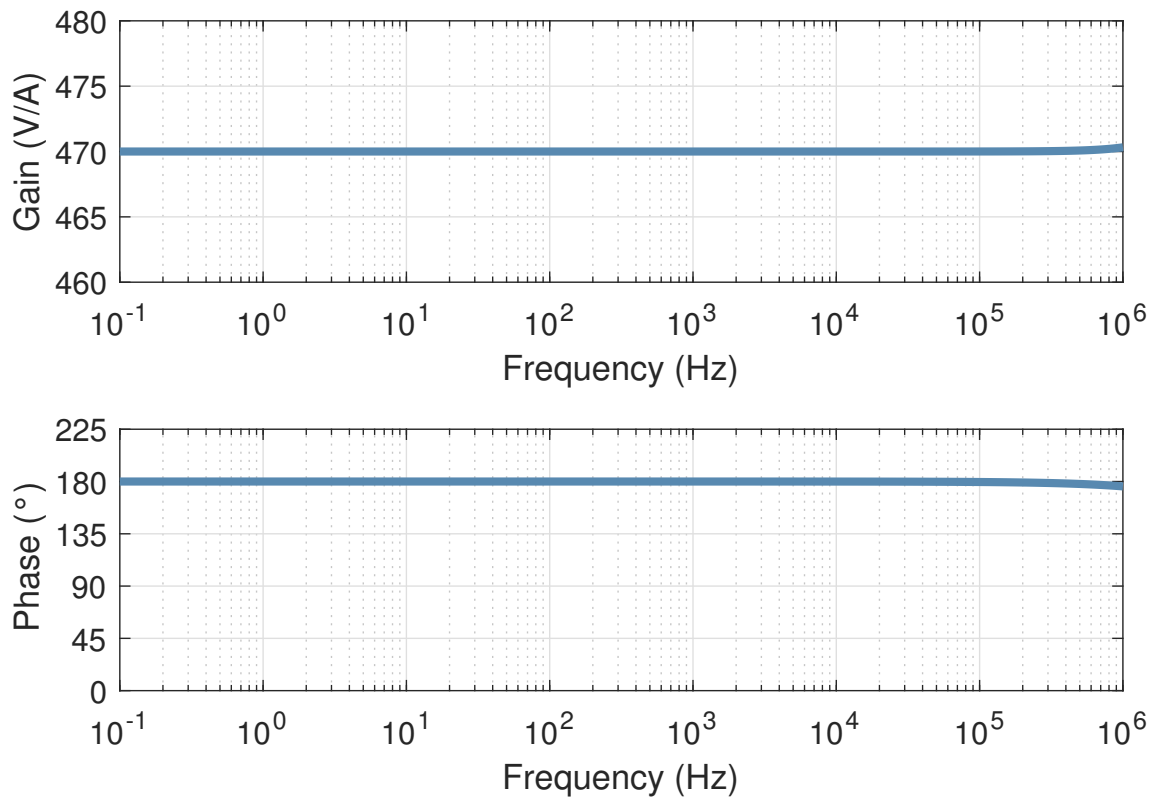


Figure B.9: LISO simulation of the transfer function of the circuit used for measuring photocurrents of  $\sim 10$  mA. This circuit is shown in Figure B.7. Note that the simulation may not be accurate above 1 MHz due to the unusually high output impedance of the AD797 and the capacitive load to ground.

### B.3 Simulations with LISO

The behaviour of circuits was simulated using LISO. This software performs a nodal analysis to calculate the voltages at each point within a circuit. LISO can calculate the noise and transfer function of circuits that include op amps. LISO has a variety of op amps in its op amp library and this can be easily expanded by specifying the noise properties, open loop gain and gain-bandwidth frequency of a new op amp.

### B.4 Transfer Function Calculation With MATLAB

The open loop transfer function of an op amp may be written as

$$A(s) = \frac{A_0}{\frac{A_0}{2\pi f_{\text{GWB}}}s + 1}, \quad (\text{B.1})$$

where  $A_0$  is the open-loop gain of the op amp,  $f_{\text{GWB}}$  is the gain-bandwidth product of the op amp and  $s$  is the complex angular frequency. The transfer function between the input current and output voltage of a transimpedance amplifier is

$$H(s) = Z_{\text{FB}} \frac{A(s)}{1 + A(s)B(s)}, \quad (\text{B.2})$$

where  $B(s)$  is the transfer function of the components between the output pin of the op amp and the inverting input of the op amp, i.e. the components in the feedback network of the transimpedance amplifier.  $Z_{\text{FB}}$  is the impedance seen by the current

flowing from the output pin to the inverting input.

Without a capacitor in parallel with the feedback resistor,  $B(s) = \frac{1}{R_{FB}C_{PD}s+1}$ . This can cause the circuit to be unstable because it can lead to the phase of the transfer function reaching or exceeding  $180^\circ$  as it crosses the unity gain point due to the photodiode's capacitance and the gain bandwidth product of the op amp. To fix this problem, a capacitor should be added in parallel to the feedback resistor, and so

$$B(s) = \frac{R_{FB}C_{FB}s + 1}{R_{FB}(C_{FB} + C_{PD})s + 1}. \quad (\text{B.3})$$

The impedance seen by the current is

$$Z_{FB} = \frac{R_{FB}}{R_{FB}(C_{FB} + C_{PD})s + 1}. \quad (\text{B.4})$$

From Equation (B.2),  $H(s)$  can be calculated with the following MATLAB code:

```
function [mag,phase] = photodiodeTransimpedance(cf, rf,cpd,gbw,A,w)
% cf = feedback capacitor (Farads). rf = feedback resistor (ohms)
% cpd = photodiode capacitance (Farads).
% gbw = gain bandwidth of the op amp (Hz)
% A = Open loop gain of the op amp. w = angular frequency range
%that transfer function will be calculated over.
A_s = tf(A,[A/(2*pi*gbw),1]);
B_s = tf([cf*rf,1],[rf*(cf+cpd),1]);
closedLoopAnalytic = -tf(rf,[rf*(cf+cpd),1])*A_s/(1+A_s*B_s);
[mag,phase] = bode(closedLoopAnalytic,w);
mag = squeeze(mag);
phase = squeeze(phase);
end
```



# Appendix C

## The Control and Data System

The LIGO interferometers use a system called CDS to acquire data and control the interferometer. A digital signal processing system built to the same standards as CDS is available at Glasgow and was used to conduct some of the experiments reported on in this thesis. As CDS is a digital system, complex servo shaping can be implemented with relative ease, e.g. the servo shown in Figure 7.12 was created with CDS. Additionally, processes such as locking a cavity on resonance, or locking an interferometer to the desired operating point, can be automated with digital logic, as signals can be monitored to trigger events. CDS can interface with a suite of software that makes interacting with an experiment easier; an example of CDS being used with the Motif Editor and Display Manager (MEDM) software [223] to lock the PMC (see Chapter 2) is shown in Figure C.1.

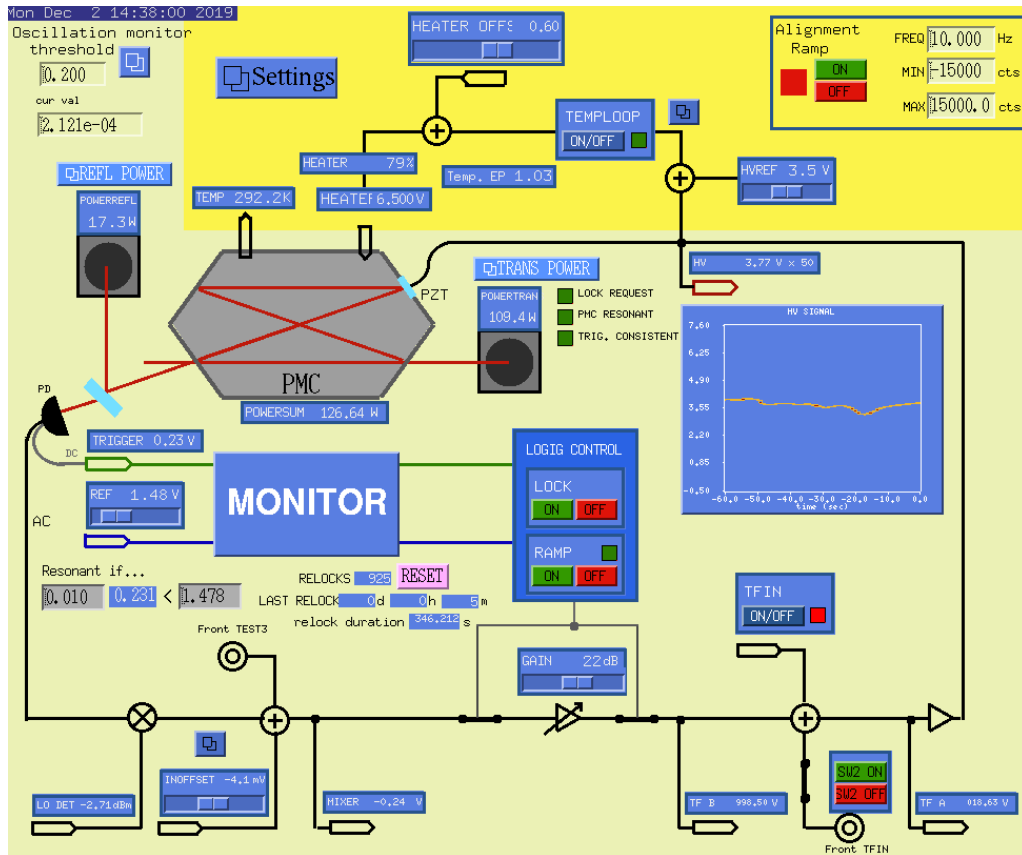


Figure C.1: This MEDM interface is used by operators of the interferometer to control and monitor the status of the PMC. Several inputs and outputs can be monitored simultaneously, and locking the PMC is reduced to simply pressing a button (LOCK). Most aspects of the locking servo can be adjusted with CDS, e.g. the gain slider adjusts the gain of the servo, thus operators have a large amount of freedom when they are trying to optimise the PMC’s locking capabilities.

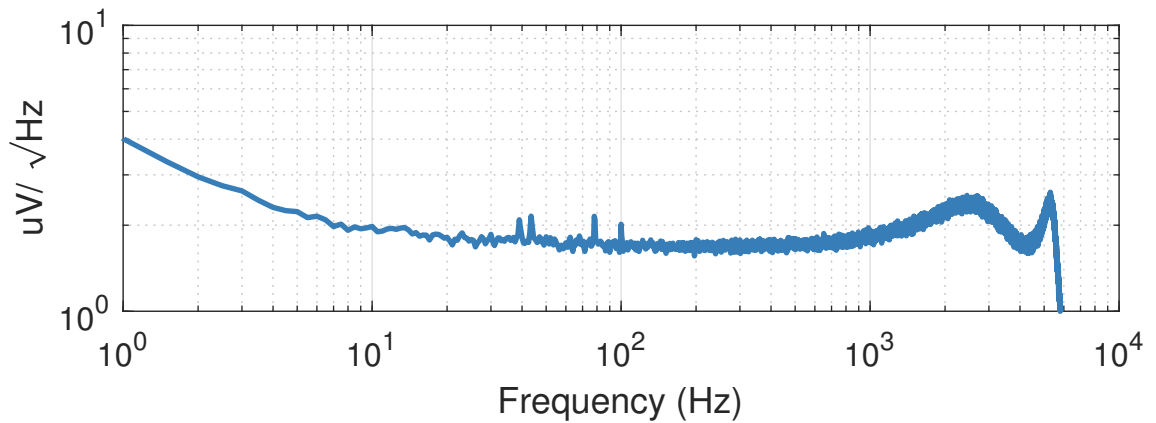


Figure C.2: Noise floor of the digitised input signals recorded by the Glasgow CDS. This was converted into a voltage using  $2^{15}$  counts per 10 Volts. The ripples above 1 kHz arise due to the 3rd order low pass filter at 9 kHz. Below  $\sim 10$  Hz, the input noise rises as  $1/f$ .

CDS contains an array of ADCs for accepting analogue signals and DACs for generating analogue outputs. An ADC measures a voltage, and the smallest voltage that it can measure is ultimately determined by the number of bits it uses. The smallest voltage measurable with the ADC corresponds to one count within CDS.

The Glasgow CDS uses ADCs with a voltage range of  $\pm 10$  V, and the sample rate of the ADCs is 65 kHz. The voltage is recorded as a signed 15 bit integer, so  $2^{15}$  counts is equivalent to 10 Volts. Note that counts can exceed  $2^{15}$  within the digital part of CDS. The digitised analogue input signals have a noise floor, and a measurement of this is shown in Figure C.2. As digitally measured signals can be aliased if they exceed the bandwidth of the ADCs, signals that are measured with CDS are low passed at 9 kHz with a third order filter. The noise of the Glasgow CDS analogue inputs is equivalent to an ADC with a 14 bit resolution.



# Appendix D

## FINESSE Simulations

The following simulations were used in Chapter 3 for determining the effect of radii of curvature errors in the signal recycling cavity at LLO. This appendix contains parameters for the simulations performed in Chapter 3, and clarifies some aspects of FINESSE's behaviour by providing tests and examples.

### D.1 Mode Matching the Laser to the Arm Cavity

The laser in a FINESSE simulation has a beam parameter. By default, the beam will have a 2 mm beam with its waist at  $z = 0$  with respect to the node at the laser. If a `cav` command is used to define a cavity, then the beam parameter of the laser is set so that it is perfectly matched to the cavity. It is crucial that the beam parameter of the input laser remains the same when the simulation is configured such that the

arms are resonant and when it is configured for a single bounce measurement.

The beam parameter of the laser can be set with the `gauss` command. To find suitable numbers to use for the `gauss` command in the simulations of single-bounce and locked-arm measurements (see Section D.4 and Figure 3.3), the following test was performed. The main simulation from Section D.4 was modified so that it did not have an X arm or the SRC. The following beam parameters were found with a `bp` detector placed at the lasers node:

- $w_0 = 0.00864064287177005$  m
- $z = 1339.83530090614$  m

To determine if the sign of  $z$  is correct, consider what happens if the beam parameter detector is moved 1m towards the cavity to `bs_a`:

- $w_0 = 0.00864064287177005$  m
- $z = 1338.83530090614$  m

$z$  increasing suggests moving from `n1` to `bs_a` causes one to be closer to the waist. Intuitively, we know this is the case since the geometry of the cavity means the waist is within the cavity, and moving towards the cavity means you are moving towards the cavity waist. In other words, we know the beam should be getting smaller as we move from the laser to the cavity, which matches the behaviour seen here.

However, setting the beam parameter at the laser with the first set of numbers gives *terrible* mode matching. The simulation below investigates this. A photodiode which is masked from the TM00 mode

```
pd HOM bs_d  
mask HOM 0 0 0
```

was placed at `bs_d`, which has the beam reflected from the arm cavity in it. The value of  $z$  for the `gauss` command was varied and the power incident on a `pd` with a `mask` applied to it, called `HOM`, was measured. To check that enough `HOM` were being used, the simulation was repeated with several `maxtem` commands. The results had a quadratic fitted to them, and the minimum was taken as the optimal value. This is shown in Figure D.1. The values:

- $w_0 = 0.00864064287177005$  m
- $z = -1339.83683935$  m

give more than 99.99999% mode matching, which is plenty for this work. This is close to the original values that we obtained, except for a minus sign. This is due to the way `FINESSE` computes the beam parameter.

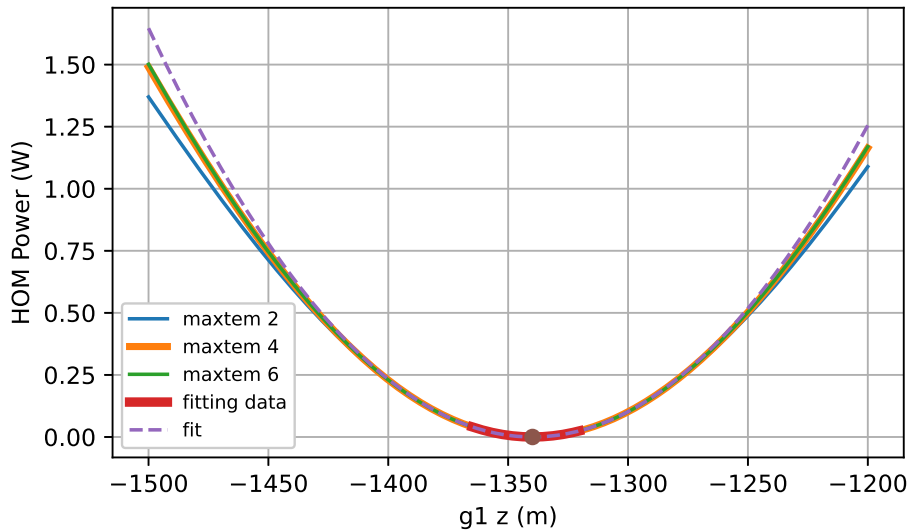


Figure D.1: Optimisation of the parameters used in the `gauss` command to mode match the laser to the arms in the simulations described in Chapter 3 and Section D.4. The blue, green and orange lines show how the mode matching changes as the beam waist location is changed. As the mode mismatch became larger, more HOMs were required; this is why the blue and green/orange lines diverge. A quadratic was fitted to the data highlighted in red, and the minimum value was used as the waist location parameter for the `gauss` command.

## D.2 Interferometer Parameters

The simulated interferometer has nominal values for the LIGO arm cavities and the LLO SRC. The simulated arm cavity geometry is based on the design values to avoid contrast defects. The following sections contain tables specifying the design and measured values for each component of the simulation.

### D.2.1 Radii of Curvature of optical components

The optics in the SRC were simulated with the values from Table D.2. The arm cavity optics were simulated using the values from Table D.1.

Optic Name	RoC (m)	Focal length (m)	Reference
SRM	-5.6938	-2.8469	[224]
SR2	-6.427	-3.2135	[224]
SR3	36	18	[224]
ITM	1934	967.0	[224]
ETM	2245	1122.5	[224]

Table D.1: The aLIGO design values of the RoCs of the optics inside the SRC and the arms.

### D.2.2 Spacings

The nominal values for the spacing between the optics at LHO/LLO, with a diagram, can be found in [86]. This information is also in [224]. The LLO Zemax parameters are found in [228]. Table D.3 contains the distances derived from the

Appendix D. FINESSE Simulations

---

Optic Name	RoC (m)	Focal length (m)	Reference
SRM-02	$-5.673 \pm 0.002$	$-2.8365 \pm 0.001$	[225]
SR2-04	$-6.406 \pm 0.006$	$-3.203 \pm 0.003$	[226], [225]
SR3-01	$35.97 \pm 0.012$	$17.985 \pm 0.006$	[227], [225]
ITM-08	1938.44	969.22	[225]
ETM-15	2245.4	1122.7	[225]

Table D.2: The measured values of the RoCs of the optics at LLO that make up the SRC and the arms.

Zemax coordinates. Most spacings do not require sub mm accuracy, however SR3 to SR2 does since the Rayleigh range of this beam is about 4 cm. The design value for the spacings are shown in Table D.4. The values used in an earlier FINESSE model of LLO made by others [229] are shown in Table D.5. The thickness of each optic is found in Table D.6.

Space Name	Length (m)
EMPTY to ITMY	3994.4850
ITMY to CP	0.02
CP to BS HR	4.8471
BS AR to SR3	19.3659
SR3 to SR2	15.4435
SR2 to SRM	15.7562

Table D.3: Measured spacings between the optics at LLO [228].

Space Name	Length (m)
EMTY to ITMY	3994.5
ITMY to CP	0.05
CP to BS HR	4.8497
BS AR to SR3	19.368
SR3 to SR2	15.4607
SR2 to SRM	15.726

Table D.4: Design value for spacings between optics in aLIGO [86].

Space Name	Length (m)
EMTY to ITMY	3994.515
ITMY to CP	0.02
CP to BS HR	4.847
BS AR to SR3	19.3661
SR3 to SR2	15.4435
SR2 to SRM	15.7566

Table D.5: Parameters used in an earlier FINESSE model of LLO [229].

Optic	Thickness (m)
ITM	0.200
CP	0.100
BS	0.0685
beam path through BS	0.1202

Table D.6: Thickness of the optics between and including the ITM and the SRM.

### D.2.3 Parameters used in the Main Simulation

The parameters used in the main simulation were a combination of design values and measured values. The arm cavities were simulated using the design values to remove the contrast defect that would occur otherwise, and the SRC was simulated using measurements taken from LLO. The ITMs that were simulated have a thickness of 0.1 m and a refractive index of 1.45. The thermal lens was implemented as shown in Figure 3.3. The parameters used are shown in Table D.7.

Parameter	Value	Description
SRM RoC	-5.673m	Measured RoC of SRM-02 installed at LLO
SR2 focal length	-3.203 m	Measured focal length of SR2-04 installed at LLO
SR3 focal length	17.985 m	Measured focal length of SR3-01 installed at LLO
ITM RoC	1934 m	Design value
ETM RoC	2245 m	Design value
ITM thermal lens	50 km	Design value
ITM to ETM distance	3994.5 m	Design value
ITM to BS Y	4.8471 m	As-built value for Y arm
ITM to BS X	4.8471 m	As-built value for Y arm
BS to SR3	19.3659 m	As-built value
SR3 to SR2	15.4435 m	As-built value
SR2 to SRM	15.7562 m	As-built value
ITM T	0.0148	Power transmission coefficient
SRM T	0.324	Power transmission coefficient
ITM L	10 ppm	Scatter loss of ITM HR surface
ETM L	10 ppm	Scatter loss of ETM HR surface

Table D.7: Parameters for the major components of the simulation.

## D.3 Finding the Correct Way to Model a Beam Splitter

Two simulations were used to model two identical Michelson interferometers which only differ in how the beam splitter was implemented. These simulations were used to generate Figure 3.2.

The following FINESSE code describes a Michelson interferometer where the beam splitter was implemented with a single `bs` command. This simulation produced an incorrect result as the phase at the beam splitter is not properly accounted for.

```
l l1 1 0 n1
s sin 1 n1 na

bs thin_bs 0.5 0.5 0 0 na nb nc nd

s Yarm 1 nb nY
m Ymirror 1 0 0 nY dump

s Xarm 1 nc nX
m Xmirror 1 0 0 nX dump

pd AS nd

xaxis Xmirror phi lin 0 180 100
```

The thin beam splitter in the above simulation was replaced with a beam splitter

that was implemented with three `bs` and two `space` commands. This is the correct way to implement a beam splitter in FINESSE. The code for this is shown below.

```
l l1 1 0 n1
s sin 1 n1 na

bs thick_bs_1 0.5 0.5 0 0 na nb nsub1 nsub3
s bs_subX 1p nsub1 nsub2
s bs_subY 1p nsub3 nsub4
bs thick_bs_X 0 1 0 0 nsub2 dump nc dump
bs thick_bs_AS 0 1 0 0 dump nsub4 dumo nd

s Yarm 1 nb nY
m Ymirror 1 0 0 nY dump

s Xarm 1 nc nX
m Xmirror 1 0 0 nX dump

pd AS nd

xaxis Xmirror phi lin 0 180 100
```

## D.4 Main Simulation

The following FINESSE code was used to simulate mode mismatches in the SRC.

```
l l1 5M 0 n1
gauss beamParaml1 l1 n1 0.00864064287177005 -1339.83683935
```

```

maxtem 12

s space1 1 n1 bs_a

#####
#bs beam_splitter 0.5 0.5 $phi_BS 0 bs_a bs_b bs_c bs_d

bs BSfront 0.5 0.5 0 0 bs_a bs_b nBSi1 nBSi3
s BSsubstrate1 1p 1.45 nBSi1 nBSi2
s BSsubstrate2 1p 1.45 nBSi3 nBSi4
bs BSback1 0 1 0 0 nBSi2 dump bs_c dump
bs BSback2 0 1 0 0 nBSi4 dump bs_d dump

#####
## Y ARM

s s_bs_to_ITMy 4.8471 bs_b nITMyARa

#ITMy
m1 ITMyAR 1 0 $phi_ITMy nITMyARa nITMyARb
s sITMy_thickness 0.05 1.45 nITMyARb nITMyTLa
lens ITMyTL 50k nITMyTLa nITMyTLb
s sITMy_thickness2 0.05 1.45 nITMyTLb nITMyHRa
m1 ITMy 0.0148 10u $phi_ITMy nITMyHRa nITMyHRb
attr ITMy Rc -1934

s space_arm_y 3994.5 nITMyHRb nETMy

m1 ETMy 0 10u $phi_ETMy nETMy dump
attr ETMy Rc 2245

```

## Appendix D. FINESSE Simulations

---

```
cav army ETMy nETMy ITMy nITMyHRb

#####

## X ARM

s s_bs_to_ITMx 4.8471 bs_c nITMxARa

#ITMx
m1 ITMxAR 1 0 $phi_ITMx nITMxARa nITMxARb
s sITMx_thickness 0.05 1.45 nITMxARb nITMxTLa
lens ITMxTL 50k nITMxTLa nITMxTLb
s sITMx_thickness2 0.05 1.45 nITMxTLb nITMxHRa
m1 ITMx 0.0148 10u $phi_ITMx nITMxHRa nITMxHRb
attr ITMx Rc -1934

s space_arm_x 3994.5 nITMxHRb nETMx

m1 ETMx 0 10u $phi_ETMx nETMx dump
attr ETMx Rc 2245

cav armx ETMx nETMx ITMx nITMxHRb

#####

## SRC

s bs_to_SR3 19.3659 bs_d nSR3a
```

```
lens SR3 17.985 nSR3a nSR3b

s SR3_to_SR2 15.4435 nSR3b nSR2a

lens SR2 -3.203 nSR2a nSR2b

s SR2_to_SRM 15.7562 nSR2b nSRMa

m1 SRM 0.324 0 0 nSRMa nSRMb
s SRM_substrate 0.07 1.45 nSRMb nSRMc
m SRM_AR 0 1 0 nSRMc nSRMd
attr SRM Rc -5.673

#cav src ITMx nITMxHRa SRM nSRMa

#####
#N.B these tunings don't represent how an IFO is kept on the dark
#fringe
const phi_ITMx 0
const phi_ITMy 0
const phi_ETMx 0
const phi_ETMy 0
const phi_BS 0
#####

beam SRM_trans nSRMd
#mask SRM_trans 0 0 0

bp SRM_trans_w0 x w0 nSRMd
bp SRM_trans_w x w nSRMd
```

## Appendix D. FINESSE Simulations

---

bp SRM\_trans\_r x r nSRMd

bp laser\_w x w0 n1

bp laser\_z x z n1

beam ITMy\_refl nITMyHRa

beam ITMy\_refl nITMyHRa

bp ITMy\_refl\_w x w nITMyHRa

bp ITMx\_refl\_w x w nITMxHRa

pd p\_in bs\_a\*

pd p\_ref bs\_a

pd p\_out nSRMd

pd p\_out\_hOM nSRMd

mask p\_out\_hOM 0 0 0

ad ad\_HOM\_2\_y 2 0 0 nSRMd

ad ad\_HOM\_2\_x 0 2 0 nSRMd

gouy src\_gouy y sITMx\_thickness sITMx\_thickness2 s\_bs\_to\_ITMx

bs\_to\_SR3 SR3\_to\_SR2 SR2\_to\_SRM

trace 64

phase 2

xaxis SRM\_trans x lin -10 10 200

## Appendix E

# Algorithm for Finding a Three-Optic Mode Matching Solution with $45^\circ$ Gouy Phase Separation between two of the Optics

An algorithm was developed for finding the static powers of the optics in HAM5/6 which gives perfect mode matching between the interferometer and the OMCs. There are three optics between the interferometer and an OMC which affect the mode matching between them, and two of these optics will have tuneable radii of curvature. Having the two tuneable optics separated by  $45^\circ$  of Gouy phase will allow for the size of the beam's waist and the location of the beam's waist to be

independently controlled.

Consider the mode matching problems shown in Figure E.1. To visualise how this algorithm works, see Figure E.2. The principle by which this algorithm works is: the continuum of modes after optic 1 and the continuum of modes just before optic 3 can be easily obtained since they must have a defined beam size, so they only vary in defocus. These two continua are propagated to optic 2, and then it is just a case of finding the optical power of a lens/mirror which will move a mode from one continuum to the other.

The continua at optic 2 Figure E.2 do not necessarily need to have the shape that they are sketched with in Figure E.2; however, if the blue-green continuum and red-yellow continuum extend far enough, they will always wrap around. It is not guaranteed that every mode in the red-yellow continuum can be reached from the blue-green continuum and vice versa. Since the mapping between the blue-green continuum and red-yellow continuum is not one-to-one, two ‘branches’ need to be considered. Both branches of the continua do not need to be analysed at the same time, but a better solution may be found by looking at different combinations of branches. This is useful in setting a limit on the size of the continuum you search.

In our implementation of this algorithm, the ‘continua’ were numerically implemented, thus they are discrete. Thus, when finding a mapping at optic two it is not guaranteed that a mode in the red-yellow continuum will have a corresponding mode of the same width in the blue-green continuum. Because of this granularity, if you were to plot optimal powers of optic 2 and optic 3 as a function of the power

of optic 1, you would see jumps in the optimal lens choices. This is especially bad around the turning point of the continua since the modes defocus changes quickly while their size does not.

## E.1 Method

This section delineates the algorithm. See Figure E.1 and Figure E.2 for the definitions of objects described in the following list.

1. **Define the target mode at optic 3.** In Figure E.2, this is mode l at optic three.
2. **Define a set of modes which share the same beam size as the target mode at optic 3 but have varying radii of curvature.** In Figure E.2, this is the red-yellow continuum at optic three.
3. **Propagate the set of modes defined at optic 3 back to the optic 2.** In Figure E.2, this is the red-yellow continuum at optic 2.
4. **Define the initial beam parameter and propagate this to optic 1.** In Figure E.2, this is mode i at optic one.
5. **Define a set of modes that have the same beam size as the initial beam at optic 1 but differ in defocus.** In Figure E.2, this is the blue-green continuum at optic one.
6. **Propagate the modes defined at optic 1 to optic 2.** In Figure E.2, this

is the blue-green continuum at optic two.

7. **Calculate the difference in optical power between mode i and a mode in the blue-green continuum (e.g. mode j).** In Figure E.2, mode j represents just one possible mode in this continuum. Save this power.
8. **Find a mode in the red-yellow continuum which is closest in size to mode j, call this mode k.** In Figure E.2, there is another possible choice on the red-yellow continua, however only one of them needs to be considered.
9. **Calculate the difference in optical power between mode j and mode k at optic 2.** Save this power.
10. **Calculate the difference in optical power of mode k and the target mode at optic 3.** Save this power.
11. **Calculate the Gouy phase separation of optic 2 and optic 3.**
12. **Repeat for every mode in the blue-green continuum, or until a Gouy phase separation of  $45^\circ$  has been found.**

The number of modes that are considered and the range of modes in the continua should be tailored for the optical layout that is being considered. Our problem had metre scale spacings between optics and Rayleigh lengths. It was found that continua with a range of the order 1-10 dioptres were suitable. This does not mean that an adaptive optic would need this actuation range, rather it allowed for the static radii of curvature for each optic that gives optimal Gouy phase separation between the active mode matching elements to be found. Using this algorithm, we were able

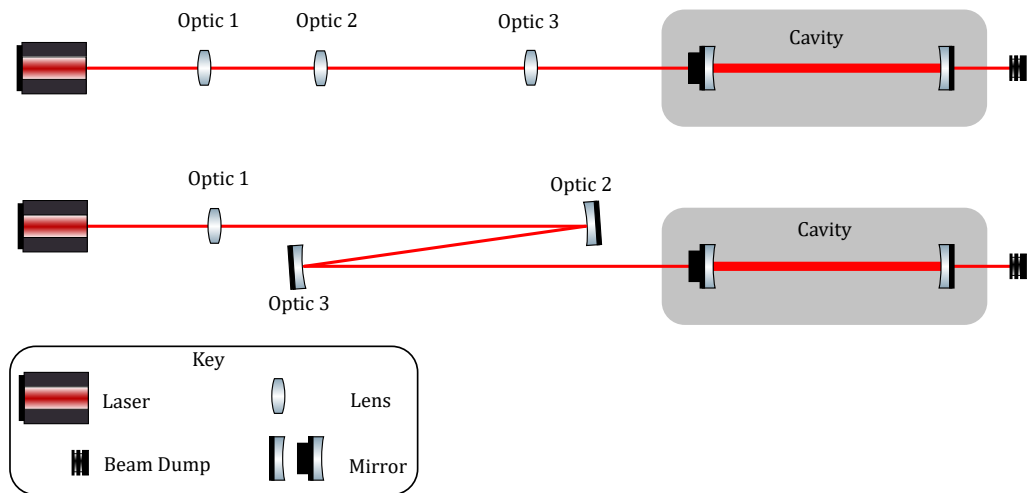


Figure E.1: Top layout: three lenses used to achieve mode matching to the cavity. These are shown as positive lenses, however negative lenses can also be used when designing mode matching systems. Bottom layout: a lens and two curved mirrors used to achieve mode matching to a cavity. The optics 1,2 and 3 correspond to the ones shown in Figure E.2. The initial and target modes are defined in these examples by the laser mode and the cavity mode.

to rapidly develop many possible HAM6 layouts. This allowed for more time to consider various engineering factors (suspension size and the like) and how to adapt the mirror strengths accordingly to accommodate for small changes in a tentative design.

Appendix E. Algorithm for Finding a Three-Optic Mode Matching Solution with  $45^\circ$  Gouy Phase Separation between two of the Optics

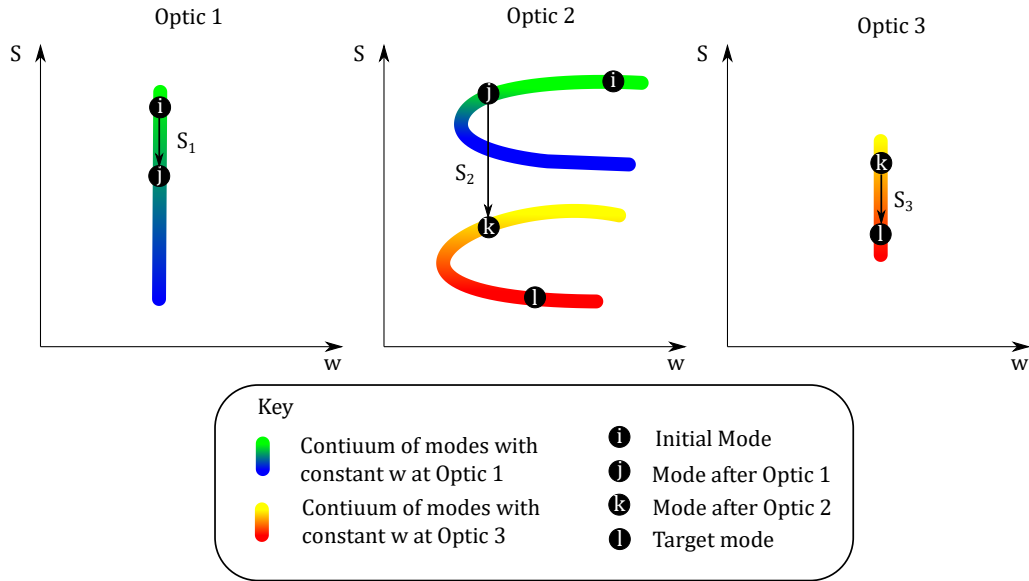


Figure E.2: Sketch of the WS phase space representations of the Gaussian beams at the three positions along the optical axis where a mirror or a lens could be. Examples of such layouts are shown in Figure E.1. The optical power of the first optic is given by the difference in the defocus between the initial mode (i) and the second mode (j). The power of the second optic is found by finding the difference in defocus from the blue-green continuum to the red-yellow continuum. There are 2 optical powers that will move the mode j to the red-yellow continuum, and two possible modes in the blue-green continuum from which k can be reached, giving 4 possible similar solutions. The algorithm can be set up so that there is only one way of moving between the blue-green and red-yellow continua by limiting their extent. The power of the third optic is found from the difference between the mode k and mode l at optic 3.

# Appendix F

## Light and Gaussian Modes

This appendix contains an overview of Gaussian modes. More in-depth explanations can be found in [181].

### F.1 The Fundamental Gaussian Mode

The simplest laser beam profile can be described by the fundamental Gaussian mode. This is a mode which has a circular intensity profile which follows a Gaussian distribution, and its surface of constant phase is spherical. As the phase fronts are spherical, Gaussian beams describe lasers in optical layouts which have spherically

curved optics. The fundamental Gaussian mode is given by

$$E(\mathbf{r}) = E_0 \sqrt{\frac{2}{\pi}} \frac{1}{w(z)} \exp(i\phi(z)) \exp\left(-ik \frac{x^2 + y^2}{2R_c(z)} - \frac{x^2 + y^2}{w^2(z)}\right) \exp(-ikz). \quad (\text{F.1})$$

Gaussian beams are characterised by the size of their waist,  $w_0$ . The width of a Gaussian beam at a position  $z$  along the optical axis is represented by  $w(z)$ , and  $w(0) = w_0$ . Gaussian beams are also characterised by  $\phi(z)$ , which gives the Gouy phase of the beam at  $z$  along the optical axis, and by  $R_c(z)$ , which gives the radius of curvature of the beam at  $z$ .

It is useful to express  $w(z)$ ,  $\phi(z)$  and  $R_c(z)$  in terms of the Rayleigh range,  $z_R$ . The Rayleigh range characterises how fast the beam will spread out. The size of the waist determines the Rayleigh range; a smaller beam waist corresponds to a shorter Rayleigh range. The Rayleigh range is given by

$$z_R = \frac{\pi w_0^2}{\lambda}. \quad (\text{F.2})$$

The width of the beam as it propagates along the optical axis can be written as

$$w(z) = w_0 \sqrt{1 + \left(\frac{z}{z_R}\right)^2}. \quad (\text{F.3})$$

In the far field ( $z > z_R$ ), Equation (F.3) becomes linear and the beam size can be

approximated as

$$w(z) \approx w_0 \frac{z}{z_R}. \quad (\text{F.4})$$

As a Gaussian beam propagates along the optical axis, it acquires an additional phase shift compared to a plane wave. This is known as the Gouy phase shift,  $\phi(z)$ , and it is given by

$$\phi(z) = \tan^{-1} \frac{z}{z_R}. \quad (\text{F.5})$$

The radius of curvature,  $R_c(z)$ , is given by

$$R_c(z) = z + \frac{z_R^2}{z}. \quad (\text{F.6})$$

The inverse of a beam's radius of curvature is known as its defocus,  $S(z) = 1/R_c(z)$ . The defocus of a beam is useful as it is easier to compute the effects of a beam interacting with a focussing element of an optical layout in terms of the defocus than it is with the radius of curvature.

### F.1.1 The Complex Beam Parameter

The fundamental Gaussian mode can be expressed in terms of a complex beam parameter,  $q(z)$ . This parameter is useful for calculating how a Gaussian beam is transformed by an optical system. From this parameter, all the physical quantities related to a Gaussian beam can be computed. The complex beam parameter is

defined as

$$q(z) = z + iz_{\text{R}}. \quad (\text{F.7})$$

The inverse of the complex beam parameter can be written in terms of the radius of curvature and width of the beam. This is given by

$$\frac{1}{q(z)} = \frac{1}{R(z)} - i \frac{\lambda}{\pi w^2(z)}. \quad (\text{F.8})$$

Equation (F.1) can be rewritten in terms of the complex beam parameter,

$$E(\mathbf{r}) = E_0 \sqrt{\frac{2}{\pi}} \frac{q_0}{w_0 q(z)} \exp(i\phi(z)) \exp\left(-ik \frac{x^2 + y^2}{2q(z)}\right) \exp(-ikz). \quad (\text{F.9})$$

The width of the beam, Gouy phase, and the defocus at a point  $z$  along the optical axis can be calculated from  $q(z)$  using

$$w(z) = \sqrt{\frac{\lambda}{-\pi \Im\left(\frac{1}{q(z)}\right)}}, \quad (\text{F.10})$$

$$\phi(z) = \tan^{-1}\left(\frac{\Re(q(z))}{\Im(q(z))}\right), \quad (\text{F.11})$$

$$S(z) = \Re\left(\frac{1}{q(z)}\right). \quad (\text{F.12})$$

### F.1.2 Astigmatism

If a beam has an elliptical profile, then the beam is astigmatic. The simplest type of astigmatism can be described with two complex Gaussian beam parameters, one for the  $yz$  (tangential) plane and one for the  $xz$  (sagittal) plane. A Gaussian beam with simple astigmatism will have a different waist size and location in the tangential and sagittal planes. This type of astigmatism can arise due to Gaussian beams passing through a cylindrical lens or by them having a non-zero angle of incidence to a mirror.

An astigmatic Gaussian beam can be split up into two orthogonal fields,

$$\begin{aligned}
 E(\mathbf{r}) &= E(x, z)E(y, z) \\
 &= E_0 \sqrt{\frac{2}{\pi}} \sqrt{\frac{q_{x0}}{w_{x0}q_x(z)}} \sqrt{\frac{q_{y0}}{w_{y0}q_y(z)}} \exp(i\phi_{Av}(z)) \\
 &\quad \times \exp\left(-ik\frac{x^2}{2q_x(z)} - ik\frac{y^2}{2q_y(z)}\right) \exp(-ikz). \tag{F.13}
 \end{aligned}$$

where  $\phi_{Av}(z)$  is the average of the Gouy phase in the sagittal and tangential planes. The equations for waist size, Gouy phase and defocus remain the same (Equation (F.10), Equation (F.11) and Equation (F.12)). A beam with astigmatism can be thought of as two independent beams, and their interaction with the optical layout can be calculated independently.

## F.2 Gaussian Beams Traversing Optical Layouts

As a Gaussian beam propagates through an optical layout, the beam parameter that describes it changes. The effect of simple optical components can be modelled with ABCD matrices, and an entire layout can be modelled by multiplying a series of ABCD matrices together. This formalism can also be used to compute cavity eigenmodes.

When a beam interacts with an optical component, it is transformed from a mode described by  $q_1$  to a new mode described by  $q_2$  according to

$$q_2 = \frac{Aq_1 + B}{Cq_1 + D}. \quad (\text{F.14})$$

The coefficients  $A, B, C, D$  are defined by an ABCD matrix,

$$\mathbf{M} = \begin{pmatrix} A & B \\ C & D \end{pmatrix}. \quad (\text{F.15})$$

The beam parameter of a laser as it passes through the first component to the  $n^{\text{th}}$  component can be calculated with the matrix obtained from multiplying the ABCD matrices of the components together,

$$\mathbf{M} = \mathbf{M}_n \mathbf{M}_{n-1} \dots \mathbf{M}_0. \quad (\text{F.16})$$

Note, the left most matrix corresponds to the final optical component in the layout.

Optical Component	ABCD Matrix
space	$\begin{pmatrix} 1 & d \\ 0 & 1 \end{pmatrix}$
Mirror or lens (normal incidence)	$\begin{pmatrix} 1 & 0 \\ -S & 1 \end{pmatrix}$
Mirror (Sagittal Plane)	$\begin{pmatrix} 1 & 0 \\ -\frac{S}{\cos \alpha} & 1 \end{pmatrix}$
Mirror (Tangential Plane)	$\begin{pmatrix} 1 & 0 \\ -S \cos \alpha & 1 \end{pmatrix}$

Table F.1: ABCD matrices for simple optical components. The length of the space is  $d$ , and the optical power of the mirror/lens is  $S$ . The angle of incidence is  $\alpha$ .

The ABCD matrices for spaces and mirrors are summarised in Table F.1.

### F.3 Higher Order Modes and Optical Imperfections

The fundamental Gaussian mode describes the electric field of a beam in an ideal optical system. Imperfections in the optical layout, such as misalignment, mode mismatch and spatial distortions in mirror surfaces, can generate light with a different intensity profile to the fundamental Gaussian mode. For instance, if a beam entering a cavity is slightly misaligned, the resulting reflected beam will have a mode profile that looks like two spots instead of one. A small difference in waist size or location, i.e. a mode mismatch, between them would result in the reflected beam having a ring-shaped mode profile. Similar effects happen when a laser and

a cavity are misaligned. These imperfections in the layout and the resulting beam shapes can be modelled as the optical layout scattering light into higher order optical modes (e.g [136]).

One complete, orthonormal basis set of functions that can be used to construct higher order modes with are the Hermite-Gaussian modes. These modes have  $xy$  symmetry and are rectangularly shaped. HG modes are useful for modelling misalignments because this type of imperfection can be naturally broken into  $xy$  coordinates.

Mode mismatches are best described by the  $r\theta$  coordinates, and so it is natural to express these in terms of another orthonormal basis set known as the Laguerre-Gauss modes. However, if the beam is astigmatic then the mode no longer has the symmetry required in order to be modelled with Laguerre-Gauss modes. Second order HG modes can also describe mode mismatch, even if the modes are astigmatic.

The spatial distribution of a higher order mode's field amplitude can be described with

$$\Psi_{nm}(x, y, z) = \Psi_n(x, z)\Psi_m(y, z). \quad (\text{F.17})$$

The functions  $\Psi_n$  have the form

$$\Psi_n(x, z) = \left(\frac{2}{\pi}\right)^{1/4} \left(\frac{\exp(i(2n+1)\phi(z))}{2^n n! w(z)}\right)^{1/2} H_n\left(\frac{\sqrt{2}x}{w(z)}\right) \exp\left(-i\frac{kx^2}{2R_c(z)} - i\frac{x^2}{w^2(z)}\right), \quad (\text{F.18})$$

where  $H_n(x)$  a Hermite polynomial of the order  $n$ . By writing  $\Psi_{nm}(x, y, z)$  out explicitly,

$$\Psi_{nm}(x, y, z) = \left(2^{(n+m-1)}n!m!\pi\right)^{1/2} \frac{1}{w(z)} \exp(i(n+m+1)\phi(z)) \\ H_n\left(\frac{\sqrt{2}x}{w(z)}\right) H_m\left(\frac{\sqrt{2}y}{w(z)}\right) \exp\left(-ik\frac{x^2+y^2}{2R_c(z)} - i\frac{x^2+y^2}{w^2(z)}\right), \quad (\text{F.19})$$

we can see that higher order modes have the same waist size and radius of curvature as the fundamental mode, but different intensity distributions and additional Gouy phase.

In general, a mode can be written as a superposition of HG modes

$$E(x, y, z) = \sum_{n=0}^{n=\infty} \sum_{m=0}^{m=\infty} A_n \Psi_n(x) A_m \Psi_m(y), \quad (\text{F.20})$$

where  $A_n$  is the amplitude of the  $n^{\text{th}}$  mode.



# Appendix G

## Mode Matching Between Two Astigmatic Beams

The electric field,  $E$ , of a Gaussian beam can be written as

$$E(x, y, z) = E_x(x, z)E_y(y, z), \quad (\text{G.1})$$

where

$$E_x(x, z) = \frac{E_0}{\sqrt{q_x(z)}} \exp\left(-ik\frac{x^2}{2q_x(z)}\right), \quad (\text{G.2})$$

$$E_y(y, z) = \frac{E_0}{\sqrt{q_y(z)}} \exp\left(-ik\frac{y^2}{2q_y(z)}\right). \quad (\text{G.3})$$

The constant  $E_0$  is such that the units of  $E^*E$  are  $\text{Wm}^{-2}$ . Mode matching depends only on the spatial distribution of the modes' intensities, denoted with  $\Psi$ , so the units of the electric field not feature in this calculation.

For a beam without astigmatism,  $x^2 + y^2 = r^2$  and  $q_x = q_y = q$ , so the spatial distribution of a mode's intensity can be expressed as

$$\Psi(r, z) = \frac{1}{q(z)} \exp\left(-ik \frac{r^2}{2q(z)}\right). \quad (\text{G.4})$$

For a beam with astigmatism, the spatial distribution of a mode's intensity is given by

$$\Psi(x, y) = \frac{1}{\sqrt{q_x}} \exp\left(\frac{ikx^2}{2q_x}\right) \frac{1}{\sqrt{q_y}} \exp\left(\frac{iky^2}{2q_y}\right). \quad (\text{G.5})$$

The mode matching,  $\mathcal{M}$ , between two beams is determined by the overlap integral of the spatial distribution of their intensities. This can be calculated with

$$\mathcal{M} = \frac{\left| \int_A \Psi_1^* \Psi_2 dA \right|}{\int_A |\Psi_1|^2 dA \int_A |\Psi_2|^2 dA}. \quad (\text{G.6})$$

The numerator of Equation (G.6) for astigmatic beams can be written as

$$\left| \int_A \Psi_1^* \Psi_2 dA \right| = \int_A \Psi_1^* \Psi_2 dA \int_A \Psi_1 \Psi_2^* dA \quad (\text{G.7})$$

$$= \int_{-\infty}^{-\infty} \Psi_{x1}^* \Psi_{x2} dx \int_{-\infty}^{-\infty} \Psi_{y1}^* \Psi_{y2} dy \int_{-\infty}^{-\infty} \Psi_{x1} \Psi_{x2}^* dx \int_{-\infty}^{-\infty} \Psi_{y1} \Psi_{y2}^* dy. \quad (\text{G.8})$$

Since this calculation is the same for the  $x$  and  $y$  coordinates, we only need to show the method for simplifying the  $x$  terms. The  $x$  terms of Equation (G.8) can be

written as

$$\int_{-\infty}^{-\infty} \Psi_{x_1}^* \Psi_{x_2} dx \int_{-\infty}^{-\infty} \Psi_{x_1} \Psi_{x_2}^* dx = \int_{-\infty}^{\infty} \frac{1}{\sqrt{q_{x_1}^*}} \exp\left(\frac{ikx^2}{2q_{x_1}^*}\right) \frac{1}{\sqrt{q_{x_2}}} \exp\left(\frac{-ikx^2}{2q_{x_2}}\right) dx \times \int_{-\infty}^{\infty} \frac{1}{\sqrt{q_{x_1}}} \exp\left(\frac{-ikx^2}{2q_{x_1}}\right) \frac{1}{\sqrt{q_{x_2}^*}} \exp\left(\frac{ikx^2}{2q_{x_2}^*}\right) dx, \quad (\text{G.9})$$

$$\begin{aligned} &= \frac{1}{|q_{x_1}| |q_{x_2}|} \left( \int_{-\infty}^{\infty} \exp\left(\frac{ikx^2}{2q_{x_1}^*}\right) \exp\left(\frac{-ikx^2}{2q_{x_2}}\right) dx \times \text{c.c.} \right), \\ &= \frac{1}{|q_{x_1}| |q_{x_2}|} \left( \int_{-\infty}^{\infty} \exp\left(\frac{ikx^2 (q_{x_2} - q_{x_1}^*)}{2q_{x_1}^* q_{x_2}}\right) dx \times \text{c.c.} \right), \end{aligned} \quad (\text{G.10})$$

where c.c. is shorthand for the complex conjugate of the preceding expression.

Using the identity

$$\mathcal{I} = \int_{-\infty}^{\infty} \exp(iax^2) dx = \frac{i\pi}{a} \quad (\text{G.11})$$

and labelling

$$a = \frac{k(q_{x_2} - q_{x_1}^*)}{2q_{x_1}^* q_{x_2}} \quad (\text{G.12})$$

allows Equation (G.10) to be simplified to

$$\frac{1}{|q_{x_1}| |q_{x_2}|} \sqrt{\frac{i\pi (2q_{x_1}^* q_{x_2})}{k (q_{x_2} - q_{x_1}^*)}} \sqrt{\frac{-i\pi (2q_{x_1} q_{x_2}^*)}{k (q_{x_2}^* - q_{x_1})}} = \frac{2\pi}{k} \frac{1}{|q_{x_2} - q_{x_1}^*|}. \quad (\text{G.13})$$

Thus, the numerator of Equation (G.6) is

$$\frac{4\pi^2}{k^2} \frac{1}{|q_{x_2} - q_{x_1}^*| |q_{y_2} - q_{y_1}^*|}. \quad (\text{G.14})$$

## Appendix G. Mode Matching Between Two Astigmatic Beams

---

Since  $\Psi_x$  and  $\Psi_y$  are orthogonal,  $|\Psi|^2 = |\Psi_x|^2 |\Psi_y|^2$ . An expression for the denominator of Equation (G.6) can be found as follows:

$$\int_A |\Psi|^2 dA = \int_{-\infty}^{\infty} \int_{-\infty}^{\infty} |\Psi_x|^2 |\Psi_y|^2 dx dy \quad (\text{G.15})$$

$$= \int_{-\infty}^{\infty} \frac{1}{|q_x|} \exp\left(\frac{ikx^2(q_x - q_x^*)}{2q_x q_x^*}\right) \times y \text{ term}. \quad (\text{G.16})$$

A similar approach to the calculation of the denominator can be used for the calculation of the numerator terms. The numerator terms take the form

$$\int_A |\Psi|^2 dA = \frac{1}{|q_x|} \sqrt{\frac{i2\pi |q_x|^2}{k(q_x - q_x^*)}} \frac{1}{|q_y|} \sqrt{\frac{i2\pi |q_y|^2}{k(q_y - q_y^*)}}, \quad (\text{G.17})$$

$$= -\frac{2\pi}{k} \frac{1}{\sqrt{(q_x - q_x^*)(q_y - q_y^*)}}. \quad (\text{G.18})$$

Thus, we get the mode matching  $\mathcal{M}$  to be

$$\mathcal{M} = \frac{\sqrt{(q_{x1} - q_{x1}^*)(q_{y1} - q_{y1}^*)(q_{x2} - q_{x2}^*)(q_{y2} - q_{y2}^*)}}{|q_{x2} - q_{x1}^*| |q_{y2} - q_{y1}^*|}. \quad (\text{G.19})$$

# Acronyms

**ADC** analogue-to-digital converter. 218, 219, 232, 273

**AOM** acousto-optic modulator. 38, 41, 53, 57, 59–63, 66, 67, 72, 88, 242

**AS** anti-symmetric. 6, 7, 11, 12, 15, 16, 20, 22, 94, 101, 102, 104, 108, 109, 138, 142, 144, 146

**AWC** active wavefront control. 93, 96, 149, 150, 158, 164, 166–168

**BBH** binary black hole. 2, 7, 137

**BHD** balanced homodyne detection. 20, 22, 30, 96, 131, 132, 134, 135, 137–139, 143, 145, 149, 209, 214, 237, 239

**BNS** binary neutron star. 2, 3, 7, 20, 137

**CDS** control and data system. 55, 67, 68, 218, 219, 228, 232, 235, 271–273

**DAC** digital-to-analogue converter. 231, 232, 273

**DBB** diagnostic bread board. 37, 39, 43, 47, 50, 53, 55, 75, 76, 86

**EOM** electro-optic modulator. 38, 40, 78, 79

- ESD** electro-static discharge. 178, 193
- ETM** end test mass. 5–7, 9, 10, 15, 17, 18, 103, 107, 108, 214, 279, 282
- FSR** free spectral range. 36, 50, 81, 83
- FWHM** full width at half maximum. 36, 81, 82
- HAM** horizontal access modules. 26, 145, 146
- HG** Hermite-Gaussian. 99, 302, 303
- HOM** higher order mode. 44, 47, 48, 51, 93–95, 98, 103, 104, 106, 108, 109, 122, 123, 127, 128, 277, 278
- HPO** high power oscillator. 33, 73, 86
- IC** integrated circuit. 59, 61, 71, 218, 257, 259
- IMC** input mode cleaner. 26, 28, 36, 54, 56, 57, 103
- ISS** intensity stabilisation servo. 39, 42, 60, 62, 63, 67, 73
- ITM** input test mass. 9, 15, 93, 103, 105, 107–109, 111, 112, 118, 123, 279, 281, 282
- LHO** LIGO Hanford Observatory, WA., USA. 26, 45, 47, 73, 279
- LLO** LIGO Livingston Observatory, LA., USA. 20, 26, 96, 97, 103, 111, 115, 117, 121, 127, 158, 164, 166, 275, 279–282
- LO** local oscillator. 20, 131, 132, 134–136, 138–140, 142–147, 149–151, 214, 222, 224

- MOPA** master-oscillator-power-amplifier. 33, 34
- ND** neutral density. 216–218, 222
- NPRO** non-planar ring oscillator. 34–36, 38–40, 51, 55, 58, 77, 79, 81, 86, 87, 217, 224, 227
- OFI** output Faraday isolator. 26, 28, 95, 152, 154, 157, 167
- OMC** output mode cleaner. 16, 24, 27, 28, 91–97, 103, 127, 128, 143, 149–153, 156–158, 162, 164–166, 168, 289
- PDH** Pound-Drever-Hall. 38, 57, 58, 78, 79, 81, 84
- PIN** p-doped, intrinsic, n-doped. 25, 172
- PMC** pre mode cleaner. 31, 34–36, 38, 39, 41, 42, 44, 46, 53–55, 57, 58, 61–64, 67, 68, 73, 74, 76–79, 81, 83, 84, 86–88, 271, 272
- PRC** power recycling cavity. 14, 26, 97, 103
- PRM** power recycling mirror. 8, 14, 26
- PSL** pre-stabilised-laser. 26, 32–34, 37, 40, 44, 66, 73, 75, 76, 86, 88
- RF** radio-frequency. 16, 24, 34, 36, 54, 57, 59, 78, 135
- RIN** relative intensity noise. 43, 55, 66
- RoC** radius of curvature. 94, 104–106, 111–113, 116, 127, 129, 150, 157, 158, 164, 167, 279, 280, 282

**RSE** resonant sideband extraction. 15, 18, 93, 107, 111, 122–128

**SAMS** suspended active matching stages. 152, 158, 168

**SNR** signal to noise ratio. 3, 16, 17, 23, 32, 93, 127, 170, 171, 180, 186, 208

**SQL** standard quantum limit. 18, 21, 22

**SRC** signal recycling cavity. 15, 91–95, 98, 103–107, 111, 112, 115–117, 119, 121–129, 138, 141, 142, 150, 152, 158, 164, 166, 167, 242, 243, 276, 279, 280, 282, 284

**SRM** signal recycling mirror. 8, 15, 18, 92–94, 97, 98, 103, 105–113, 115–119, 121–126, 128, 129, 140, 150, 152, 156–158, 162, 164, 166, 242, 243, 279–282

**TEM** transverse electro-magnetic. 99, 119, 123

**WS** waist-defocus. 158, 160–166, 168, 294

# Bibliography

- [1] Nina Bode, Joseph Briggs, Xu Chen, Maik Frede, Peter Fritschel, Michael Fyffe, Eric Gustafson, Matthew Heintze, Peter King, Jian Liu, Jason Oberling, Richard L. Savage, Andrew Spencer, and Benno Willke. Advanced ligo Laser Systems for O3 and Future Observation Runs. *Galaxies*, 8(4):84, Dec 2020.
  
- [2] Thomas A Caswell, Michael Droettboom, Antony Lee, Elliott Sales De Andrade, John Hunter, Tim Hoffmann, Eric Firing, Jody Klymak, David Stansby, Nelle Varoquaux, Jens Hedegaard Nielsen, Benjamin Root, Ryan May, Phil Elson, Jouni K. Seppänen, Darren Dale, Jae-Joon Lee, Damon McDougall, Andrew Straw, Paul Hobson, Christoph Gohlke, Tony S Yu, Eric Ma, Adrien F. Vincent, , Hannah, Steven Silvester, Charlie Moad, Nikita Kniazev, Elan Ernest, and Paul Ivanov. matplotlib/matplotlib: Rel: v3.4.0rc3, 2021.
  
- [3] Alexander Franzen. Componentlibrary. <http://www.gwoptics.org/ComponentLibrary/>.
  
- [4] LIGO Virgo Collaboration. observation of Gravitational Waves From a Binary Black Hole Merger. *Phys. Rev. Lett.*, 116:061102, Feb 2016.

- [5] The LIGO Scientific Collaboration. Advanced LIGO. *Classical and Quantum Gravity*, 32(7):074001, Mar 2015.
- [6] LIGO Virgo Collaboration. GW170814: A Three-detector Observation of Gravitational Waves From a Binary Black Hole Coalescence. *Phys. Rev. Lett.*, 119:141101, Oct 2017.
- [7] The LIGO Virgo Collaboration. GW190412: Observation of a Binary-black-hole Coalescence with Asymmetric Masses. *Physical Review D*, 102(4), Aug 2020.
- [8] The LIGO Virgo Collaboration. GW190521: A Binary Black Hole Merger with a Total Mass of  $150 M_{\odot}$ . *Physical Review Letters*, 125(10), Sep 2020.
- [9] The LIGO Virgo Collaboration. GW170817: Observation of Gravitational Waves from a Binary Neutron Star Inspiral. *Physical Review Letters*, 119(16), oct 2017.
- [10] The LIGO Virgo Collaboration. GW190425: Observation of a Compact Binary Coalescence with Total Mass  $\sim 3.4 M_{\odot}$ . *The Astrophysical Journal*, 892(1):L3, Mar 2020.
- [11] The LVK collaboration. GW190814: Gravitational Waves From the Coalescence of a 23 Solar Mass Black Hole with a 2.6 Solar Mass Compact Object. *The Astrophysical Journal*, 896(2):L44, Jun 2020.
- [12] The LIGO Virgo Collaboration. GWTC-2: Compact Binary Coalescences Observed by Ligo and Virgo During the First Half of the Third Observing Run. *arXiv:1410.5093*, 2021.

- [13] B. P. Abbott et al. Tests of General Relativity with GW150914. *Physical Review Letters*, 116(22), May 2016.
- [14] B. P. Abbott et al. Properties of the Binary Black Hole Merger GW150914. *Physical Review Letters*, 116(24), Jun 2016.
- [15] The LIGO Scientific Collaboration, The Virgo Collaboration, The 1M2H Collaboration, The Dark Energy Camera GW-EM Collaboration, the DES Collaboration, The Las Cumbres Observatory Collaboration The DLT40 Collaboration, and The VINROUGE Collaboration & The MASTER Collaboration. A Gravitational-wave Standard Siren Measurement of the Hubble Constant. *Nature*, Oct 2017.
- [16] B. P. Abbott et al. GW170817: Measurements of neutron star radii and equation of state. *Physical Review Letters*, 121(16), Oct 2018.
- [17] B. P. Abbott et al. Estimating the Contribution of Dynamical Ejecta in the Kilonova Associated with GW170817. *The Astrophysical Journal*, 850(2):L39, Dec 2017.
- [18] The LIGO Virgo Collaboration. The Basic Physics of the Binary Black Hole Merger GW150914. *Annalen der Physik*, 529(1-2):1600209, Oct 2016.
- [19] The LIGO Scientific Collaboration and the Virgo Collaboration. Tests of General Relativity with Binary Black Holes From the Second LIGO-Virgo Gravitational-wave Transient Catalog. *arXiv:2010.14529*, 2020.
- [20] Charles W. Misner. *Gravitation*. Princeton University Press, 2nd edition, Oct 2017.

- [21] Bernard Schutz. *A First Course in General Relativity; 2nd Edition*. Cambridge University Press, 2009.
  
- [22] LVK collaboration. Narrow-band Search For Gravitational Waves From Known Pulsars Using the Second LIGO Observing Run. *Physical Review D*, 99(12), Jun 2019.
  
- [23] The LIGO Virgo Collaboration. Searches For Continuous Gravitational Waves From 15 Supernova Remnants and Fomalhaut B with Advanced LIGO. *The Astrophysical Journal*, 875(2):122, Apr 2019.
  
- [24] The LIGO Virgo Collaboration. Search For Transient Gravitational-wave Signals Associated with Magnetar Bursts During Advanced LIGO's Second Observing Run. *The Astrophysical Journal*, 874(2):163, Apr 2019.
  
- [25] B. S. Sathyaprakash and Bernard F. Schutz. Physics, Astrophysics and Cosmology with Gravitational Waves. *Living Reviews in Relativity*, 12(1), Mar 2009.
  
- [26] Ernazar Abdikamalov, Giulia Pagliaroli, and David Radice. Gravitational Waves From Core-collapse Supernovae. *arXiv:2010.04356*, 2020.
  
- [27] Teng Zhang, Jiří Smetana, Yikang Chen, Joe Bentley, Denis Martynov, Haixing Miao, William E. East, and Huan Yang. Toward observing neutron star collapse with gravitational wave detectors. *Physical Review D*, 103(4), feb 2021.

- 
- [28] The LIGO Virgo Collaboration. Search For the Isotropic Stochastic Background Using Data From Advanced LIGOS's Second Observing Run. *Physical Review D*, 100(6), Sep 2019.
- [29] Juan García-Bellido. Massive Primordial Black Holes As Dark Matter and Their Detection with Gravitational Waves. *Journal of Physics: Conference Series*, 840:012032, May 2017.
- [30] Simeon Bird, Ilias Cholis, Julian B. Muñoz, Yacine Ali-Haïmoud, Marc Kamionkowski, Ely D. Kovetz, Alvis Raccanelli, and Adam G. Riess. Did LIGO Detect Dark Matter? *Physical Review Letters*, 116(20), May 2016.
- [31] T. Regimbau, M. Evans, N. Christensen, E. Katsavounidis, B. Sathyaprakash, and S. Vitale. Digging Deeper: Observing Primordial Gravitational Waves Below the Binary-black-hole-produced Stochastic Background. *Physical Review Letters*, 118(15), Apr 2017.
- [32] Yanou Cui, Marek Lewicki, David E. Morrissey, and James D. Wells. Probing the Pre-BBN Universe with Gravitational Waves From Cosmic Strings. *Journal of High Energy Physics*, 2019(1), Jan 2019.
- [33] Piotr Jaranowski, Andrzej Królak, and Bernard F. Schutz. Data analysis of gravitational-wave signals from spinning neutron stars: The signal and its detection. *Physical Review D*, 58(6), August 1998.
- [34] LIGO Virgo Collaboration. Prospects For Observing and Localizing Gravitational-wave Transients with Advanced LIGO, Advanced Virgo and KAGRA. *Living Reviews in Relativity*, 19(1), Feb 2020.

- [35] F Acernese et al. Advanced Virgo: a Second-generation Interferometric Gravitational Wave Detector. *Classical and Quantum Gravity*, 32(2):024001, Dec 2014.
- [36] Yoichi Aso, Yuta Michimura, Kentaro Somiya, Masaki Ando, Osamu Miyakawa, Takanori Sekiguchi, Daisuke Tatsumi, and Hiroaki Yamamoto. Interferometer Design of the KAGRA Gravitational Wave Detector. *Physical Review D*, 88(4), Aug 2013.
- [37] S M Aston, M A Barton, A S Bell, N Beveridge, B Bland, A J Brummitt, G Cagnoli, C A Cantley, L Carbone, A V Cumming, L Cunningham, R M Cutler, R J S Greenhalgh, G D Hammond, K Haughian, T M Hayler, A Heptonstall, J Heefner, D Hoyland, J Hough, R Jones, J S Kissel, R Kumar, N A Lockerbie, D Lodhia, I W Martin, P G Murray, J O'Dell, M V Plissi, S Reid, J Romie, N A Robertson, S Rowan, B Shapiro, C C Speake, K A Strain, K V Tokmakov, C Torrie, A A van Veggel, A Vecchio, and I Wilmot. Update on Quadruple Suspension Design For Advanced LIGO. *Classical and Quantum Gravity*, 29(23):235004, Oct 2012.
- [38] Gregory M Harry, Matthew R Abernathy, Andres E Becerra-Toledo, Helena Armandula, Eric Black, Kate Dooley, Matt Eichenfield, Chinyere NwabuGwu, Akira Villar, D R M Crooks, Gianpietro Cagnoli, Jim Hough, Colin R How, Ian MacLaren, Peter Murray, Stuart Reid, Sheila Rowan, Peter H Sneddon, Martin M Fejer, Roger Route, Steven D Penn, Patrick Ganau, Jean-Marie Mackowski, Christophe Michel, Laurent Pinard, and Alban Remillieux. Titania-doped Tantalum/silica Coatings For Gravitational-wave Detection. *Classical and Quantum Gravity*, 24(2):405–415, Dec 2006.

- 
- [39] S Hild, H Grote, J Degallaix, S Chelkowski, K Danzmann, A Freise, M Hewitson, J Hough, H Lück, M Prijatelj, K A Strain, J R Smith, and B Willke. dc-readout of a Signal-recycled Gravitational Wave Detector. *Classical and Quantum Gravity*, 26(5):055012, Feb 2009.
- [40] Tobin T Fricke, Nicolás D Smith-Lefebvre, Richard Abbott, Rana Adhikari, Katherine L Dooley, Matthew Evans, Peter Fritschel, Valery V Frolov, Keita Kawabe, Jeffrey S Kissel, Bram J J Slagmolen, and Sam J Waldman. DC Readout Experiment in Enhanced LIGO. *Classical and Quantum Gravity*, 29(6):065005, Feb 2012.
- [41] J. Mizuno. *Comparison of Optical Configurations For Laser-interferometric Gravitational-wave Detectors*. PhD thesis, AEI-Hannover, MPI for Gravitational Physics, Max Planck Society, 1995.
- [42] Gerhard Heinzl. *Advanced Optical Techniques For Laser-interferometric Gravitational-wave Detectors*. PhD thesis, Hannover: Universität, Diss, 1999. <https://doi.org/10.15488/5622>.
- [43] B.J. Meers. The Frequency Response of Interferometric Gravitational Wave Detectors. *Physics Letters A*, 142(8-9):465–470, Dec 1989.
- [44] Charlotte Bond, Daniel Brown, Andreas Freise, and Kenneth A. Strain. Interferometer Techniques For Gravitational-wave Detection. *Living Reviews in Relativity*, 19(1), Dec 2016.
- [45] Vladimir B. Braginsky. Energetic Quantum Limit in Large-scale Interferometers. In *aip Conference Proceedings*. AIP, 2000.

- [46] Carlton M. Caves. Quantum-mechanical Noise in an Interferometer. *Physical Review D*, 23(8):1693–1708, Apr 1981.
- [47] Stefan L. Danilishin and Farid Ya. Khalili. Quantum Measurement Theory in Gravitational-wave Detectors. *Living Reviews in Relativity*, 15(1), Apr 2012.
- [48] Brian J. Meers. Recycling in Laser-interferometric Gravitational-wave Detectors. *Physical Review D*, 38(8):2317–2326, Oct 1988.
- [49] K. A. Strain and B. J. Meers. Experimental Demonstration of Dual Recycling For Interferometric Gravitational-wave Detectors. *Physical Review Letters*, 66(11):1391–1394, Mar 1991.
- [50] D. Schnier, J. Mizuno, G. Heinzl, H. Lück, A. Rüdiger, R. Schilling, M. Schrempel, W. Winkler, and K. Danzmann. Power Recycling in the Garching 30m Prototype Interferometer For Gravitational-wave Detection. *Physics Letters A*, 225(4-6):210–216, Feb 1997.
- [51] R. W. P. Drever, J. L. Hall, F. V. Kowalski, J. Hough, G. M. Ford, A. J. Munley, and H. Ward. Laser Phase and Frequency Stabilization Using An Optical Resonator. *Applied Physics B*, 31(2):97–105, Jun 1983.
- [52] Muzammil A. Arain and Guido Mueller. Design of the Advanced LIGO Recycling Cavities. *Optics Express*, 16(14):10018, Jun 2008.
- [53] G. Heinzl, J. Mizuno, R. Schilling, W. Winkler, A. Rüdiger, and K. Danzmann. An Experimental Demonstration of Resonant Sideband Extraction For Laser-interferometric Gravitational Wave Detectors. *Physics Letters A*, 217(6):305–314, Jul 1996.

- 
- [54] J. Mizuno, K.A. Strain, P.G. Nelson, J.M. Chen, R. Schilling, A. Rüdiger, W. Winkler, and K. Danzmann. Resonant Sideband Extraction: a New Configuration For Interferometric Gravitational Wave Detectors. *Physics Letters A*, 175(5):273–276, Apr 1993.
- [55] Dhruva Ganapathy, Lee McCuller, Jameson Graef Rollins, Evan D. Hall, Lisa Barsotti, and Matthew Evans. Tuning Advanced LIGO To Kilohertz Signals From Neutron-star Collisions. *Physical Review D*, January 2021.
- [56] B Sorazu, P J Fulda, B W Barr, A S Bell, C Bond, L Carbone, A Freise, S Hild, S H Huttner, J Macarthur, and K A Strain. Experimental Test of Higher-order Laguerre–Gauss Modes in the 10 m Glasgow Prototype Interferometer. *Classical and Quantum Gravity*, 30(3):035004, January 2013.
- [57] Koji Arai, Sam Barnum, Peter Fritschel, Jeff Lewis, and Sam Waldman. Output Mode Cleaner (OMC) Design. LIGO-T1000276-v5.
- [58] M Prijatelj, J Degallaix, H Grote, J Leong, C Affeldt, S Hild, H Lück, J Slutsky, H Wittel, K Strain, and K Danzmann. The Output Mode Cleaner of GEO 600. *Classical and Quantum Gravity*, 29(5):055009, Feb 2012.
- [59] H. J. Kimble, Yuri Levin, Andrey B. Matsko, Kip S. Thorne, and Sergey P. Vyatchanin. Conversion of Conventional Gravitational-wave Interferometers Into Quantum Nondemolition Interferometers by Modifying Their Input and/or Output Optics. *Physical Review D*, 65(2), Dec 2001.
- [60] V. B. Braginsky and F. Ya. Khalili. Quantum Nondemolition Measurements: the Route From Toys To Tools. *Reviews of Modern Physics*, 68(1):1–11, Jan 1996.

- [61] Alessandra Buonanno and Yanbei Chen. Quantum Noise in Second Generation, Signal-recycled Laser Interferometric Gravitational-wave Detectors. *Physical Review D*, 64(4), Jul 2001.
- [62] R Flaminio, J Franc, C Michel, N Morgado, L Pinard, and B Sassolas. A Study of Coating Mechanical and Optical Losses in View of Reducing Mirror Thermal Noise in Gravitational Wave Detectors. *Classical and Quantum Gravity*, 27(8):084030, Apr 2010.
- [63] Rainer Weiss. Quarterly Progress Report: Electromagnetically Coupled Broadband Gravitational Antenna. DCC LIGO-P720002-v1, April 1972.
- [64] A. Buikema, C. Cahillane, G. L. Mansell, C. D. Blair, R. Abbott, C. Adams, R. X. Adhikari, A. Ananyeva, S. Appert, K. Arai, J. S. Areeda, Y. Asali, S. M. Aston, C. Austin, A. M. Baer, M. Ball, S. W. Ballmer, S. Banagiri, D. Barker, L. Barsotti, J. Bartlett, B. K. Berger, J. Betzwieser, D. Bhattacharjee, G. Billingsley, S. Biscans, R. M. Blair, N. Bode, P. Booker, R. Bork, A. Bramley, A. F. Brooks, D. D. Brown, K. C. Cannon, X. Chen, A. A. Ciobanu, F. Clara, S. J. Cooper, K. R. Corley, S. T. Countryman, P. B. Covas, D. C. Coyne, L. E. H. Datrier, D. Davis, C. Di Fronzo, K. L. Dooley, J. C. Driggers, P. Dupej, S. E. Dwyer, A. Effler, T. Etzel, M. Evans, T. M. Evans, J. Feicht, A. Fernandez-Galiana, P. Fritschel, V. V. Frolov, P. Fulda, M. Fyffe, J. A. Giaime, K. D. Giardina, P. Godwin, E. Goetz, S. Gras, C. Gray, R. Gray, A. C. Green, E. K. Gustafson, R. Gustafson, J. Hanks, J. Hanson, T. Hardwick, R. K. Hasskew, M. C. Heintze, A. F. Helmling-Cornell, N. A. Holland, J. D. Jones, S. Kandhasamy, S. Karki, M. Kasprzack, K. Kawabe, N. Kijbunchoo, P. J. King, J. S. Kissel, Rahul Kumar, M. Landry, B. B. Lane, B. Lantz,

---

M. Laxen, Y. K. Lecoche, J. Leviton, J. Liu, M. Lormand, A. P. Lundgren, R. Macas, M. MacInnis, D. M. Macleod, S. Márka, Z. Márka, D. V. Martynov, K. Mason, T. J. Massinger, F. Matichard, N. Mavalvala, R. McCarthy, D. E. McClelland, S. McCormick, L. McCuller, J. McIver, T. McRae, G. Mendell, K. Merfeld, E. L. Merilh, F. Meylahn, T. Mistry, R. Mittleman, G. Moreno, C. M. Mow-Lowry, S. Mozzon, A. Mullavey, T. J. N. Nelson, P. Nguyen, L. K. Nuttall, J. Oberling, Richard J. Oram, B. O'Reilly, C. Osthelder, D. J. Ottaway, H. Overmier, J. R. Palamos, W. Parker, E. Payne, A. Pele, R. Penhorwood, C. J. Perez, M. Pirello, H. Radkins, K. E. Ramirez, J. W. Richardson, K. Riles, N. A. Robertson, J. G. Rollins, C. L. Romel, J. H. Romie, M. P. Ross, K. Ryan, T. Sadecki, E. J. Sanchez, L. E. Sanchez, T. R. Saravanan, R. L. Savage, D. Schaetzl, R. Schnabel, R. M. S. Schofield, E. Schwartz, D. Sellers, T. Shaffer, D. Sigg, B. J. J. Slagmolen, J. R. Smith, S. Soni, B. Sorazu, A. P. Spencer, K. A. Strain, L. Sun, M. J. Szczepańczyk, M. Thomas, P. Thomas, K. A. Thorne, K. Toland, C. I. Torrie, G. Traylor, M. Tse, A. L. Urban, G. Vajente, G. Valdes, D. C. Vander-Hyde, P. J. Veitch, K. Venkateswara, G. Venugopalan, A. D. Viets, T. Vo, C. Vorvick, M. Wade, R. L. Ward, J. Warner, B. Weaver, R. Weiss, C. Whittle, B. Willke, C. C. Wipf, L. Xiao, H. Yamamoto, Hang Yu, Haocun Yu, L. Zhang, M. E. Zucker, and J. Zweizig. Sensitivity and Performance of the Advanced LIGO Detectors in the Third Observing Run. *Physical Review D*, 102(6), Sep 2020.

- [65] Carlton M. Caves and Bonny L. Schumaker. New Formalism For Two-photon Quantum Optics. I. Quadrature Phases and Squeezed States. *Physical Review A*, 31(5):3068–3092, May 1985.

- [66] Bonny L. Schumaker and Carlton M. Caves. SNew Formalism For Two-photon Quantum Optics. II. Mathematical Foundation and Compact Notation. *Physical Review A*, 31(5):3093–3111, May 1985.
- [67] M. Tse, Haocun Yu, N. Kijbunchoo, A. Fernandez-Galiana, P. Dupej, L. Barsotti, C. D. Blair, D. D. Brown, S. E. Dwyer, A. Effler, M. Evans, P. Fritschel, V. V. Frolov, A. C. Green, G. L. Mansell, F. Matchard, N. Mavalvala, D. E. McClelland, L. McCuller, T. McRae, J. Miller, A. Mullavey, E. Oelker, I. Y. Phinney, D. Sigg, B. J. J. Slagmolen, T. Vo, R. L. Ward, C. Whittle, R. Abbott, C. Adams, R. X. Adhikari, A. Ananyeva, S. Appert, K. Arai, J. S. Areeda, Y. Asali, S. M. Aston, C. Austin, A. M. Baer, M. Ball, S. W. Ballmer, S. Banagiri, D. Barker, J. Bartlett, B. K. Berger, J. Betzwieser, D. Bhattacharjee, G. Billingsley, S. Biscans, R. M. Blair, N. Bode, P. Booker, R. Bork, A. Bramley, A. F. Brooks, A. Buikema, C. Cahillane, K. C. Cannon, X. Chen, A. A. Ciobanu, F. Clara, S. J. Cooper, K. R. Corley, S. T. Countryman, P. B. Covas, D. C. Coyne, L. E. H. Datrier, D. Davis, C. Di Fronzo, J. C. Driggers, T. Etzel, T. M. Evans, J. Feicht, P. Fulda, M. Fyffe, J. A. Giaime, K. D. Giardina, P. Godwin, E. Goetz, S. Gras, C. Gray, R. Gray, Anchal Gupta, E. K. Gustafson, R. Gustafson, J. Hanks, J. Hanson, T. Hardwick, R. K. Hasskew, M. C. Heintze, A. F. Helmling-Cornell, N. A. Holland, J. D. Jones, S. Kandhasamy, S. Karki, M. Kasprzack, K. Kawabe, P. J. King, J. S. Kissel, Rahul Kumar, M. Landry, B. B. Lane, B. Lantz, M. Laxen, Y. K. Lecoecuche, J. Leviton, J. Liu, M. Lormand, A. P. Lundgren, R. Macas, M. MacInnis, D. M. Macleod, S. Márka, Z. Márka, D. V. Martynov, K. Mason, T. J. Massinger, R. McCarthy, S. McCormick, J. McIver, G. Mendell, K. Merfeld, E. L. Merilh, F. Meylahn,

- T. Mistry, R. Mittleman, G. Moreno, C. M. Mow-Lowry, S. Mozzon, T. J. N. Nelson, P. Nguyen, L. K. Nuttall, J. Oberling, R. J. Oram, B. O'Reilly, C. Osthelder, D. J. Ottaway, H. Overmier, J. R. Palamos, W. Parker, E. Payne, A. Pele, C. J. Perez, M. Pirello, H. Radkins, K. E. Ramirez, J. W. Richardson, K. Riles, N. A. Robertson, J. G. Rollins, C. L. Romel, J. H. Romie, M. P. Ross, K. Ryan, T. Sadecki, E. J. Sanchez, L. E. Sanchez, T. R. Saravanan, R. L. Savage, D. Schaetzl, R. Schnabel, R. M. S. Schofield, E. Schwartz, D. Sellers, T. J. Shaffer, J. R. Smith, S. Soni, B. Sorazu, A. P. Spencer, K. A. Strain, L. Sun, M. J. Szczepańczyk, M. Thomas, P. Thomas, K. A. Thorne, K. Toland, C. I. Torrie, G. Traylor, A. L. Urban, G. Vajente, G. Valdes, D. C. VanderHyde, P. J. Veitch, K. Venkateswara, G. Venugopalan, A. D. Viets, C. Vorvick, M. Wade, J. Warner, B. Weaver, R. Weiss, B. Willke, C. C. Wipf, L. Xiao, H. Yamamoto, M. J. Yap, Hang Yu, L. Zhang, M. E. Zucker, and J. Zweizig. Quantum-enhanced Advanced LIGO Detectors in the Era of Gravitational-wave Astronomy. *Physical Review Letters*, 123(23), Dec 2019.
- [68] James Lough, Emil Schreiber, Fabio Bergamin, Hartmut Grote, Moritz Mehmet, Henning Vahlbruch, Christoph Affeldt, Marc Brinkmann, Aparna Bisht, Volker Kringel, Harald Lück, Nikhil Mukund, Séverin Nadji, Borja Sorazu, Kenneth Strain, Michael Weinert, and Karsten Danzmann. First Demonstration of 6 dB Quantum Noise Reduction in a Kilometer Scale Gravitational Wave Observatory. *Physical Review Letters*, 126(041102), 2021.
- [69] D. F. Walls. Squeezed States of Light. *Nature*, 306(5939):141–146, Nov 1983.
- [70] Haocun Yu, , L. McCuller, M. Tse, N. Kijbunchoo, L. Barsotti, and N. Mavalvala. Quantum Correlations Between Light and the Kilogram-mass Mirrors

- of LIGO. *Nature*, 583(7814):43–47, Jul 2020.
- [71] Kentaro Komori, Dhruva Ganapathy, Chris Whittle, Lee McCuller, Lisa Barsotti, Nergis Mavalvala, and Matthew Evans. Demonstration of An Amplitude Filter Cavity At Gravitational-wave Frequencies. *Physical Review D*, 102(10), Nov 2020.
- [72] Joe Bentley, Philip Jones, Denis Martynov, Andreas Freise, and Haixing Miao. Converting the Signal-recycling Cavity Into An Unstable Optomechanical Filter To Enhance the Detection Bandwidth of Gravitational-wave Detectors. *Physical Review D*, 99(10), May 2019.
- [73] Haixing Miao, Yiqiu Ma, Chunnong Zhao, and Yanbei Chen. Enhancing the Bandwidth of Gravitational-wave Detectors with Unstable Optomechanical Filters. *Physical Review Letters*, 115(21), Nov 2015.
- [74] Xiang Li, Maxim Goryachev, Yiqiu Ma, Michael E. Tobar, Chunnong Zhao, Rana X Adhikari, , and Yanbei Chen. Broadband Sensitivity Improvement Via Coherent Quantum Feedback with Pt Symmetry. *arXiv:2012.00836*, 2020.
- [75] Vladimir B. Braginsky, Yuri I. Vorontsov, and Kip S. Thorne. Quantum Nondemolition Measurements. *Science*, 209(4456):547–557, 1980.
- [76] Patricia Purdue and Yanbei Chen. Practical Speed Meter Designs For Quantum Nondemolition Gravitational-wave Interferometers. *Physical Review D*, 66(12), Dec 2002.
- [77] T. Zhang, E. Knyazev, S. Steinlechner, F. Y. Khalili, B. W. Barr, A. S. Bell, P. Dupej, J. Briggs, C. Gräf, J. Callaghan, J. S. Hennig, E. A. Houston,

- S. H. Huttner, S. S. Leavey, D. Pascucci, B. Sorazu, A. Spencer, J. Wright, K. A. Strain, S. Hild, and S. L. Danilishin. Quantum Noise Cancellation in Asymmetric Speed Metres with Balanced Homodyne Readout. *New journal of physics*, 20(10):103040, 2018.
- [78] S H Huttner, S L Danilishin, S Hild, and K A Strain. Comparison of Different Sloshing Speedmeters. *Classical and Quantum Gravity*, 37(8):085022, Mar 2020.
- [79] L. McCuller, C. Whittle, D. Ganapathy, K. Komori, M. Tse, A. Fernandez-Galiana, L. Barsotti, P. Fritschel, M. MacInnis, F. Matchard, K. Mason, N. Mavalvala, R. Mittleman, Haocun Yu, M.E. Zucker, and M. Evans. Frequency-dependent Squeezing For Advanced LIGO. *Physical Review Letters*, 124(17), Apr 2020.
- [80] G. Gasparian. personal communication, September 2018. GPD optoelectronics Corperation.
- [81] T. Hornby. personal communication, September 2018. Laser Components (UK) Ltd.
- [82] R. Miron. personal communication, September 2018. Thorlabs Ltd.
- [83] K. Kalinina. personal communication, September 2018. LED Microsensor.
- [84] Georgia L. Mansell, Terry G. McRae, Paul A. Altin, Min Jet Yap, Robert L. Ward, Bram J. J. Slagmolen, Daniel A. Shaddock, and David E. McClelland. Observation of Squeezed Light in the  $2\mu\text{m}$  Region. *Physical Review Letters*, 120(20), May 2018.

- [85] M. J. Yap, D. W. Gould, T. G. McRae, P. A. Altin, N. Kijbunchoo, G. L. Mansell, R. L. Ward, D. A. Shaddock, B. J. J. Slagmolen, and D. E. McClelland. Squeezed Vacuum Phase Control At  $2\mu\text{m}$ . *Optics Letters*, 44(21):5386, Nov 2019.
- [86] P. Fritschel and E. Gustafson. Advanced LIGO Optical Layout. LIGO Document D0902838-v5 <https://dcc.ligo.org/LIGO-D0902838>.
- [87] L. Barsotti, S. Gras, M. Evans, and P. Fritschel. Updated Advanced LIGO Sensitivity Design Curve. LIGO DCC, April 2018. LIGO Document T1800044-v5 <https://dcc.ligo.org/LIGO-T1800044/public>.
- [88] L. Barsotti, L. McCuller, M. Evans, and P. Fritschel. The A+ Design Curve. LIGO DCC, April 2018. LIGO Document T1800042-v5 <https://dcc.ligo.org/LIGO-T1800042/public>.
- [89] M Punturo, M Abernathy, F Acernese, B Allen, N Andersson, K Arun, F Barone, B Barr, M Barsuglia, M Beker, N Beveridge, S Birindelli, S Bose, L Bosi, S Braccini, C Bradaschia, T Bulik, E Calloni, G Cella, E Chassande Mottin, S Chelkowski, A Chincarini, J Clark, E Coccia, C Colacino, J Colas, A Cumming, L Cunningham, E Cuoco, S Danilishin, K Danzmann, G De Luca, R De Salvo, T Dent, R De Rosa, L Di Fiore, A Di Virgilio, M Doets, V Fafone, P Falferi, R Flaminio, J Franc, F Frasconi, A Freise, P Fulda, J Gair, G Gemme, A Gennai, A Giazotto, K Glampedakis, M Granata, H Grote, G Guidi, G Hammond, M Hannam, J Harms, D Heinert, M Hendry, I Heng, E Hennes, S Hild, J Hough, S Husa, S Huttner, G Jones, F Khalili, K Kokeyama, K Kokkotas, B Krishnan, M Lorenzini, H Lück, E Majo-

- 
- rana, I Mandel, V Mandic, I Martin, C Michel, Y Minenkov, N Morgado, S Mosca, B Mours, H Müller–Ebhardt, P Murray, R Nawrodt, J Nelson, R Oshaughnessy, C D Ott, C Palomba, A Paoli, G Parguez, A Pasqualetti, R Passaquieti, D Passuello, L Pinard, R Poggiani, P Popolizio, M Prato, P Puppò, D Rabeling, P Rapagnani, J Read, T Regimbau, H Rehbein, S Reid, L Rezzolla, F Ricci, F Richard, A Rocchi, S Rowan, A Rüdiger, B Sassolas, B Sathyaprakash, R Schnabel, C Schwarz, P Seidel, A Sintes, K Somiya, F Speirits, K Strain, S Strigin, P Sutton, S Tarabrin, A Thüring, J van den Brand, C van Leewen, M van Veggel, C van den Broeck, A Vecchio, J Veitch, F Vetrano, A Vicere, S Vyatchanin, B Willke, G Woan, P Wolfango, and K Yamamoto. The Einstein Telescope: a Third-generation Gravitational Wave Observatory. *Classical and Quantum Gravity*, 27(19):194002, Sep 2010.
- [90] S Hild, M Abernathy, F Acernese, P Amaro-Seoane, N Andersson, K Arun, F Barone, B Barr, M Barsuglia, M Beker, N Beveridge, S Birindelli, S Bose, L Bosi, S Braccini, C Bradaschia, T Bulik, E Calloni, G Cella, E Chassande Mottin, S Chelkowski, A Chincarini, J Clark, E Coccia, C Colacino, J Colas, A Cumming, L Cunningham, E Cuoco, S Danilishin, K Danzmann, R De Salvo, T Dent, R De Rosa, L Di Fiore, A Di Virgilio, M Doets, V Fafone, P Falferi, R Flaminio, J Franc, F Frasconi, A Freise, D Friedrich, P Fulda, J Gair, G Gemme, E Genin, A Gennai, A Giazotto, K Glampedakis, C Gräf, M Granata, H Grote, G Guidi, A Gurkovsky, G Hammond, M Hannam, J Harms, D Heinert, M Hendry, I Heng, E Hennes, J Hough, S Husa, S Huttner, G Jones, F Khalili, K Kokeyama, K Kokkotas, B Krishnan, T G F Li, M Lorenzini, H Lück, E Majorana, I Mandel, V Mandic, M Manto-

- vani, I Martin, C Michel, Y Minenkov, N Morgado, S Mosca, B Mours, H Müller–Ebhardt, P Murray, R Nawrodt, J Nelson, R Oshaughnessy, C D Ott, C Palomba, A Paoli, G Parguez, A Pasqualetti, R Passaquieti, D Passuello, L Pinard, W Plastino, R Poggiani, P Popolizio, M Prato, M Punturo, P Puppo, D Rabeling, P Rapagnani, J Read, T Regimbau, H Rehbein, S Reid, F Ricci, F Richard, A Rocchi, S Rowan, A Rüdiger, L Santamaría, B Sassolas, B Sathyaprakash, R Schnabel, C Schwarz, P Seidel, A Sintes, K Somiya, F Speirits, K Strain, S Strigin, P Sutton, S Tarabrin, A Thüring, J van den Brand, M van Veggel, C van den Broeck, A Vecchio, J Veitch, F Vetrano, A Vicere, S Vyatchanin, B Willke, G Woan, and K Yamamoto. Sensitivity Studies for Third-generation Gravitational Wave Observatories. *Classical and Quantum Gravity*, 28(9):094013, Apr 2011.
- [91] R X Adhikari, K Arai, A F Brooks, C Wipf, O Aguiar, P Altin, B Barr, L Barsotti, R Bassiri, A Bell, G Billingsley, R Birney, D Blair, E Bonilla, J Briggs, D D Brown, R Byer, H Cao, M Constancio, S Cooper, T Corbitt, D Coyne, A Cumming, E Daw, R deRosa, G Eddolls, J Eichholz, M Evans, M Fejer, E C Ferreira, A Freise, V V Frolov, S Gras, A Green, H Grote, E Gustafson, E D Hall, G Hammond, J Harms, G Harry, K Haughian, D Heinert, M Heintze, F Hellman, J Hennig, M Hennig, S Hild, J Hough, W Johnson, B Kamai, D Kapasi, K Komori, D Koptsov, M Korobko, W Z Korth, K Kuns, B Lantz, S Leavey, F Magana-Sandoval, G Mansell, A Markosyan, A Markowitz, I Martin, R Martin, D Martynov, D E McClelland, G McGhee, T McRae, J Mills, V Mitrofanov, M Molina-Ruiz, C Mow-Lowry, J Munch, P Murray, S Ng, M A Okada, D J Ottaway, L Prokhorov, V Quetschke, S Reid, D Reitze,

- J Richardson, R Robie, I Romero-Shaw, R Route, S Rowan, R Schnabel, M Schneewind, F Seifert, D Shaddock, B Shapiro, D Shoemaker, A S Silva, B Slagmolen, J Smith, N Smith, J Steinlechner, K Strain, D Taira, S Tait, D Tanner, Z Tornasi, C Torrie, M Van Veggel, J Vanheijningen, P Veitch, A Wade, G Wallace, R Ward, R Weiss, P Wessels, B Willke, H Yamamoto, M J Yap, and C Zhao. A Cryogenic Silicon Interferometer For Gravitational-wave Detection. *Classical and Quantum Gravity*, 37(16):165003, Jul 2020.
- [92] The LIGO Virgo Collaboration. Exploring the Sensitivity of Next Generation Gravitational Wave Detectors. *Classical and Quantum Gravity*, 34(4):044001, Jan 2017.
- [93] David Reitze, Rana X Adhikari, Stefan Ballmer, Barry Barish, Lisa Barsotti, GariLynn Billingsley, Duncan A. Brown, Yanbei Chen, Dennis Coyne, Robert Eisenstein, Matthew Evans, Peter Fritschel, Evan D. Hall, Albert Lazzarini, Geoffrey Lovelace, Jocelyn Read, B. S. Sathyaprakash, David Shoemaker, Joshua Smith, Calum Torrie, Salvatore Vitale, Rainer Weiss, Christopher Wipf, and Michael Zucker. Cosmic Explorer: The U.S. Contribution To Gravitational-wave Astronomy Beyond LIGO. *arXiv:1907.04833*, 2019.
- [94] Evan D. Hall, Kevin Kuns, Joshua R. Smith, Yuntao Bai, Christopher Wipf, Sebastien Biscans, Rana X Adhikari, Koji Arai, Stefan Ballmer, Lisa Barsotti, Yanbei Chen, Matthew Evans, Peter Fritschel, Jan Harms, Brittany Kamai, Jameson Graef Rollins, David Shoemaker, Bram Slagmolen, Rainer Weiss, and Hiro Yamamoto. Gravitational-wave Physics with Cosmic Explorer: Limits to Low-frequency Sensitivity. *arXiv:2012.03608*, 2020.

- [95] the LIGO Scientific Collaboration. Instrument Science White Paper 2019. LIGO internal document LIGO-T1900409–v3.
- [96] Anja Schroeter, Ronny Nawrodt, Roman Schnabel, Stuart Reid, Iain Martin, Sheila Rowan, Christian Schwarz, Torsten Koettig, Ralf Neubert, Matthias Thürk, Wolfgang Vodel, Andreas Tünnermann, Karsten Danzmann, and Paul Seidel. On the Mechanical Quality Factors of Cryogenic Test Masses From Fused Silica and Crystalline Quartz. *arXiv:0709.4359*, 2007.
- [97] Martin A. Green and Mark J. Keevers. Optical Properties of Intrinsic Silicon At 300 K. *Progress in Photovoltaics: Research and Applications*, 3(3):189–192, 1995.
- [98] I Martin, H Armandula, C Comtet, M M Fejer, A Gretarsson, G Harry, J Hough, J-M M Mackowski, I MacLaren, C Michel, J-L Montorio, N Morgado, R Nawrodt, S Penn, S Reid, A Remillieux, R Route, S Rowan, C Schwarz, P Seidel, W Vodel, and A Zimmer. Measurements of a Low-temperature Mechanical Dissipation Peak in a Single Layer of Ta<sub>2</sub>O<sub>5</sub> Doped with TiO<sub>2</sub>. *Classical and Quantum Gravity*, 25(5):055005, Feb 2008.
- [99] I W Martin, R Bassiri, R Nawrodt, M M Fejer, A Gretarsson, E Gustafson, G Harry, J Hough, I MacLaren, S Penn, S Reid, R Route, S Rowan, C Schwarz, P Seidel, J Scott, and A L Woodcraft. Effect of Heat Treatment on Mechanical Dissipation in Ta<sub>2</sub>O<sub>5</sub> Coatings. *Classical and Quantum Gravity*, 27(22):225020, Oct 2010.
- [100] I W Martin, R Nawrodt, K Craig, C Schwarz, R Bassiri, G Harry, J Hough, S Penn, S Reid, R Robie, and S Rowan. Low Temperature Mechanical Dissi-

- 
- pation of An Ion-beam Sputtered Silica Film. *Classical and Quantum Gravity*, 31(3):035019, Jan 2014.
- [101] Kieran Craig, Jessica Steinlechner, Peter G. Murray, Angus S. Bell, Ross Birney, Karen Haughian, Jim Hough, Ian MacLaren, Steve Penn, Stuart Reid, Raymond Robie, Sheila Rowan, and Iain W. Martin. Mirror Coating Solution For the Cryogenic Einstein Telescope. *Physical Review Letters*, 122(23), Jun 2019.
- [102] B. Willke, P. King, R. Savage, and P. Fritschel. Pre-stabilized Laser Design Requirements. DCC LIGO-T050036-v4, July 2011.
- [103] E. A. Shcherbakov, V. V. Fomin, A. A. Abramov, A. A. Ferin, D. V. Mochalov, and V. P. Gapontsev. Industrial Grade 100kW Power CW Fiber Laser. In *Advanced Solid-state Lasers Congress*. OSA, 2013.
- [104] Junsu Lee, Kwang Hyun Lee, Hwanseong Jeong, Minkyu Park, Ji Hoon Seung, and Jung Hwan Lee. 205 kW All-fiber High-beam-quality Fiber Amplifier with Stimulated Brillouin Scattering Suppression Incorporating a Narrow-linewidth Fiber-bragg-grating-stabilized Laser Diode Seed Source. *Applied Optics*, 58(23):6251, Aug 2019.
- [105] Yusheng Huang, Ping Yan, Zehui Wang, Jiading Tian, Dan Li, Qirong Xiao, and Mali Gong. 219kW Narrow Linewidth fbg-based mopa Configuration Fiber Laser. *Optics Express*, 27(3):3136, Jan 2019.
- [106] Pengfei Ma, Rumao Tao, Rongtao Su, Xiaolin Wang, Pu Zhou, and Zejin Liu. 189kW All-fiberized and Polarization-maintained Amplifiers with Nar-

- row Linewidth and Near-diffraction-limited Beam Quality. *Optics Express*, 24(4):4187, Feb 2016.
- [107] Craig Robin, Iyad Dajani, and Benjamin Pulford. Modal Instability-suppressing, Single-frequency Photonic Crystal Fiber Amplifier with 811 W Output Power. *Optics Letters*, 39(3):666, Jan 2014.
- [108] Clément Dixneuf, Germain Guiraud, Yves-Vincent Bardin, Quentin Rosa, Mathieu Goepfner, Adèle Hilico, Christophe Pierre, Johan Boulet, Nicholas Traynor, and Giorgio Santarelli. Ultra-low Intensity Noise, All Fiber 365W Linearly Polarized Single Frequency Laser At 1064 nm. *Optics Express*, 28(8):10960, Mar 2020.
- [109] L. Winkelmann, O. Puncken, R. Kluzik, C. Veltkamp, P. Kwee, J. Poeld, C. Bogan, B. Willke, M. Frede, J. Neumann, P. Wessels, and D. Kracht. Injection-locked Single-frequency Laser with an Output Power Of 220W. *Applied Physics B*, 102(3):529–538, Feb 2011.
- [110] Felix Wellmann, Michael Steinke, Fabian Meylahn, Nina Bode, Benno Willke, Ludger Overmeyer, Jörg Neumann, and Dietmar Kracht. High Power, Single-frequency, Monolithic Fiber Amplifier For the Next Generation of Gravitational Wave Detectors. *Optics Express*, 27(20):28523, Sep 2019.
- [111] Aaron Buikema, Franklin Jose, Steven J. Augst, Peter Fritschel, and Nergis Mavalvala. Narrow-linewidth Fiber Amplifier For Gravitational-wave Detectors. *Optics Letters*, 44(15):3833, Jul 2019.

- [112] Nina Bode, Fabian Meylahn, and Benno Willke. Sequential High Power Laser Amplifiers For Gravitational Wave Detection. *Optics Express*, 28(20):29469, Sep 2020.
- [113] Fabian Thies, Nina Bode, Patrick Oppermann, Maik Frede, Bastian Schulz, and Benno Willke. Nd:YVO<sub>4</sub> High-power Master Oscillator Power Amplifier Laser System for Second-generation Gravitational Wave Detectors. *Optics Letters*, 44(3):719, Jan 2019.
- [114] P. Kwee, C. Bogan, K. Danzmann, M. Frede, H. Kim, P. King, J. Pödl, O. Puncken, R. L. Savage, F. Seifert, P. Wessels, L. Winkelmann, and B. Willke. Stabilized High-power Laser System for the Gravitational Wave Detector Advanced LIGO. *Optics Express*, 20(10):10617, Apr 2012.
- [115] neoLase Amplifiers. <https://neolase.com/produkte/laser-verstaerker/?lang=en>. Accessed 18/03/2021.
- [116] Andrew P. Spencer. *Advanced Techniques in Laser Interferometry for Current and Future Gravitational Wave Detectors*. PhD thesis, University of Glasgow, August 2019.
- [117] Thomas J. Kane and Robert L. Byer. Monolithic, Unidirectional Single-mode Nd:YAG Ring Laser. *Optics Letters*, 10(2):65, Feb 1985.
- [118] I Freitag, A Tünnermann, and H Welling. Power Scaling of Diode-pumped Monolithic Nd:YAG Lasers To Output Powers of Several Watts. *Optics Communications*, 115(5-6):511–515, Apr 1995.

- [119] Michèle Heurs, Volker M. Quetschke, Benno Willke, Karsten Danzmann, and Ingo Freitag. Simultaneously Suppressing Frequency and Intensity Noise in a Nd:YAG Nonplanar Ring Oscillator by Means of the Current-lock Technique. *Optics Letters*, 29(18):2148, Sep 2004.
- [120] Mephisto Laser, Coherent. <https://www.coherent.com/lasers/main/mephisto-lasers>. Accessed 18/03/2021.
- [121] J. Lui, R. Savage, P. King, L. Zhang, and S. et al. Appert. aLIGO All-bolted PMC Summary. LIGO Document T1700543-v2 <https://dcc.ligo.org/LIGO-T1700543>.
- [122] M. Heintze. Information regarding the two failed PSL Pre-mode cleaners (PMC's) at LLO, September 2015. LIGO- T1500492-V1 <https://dcc.ligo.org/LIGO-T1500492/public>.
- [123] Jian Liu and Rick Savage. Update on aLIGO PSL PMC Upgrade to Address Contamination Issues, August 2017. LIGO Document G1701481-v1 <https://dcc.ligo.org/LIGO-G1701481>.
- [124] Patrick Kwee, Frank Seifert, Benno Willke, and Karsten Danzmann. Laser Beam Quality and Pointing Measurement with An Optical Resonator. *Review of Scientific Instruments*, 78(7):073103, Jul 2007.
- [125] P. Kwee. *Laser Characterization and Stabilization For Precision Interferometry*. PhD thesis, Max Planck Institute for Gravitational Physics, 2010.
- [126] Beckhoff. <https://www.beckhoff.com/en-gb/>. Accessed 18/03/2021.

- 
- [127] C. Bogan. Intensity Stabilization Servo Module (inner Loop). LIGO Document D1001985-v2 <https://dcc.ligo.org/LIGO-D1001985/public>.
- [128] P. Kwee. aLIGO PSL ISS Inner-loop Photodiode. LIGO Document D1001998-v2 <https://dcc.ligo.org/LIGO-D1001998/public>.
- [129] R. S. Abbott and P. J. King. Diode-pumped Nd:YAG Laser Intensity Noise Suppression Using a Current Shunt. *Review of Scientific Instruments*, 72(2):1346, 2001.
- [130] B W Barr, K A Strain, and C J Killow. Laser Amplitude Stabilization For Advanced Interferometric Gravitational Wave Detectors. *Classical and Quantum Gravity*, 22(20):4279–4283, Oct 2005.
- [131] Jameson Rollins, David Ottaway, Michael Zucker, Rainer Weiss, and Richard Abbott. Solid-state Laser Intensity Stabilization At the  $10^{-8}$  Level. *Optics Letters*, 29(16):1876, Aug 2004.
- [132] I Zawischa, M Brendel, K Danzmann, C Fallnich, M Heurs, S Nagano, V Quetschke, H Welling, and B Willke. The GEO 600 Laser System. *Classical and Quantum Gravity*, 19(7):1775–1781, Mar 2002.
- [133] F. Nocera. LIGO Laser Intensity Noise Suppression. *Classical and Quantum Gravity*, 21(5):S481–S485, Feb 2004.
- [134] P. Horowitz and W. Hill. *The Art of Electronics*. Cambridge University Pr., 3rd edition, 2015.
- [135] G. Mueller. Pointing Requirements For Advanced LIGO. LIGO Document T0900142-v2 <https://dcc.ligo.org/LIGO-T0900142>.

- [136] Euan Morrison, Brian J. Meers, David I. Robertson, and Henry Ward. Automatic Alignment of Optical Interferometers. *Applied Optics*, 33(22):5041, Aug 1994.
- [137] H. Kim, P. King, C. Krämer, P. Kwee, J. Pöld, R. Savage, P. Weßels, and B. Willke. PSL Final Design. DCC LIGO T0900649-v4, February 2010.
- [138] N. Uehara and K. Ueda. Accurate Measurement of the Radius of Curvature of a Concave Mirror and the Power Dependence in a High-finesse Fabry–Perot Interferometer. *Applied Optics*, 34(25):5611, Sep 1995.
- [139] Henrik Tünnermann, Jan Hendrik Pöld, Jörg Neumann, Dietmar Kracht, Benno Willke, and Peter Weßels. Beam Quality and Noise Properties of Coherently Combined Ytterbium Doped Single Frequency Fiber Amplifiers. *Optics Express*, 19(20):19600, Sep 2011.
- [140] Li-Wei Wei, Frédéric Cleva, and Catherine Nary Man. Coherently Combined Master Oscillator Fiber Power Amplifiers For Advanced Virgo. *Optics Letters*, 41(24):5817, Dec 2016.
- [141] V. Frolov. DARM Optical Gain and Losses. <https://alog.ligo-la.caltech.edu/aLOG/index.php?callRep=42231>.
- [142] L. McCuller. Frequency Dependence of Squeezing Loss and Angle, Power Measurement by Radiation Pressure. <https://alog.ligo-la.caltech.edu/aLOG/index.php?callRep=52718>.
- [143] L. McCuller. Squeezing with Mode Mismatch Observations in LIGO. LIGO Document G2001503-v1 <https://dcc.ligo.org/LIGO-G2001503>.

- 
- [144] L. McCuller. Frequency Dependent Squeezing Effects in the LIGO Interferometers. LIGO Document G2000863-v2 <https://dcc.ligo.org/LIGO-G2000863>.
- [145] V. Frolov. Arm Cavity Power, Power Recycling Gain, IFO Reflectivity and Arm Cavity Losses. <https://alog.ligo-la.caltech.edu/aLOG/index.php?callRep=42639>.
- [146] C. Blair, V. Frolov, and A. Effler. SRM CO<sub>2</sub> Chop. <https://alog.ligo-la.caltech.edu/aLOG/index.php?callRep=38689>.
- [147] C. Blair. Annular CO<sub>2</sub> 1W at Various IFO Power. <https://alog.ligo-la.caltech.edu/aLOG/index.php?callRep=43065>.
- [148] C. Blair. OMC Scans. <https://alog.ligo-la.caltech.edu/aLOG/index.php?callRep=37742>.
- [149] C. Blair and V. Frolov. 40W OMC Scans Method and Preliminary Data. <https://alog.ligo-la.caltech.edu/aLOG/index.php?callRep=45830>.
- [150] A. Effler, V. Frolov, and C. Blair. OMC Scans of Cooling Interferometer. <https://alog.ligo-la.caltech.edu/aLOG/index.php?callRep=41428>.
- [151] M. Kasprzack, A. Effler, A. Mullavey, and M. Tse. HAM6 Work - M12 Move. <https://alog.ligo-la.caltech.edu/aLOG/index.php?callRep=37291>.
- [152] A. Effler and M. Kasprzack. LLO Interferometer Output Beam Study. LIGO Document T1800089-v2 <https://dcc.ligo.org/LIGO-T1800089>.
- [153] J. Richardson, M. Tse, and C. Austin. Measurement of SRC Gouy Phase. <https://alog.ligo-la.caltech.edu/aLOG/index.php?callRep=39779>.

- [154] A Freise, G Heinzl, H Lück, R Schilling, B Willke, and K Danzmann. Frequency-domain Interferometer Simulation with Higher-order Spatial Modes. *Classical and Quantum Gravity*, 21(5):S1067–S1074, Feb 2004.
- [155] D. Brown C. Bond and A. Freise. Finesse 2, May 2014. Software can be downloaded from <http://www.gwoptics.org/finesse>.
- [156] Daniel David Brown and Andreas Freise. Pykat, July 2017. <http://www.GWoptics.org/pykat>.
- [157] C. Blair. PRC Gouy Phase Measurement. <https://alog.ligo-la.caltech.edu/aLOG/index.php?callRep=49409>.
- [158] M. S. Stefszky, C. M. Mow-Lowry, S. S. Y. Chua, D. A. Shaddock, B. C. Buchler, H. Vahlbruch, A. Khalaidovski, R. Schnabel, P. K. Lam, and D. E. McClelland. Balanced Homodyne Detection of Optical Quantum States at Audio-band Frequencies and Below. *Classical and Quantum Gravity*, 29(14):145015, Jun 2012.
- [159] E. Oelker. Personal Communication, 2021.
- [160] L. McCuller. Nov Squeezing Data Infers Lo/readout Angle of  $11.5 \pm 2$  Deg, Good Side. <https://alog.ligo-la.caltech.edu/aLOG/index.php?callRep=53867>.
- [161] Peter Fritschel, Matthew Evans, and Valery Frolov. Balanced Homodyne Readout for Quantum Limited Gravitational Wave Detectors. *Optics Express*, 22(4):4224, Feb 2014.

- [162] Daniel Sigg and the LIGO Scientific Collaboration. Status of the LIGO Detectors. *Classical and Quantum Gravity*, 25(11):114041, May 2008.
- [163] Brian J. Meers and Kenneth A. Strain. Modulation, Signal, and Quantum Noise in Interferometers. *Physical Review A*, 44(7):4693–4703, Oct 1991.
- [164] Sebastian Steinlechner, Bryan W. Barr, Angus S. Bell, Stefan L. Danilishin, Andreas Gläfke, Christian Gräf, Jan-Simon Hennig, E. Alasdair Houston, Sabina H. Huttner, Sean S. Leavey, Daniela Pascucci, Borja Sorazu, Andrew Spencer, Kenneth A. Strain, Jennifer Wright, and Stefan Hild. Local-oscillator Noise Coupling in Balanced Homodyne Readout For Advanced Gravitational Wave Detectors. *Physical Review D*, 92(7), Oct 2015.
- [165] D.E. McClelland, N. Mavalvala, Y. Chen, and R. Schnabel. Advanced Interferometry, Quantum Optics and Optomechanics in Gravitational Wave Detectors. *Laser & Photonics Reviews*, 5(5):677–696, Mar 2011.
- [166] The LIGO Scientific Collaboration. A Gravitational Wave Observatory Operating Beyond the Quantum Shot-noise Limit. *Nature Physics*, 7(12):962–965, Sep 2011.
- [167] Kiwamu Izumi and Daniel Sigg. Advanced LIGO: Length Sensing and Control in a Dual Recycled Interferometric Gravitational Wave Antenna. *Classical and Quantum Gravity*, 34(1):015001, Dec 2016.
- [168] T. Zhang. *Advanced Techniques For Future Generation Gravitational Wave Detectors*. PhD thesis, University of Glasgow, 2019.

- [169] Hang Yu Peter Fritschel, Vivishek Sudhir. Exploring the BHD Readout Sensitivity and Requirements. LIGO DCC Document G1702485-v1. LIGO DCC Document G1702485-v1 <https://dcc.ligo.org/G1702485>.
- [170] P. Fritschel and S. Hild. Requirements For the Ham Relay Triple Suspension (HRTS). LIGO Document T1800413-v1 <https://dcc.ligo.org/LIGO-T1900817>.
- [171] R. Jones K.A. Strain. Ham Relay-optics Suspension: Pre-conceptual Design. LIGO-T1900036-v5 <https://dcc.ligo.org/LIGO-T1900036>.
- [172] B. Lantz, R. Mittleman, J. Kissel, J. Warner, and A. Pele. Typical Motion of HAM Suspension Points in O2. LIGO Document T1800066-v2 <https://dcc.ligo.org/T1800066>.
- [173] K. A. Strain, J. Briggs, M. Barton, R. Jones, S. Webster, and E. Oelker. Conceptual Design: Balanced Homodyne Detection For A+. LIGO Document E1900377-v3 <https://dcc.ligo.org/LIGO-E1900377>.
- [174] J. Briggs, M. Barton, J. Jones, E. Oelker, S. Webster, and K.A. Strain. A+ BHD ISC Additional Design Requirements. LIGO Document E2000072-v2 <https://dcc.ligo.org/LIGO-E2000072-v2>.
- [175] A. Brookes, P. Fritschel, F. Matchard, L. McCuller, M. Noh, and C. Torrie. SAMS Design Requirements Document. LIGO DCC, February 2019. E1800314 <https://dcc.ligo.org/LIGO-T1800042/public>.

- 
- [176] L. Barsotti. aLIGO ISC Anti-symmetric Port: Beam Parameters and Optical Layout. LIGO Document T1200410-v2 <https://dcc.ligo.org/LIGO-T1200410/public>.
- [177] Evgenia Kochkina. *Stigmatic and Astigmatic Gaussian Beams in Fundamental Mode: impact of Beam Model Choice on Interferometric Pathlength Signal Estimates*. PhD thesis, Hannover U., 2013.
- [178] A. Brookes, L. Barsotti, G. Billingsley, K.A. Strain, and M. Zucker. A+ O5-HAM6 Design Considerations and Requirements. LIGO DCC, April 2020. E1900385-v1 <https://dcc.ligo.org/LIGO-E1900385>.
- [179] F. Bayer-Helms. Coupling Coefficients of An Incident Wave and the Modes of a Spherical Optical Resonator in the Case of Mismatching and Misalignment. *Applied Optics*, 23(9):1369, May 1984.
- [180] Antonio Perreca, Aidan F. Brookes, Jonathan W. Richardson, Daniel Töyrä, and Rory Smith. Analysis and Visualization of the Output Mode-matching Requirements For Squeezing in Advanced ligo and Future Gravitational Wave Detectors. *Physical Review D*, 101(10), May 2020.
- [181] A.E. Siegman. *Lasers*. University Science Books, 1986.
- [182] L. Schnupp. (unpublished).
- [183] T. M. Niebauer, R. Schilling, K. Danzmann, A. Rüdiger, and W. Winkler. Nonstationary Shot Noise and Its Effect on the Sensitivity of Interferometers. *Physical Review A*, 43(9):5022–5029, May 1991.

- [184] Teng Zhang, Denis Martynov, Andreas Freise, and Haixing Miao. Quantum Squeezing Schemes For Heterodyne Readout. *Physical Review D*, 101(12), Jun 2020.
- [185] Marius Grundmann. *The Physics of Semiconductors*. Springer Berlin Heidelberg, 2010.
- [186] Vladimir Protopopov. *Practical Opto-electronics*. Springer International Publishing, 2014.
- [187] Ramon U. Martinelli, Thomas J. Zamerowski, and Paul A. Longeway. 2.6  $\mu\text{m}$  InGaAs Photodiodes. *Applied Physics Letters*, 53(11):989–991, Sep 1988.
- [188] M. S. Alam, M. S. Rahman, M. R. Islam, A. G. Bhuiyan, and M. Yamada. Refractive Index, Absorption Coefficient, and Photoelastic Constant: Key Parameters of ingaas Material Relevant To InGaAs-based Device Performance. In *2007 IEEE 19th International Conference on Indium Phosphide & Related Materials*. IEEE, May 2007.
- [189] Xing you Chen, Yi Gu, and Yong gang Zhang. Epitaxy and Device Properties of InGaAs Photodetectors with Relatively High Lattice Mismatch. In *Epitaxy*. InTech, Mar 2018.
- [190] M. Gendry, V. Drouot, C. Santinelli, and G. Hollinger. Critical Thicknesses of Highly Strained InGaAs Layers Grown on InP by Molecular Beam Epitaxy. *Applied Physics Letters*, 60(18):2249–2251, May 1992.
- [191] Abhay M. Joshi, Gregory H. Olsen, S. M. Mason, M. Kazakia, and Vladimir S. Ban. Near-infrared (1-3 Micron) InGaAs Detectors and Arrays - Crystal

- 
- Growth Leakage Current and Reliability. In Harold I. Schiff and Ulrich Platt, editors, *Optical Methods in Atmospheric Chemistry*. SPIE, Feb 1993.
- [192] Xiaowei Li, Ning Li, S. Demiguel, J.C. Campbell, D. Tulchinsky, and K.J. Williams. A Comparison of Front- and Backside-illuminated High-saturation Power Partially Depleted Absorber Photodetectors. *IEEE Journal of Quantum Electronics*, 40(9):1321–1325, Sep 2004.
- [193] Y. Uchida, H. Kakibayashi, and S. Goto. Electrical and Structural Properties of Dislocations Confined in a InGaAs/GaAs Heterostructure. *Journal of Applied Physics*, 74(6720), August 1993.
- [194] Pamela Jurczak, Kimberly A. Sablon, Marina Gutiérrez, Huiyun Liu, and Jiang Wu. 2.5- $\mu\text{m}$  InGaAs Photodiodes Grown on GaAs Substrates by Interfacial Misfit Array Technique. *Infrared Physics & Technology*, 81:320–324, Mar 2017.
- [195] Lars Zimmermann, Joachim John, Stefan Degroote, Gustaaf Borghs, Chris Van Hoof, and Stefan Nemeth. Extended Wavelength InGaAs on GaAs Using InAlAs Buffer For Back-side-illuminated Short-wave Infrared Detectors. *Applied Physics Letters*, 82(17):2838–2840, Apr 2003.
- [196] F N Hooge, T G M Kleinpenning, and L K J Vandamme. Experimental Studies on 1/f Noise. *Reports on Progress in Physics*, 44(5):479–532, May 1981.
- [197] M. D'Hondt, I. Moerman, and P. Demeester. Dark Current Optimisation of 2.5  $\mu\text{m}$  Wavelength, 2% Mismatched InGaAs Photodetectors on InP. In

*Conference Proceedings. 1998 International Conference on Indium Phosphide and Related Materials (cat. No.98ch36129)*. IEEE, 1998.

- [198] M. López, H. Hofer, K. D. Stock, J. C. Bermúdez, A. Schirmacher, F. Schneck, and S. Kück. Spectral Reflectance and Responsivity of Ge- and InGaAs-photodiodes in the Near-infrared: Measurement and Model. *Applied Optics*, 46(29):7337, Oct 2007.
- [199] S. Forrest. Performance of  $\text{In}_x\text{Ga}_{1-x}\text{As}_y\text{P}_{1-y}$  Photodiodes with Dark Current Limited by Diffusion, Generation Recombination, and Tunneling. *IEEE Journal of Quantum Electronics*, 17(2):217–226, Feb 1981.
- [200] InGaAs Photodiode FD10D, October 2017. Rev. D.
- [201] Hamamatsu. G12183 Series, July 2019.
- [202] Laser Components. Extended Ingaas Photodiodes IG26 Series. Accessed Jan 2021 <https://www.lasercomponents.com/uk/product/ingaas-500-2600-nm/>.
- [203] Laser Components. Extended Ingaas Photodiodes IG24 Series. Accessed Jan 2021 <https://www.lasercomponents.com/uk/product/ingaas-500-2600-nm/>.
- [204] Laser Components. Extended Ingaas Photodiodes IG22 Series. Accessed Jan 2021 <https://www.tme.eu/gb/details/ig22x1000s4i/photodiodes/laser-components/>.
- [205] Hamamatsu. G12182 Series, March 2019.

- [206] C. Huang, C. Ho, and M. Wu. Large-Area Planar Wavelength-Extended In-GaAs p-i-n Photodiodes Using Rapid Thermal Diffusion With Spin-On Dopant Technique. *IEEE Electron Device Letters*, 36(8):820–822, 2015.
- [207] Henning Vahlbruch, Moritz Mehmet, Karsten Danzmann, and Roman Schnabel. Detection of 15 dB Squeezed States of Light and Their Application For the Absolute Calibration of Photoelectric Quantum Efficiency. *Physical Review Letters*, 117(11), Sep 2016.
- [208] M. López, J. C. Molina, H. Hofer, A. Sperling, and S. Kück. Measurement of the Nonlinearity of Ge-and InGaAs-photodiodes At High Irradiance Levels. *MAPAN*, 25(1):47–52, Mar 2010.
- [209] <https://www.iceoxford.com/Low-Temperature-Varnish-ICEles03-.htm>, Accessed 15/03/2021.
- [210] J R Smith, P Ajith, H Grote, M Hewitson, S Hild, H Lück, K A Strain, B Willke, J Hough, and K Danzmann. Linear Projection of Technical Noise For Interferometric Gravitational-wave Detectors. *Classical and Quantum Gravity*, 23(2):527–537, Dec 2005.
- [211] Klaus W. Hodapp, Joseph B. Jensen, Everett M. Irwin, Hubert Yamada, Randolph Chung, Kent Fletcher, Louis Robertson, Joseph L. Hora, Douglas A. Simons, Wendy Mays, Robert Nolan, Matthieu Bec, Michael Merrill, and Albert M. Fowler. The Gemini Near-infrared Imager (niri). *Publications of the Astronomical Society of the Pacific*, 115(814):1388–1406, Dec 2003.
- [212] Alan R. Beattie. Quantum Efficiency in InSb. *Journal of Physics and Chemistry of Solids*, 23(8):1049–1056, Aug 1962.

- [213] Hamamatsu. InSb Photovoltaic Detectors, P5986/p4247 Series, December 2011. datasheet [https://www.hamamatsu.com/resources/pdf/ssd/p5968-060\\_etc\\_kird1039e.pdf](https://www.hamamatsu.com/resources/pdf/ssd/p5968-060_etc_kird1039e.pdf).
- [214] Ibrahim Kimukin, Necmi Biyikli, and Ekmel Ozbay. InSb High-speed Photodetectors Grown on GaAs Substrate. *Journal of Applied Physics*, 94(8):5414, 2003.
- [215] A.J. Moseley, M.D. Scott, A.H. Moore, and R.H. Wallis. High-efficiency, Low-leakage MOCVD-grown GaInAs/AlInAs Heterojunction Photodiodes For Detection to  $2.4\mu\text{m}$ . *Electronics Letters*, 22(22):1206, 1986.
- [216] Gilberto A. Umana-Membreno. Personal communication, December 2020. University of Western Australia.
- [217] C30665 series datasheet. <https://www.excelitas.com/product/c30665gh-ingaas-pin-3mm-5>, Accessed 12/03/2021.
- [218] S S Y Chua, S Dwyer, L Barsotti, D Sigg, R M S Schofield, V V Frolov, K Kawabe, M Evans, G D Meadors, M Factourovich, R Gustafson, N Smith-Lefebvre, C Vorvick, M Landry, A Khalaidovski, M S Stefszky, C M Mow-Lowry, B C Buchler, D A Shaddock, P K Lam, R Schnabel, N Mavalvala, and D E McClelland. Impact of Backscattered Light in a Squeezing-Enhanced Interferometric Gravitational-Wave Detector. *Classical and Quantum Gravity*, 31(3):035017, January 2014.
- [219] C Gräf, B W Barr, A S Bell, F Campbell, A V Cumming, S L Danilishin, N A Gordon, G D Hammond, J Hennig, E A Houston, S H Huttner, R A

- 
- Jones, S S Leavey, H Lück, J Macarthur, M Marwick, S Rigby, R Schilling, B Sorazu, A Spencer, S Steinlechner, K A Strain, and S Hild. Design of a Speed Meter Interferometer Proof-of-principle Experiment. *Classical and Quantum Gravity*, 31(21):215009, Oct 2014.
- [220] J. Hennig. *Mirror Suspensions For the Glasgow Sagnac Speed Meter*. PhD thesis, University of Glasgow., 2018.
- [221] B. J. Meers and K. A. Strain. Wave-front Distortion in Laser-interferometric Gravitational-wave Detectors. *Physical Review D*, 43(10):3117–3130, May 1991.
- [222] Analog Devices. *AD797 Ultralow Distortion,ultralow Noise Op Amp*. Rev. K.
- [223] Argonne National Laboratory. Experimental Physics and Industrial Control System, MEDM: Motif Editor and Display Manager. <https://epics.anl.gov/extensions/medm/>, Accessed 10/03/2021.
- [224] A. A. Muzammil, C. Mueller, and G. Mueller. Optical Layout and Parameters for the Advanced LIGO Cavities. LIGO Document T0900043-v11 <https://dcc.ligo.org/LIGO-T0900043/public>.
- [225] LIGO Optics Database. <https://galaxy.ligo.caltech.edu/optics/> Accessed 09/03/2021.
- [226] R. Martin and G. Billingsley. Measurement Uncertainties in Determining the Radius of Curvature For SR2-04. LIGO Document T1300653-v1 <https://dcc.ligo.org/LIGO-T1300653>.

- [227] G. Billingsley. SR301 Figure Measurement. LIGO Document E1101231-v1  
<https://dcc.ligo.org/E1101231-v1>.
  
- [228] M. Smith and D. Coyne. Advanced LIGO L1 Optical Layout, Zemax. LIGO Document D0902216-v8 <https://dcc.ligo.org/LIGO-D0902216>.
  
- [229] C. Bond, P. Fulda, A. Freise, D. Brown, K. Kokeyama, L. Carbone, and A. Perreca. Finesse Input Files For the L1 Interferometer. LIGO Document T1300901-v5 <https://dcc.ligo.org/LIGO-T1300901>.